MICROBIOLOGICALLY INFLUENCED CORROSION (MIC) OF STAINLESS STEEL 304 AND COPPER-NICKEL ALLOY (70:30) AND ITS INHIBITION IN SEAWATER ENVIRONMENTS

By

YUAN SHAOJUN

(B. Sc., M. Eng. Tianjin University)

A THESIS SUBMITTED
FOR THE DEGREE OF DOCTOR OF PHILOSOPHY
DEPARTMENT OF CHEMICAL AND
BIOMOLECULAR ENGINEERING
NATIONAL UNIVERSITY OF SINGAPORE
2007

ACKNOWLEDGEMENTS

First of all I would to express my sincere gratitude to my supervisor: Dr. **Simo Olavi Pehkonen** for his inspired guidance, invaluable advice, constant supervision and great patience throughout the long period of this work. Dr. **Simo Olavi Pehkonen** gave me an opportunity to work with him. He has always been so generous in providing help and solutions when difficulties were encountered in my research. His advice was the key in improving the depth of the research; his serious attitude to scientific research and profound insight to my project are strongly impressed on my memory.

Special appreciation goes to Professor Kang En Tang and Associate Professor Ting Yen Peng for giving their help, supervision and significant comments for revising my thesis during the last semester.

Further thanks to Dr. Choong Mei Fun, Amy (TMSI) for her guidance in bacterial cultivating, and to Associate Professor Hong Liang for his kindly permission to access the electrochemical instruments, which was the most important tool in the my research.

I would also like to thank all my colleagues in- and outside our groups who contributed to bring this work to completion. Special thanks to Dr. Xu Fujian for sharing with me his great experience in surface modification. Thanks to Ms. Wang Xiaoling for the friendly atmosphere in the office. I am also grateful to my lab officers Ms. Susan Chia and Ms. Li Xiang for their assistance in the project.

Finally, I wish to give thanks to my deeply beloved wife Ye Zi, who had put up with me all the good and bad times. I specially thank my parents for their unconditional love and support. This work can not be completed without their constant encouragement.

TABLE OF CONTENTS

SUMMARY

Microbiologically influenced corrosion (MIC) is extremely harmful to maritime industries and to the environment, as approximately 20% of corrosion is estimated to be caused by MIC. This study was conducted to investigate the roles of microorganisms in the aerobic and anaerobic corrosion processes of stainless steel and copper nickel alloys in simulated seawater environments. Based on the results of MIC studies, novel surface modification techniques were developed to inhibit MIC of the metallic materials.

In the presence of aerobic *Pseudomonas* NCIMB 2021 bacterium, the corrosion of 304 SS was intensified and accelerated in nutrient-rich simulated seawater. The extensive pitting corrosion was found to occur underneath the heterogeneous biofilms due to the synergistic effect of aggressive chloride ions and the colonization of bacterial cells and their extra-cellular polymeric substances (EPS). The pits on the coupon surface were quantified through atomic force microscopy (AFM) sectional analyses, and the depth of pits increased linearly with exposure time. X-ray photoelectron spectroscopy (XPS) results revealed that the outermost layer of the surface films underwent a substantial change in elemental composition induced by the bacterial colonization. The enrichment of Cr and depletion of Fe in the surface film can be correlated with the pitting corrosion under the biofilms.

The involvement of aerobic *Pseudomonas* NCIMB 2021 bacterium in the corrosion process of 70/30 Cu-Ni alloys was verified. The corrosion rate of the alloy coupons was found to undergo a notable increase with exposure time due to extensive micro-pitting corrosion underneath the discrete biofilms and corrosion products. XPS results further revealed that the change in corrosion behavior of the alloy coupons could be correlated with the change in formation process of the oxide layers by the aerobic *Pseudomonas* bacteria.

A novel surface modification technique was developed to impart antibacterial and anticorrosive properties onto the surface-oxidized Cu-Ni alloy to inhibit MIC. The functionalized substrate exhibited high efficiency in preventing the bacterial attachment as well as a desirable resistance to MIC by a combination of the bactericidal properties of the quaternary ammonium salts and the inactive properties of the silanized surfaces. On the contrary, the oxide layers of Cu-Ni alloys were found to be vulnerable to MIC, although they could dramatically decrease the corrosion rate of the Cu-Ni alloy in the sterile medium.

Anaerobic corrosion of 304 SS was found to be significantly accelerated by *D. desulfuricans* in a simulated seawater-based Modified Baar's (SSMB) medium due to the occurrence of extensive localized corrosion underneath the deposits of bacterial cells and sulfide films. XPS results revealed that sulfide films were mainly composed of mackinawite (FeS) and pyrite (FeS_2), and mackinawite gradually converted to pyrite with exposure time in the biotic medium.

Well-defined multilayer coatings of Ti oxide/butoxide were built up on the surface of stainless steel coupons via layer-by-layer sol-gel processing to minimize MIC. It was demonstrated that not only did the passivity of the Ti oxide/butoxide coatings remain almost unchanged under the harsh environment of *D. desulfuricans* inoculated SSMB medium, the passivity was slightly enhanced with exposure time due to the deposition of apatite compounds. The well-structured coatings also prevented the substrate surface from initiating localized corrosion.

LIST OF ABBREVIATIONS

AC	Alternative Current
APB	Acid-Producing Bacteria
AES	Auger Electron Spectroscopy
AFM	Atomic Force Microscopy
BE	Binding Energy
β_a	Anodic Tafel Slopes
β_c	Cathodic Tafel Slopes
CCURB	Corrosion Control Using Regenerative Biofilms
CLSM	Confocal Laser Microscopy
CP	Cathodic Protection
CPE	Constant Phase Element
CTS	4-(Chloromethyl)-Phenyl Tricholorosilane
CV	Cyclic Voltammetry
DC	Direct Current
DMF	N,N'-Dimethylformamide
DO	Dissolved Oxygen
E_{corr}	Potentials Where the Current Reaches Zero under Polarization
EDL	Electric Double Layer
EDS	Energy Dispersive X-Ray Spectroscopy
EIS	Electrochemical Impedance Spectroscopy
ENA	Electrochemical Noise Analysis
EPS	Extracellular Polymeric Substances

FTIR	Fourier Transformation Infrared Spectroscopy
i_{corr}	Corrosion Current Densities
IOB	Iron-Oxidizing Bacteria
LPR	Linear Polarization Resistance
MIC	Microbiologically Influenced Corrosion
OCP	Open Circuit Potential
OD	Optical Density
PBS	Phosphate Buffered Saline Solution
QUATS	Quaternary Ammonium Compounds
Ra	Average Surface Root-Mean-Square Roughness
R_{ct}	Charge Transfer Resistance
RACE	Relative Atomic Concentrations of Elements
SAM	Self-Assembled Monolayer
SEM	Scanning Electron Microscopy
SOB	Sulfur-Oxidizing Bacteria
SOM	Surface-Oxidized Metal
SRB	Sulfate-Reducing Bacteria
SS	Stainless Steel
SSMB	Simulated Seawater-Based Modified Baar's Medium
SVEM	Scanning Vibrating Electrode Mapping
TEM	Transmission Electron Microscopy
Viologen	1,1'-Substituted-4,4'-Bipyridinium Salt
XPS	X-Ray Photoelectron Spectroscopy

LIST OF FIGURES

LIST OF TABLES

CHAPTER 1

INTRODUCTION

1.1 Overview of MIC

Microbiologically influenced corrosion or biocorrosion, is the initiation, facilitation or acceleration of corrosion due to the interaction between microbial activity and corrosion process. It is a common phenomenon in natural aquatic environments due to the ubiquitous distribution of microorganisms (Flemming, 1996). The electrochemical model of corrosion still remains valid for MIC (Videla, 1996). However, the participation of microorganisms in the corrosion process introduces several specific features: (i) from a two-component system of electrochemical corrosion: metals and an electrolyte, MIC becomes a three-component system: metals, electrolyte and microorganisms; (ii) microbial activity at the metal/solution interface can affect the kinetics and/or anodic reactions (Jones and Amy, 2002), and can also modify the chemistry of any protective layers, leading to either the acceleration or inhibition of corrosion (Little and Ray, 2002, Pak et al., 2003). Therefore, the study of MIC, as well as the build-up of any mechanisms to interpret a particular case of metal deterioration, must take into account the interactions between these three elements involved in the corrosion process.

Bacteria are considered the primary colonizers of inanimate surfaces in both natural and man-made environments. Therefore, the majority of MIC investigators have addressed the impact of pure or mixed culture bacteria on corrosion behavior of iron, copper, aluminum and their alloys. The main types of bacteria associated with metals in terrestrial and aquatic habitats are summarized in Table 1.1. These organisms typically coexist in naturally occurring biofilms, forming complex consortia on corroding metal surfaces (Zhang et al., 2003; Kjellerup et al., 2003).

Table 1.1 Bacteria known to cause microbiologically influenced corrosion

Genus of species	pH range	Temperature range °C	Oxygen requirement	Metals affect	Action
Bacteria					
Desulfovibrio					
Best known: *D. desulfuricans*	4-8	10-40	Anaerobic	Iron and steel, Stainless steel, Zinc, Aluminum, Copper alloys	Utilize hydrogen in reducing SO_4^{2-} to S^{2-} and H_2S; promote the formation of sulfide films
Desulfotomaculum					
Best known: *D. nigrificans*					
(also know as *Clostridium*)	6-8	10-40 (some 45-75)	Anaerobic	Iron and steel, Stainless steel	Reduce SO_4^{2-} to S^{2-} and H_2S (spore formers)
Desulfomonas	....	10-40	Anaerobic	Iron and steel	Reduce SO_4^{2-} to S^{2-} and H_2S
Thiobacillus thioxidans	0.5-8	10-40	Aerobic	Iron and steel, Copper alloy, Concrete	Oxidize sulfur and sulfide to form H_2SO_4; damages protective coatings
Thiobacillus ferrooxidans	1-7	10-40	Aerobic	Iron and steel	Oxidize ferrous (Fe^{2+}) to ferric (Fe^{3+})
Gallionella	7-10	20-40	Aerobic	Iron and steel	Oxidize Fe^{2+} (Mn^{2+}) to Fe^{3+} (Mn^{4+}); promote tubercle formation
Sphaerotillus	7-10	20-40	Aerobic	Iron and steel	Oxidize Fe^{2+} (Mn^{2+}) to Fe^{3+} (Mn^{4+}); promote tubercle formation
S. natans	....	....	....	Aluminum alloys	
Pseudomonas	4-9	20-40	Aerobic	Iron and steel, Stainless steel	Some strains can reduce Fe^{3+} to Fe^{2+}
P. aeruginosa	4-8	20-40	Aerobic	Aluminum alloys	
Fungi					
Cladosporium resinae	3-7	1-45 (best 30-35)	....	Aluminum alloys	Produces organic acids in metabolizing certain fuel constituents

From Dexter, S.C. metals handbook, Vol. 13, corrosion, 9th ed., ASM international, p.114, 1987

MIC is a result of interactions, which are often synergistic, among the metal surface, abiotic corrosion products, and bacterial cells and their metabolites. The process is normally accompanied by biofilm formation (Siedlarek et al., 1994). Biofilms are structurally and dynamically complex biological systems, consisting of cells embedded in a highly hydrated, extracellular polymeric matrix (Costerton et al., 1981). The biofilm formation on the metal surface results in drastic changes at the metal/biofilm interface, such as highly localized changes in concentration of electrolyte constituents, lowering of pH due to the secretion of acidic metabolites, the local depletion of oxygen as a result of microbial respiration within the biofilm, and the selective dissolution of alloying elements (George et al., 2000, 2003; Gubner et al., 2000). These changes may have different effects, ranging from facilitating or impeding anodic and cathodic reactions of the corrosion process, to the induction of localized corrosion (Videla and Herrera, 2005). The forms of corrosion caused by microorganisms are manifested in diverse localized corrosion, including pitting corrosion, crevice corrosion, selective dealloying, stress cracking and under-deposit corrosion (Little et al., 1999).

1.2 A brief historical review of MIC research

Even though the first reports on MIC go back to the turn of the twentieth century (Gaines, 1910), its rational interpretation only began to be rigorous in the mid-1960s. The only exception is the pioneering work of von Wolzogen Kuhr and van der Flugt in 1934, which can be considered the first attempt to interpret MIC electrochemically with the classic cathodic depolarization theory. Until the 1960s, the relatively few publications on the subject only dealt with practical cases, mainly those involving underground bacterial corrosion of iron pipes and structures (Starkey and Wight, 1945; Hadley, 1948). During 1960s and early 1970s, research on MIC was devoted either to objecting to or validating the anaerobic corrosion of iron by SRB as explained by the cathodic depolarization theory. Within that period, electrochemical techniques, such as polarization experiments, corrosion potential versus time measurements, coupled with microbiological methods, were introduced to assess the effect of SRB on iron corrosion (Booth and Tiller, 1962; Iverson, 1966).

However, the role of MIC is often ignored if an abiotic mechanism can be invoked to explain the observed corrosion phenomenon. MIC, as a significant phenomenon, was not considered seriously as a practical form of destruction of modern industry until the mid-1970s, when the involvement of microbes in a rapid through-wall pitting of stainless steel water tanks was positively identified as the cause of the otherwise puzzling attack. Since that time, MIC has received considerable attention in power generation, oil production, chemical processing, transportation, and the pulp and paper industries (Geesey et al., 1994). In the 1980s, with the development of new sophisticated techniques for the study of the metal-solution interface, MIC has attracted more attention of different research disciplines, including microbiology, electrochemistry, and materials science, and has been increasingly acknowledged. Several possible mechanisms have been therefore proposed to interpret the MIC of metallic materials by different genus of bacterial strains.

In recent years, with the rapid development of advance surface analytical, biological, and electrochemical techniques, such as SEM-EDX, AFM, XPS, and EIS, the investigations into MIC have focused on the subtle changes at the biofilm/metal interface induced by the microbial activities, such as biomineralization processes taking place on metallic surfaces, and the impact of extracellular enzymes within the biofilm matrix on the electrochemical reactions at the biofilm/metal interface etc (Beech et al., 2004).

1.3 The economic significance of MIC research

Corrosion of metallic materials causes vast economic damages, and is therefore of great concern. According to recent investigations, damage due to material corrosion in the United States resulted in costs of $276 billions in many field of the industry (Koch et al., 2002). Among the various corrosion processes, the MIC of materials is reported to account for up to 50% of the damage costs (Hamilton, 1985; Tiller, 1988; Fleming, 1996). The industries that are suffering loss due to MIC most severely include the nuclear and fuel electric power generating sectors, pipelines, oil fields and offshore industry (Dowling and Guezennec, 1997). In some municipal systems, such as drinking water distribution system, high rates of MIC not only cause significant losses to the economy, but also directly affect the public health by the release of toxic ions (Volk et al., 2000). It is therefore of great significance to understand the mechanisms of MIC, and to find an environmental and economic way to inhibit MIC.

1.4 Research Objectives and Scope

Despite the considerable efforts over the years to determine the roles of microorganisms in MIC, the detailed mechanism of MIC are still poorly understood. This is due to the inefficacy of conventional methodologies in studying the interaction between microorganisms and metal surface at the interface, the changes in surface chemistry caused by the presence and physiological activities of the microbial consortia. Thereby, much controversy still remains in interpreting the way in which microorganisms are involved in the corrosion process and whether they are able to modify the electrochemical reactions. Furthermore, many challenges also remain in establishing feasible methods to inhibit MIC by biocide treatments, which are usually detrimental to environments. In recent years, there has been a renaissance in the investigation of MIC mechanisms with the development of novel electrochemical and surface spectroscopic techniques. The diverse activities in this project therefore constitute a concerted effort to address several major aspects and problems associated with the MIC of stainless steel and copper alloys.

The purpose of this project is to determine the roles of microorganisms in the aerobic and anaerobic corrosion processes of stainless steel and copper nickel alloys in simulated seawater environments. Two types of marine bacteria strains are therefore selected as inoculums: one is a marine aerobic *Pseudomonas* NCIMB 2021 bacterium and the other is a marine anaerobic *Desulfovibrio desulfuricans* (ATCC 27774) bacterium. The aerobic *Pseudomonas* strain is chosen owing to its abundance in marine water and its propensity to enhance corrosion in steels and aluminum alloys (Vaidya et al., 1997). The anaerobic sulfate-reducing bacteria of *D. desulfuricans* strain are one of the most abundant anaerobic bacteria in seawater and commonly associated with the deterioration of iron, steels, coppers and their alloys (Fleming, 1996). Based on the results of MIC studies, a novel surface modification technique, which attempts to combine the bactericidal properties of the quaternary ammonium salts with the inactive properties of the silane and pyridinium-type polymer layers, are developed to endow copper nickel alloys with antibacterial and anticorrosive properties to combat MIC. At the same time, the well-defined multilayer sol-gel coatings of Ti oxide/butoxide are also incorporated on the stainless steel surface to minimize the effect of microorganisms.

Chapter 2 presents an overview of the related literatures on MIC and its inhibition.

Chapter 3 delineates the influence of the aerobic *Pseudomonas* strain on the corrosion behavior of 304 SS in nutrient-rich simulated seawater, as investigated by electrochemical and SEM-EDX measurements in comparison with the sterile control experiments. Emphasis was placed on the electrochemical impedance spectroscopy (EIS) data to elucidate the sequence of process occurring at the metal/biofilm interface. Cyclic polarization curves coupled with SEM observation were used to verify the localized corrosion underneath the biofilms. Energy dispersive X-ray (EDX) spectra were recorded inside the pits to reveal the implication of aggressive chloride ions and bacterial cells in the localized corrosion on the coupon surface.

In chapter 4, the biofilm formation and the biocorrosion of 304 SS by the aerobic *Pseudomonas* strain were investigated using AFM and XPS. AFM not only can provide the topographical images of the coupon surface at molecular resolution, but can perform accurate measurement in vertical dimension with sectional analysis. The depth of pits on the coupon surface was further monitored at various exposure times by AFM to determine the corrosion damage of coupon surface underneath biofilms. The subtle change in the surface chemistry induced by the colonized *Pseudomonas* bacteria was further explored using XPS.

The influence of the aerobic *Pseudomonas* stain on the corrosion behavior of 70/30 Cu-Ni alloys in nutrient-rich simulated seawater was explored by electrochemical measurements and XPS in chapter 5. An attempt was made to correlate the corrosion behavior of the alloy coupons with the change in the structure of the surface film caused by the colonizing bacteria on the coupon surface. Thus, the evolutions of passive films on the coupon surface with exposure time in the presence and the absence of the *Pseudomonas* bacteria were thoroughly investigated.

Chapter 6 describes a novel surface modification method to impart the bactericidal and anticorrosive properties on the surface-oxidized Cu-Ni alloys. A viologen monolayer and a silane layer were immobilized on the substrate surface via a series of chemical reactions to mitigate MIC by the aerobic *Pseudomonas* strain. The success of each functionalized step was ascertained by XPS, AFM and static water contact angle measurements. The assessment of bactericidal efficiency was performed with SEM, while the inhibition efficiency of the polymeric layers was evaluated by the measurement of Tafel plots and EIS data. Combination of the properties of the pyridinium-type polymer and the silane layers yields a simple and effective method for minimizing the influence of microorganisms on the metallic substrates.

In chapter 7, the anaerobic corrosion behavior of 304 SS in a biotic simulated seawater-based Modified Barr's medium containing *D. desulfuricans* bacteria was explored with AFM, XPS and SEM-EDX to reveal the occurrence of localized corrosion under the bacterial cells and sulfide films. The evolution of sulfide films with exposure time was monitored with XPS. On the other hand, well-defined multilayer Ti oxide/butoxide coatings were built up via layer-by-layer sol-gel processing on the 304 SS surface. The corrosion resistance and the structure of the Ti oxide/butoxide coatings were evaluated respectively with Tafel plots and EIS measurement in the biotic SSMB medium containing *D. desulfuricans* bacteria, and compared with those of the three types of uncoated coupons. The bioactive properties of the coatings were verified by EDX spectra.

Finally, Chapter 8 summarizes all the salient findings of this work and suggestions for further studies.

CHAPTER 2

LITERATURE REVIEW

2.1 Biofilm formation

MIC is due to the formation of biofilm on the solid surface in the aquatic environments. Microorganisms attach themselves to the surface by secreting extracellular polymeric substances (EPS) to form colonies, then proliferate and excrete EPS to form a biofilm, which is schematically shown as the Figure 2.1. Biofilm is a micro-environment comprising of microbial cells, their EPS, inorganic precipitates derived from the bulk aqueous phase and/or corrosion products of the metal substratum. EPS consist of a complex mixture of cell-derived polysaccharides, proteins, lipids and nucleic acids, and are responsible for the structural and functional integrity of the biofilm as well as the key component that determines its physicochemical and biological properties (Wingender et al., 1999). Generally, EPS may account for 50-90% of the total organic matters in the biofilm (Christense and Characlis, 1990; Nielsen et al., 1997).

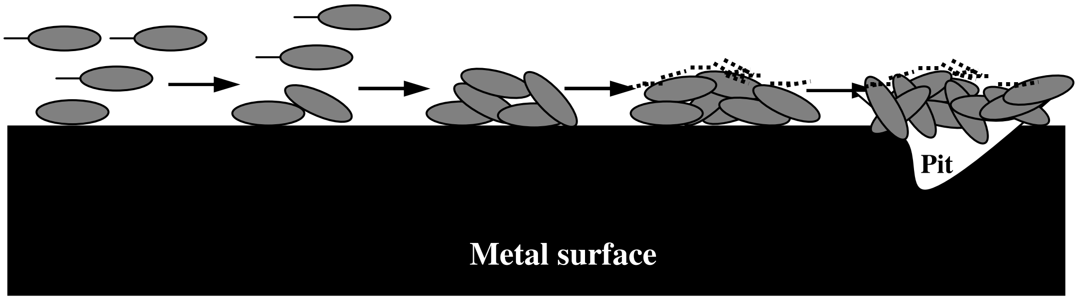

Figure 2.1 Schematic illustration of biofilm formation and pit corrosion

Biofilm formation is a combined physical, chemical and biological process (Christense and Characklis, 1990). It may be influenced by the properties of substratum surface, nutrient availability, pH, temperature, hydrodynamic shear stress, etc. (Little et al., 1997). Microorganisms within the biofilm are capable of maintaining an environment that is radically different from that of the bulk medium in pH and dissolved oxygen (DO), as well as concentrations of various inorganic and organic species. Such concentration gradients and functional heterogeneities inside the biofilm result in the localized corrosion conditions, and accelerate corrosion (Hamilton, 1990). On the other hand, biofilm may be protective to the surface, preventing diffusion of DO, aggressive anions such as chloride, and metabolic products (Jayaraman et al., 1997a, 1997b). However, the heterogeneous biofilm usually leads to the localized corrosion of the metallic substratum.

2.2 Mechanism of MIC

The colonization of metal surfaces by microorganisms or biofilms drastically changes the classical concept of the electrical interface commonly used in inorganic corrosion: important changes in the type and concentration of ions, oxygen, pH, and oxidation-reduction potential are induced by the biofilm, altering the passive or active behavior of the metallic substratum and its corrosion products, as well as the electrochemical variables used for assessing corrosion rates (Chamberlain and Garner, 1988; Lewandowski et al., 1988; Ghiorse, 1988; Videla and Characklis, 1992). As a result, the role of microorganisms or biofilms in enhancing corrosion in a biologically conditioned metal-solution interface is diverse, and may proceed through simultaneous or successive mechanisms as summarized below:

(1) The formation of concentration cells

Under aerobic conditions, non-uniform or patchy colonization by microbial biofilms result in the formation of differential aeration cells, where areas under respiring colonies are depleted of oxygen relative to surrounding non-colonized areas. These effects give rise to potential differences and, consequently, to corrosion currents. The areas under respiring colonies become anodic, leading to metal dissolution. Conversely, in the surrounding cathodic areas the counter-reactions of oxygen reduction take place.

Differential aeration cells can produce severe localized corrosion in the forms of crevices and pits. The differential aeration cells formed by oxygen depletion under a microbial surface film are illustrated as the following Figure 2.2 (Ford and Mitchell, 1990). Apart from oxygen concentration cell, the microbial activities in biofilm can also result in the localized ionic exchanges within the biofilm, and produce pH and ionic concentration cells. The profiles of oxygen and pH across the biofilm have been determined by microelectrodes (Beer et al., 1994; Lee and Beer, 1995; Xu et al., 1998; Dexter and Chandrasekaran, 2000).

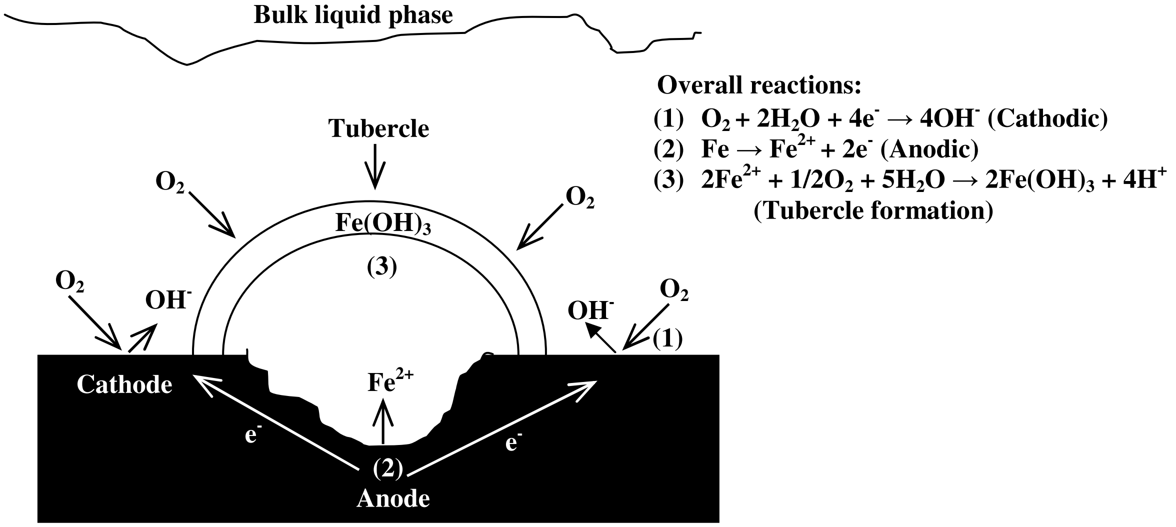

Overall reactions:

(1) $O_2 + 2H_2O + 4e^- \rightarrow 4OH^-$ (Cathodic)

(2) $Fe \rightarrow Fe^{2+} + 2e^-$ (Anodic)

(3) $2Fe^{2+} + 1/2O_2 + 5H_2O \rightarrow 2Fe(OH)_3 + 4H^+$ (Tubercle formation)

Figure 2.2 Differential aeration cells formed by oxygen depletion under a microbial surface film (Ford & Mitchell, 1990).

(2) Production of corrosive metabolites

Due to the wide variety of metabolic products derived from the microbial activity, this mechanism was subdivided by Miller (1981) as follows: (i) production of substance with surfactant properties; (ii) production of inorganic acid; (iii) production of carboxylic acid as metabolic end-products or by leakage of tri-carboxylic acid cycle intermediates; (iv) production of sulfide ions as in case of SRB. MIC by sulfur-oxidizing bacteria (SOB) seems to be one of the simpler cases of metal attack due to biological agents. *T.*

thiooxidans and *T. ferroxidans* can produce hazardous quantities of sulfuric acid and still active at a pH as low as 0.7. Under these conditions, cast-iron or mild steel structures are severely attacked (Tuovinen and Kelly, 1974; Cragnolino and Tuovinen, 1984). Nitric acid and nitrous acid are also produced by bacteria belonging to the groups of ammonia-oxidizing and nitrite-oxidizing bacteria (Beech et al., 2000). EPS secreted by slime-producing bacteria (SPB) are usually acidic. They may contain functional groups, such as carboxylic and amino acids. EPS produced by sulfate-reducing bacteria (SRB) have been reported to be responsible for the corrosion of mild steel (Beech et al., 1998).

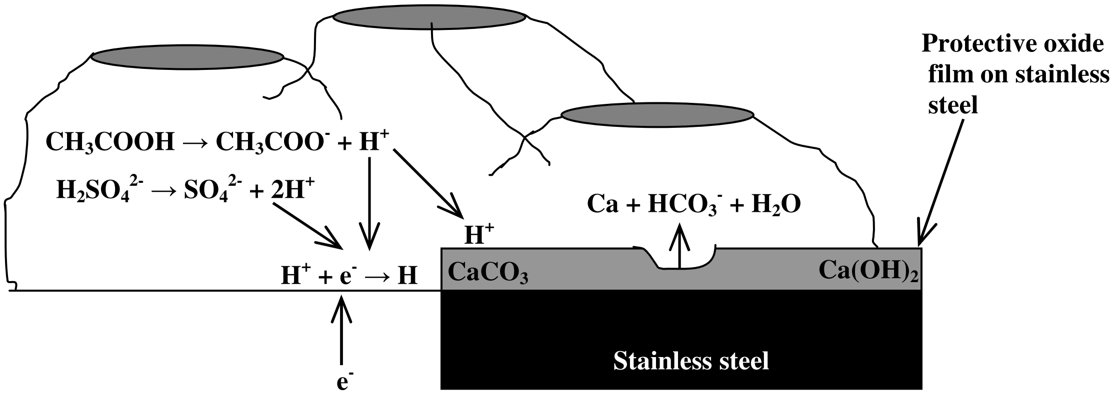

Figure 2.3 Acid productions (organic or inorganic) by adherent film-forming bacteria with consequent promotion of electron removal from cathode by hydrogen or dissolution of protective calcareous film on stainless steel surface (Borenstein, 1994)

Most heterotrophic bacteria can release organic acids, such as acetic, succinic, isobuteric etc., during fermentation of organic substrates. The kinds and amounts of acids produced depend on the type of microorganisms and the available substrate molecules. The impact of acidic metabolites is intensified when they are trapped at the biofilm/metal interface (Little et al., 1992). According to Borenstein (1994), Figure 2.3 showed that under laboratory conditions, aerobic acetic acid-producing bacteria could accelerate the corrosion of cathodically protected stainless steel in synthetic salt solution. The acetic acid destabilizes or dissolves the calcareous film that formed during cathodic polarization.

(3) Depolarization of the cathodic reaction

A classical depolarization mechanism was proposed to interpret the anaerobic SRB-induced corrosion of iron by von Wolzogen Kühr and van der Vlugt (1934). SRB have the ability to remove the cathodic hydrogen via hydrogenase and accelerate the anodic dissolution. Booth and Tiller (1960, 1962), using polarization techniques and weight loss measurements versus hydrogenase activity, have presented evidence for the theory. Iverson (1966) demonstrated the cathodic depolarization of mild steel by *Desulfovibrio desulfuricnas* with benzyl viologens used as an electron acceptor. Details of cathodic depolarization and other mechanisms proposed for SRB-induced corrosion will be discussed in detail in Section 2.4.3.1.

(4) Metal oxide deposition due to microbial activity

Some bacteria of different genera participate in the biotransformation of oxides of metals, such as iron-oxidizing bacteria (IOB) and manganese-oxidizing bacteria (MOB). Iron-depositing bacteria (IOB), such as *Sphaerotilus*, *Gallionella* and *Leptothrix* etc., produce orange-red tubercles of iron oxides and hydroxides by oxidizing ferrous ions (Fe^{2+}) to ferric ions (Fe^{3+}), catalyzing the deposition of tubercles, especially on stainless steel weld seams (Brözel & Cloete, 1989). Tubercle formation may result in under-deposit corrosion for susceptible alloys. Manganese-oxidizing bacteria (MOB) are capable of oxidizing manganous ions (Mn^{2+}) to manganic ions (Mn^{4+}) with a concomitant deposition of manganese dioxide. The formation of organic and inorganic deposits by metal-depositing bacteria on the oxide surface can compromise the stability of the passive oxide film of alloys, and thus promote corrosion reactions with the catalysis of ferric and manganic oxides or creating differential aeration cells (Dickinson and Lewandowski, 1996). Furthermore, the iron/manganese-oxidizing bacteria can also attract chloride to produce ferric chloride, which is extremely aggressive and readily pits stainless steel (Borenstein, 1994). Figure 2.4 delineates the process of metal deposition due to microbial activity and the induction of pitting corrosion.

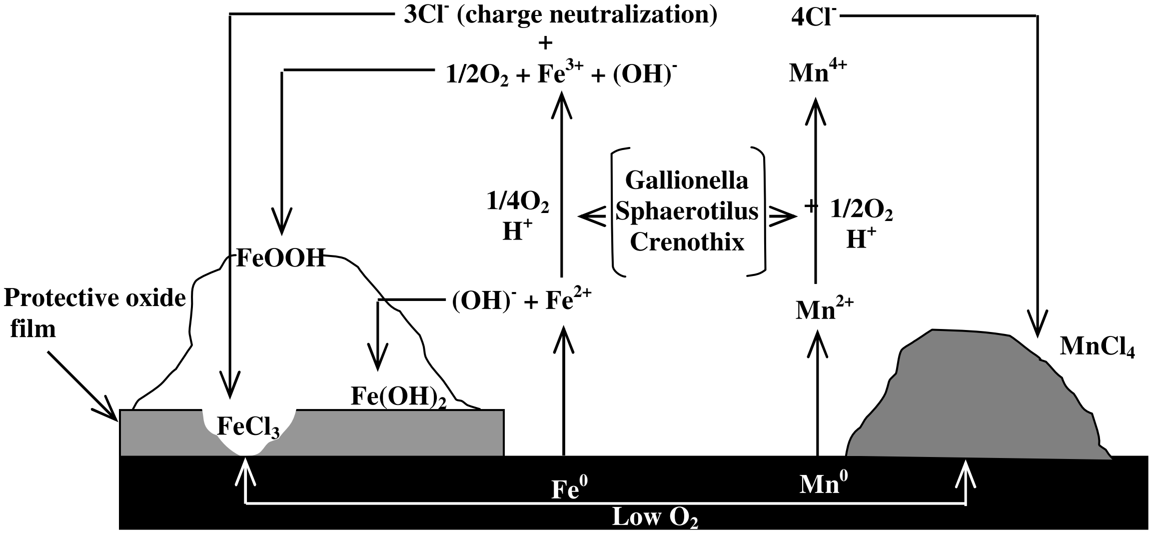

Figure 2.4 Iron and manganese oxidation and precipitation in presence of filamentous bacteria. Stainless steel pitting in the presence of chloride ions concentrated at surface in the response to charge neutralize of ferric and manganic cations (Borenstein, 1994)

In addition, metal-depositing bacteria have been found to contribute to a noble shift in the corrosion potential and increase in cathodic current density, which are common phenomena in MIC of stainless steel (Lewandowski et al., 1997; Linhardt, 1997; Ruppel et al., 2001; Dexter et al., 2003; Dexter, 2003).

2.3 Aerobic microbial corrosion

Aerobic microbial corrosion involves complex chemical and microbial processes due to metabolic activities of different groups of microorganisms. Usually, even in aerobic corrosion, oxygen concentration may be very low, for instance underneath microbial colonies or biofilms (Costerton et al., 1995; Santegoeds et al., 1999; De Beer and Stoodley, 2000). The anodic dissolution of iron (Fe) to ferrous ions (Fe^{2+}) preferentially occurs at such microoxic to anoxic sites, whereas electrons flow to the other sites where they can reduce molecular oxygen (Miller, 1981). It has been reported that the importance of microorganisms in aerobic degradation of metals may be significantly underrated due to the fact that microbial and chemical corrosion enhance each other under aerobic conditions, and it is difficult to differentiate between the two processes (Ford and Mitchell, 1990).

The most apparent influence of an aerobic community on a metal surface is the creation of differential aeration cells. This process is know as tuberculation (Lee et al, 1995), and is schematically shown as Figure 2.2. Other aerobic microbial processes, such as the formation of ion concentration cells, bacterial polymer-metal interactions, activities of metal-transforming and acid-producing bacteria, and thermophillic reactions may also accelerate corrosion (Ford and Mitchell, 1990). The acid-producing bacteria and metal-depositing bacteria as described in Section 2.2 are common aerobic bacteria that contribute to the acceleration of corrosion of metals. Another group of aerobic bacteria that may be also involved in metal deterioration are fungi and algae. In fuel and oil storage tanks, fungi species, such as *Aspergillus*, *Penicillium* and *Fusarium*, may grow on fuel components and produce carboxylic acids to corrode iron (Iverson, 1987; Little and Wagner, 1997; Little et al., 2001). In the presence of light, algae can produce organic acids and decrease the local pH, thereby favoring corrosion of metals (Mara and Williams, 1972).

In addition to acid-producing bacteria and metal-depositing bacteria, bacteria in the genus *Pseudomonas* and pseudomonas-like organisms have been reported in connection with cases of corrosion (Iverson, 1987). *Pseudomonas* species, most prevalent in industrial water and seawater environments, have been found to be involved in the corrosion of mild steel, stainless steel and aluminum alloys in numerous marine habitats (Morales et al., 1993; Moreno et al., 1993; Pedersen et al., 1988; Beech et al., 2000; Coetser et al., 2005; Valcarce et al., 2005). Initially, aerobic *Pseudomonas* strains are recognized to be the pioneer colonizer in the process of bioiflm formation, and their primary role appears to create oxygen-free environment to harbor the SRB. However, it was subsequently found that these strains are aerobic slime-formers and often grow in a patchy distribution over the metal surface and exclude oxygen via respiration; the slime impedes oxygen diffusion, creating an oxygen concentration cell (Borenstein, 1994). Various *Pseudomonas* isolates have also been demonstrated to be implicated in the reduction of ferric (Fe^{3+}) to ferrous iron (Fe^{2+}), exposing steel to further oxidation since ferrous iron is more soluble and the protective ferric iron layer is solubilized by this process (Coetser and Cloete, 2005). Several previous studies have been conducted to elucidate the contribution of *Pseudomonas* to the corrosion process. Pedersen et al. (1988) and Videla (1996) reported that *Pseudomonas* sp. facilitated the passivity breakdown by excreting organic acids, thus resulting in the increase in the corrosion rates of metals. Morales et al. (1993) and Franklin et al. (1991) found that the heterogeneous biofilm of *Pseudomonas aeruginosa* formed on the metal surface could create differential aeration cells or metal ion concentration cells, thereby causing the occurrence of pitting corrosion. Busalmen et al. (1998, 2002) attributed the acceleration of the cathodic oxygen reduction to the catalytic effect of biogenetic catalase, which was excreted by the *Pseudomonas* bacterial cells attached on the metal surface.

Recently, Beech et al. (2000, 2004) proposed that the metal cation binding by EPS promoted the ionization of the metal surface, thus resulting in metal ion concentration cells and changing the electrochemical nature of the metal surface. The capacity of EPS to bind metal ions is important to MIC (Kinzler et al., 2003; Rohwerder et al., 2003) and depends on bacterial species, and on the type of metal ions (Beech and Sunner, 2004). Metal binding by EPS involves interaction between the metal ions and anionic functional groups, such as carboxyl, glycerate, pyruvate and succinate groups, which are common on the protein and carbohydrate components of exopolymers. In particular, the affinity of multidentate anionic ligands for multivalent ions, such as Cu^{2+}, Ca^{2+} and Fe^{3+}, can be very strong. The presence of, and affinity for, metal ions in different oxidation states in the biofilm matrix can result in substantial shifts in the standard reduction potentials. EPS-bound metal ions can, therefore, act as electron 'shuttles' and open up novel redox reaction pathways in the biofilm-metal interface. Figure 2.5 depicts a schematic model of

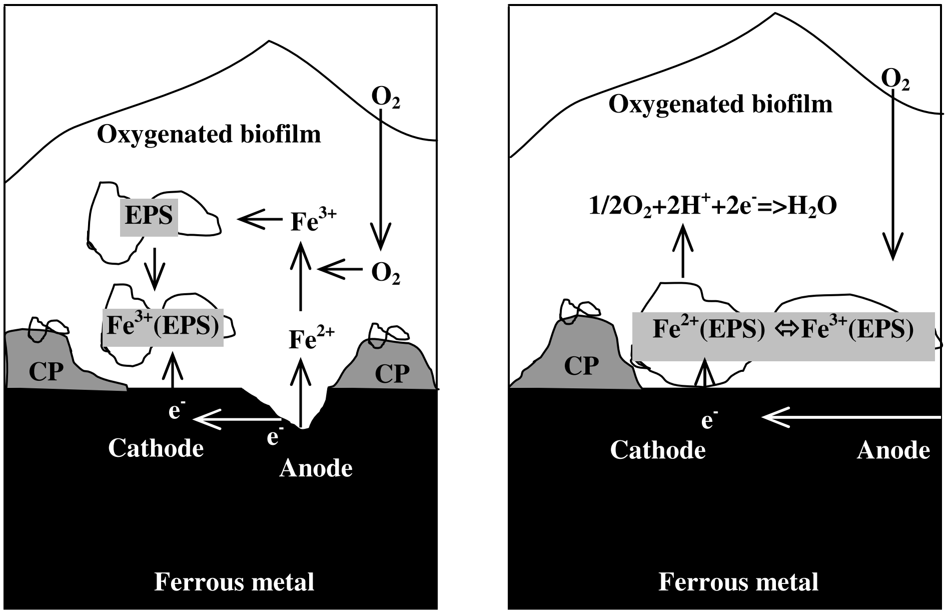

Figure 2.5 Schematic representation of the cathodic depolarization reaction of a ferrous sample in the presence of an oxygenated biofilm, owing to Fe^{3+} binding by EPS. (a) Fe^{3+}, obtained as a result of oxidation of anodically produced Fe^{2+}, is bound with ESP, and Fe^{3+}-EPS complex is deposited on the metal surface. (b) Electrons are transferred directly from the zero valent Fe to EPS-bound Fe^{3+}, reducing it to Fe^{2+}. In the presence of oxygen, acting as a terminal electron acceptor, Fe^{2+} in EPS is reoxidized to Fe^{3+}. Note that a similar type of reaction can take place on the surface of corrosion products, such as oxides, hydroxides and sulfide, which contain divalent iron (Beech and Sunner, 2004).

corrosion reactions involving EPS-bound metal ions in oxygenated biofilms using ferrous metal as an example. A recent study of iron-hydroxide-encrusted biofilms collected from a subterranean location revealed bacterial EPS, most likely acidic polysaccharides, could act as a template for the assembly of akaganeite (β-FeOOH) Pseduo-single crystals (Chan et al. 2003).

2.4 Anaerobic microbial corrosion

Various investigators have associated the sulfate-reducing bacteria (SRB) as the most widely distributed and economically important organisms with anaerobic microbial corrosion, especially *Desulfovibrio desulfuricans*. SRB are also proposed to be the principal causative organism of MIC in environments with a high sulfate concentration, such as seawater (Hamilton, 1985; Ford and Mitchell, 1990; Boivin and Costerton, 1991; Lee et al., 1995; Barton, 1997). They have been also branded as the most troublesome microorganisms to control due to their anaerobic growth potential underneath biological slimes or biofilms (Von Holy, 1987). Other microorganisms involved in anaerobic biocorrosion are APB, iron-reducing bacteria (IRB) and hydrogen-producing bacteria (Ford and Mitchell, 1990; Brözel, 1990; Boopathy and Daniels, 1991; Little et al., 1997)

2.4.1 Physiology and phylogeny of SRB

SRB are a ubiquitous group of prokaryotic microorganisms, which are abundant in natural habitats, such as marine and fresh water sediments or sludges, and play a key role in the biogeochemical sulfur cycle (Widdel, 1988; Fauque, 1995). They are obligate anaerobes that gain energy for growth by oxidizing organic compounds or hydrogen (H_2) with sulfate (SO_4^{2-}), and releasing hydrogen sulfide (H_2S) (Postgate, 1984; Barton and Tomei, 1995; Rabus et al., 2000). This process is especially important in marine systems because the abundance of sulfate in seawater allows SRB to overwhelm methanogens in the anaerobic environments. Alternatively, several SRB may reduce nitrate, sulfite, thiosulfate or fumarate with organic compounds or H_2 to gain energy for growth (Widdel, 1988; Rabus et al., 2000).

SRB are mostly curved, oval- or rod-shaped, with diameters normally ranging from 0.5 to 2.0 µm. Many SRB are motile due to their presence of flagella. Some SRB are spherical long multi-cellular filaments. Physiologically, SRB are divided into two broad categories distinguished by their nutritional and biochemical characteristics. The incomplete oxidizers degrade organic substrates, such as lactate or higher fatty acids, to acetate as the final product. The complete oxidizers, in contrast, mineralize organic substrates including acetate to CO_2 (Postgate, 1984; Widdel and Bak, 1992; Rabus et al., 2000). It was reported that the incomplete oxidizers do not have the operating enzymatic substrate (Hansen, 1993). Typical oxidation pathways by these two genera are listed as

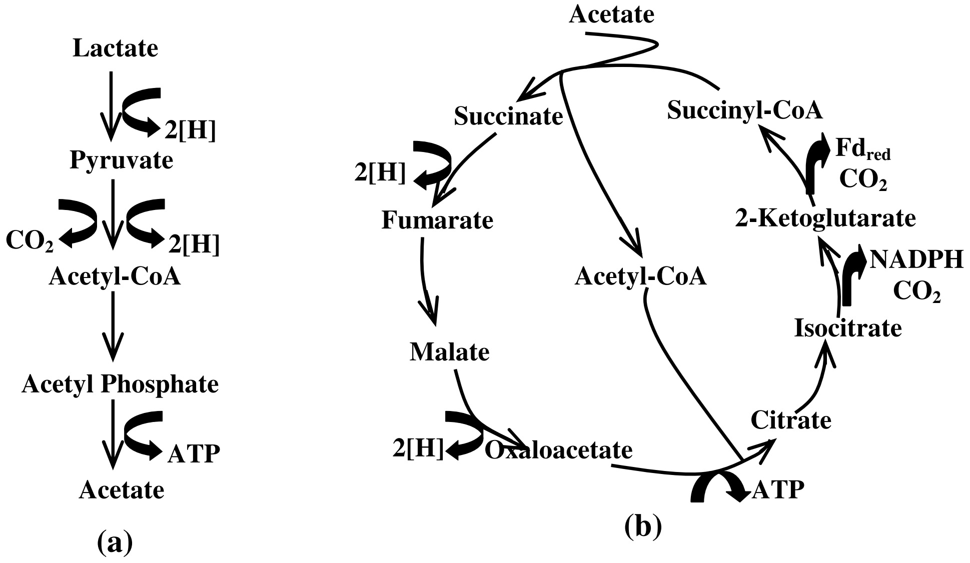

Figure 2.6 Schematic illustration of the oxidation pathway for two different genera. (a) pathway of lactate oxidation by *Desulfovibrio*; (b) pathway of acetate oxidation by *Desulfobacter* (Fd_{red}: reduced ferredoxin). (Hansen, 1993).

mechanism that allows the oxidation of the acetyl-CoA produced from the degradation of Figure 2.6. The incomplete oxidizers may grow significantly faster than the complete oxidizer. For example, *Desulfovibrio* species using hydrogen, lactate or pyruvate may have a doubling time of 3 to 4 hours under optimum conditions; whereas *Desulfobacter* species using acetate as their sole or preferred substrate may have a doubling time of 20 hours.

2.4.2 Hydrogenases in SRB

An important metabolic feature of many anaerobic microorganisms is the hydrogenase system responsible for the oxidation and production of molecular hydrogen (Fauque et al., 1988). The enzyme hydrogenase (H_2ase) catalyzes the reversible reaction:

$$H_2 \Leftrightarrow 2H^+ + 2e^- \tag{2-1}$$

The enzyme, mostly in *Desulfovibio* species, has been investigated biochemically as well as genetically. SRB have been shown to possess species-specific combination of three classes of hydrogenases, which differ by their metal content and are accordingly designated as [Fe]-, [NiFe]- and [NiFeSe]-hydrogenases (Odom and Peck, 1984; Fauque et al., 1988; Rabus et al., 2000). These three types of hydrogenases are remarkably different from each other in their catalytic activities, their molecular structures and their sensitivity to specific inhibitors, such as CO, NO, NO_2^- and acetylene (Fauque et al., 1988; Rabus et al., 2000). Most hydrogenases are located in the periplasmic space, and more than one type of hydrogen is frequently observed (Glick et al., 1980; Odom and Peck, 1984; Fauque et al., 1988). The oxidation of hydrogen (H_2) in *Desulfovibio* is reported to occur on the periplasmic side of the cytoplasmic membrane. Figure 2.7 depicts the function of hydrogenase in anaerobic biocorrosion (Bryant and Laishley, 1989).

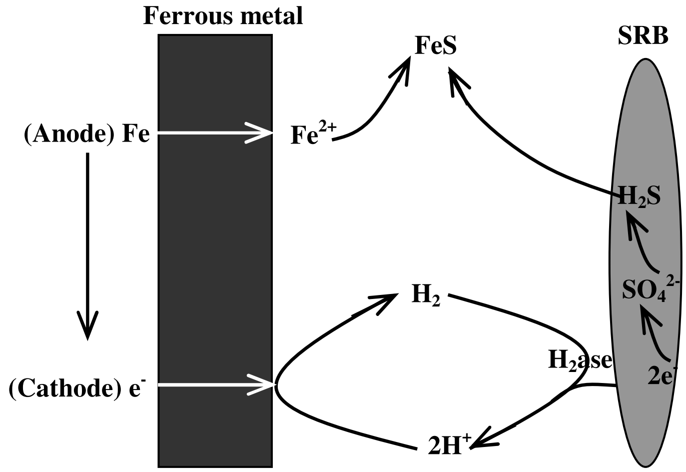

Figure 2.7 The proposed function of hydrogenase in anaerobic biocorrosion (Bryant and Laishley, 1989)

Hydrogen is an interspecies electron and proton transfer metabolite in microbial food chains, and its metabolism in these organisms helps to explain corrosion of metals (Odom and Peck, 1981). The following mechanism for the hydrogen electrode reaction in the absence of H_2S is generally accepted (Bockris and Pentland, 1952):

$$M + H^+ \rightarrow M - H_{ads} \tag{2-2}$$

$$M - H_{ads} + M - H_{ads} \rightarrow H_2 + 2M \tag{2-3}$$

$$M - H_{ads} + H^+ + e^- \rightarrow H_2 + M \tag{2-4}$$

The enzyme hydrogenase produced by SRB was reported to play an important role in the cathodic depolarization process (Booth and Tiller, 1960; Hardy, 1983; Bryant et al., 1991). Booth and Tiller (1960) observed a direct relationship between the hydrogenase activity and the cathodic depolarization in the culture of *Desulfovibrio desulfuricans*. Using [^{35}S] sulfate to follow respiration, Hardy (1983) demonstrated that the utilization of cathodic hydrogen by SRB. Bryant et al. (1991) reported that hydrogenase activity in the SRB might influence the biocorrosion process and also was subject to repression or induction mechanisms. However, when H_2S is present, there is an increase in proton discharge but the hydrogen evolution rate is suppressed (Lee et al., 1995).

2.4.3 Mechanisms of anaerobic corrosion induced by SRB

Since the beginning of investigations into the effects of SRB on corrosion of cast iron in 1930s, the role of these bacteria in the pitting corrosion of various metal and their alloys in both aquatic and terrestrial environments has been confirmed under anoxic as well as oxygenated conditions. Different mechanisms, which have been proposed to explain the mechanisms by which SRB can influence the corrosion of metals, are summarized as Table 2.1. The detailed mechanisms are discussed as the follows:

Table 2.1 Proposed mechanism of metal corrosion induced by SRB

Corrosive process/substance	Reference
Cathodic depolarization* by hydrogenase	von Wolzogen Kühr et al.,1934; Bryant et al., 1991
Anodic depolarization	Daumas et al., 1988; Crolet, 1992
Sulfide	Little et al., 1998
Iron sulfide	King and Wakerley, 1973
A volatile phosphorous compound	Iverson and Ohlson, 1983
Fe-binding exopolymers	Beech and Cheung, 1995; Beech et al., 1996, 1998
Sulfide-induced stress corrosion cracking	Edyvean et al., 1998
Hydrogen-induced cracking or blistering	Edyvean et al., 1998

*Depolarization is an acceleration of the corrosion reaction and may involve removal of cathodic or anodic reactants.

2.4.3.1 Cathodic depolarization theory

The more frequently discussed mechanism of corrosion mediated by SRB is a depolarization via the oxidation of the cathodic hydrogen as formulated in the cathodic depolarization theory (von Wolzogen Kühr and van ver Vlugt, 1934). The proposed electrochemical reactions of steel corrosion are listed as follows:

$$4Fe \rightarrow 4Fe^{2+} + 8e^- \qquad \text{(Anodic reaction)} \qquad (2\text{-}5)$$

$$8H_2O \rightarrow 8H^+ + 8OH^- \qquad \text{(Water dissociation)} \qquad (2\text{-}6)$$

$$8H^+ + 8e^- \rightarrow 8H(ads) \qquad \text{(Cathodic reaction)} \qquad (2\text{-}7)$$

$$SO_4^{\ 2-} + 8H(ads) \rightarrow S^{2-} + 4H_2O \qquad \text{(Microbial depolarization)} \qquad (2\text{-}8)$$

$$Fe^{2+} + S^{2-} \rightarrow FeS \qquad \text{(Corrosion product)} \qquad (2\text{-}9)$$

$$3Fe^{2+} + 6OH^- \rightarrow 3Fe(OH)_2 \qquad \text{(Corrosion product)} \qquad (2\text{-}10)$$

$$4Fe + SO_4^{\ 2-} + 4H_2O \rightarrow 3Fe(OH)_2 + FeS + 2OH^- \qquad \text{(Overall reaction)} \qquad (2\text{-}11)$$

In aqueous environments, atomic hydrogen is produced on the metal surface. When the hydrogen is not removed, equilibrium is established, resulting in the polarization of anodic and cathodic sites. Cathodic depolarization takes place as the SRB remove the accumulated hydrogen. Experimental evidence to support the cathodic depolarization theory has been provided mostly with *Desulfovibrio* species since they utilize H_2 very effectively and can be cultivated under laboratory conditions (Booth and Tiller, 1968; Pankhania, 1988). Cord-Ruwisch and Widdel (1986) also demonstrated oxidation of cathodic hydrogen with sulfate in different growth cultures of hydrogenase-positive *Desulfovibrio* species. They also revealed that the process occurred only if an organic electron donor, such as lactate, was present. The corrosion is schematically illustrated in Figure 2.8. The enzyme hydrogenase produced by SRB was thought to play an important role in the cathodic depolarization processes (Booth and Tiller, 1960).

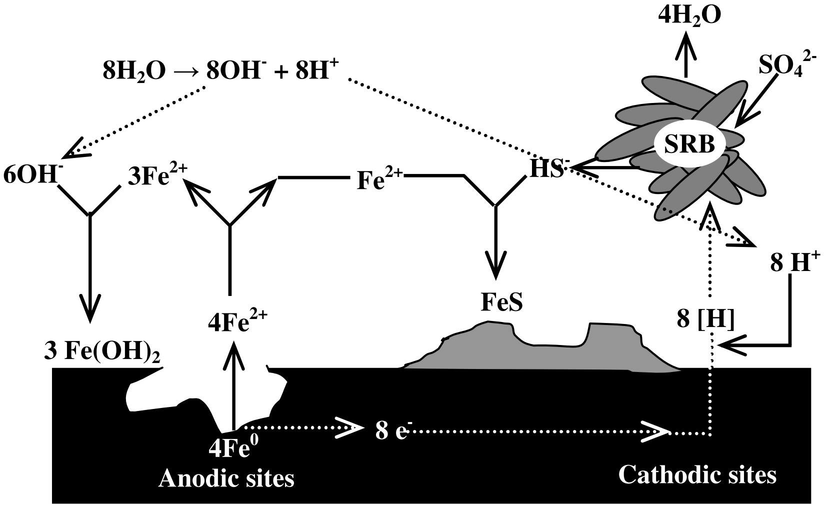

Figure 2.8 Generalized scheme of cathodic depolarization by SRB (Miller, 1981).

2.4.3.2 Hydrogen sulfide as the depolarizer

Under abiotic conditions, hydrogen sulfide was demonstrated to be corrosive for ferrous materials. It accelerates iron corrosion by acting as a source of bound protons and by precipitation of ferrous ions (Fe^{2+}) to produce insoluble sulfides (Costello, 1974):

$$Fe + H_2S \rightarrow FeS + H_2 \qquad (2\text{-}12)$$

$$Fe^{2+} + H_2S \rightarrow FeS + 2H^+ \qquad (2\text{-}13)$$

The formed H_2 may be utilized further by SRB or other H_2-scavenging microorganisms.

2.4.3.3 Stimulation of cathodic reaction by iron sulfide

It was demonstrated that iron sulfide increased the corrosion rate by decreasing hydrogen overvoltage and/or adsorbing the cathodically produced hydrogen (King et al., 1973).Severe corrosion cells develop as sulfide combines with ferrous ions to produce insoluble black sulfides. A galvanic couple formed between Fe and FeS is sustained and extended by the active involvement of SRB (King and Miller, 1971). The way in which electrons are transferred from ion sulfide to the SRB is not well understood. It may occur directly via formation of cathodic hydrogen (Figure 2.9) or by another reaction involving in reduction of H_2S (Scott, 1993).

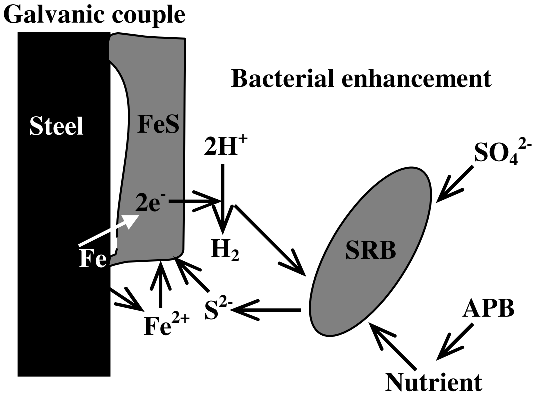

Figure 2.9 Schematic diagram of the mechanism in a FeS corrosion cell created by the action of SRB. Iron sulfide sets up a galvanic couple with steel, sustained and extended by the further action of SRB. (Scott, 1993).

The corrosion of steel is significantly related to the natures and structures of iron sulfide formed. The adherent, thin sulfide films are protective, whereas loose, bulky precipitates enhance the corrosion rates. The evolution of iron sulfide on steel was reported to progress from iron-rich to sulfur-rich phases as the follows: mackinawite (tetragonal FeS_{1-x}) → ferrous sulfide (cubic FeS) → troilite (hexagonal FeS) → pyrrhotite (hexagonal $Fe_{1-x}S$) → pyrite (cubic FeS_2) (Wikjord et al., 1980). The conversion of mackinawite to pyrite cannot increase the protective ability of the surface film due to the disruption of surface film during the evolution of iron sulfide; on the contrary, the corrosion of iron and steel are accelerated (McNeil and Little, 1990).

2.4.3.4 Corrosive metabolic products

SRB produce several sulfur compounds of corrosive characteristics at the metal-solution interface, either as final metabolic products of sulfide, biosulfides or hydrogen sulfide, or intermediate products of thiosulfates or polythiosulfates. These sulfur compounds are corrosive to carbon steel mainly through their transformation to sulfide, which stimulates corrosion by the mechanism of anodic depolarization (Videla, 1995). Another corrosive metabolic product involved in SRB corrosion is the phosphorous compound, probably phosphide (Iverson, 1968). Recently, a volatile P-containing compound, probably inositol hexaphosphate was found to result in a significant increase in the corrosion rate of mild steel (Iverson, 2001). More than 7% by weight of phosphorous compounds were further detected in the corrosion products containing mackinawite, indicative of phosphorous participation in the corrosion mechanism.

2.4.3.5 EPS-metal interactions

Recent studies demonstrated that EPS produced by SRB were responsible for corrosion of mild steel and a polysaccharide-protein EPS complex was capable of accelerating the deterioration of mild steel (Beech et al., 1998; Chan et al., 2002). Metal binding by EPS has been discussed in detail in Section 2.3.

2.5 Prevention and control of MIC

To prevent and control MIC, the basic principle in the industrial systems is “to keep the system clean”. However, it is seldom implemented at the early stages of the operation of the system due to the poor understanding of biocorrosion and biofouling process. On the other hand, prevention and treatment of MIC should be mainly focused on avoiding or minimizing the development of biofilms, as MIC is directly related to the presence of microorganisms that by adhering to different industrial surfaces can damage the metals. In industrial systems, the prevalent strategies of controlling MIC are to protect the integrity of metals, and are summarized as Table 2.2 (Jack and Westlake, 1995). In general, metal surfaces exposed to air are protected by the selection of appropriate materials and the use of protective coatings. Those in contact with soil or natural waters are primarily protected by coatings and cathodic protection (CP). The internal surface of metal structure can be protected by a combination of material selections, water removal (for nonaqueous systems), cleaning, and chemical treatment, with coatings and CP being applied in special cases.

Table 2.2 Prevention of corrosion in industrial facilities

	Prevention approach					
Facility	Material selection	coatings	Cathodic protection	Water removal	Cleaning	Chemical treatment
Upstream oil and gas	–	–	–	–	–	–
Well casings	√	–	√	–	–	√
Piping	–	–	√	–	√	√
Tanks, batteries	–	√	√	–	√	√
External pipelines	–	√	√	–	–	–
Internal pipelines	–	–	–	–	–	–
Gas	–	√	–	√	√	–
Oil	–	–	–	√	√	√
Storage tanks	√	√	√	√	√	√
Cooling systems*	√	–	√	–	√	√

2.5.1 Materials selection

Most metals and alloys are more or less susceptible to MIC, with the possible exception of beryllium and titanium and precious metals (such as Au, Pt and Pd etc). In some cases, nonmetallic materials or electro-active ceramics (EAC) have been substituted for metallic ones to avoid microbial corrosion; however, these materials may undergo microbial degradation (Revie, 2000)

2.5.2 Coatings

The use of coatings as a method of protection against MIC is focused on the application of the following compounds: silicone, epoxy resins and fluorinated compounds (Videla, 2002). Generally, coating is a good method of protection, provided that it is continuous. Any discontinuity in coating creates a preferential site for localized attack to occur. It is reported that coatings should not be altered by bacterial attack and should not release corrosive products during degradation (Videla, 2002). Based on practical experience, it has been shown that coal-tar and epoxy resin coatings perform well; while PVC-based coatings offer a poor performance (Videla, 1996). Cement linings were reported to probably reduce microbial fouling, although they are attacked by sulfur-oxidizing bacteria (Borenstein, 1994).

2.5.3 Cathodic protection

Cathodic protection can prevent all kinds of corrosion, including MIC, if adequate potentials are sustained. CP is generally applied to the external surfaces of structures buried underground or submerged in water, but it has also been applied to the inside of tanks, clarifiers, and heat exchangers in some circumstances (Manian and Hutt, 2001). CP was reported to be effective in inhibiting the growth of biofilms formed by aerobic bacteria on the surface of mild steel; whereas the opposite effect was detected for the anaerobic biofilms of SRB (Guezennec, 1991). In the presence of anaerobic bacteria, the applied CP potential must be more negative than usual to achieve a good protection for exposed steel (Little and Wagner, 1995). However, these highly-negative potentials do not affect bacterial attachment to protected surfaces, and applied current densities up to 100 $\mu A \cdot cm^{-2}$ fail to remove attached biofilms from stainless steel (Guezennec, 1991). It was further noted that CP seemed unable to stop localized corrosion initiation when a stable biofilm of SRB was already established on stainless steel in a chloride-containing medium (de Mele et al., 1995). The combined use of CP and protective coatings can be very effective in controlling MIC of pipes and structures exposed to seawater or buried to potentially aggressive soils.

2.5.4 Chemical treatment

Chemical treatment involves the planned addition of a site-specific combination of chemicals to an operating system. The treatment may include agents designed to inhibit corrosion, scavenge oxygen, alter pH, control scaling, suspend solids, control microbial activity, etc. Among them, biocides are widely applied to the cooling water systems, water handling systems, and oil and gas systems (Pope et al., 1990; Jack et al., 1994; Brandon et al., 1995; Choudhary, 1998). The biocides are single compounds (or a mixture of compounds) capable of killing microorganisms or inhibiting microbial growth. Biocidal compounds can be inorganic, such as chlorine, ozone, bromine, etc., or organic including isothiazolones, quaternary ammonium compounds, aldehydes (i.e., acrolein and glutaraldehyde) (Videla, 2002; Guiamet and Gómez de Saravia, 2005). Table 2.3 gives a summary of the properties of biocides and their concentrations most commonly used in the treatment of water in industrial systems.

Quaternary ammonium compounds (QUATS) form a class of cationic compounds (positively charged), which are used as biocides and corrosion inhibitors. As biocides

QUATS act on the microbial cells as detergents, dissolving lipids and thus causing the loss of the cellular content. The following sequential steps have been proposed for the antibacterial mechanism involving QUATS: (i) adsorption onto the bacterial cell surface; (ii) diffusion through the cell wall; (iii) binding to the cytoplasmic membrane; (iv) disruption of the cytoplasmic membrane; (v) release of K^+ ion and other cytoplasmic constituents; (vi) precipitation of cell contents and death of the cell (McDonnell and Russell, 1999). Detergenic properties of these compounds provide additional protection against the formation of polysaccharidic materials released during the process of bacterial colonization. As corrosion inhibitors, QUATS form a protective layer on the internal parts of the treated system, and have been tested to control or even prevent MIC by inhibiting biofilm formation (Enzien et al., 1996; Prasad, 1998). The main application of QUATS is found in closed systems and in gas-liquid separators. The majority of QUATS are biodegradable and do not require chemical deactivation following their use.

Table 2.3 Biocides commonly used in industrial water systems for MIC control

Biocides	Genus of biocides	Properties	Concentration
Chlorine	Oxidizing	Effective against bacteria and algae, pH dependant	0.1-0.2 ppm
Chlorine dioxides	Oxidizing	Effective against bacteria, to lesser extent against fungi and algae, independent of pH	0.1-1.0 ppm
Bromine	Oxidizing	Effective against bacteria and algae, broad range of pH	0.05-0.1 ppm
Ozone	Oxidizing	Effective against bacteria and biofilm, pH dependant	0.2-0.5 ppm
MBT[a]	Non-oxidizing	Effective against bacteria, hydrolysis at pH higher than 8.0	1.5-8.0 ppm
Isothiazolones	Non-oxidizing	Effective against bacteria, algae, biofilms; not pH dependant	0.9-10 ppm
QUATS[b]	Non-oxidizing	Effective against bacteria and algae, surfactant	8-35 ppm
Glutaraldehyde	Non-oxidizing	Effective against bacteria, algae, fungi and biofilms, broad pH range	10-70 ppm
THPS[c]	Non-oxidizing	Effective against bacteria, algae and biofilms, not pH dependant, very low environmental toxicity	10-90 ppm

a) MBT refers to methylene-bisthiocyanate;
b) QUATS refers to quaternary ammonium compounds;
c) THPS refer to tetrakishydroxymethyl phosphonium sulfate.

2.5.4 Corrosion inhibition by biofilms

Microorganisms are able to dramatically change the electrochemical conditions at the metal/solution interface. These changes can range from the induction or acceleration of corrosion to corrosion inhibition (Videla, 1996). The general concept of MIC is based on the assumption that microorganisms accelerate the kinetics of electrochemical reactions, thereby producing increased corrosion rates without, in most case, changing the corrosion mechanisms (Dowling et al., 1990). On the other hand, evidence that bacteria may be beneficial has been presented by many investigators in recent years (Pedersen and Hermansson, 1989, 1991; Hermandez et al., 1994; Jayaraman et al., 1997a, 1997b, 1997c, 1999; Örnek et al., 2001, 2002a, 2002b; Mansfeld et al., 2002; Nagiub and Mansfeld, 2002). They have shown that protective biofilms decreased the corrosion rate of mild steel, brass and copper by reducing the oxygen concentration or by secreting corrosion inhibitors. The beneficial biofilms and other observations have thus led to a new approach termed corrosion control using regenerative biofilms (CCURB).

However, the CCURB approach has not addressed the stochastic nature of bioiflm formation, the impact of nutrients on the measurement of specific electrochemical parameters or natural competition. One of the fundamental assumptions in the CCURB approach is that biofilm formation is predictable and controllable. As a matter of fact, biofilm composition can be affected by small perturbation in the environments (e.g., temperature, nutrient concentration, pH and flow). The response of microorganisms within biofilms cannot be predicted with certainty (Little and Ray, 2002). Moreover, the biofilm formed on the metal surface is believed to be robust, uniform and thick in these studies (Pedersen and Hermansson, 1989, 1991; Hermandez et al., 1994; Jayaraman et al., 1997a, 1997b, 1997c, 1999; Örnek et al., 2001, 2002a, 2002b; Mansfeld et al., 2002; Nagiub and Mansfeld, 2002). However, the preferential colonization or microbial attraction to anodic sites commonly occurs in the process of biofilm formation (Little et al., 1999). The discontinuities in biofilms cannot be avoided due to the sloughing phenomenon of all biofilms. It is therefore not possible to use this approach in field before additional research is performed to clarify the complex biological and chemical processes of biofilm formation.

2.6 Techniques for MIC studies

Appropriate application of techniques for detecting and monitoring MIC is essential for understanding the mechanistic nature of interactions and for obtaining control methods. Techniques utilized to investigate MIC may be classified as electrochemical, microscopic and spectroscopic (Chen et al., 1997).

2.6.1 Electrochemical techniques

The basic concepts of electrochemical corrosion can be used to interpret the acceleration of the corrosion process carried out by microorganisms under either anaerobic or aerobic conditions. Conventional direct current (DC) methods, including the measurement of redox potentials and open circuit potentials (OCP), linear polarization resistance (LPR), Tafel plots and potentiodynamic polarization curves, have been used in MIC studies (Dexter et al., 1991; Little et al., 1991). Alternative current (AC) techniques of electrochemical impedance spectroscopy (EIS) and electrochemical noise analysis (ENA) are also extensively used in detecting MIC in recent years (Dowling et al., 1988; Mansfeld and Little, 1991). However, most of these techniques assume that the chemical and electrochemical conditions on the metal surface are uniform. As a matter of fact, biofilms tend to create non-uniform surface conditions leading to localized corrosion. The advantages and limitations of electrochemical techniques have been reviewed by several investigators (Dexter et al., 1991; Little et al., 1991; Mansfeld and Little, 1991).

In addition, two dimensional (2-D) scanning vibrating electrode mapping (SVEM) is also applied to measure current density during corrosion (Isaacs, 1989), which uses a highly capacitance-sensitive microelectrode to scan over a metal surface exposed to an electrolyte, and detects potential difference between anodic and cathodic areas. Current density in pitting areas is recorded in order that cathodic and anodic areas are mapped. This technique has been applied to study MIC as heterogeneous bacterial colonization on metal substrata usually results in distinct anodic and cathodic areas associated with gradients of pH, of oxygen and of chloride (Little et al., 1991; Mansfeld and Little, 1991).

2.6.2 Microscopic techniques

Microscopic techniques used for investigating MIC mainly include scanning electron microscopy (SEM), atomic force microscopy (AFM), and confocal laser scanning microscopy (CLSM). SEM coupled with energy dispersive X-ray spectroscopy (EDS) is capable of revealing the existence of bacteria in pitted areas and the compositions of pits and corrosion products (Lee and Charaklis, 1992; Jack et al., 1996). AFM was applied to MIC soon after its development (Bremer et al., 1992; Steel et al., 1994). AFM utilize a microprobe mounted on a flexible cantilever to detect surface topography by scanning at a subnanometer scale. AFM has the advantage of enabling analysis of the sample topography in as-received state as well as enabling to reveal profiles, depth and size of pits. Another new imaging technology that may be used to monitor *in situ* biofilm formation in MIC is CLSM (Lawrence et al., 1994). CLSM has the advantage in that it resolves three-dimensional images, and thus allows study of the structure of living biofilms without damage their viability (Costerton, 1994). The use of this technique revealed that EPS matrix occupied most of volume of biofilms (75 to 95%);

whereas bacterial cells taking up only 5 to 25% of bioiflm volume may be concentrated either in the lower or upper regions of biofilms (Caldwell et al., 1992). CLSM has been utilized to determine the diffusion coefficient in biofilms combined with fluorescein and size-fractionated fluoro-conjugated dextrans. This has the potential of becoming an important method in study of kinetics of MIC (Chen et al., 1997).

2.6.3 Spectroscopic analysis

Spectroscopic techniques of studying MIC usually include Fourier transfer infrared spectroscopy (FTIR), X-ray photoelectron spectroscopy (XPS), and Auger electron spectroscopy (AES). FTIR is a non-destructive technique, which provides fingerprint spectra, allowing the rapid characterization of microbes and EPS (Schmitt and Flemming, 1996). Advantages of FTIR have been well recognized for studies of living biofilm (Nivens et al., 1995). Attenuated total reflection (ATR) FTIR is designed for study of biofilms in aqueous environments using an IR-transparent internal reflection element (IRE) as a substratum, such as Ge. Copper corrosion under the biofilm has been monitored using FTIR (Bremer et al., 1991a; Geesey et al., 1990). A major disadvantage of FTIR is its inability to differentiate dead cells from living ones. In addition, application of this technique to MIC is also limited by strong absorption of IR by water. Nevertheless, if properly combined with electrochemical technique, FTIR has the potential of *in situ* monitoring interfacial interactions between a biofilm and a metal substratum.

Surface analytical techniques, XPS and AES, have been applied to study MIC in recent years (Bremer et al., 1991b; Chen et al., 1995, 1996). The XPS spectrum and fine structure of Auger electron spectrum provide information about the surface composition and chemical states due to the binding energies of the photoelectrons and Auger electrons being specific for an atom and electron distribution around the atom. In addition, a compositional depth profile can be determined using Ar^+ bombardment to remove the top layers by varying take-off angles of photoelectrons with respect to sample surface (Hofmann, 1990). XPS has been successfully employed in the investigation of the loss of passivity of stainless steel exposed to SRB as well as the mechanisms of induced pitting information (Chen and Clayton, 1997; 1998). The mechanistic nature of the interaction between microorganisms with metal can also be explored. XPS provided information about composition and valence states of surface elements over a relatively large area; in contrast, AES may be used to analyze smaller areas ($0.1\ \mu m^2$) by adjusting the size of incident electron beams. AES may obtain chemical information of pits and provide secondary electron images. However, chemical shifts in AES spectrum are more difficult to interpret and electron bombardment may damage the surface compounds by causing reduction of metal oxide and evaporation of unstable species, because the density of energy is much higher than x-ray beams used in XPS. Because both XPS and AES are operated under ultrahigh vacuum ($\leq 10^{-9}$ torr), appropriate cooling devices should be used when analyzing bioproducts in order to prevent evaporation and decomposition. In particular, it is important to confirm the chemical states derived from these analyses using alternative methods suitable for liquid analysis because dehydration by ultrahigh vacuum may cause changes.

Table 2.4 A summary of advantages and limitations of techniques for MIC research

A. Electrochemical techniques (Chen et al., 1997; Xu, 2001)

Techniques	Advantages	Limitations	Reference
1. Open circuit potential measurement	Simplicity, provides information about changes in the passive film and trend of aninteraction	Time-consuming, insufficient to indicate pitting initiation	Esteso et al., 1992 Dexter, 1995 Fonseca et al., 1998
2. Redox potential measurement	Simplicity, assists understanding of changes in open circuit potential	Provides limited information, not useful for evaluation corrosion rate	Salvarezza et al., 1981
3.Direct current polarization	Determine uniform corrosion rates, linear polarization resistance	Cannot indicate localized corrosion rate	Dexter et al., 1991 Little et al., 1992 Fonseca et al., 1998
4. Split cell measurement	Creates anodic and cathodic areas, desirable to demonstrate various effects of microbes on corrosion	Needs sufficient potential difference	Keresztes et al., 1998 Gerchakov et al. 1986 Daumas et al., 1988
5. Microelectrode measurement	Directly evaluates the environment within biofilm, such as pH, oxygen, potential etc.	Difficult to operate, electrode is sensitive and can easily be damaged	Lewandowski et al., 1989, 1994; Lee and Beer, 1995
6. SVEM	Able to identify anodic and cathodic current	Performance of SVEM may be affected by biofilm forming on the tip	Franklin et al., 1991, 1992
7. EIS	Able to detect pitting initiation promptly, provides useful information on biofilm-metal	Biofilm may complicate system	Mansfeld and Xiao, 1994a; Gonzalez et al., 1998
8. ENA	Easy to be applied, does not need an external signal	Only provide information on uniform conditions	Iverson et al., 1986 Mansfeld and Xiao, 1994b

Table 2.4 (continued)

B. Microscopic techniques (Chen et al., 1997; Xu, 2001)

Techniques	Advantages	Limitations	Reference
9. SEM-EDS	Commonly available and straight forward, good technique for failure analysis of corroded metals	Sample need conductive, and operation is in high vacuum chamber	Coutinho et al., 1993 Lee and Charaklis, 1993 Jones-Meeham et al, 1995
10. AFM	High resolution, non-destructive, visualizes the topography of corroded sample in as-received state	Does not provide compositional information	Bremer et al., 1992 Steele et al., 1994 Beech, 1996
11. CLSM	Non-destructive, *in-situ* monitors biofilm structure and visualizes pitting information	Not high resolution, sample must be translucent for light, staining methods for different bacteria may alter normal growth conditions	Caldwell et al., 1992 Costerton, 1994 Neu and Lawrence, 1999

C. Spectroscopic techniques (Chen et al., 1997; Xu, 2001)

Techniques	Advantages	Limitations	Reference
12. FTIR	Non-destructive, *in-situ* analyze changes in the composition of a biofilm	Water strongly absorbs infrared light, only used in thin biofilm, cannot tell the difference between living from the dead ones	Geesey and Bremer, 1990 Bremer and Geesey, 1991a, 1991b Schmitt and Flemming, 1996
13. XPS	Analyze changes in the surface chemical states, does not need large amount of samples	Dehydration may change the chemical states of interaction products, some chemical states may need confirmation by another technique	Chen and Clayton, 1997, 1998 Natishan et al. 1999
14. AES	Similar to XPS, but can analyze far smaller areas than XPS	For chemical information, spectra are difficult to be interpreted	Jolley et al, 1989

CHAPTER 3

A COMPARATIVE STUDY OF THE CORROSION BEHAVIOR OF 304 STAINLESS STEEL IN A SIMULATED SEAWATER IN THE PRESENCE AND ABSENCE OF *PSEUDOMONAS* NCIMB 2021 BACTERIUM

3.1 General background

Type 304 stainless steel (or 304 SS) exhibits excellent corrosion resistance in aquatic environments due to the formation of a thin chromium-enriched oxide layers (Borenstein, 1996; Féron et al, 1998). It has therefore been widely used in industrial cooling water systems and for marine applications. Nevertheless, 304 SS, as a low grade austenitic stainless steel, is particularly susceptible to microbiologically influenced corrosion (MIC). The presence and activities of microorganisms can alter the structure of inorganic passive layers and increase their dissolution and removal from the metal surface.

This chapter is devoted to understanding of the influence of the marine aerobic *Pseudomonas* NCIMB 2021 bacterium on the corrosion behavior of 304 SS as a function of exposure time (including short-term and long term exposures). Emphasis is placed on the long-term experiments, since little literature has reported the evolution of passive film of SS under the effect of microorganisms over a long time. SEM was used to monitor the development of biofilms, and to further assess the degree of corrosion damage underneath the biofilms. The corrosion product at the representative areas on the coupon surface was evaluated using EDX studies.

3.2 Experimental Section

3.2.1 Metal samples preparation

The 304 stainless steel coupons were purchased from Metal Samples Company (Alabama, USA), the nominal elemental composition was (wt %): Fe 71.376%, Ni 8.18%, C 0.053%, Cr 18.08%, Cu 0.06%, Mn 1.68%, Mo 0.05%, N 0.047%, P 0.037%, S 0.007% and Si 0.43%. Disk shape coupons with a diameter of 15 mm and thickness of 3 mm were cut from the original plate samples with dimensions of 100×50×3 mm. Prior to the experiments, coupons were sequentially ground with a series of grit silicon carbide papers (180, 500, 800, and 1200) to a smooth surface, rinsed with sterile deionized water thrice, degreased in acetone, followed by sterilizing in 70% ethanol for 8 h, then dried aseptically in laminar flow cabinets.

3.2.2 Medium and inoculum cultivation

All tests were conducted using a nutrient-rich simulated seawater-based medium. According to Burkhoder's formula B (Bidwell and Spotte, 1985), the medium consists of 23.476 g/L NaCl, 3.917 g/L Na_2SO_4, 0.192 g/L $NaHCO_3$, 0.664 g/L KCl, 0.096 g/L KBr, 10.61 g/L $MgCl_2 \cdot 6H_2O$, 1.469 g/l $CaCl_2 \cdot 2H_2O$, 0.026 g/L H_3BO_3, 0.04 g/L $SrCl_2{\cdot}6H_2O$, 3 g/l bacteriological peptone and 1.5 g/L yeast extract. The pH of the medium was adjusted to 7.2 ± 0.1 using a 5 M NaOH solution, and sterilized by autoclaving for 20 min at 121°C and at 15 psi pressure.

A marine aerobic *Pseudomonas* NCIMB 2021 bacterium was obtained from the National Collection of Marine Bacteria (Sussex, UK). A new culture was resuscitated from a freeze-dried ampoule, and sub-cultured twice in 5 ml of NCIMB medium 210 before use. After the resuscitation, the bacteria were cultured for 3 days in a 125 ml Erlenmeyer flask containing 20 ml of the fresh culture medium on a rotary shaker (20°C), 150 rpm). A total of 20 ml of the cultured bacteria stored in a -20°C refrigerator was used as the inoculums in all the experiments to ensure the purity of the *Pseudomonas* bacteria.

3.2.3 Corrosion experiments with *Pseudomonas* inoculation

A 1 ml aliquot of the 3-day-old *Pseudomonas* culture was introduced into 500 ml of the culture medium in a 2-L conical flask. The conical flask was subsequently placed on a rotary incubator shaker at 150 rpm and 25°C. The bacterial cell concentration was measured by the optical density (OD) at 600 nm, and the cell number was calculated based on the standard calibration with the assumption that an optical density of 1.0 is equivalent to ~10^9 cells/mL (Hogt et al., 1986). When the OD value was close to 1.0, the prepared specimens hung on the Nylon string were aseptically introduced into the inoculated medium. The coupons were fully and vertically immersed in the medium. The flasks were capped with Bug-stoppers (Whatman, USA) to prevent contamination by airborne bacteria. To maintain the bacterial density at the steady-state growth phase throughout the study period, a semi-continuous mode of *Pseudomonas* culture growth was employed, i.e., 75% medium were drained and replaced with an equal amount of a fresh sterile medium every 7 days. It is noteworthy that the coupons were continuously immersed in the medium during the process of draining and replacing the culture medium. Specimens were retrieved from the inoculated medium after 7, 14, 21, 35, 49, 63 and 77 days for the electrochemical studies and surface analyses. Both the electrochemical measurement and surface analyses were repeated twice employing four coupons at each predetermined exposure time. For a comparison, the same stainless steel specimens were exposed to the sterile nutrient-rich medium, which had exactly the same composition as the inoculated medium, except for the absence of *Pseudomonas* bacteria, to act as the control samples. All the experiments were carried out in a batch mode in an incubator at 25 °C.

3.2.4 Electrochemical measurements

A conventional three-electrode glass corrosion cell with a capacity of 500 ml, as shown in Figure 3.1, was used to measure the Tafel plots, cyclic polarization curves, and the electrochemical impedance spectra. An $Ag/AgCl/KCl_{(sat)}$ electrode was used as the reference electrode and a platinum rod was used as the counter electrode. After the prescribed exposure time, the 304 SS coupons were mounted in a PVDF electrode holder leaving a circular area of 0.785 cm^2, and fixed at the bottom of the corrosion cell to serve as the working electrode. It is noteworthy that the coupons were tightly fixed in the PVDF holder, thus adequately shielding the contact point from electrolyte and avoiding the occurrence of crevice corrosion. All electrochemical measurements were performed using an Autolab PGSTAT 30 (Ecochemie, Netherlands), controlled by GPES software for the Tafel plot measurements and FRA software for the EIS measurements. The Tafel plots were recorded at a scan rate of 2 $mV \cdot s^{-1}$ within the range of -250 mV to 250 mV versus the open circuit potential (OCP) to determine the corrosion current density ($i_{corr.}$) and the corrosion potentials ($E_{corr.}$). The cyclic polarization curves were determined potentiodynamically at a scan rate of 10 $mV \cdot s^{-1}$ in a potential range of -0.5 V and 1.0 V to confirm the presence of pitting or crevice corrosion on the coupon surfaces. EIS measurements were carried out at the OCP using a 10 mV amplitude sinusoidal signal over frequencies ranging from 100,000 to 0.005 Hz.

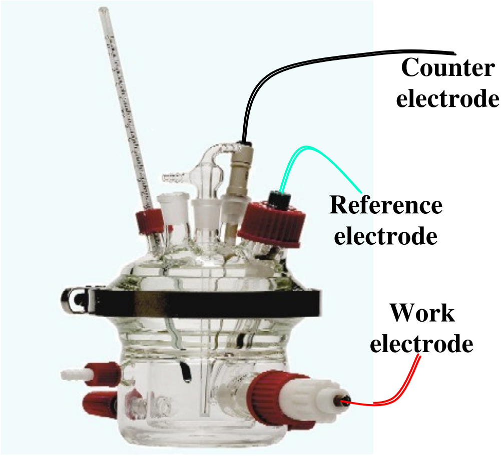

Figure 3.1 The diagram of corrosion cells used in electrochemical measurements

3.2.5 Surface analysis with SEM-EDX

The 304 SS specimens were examined for their surface morphology and corrosion features using SEM and EDX (Jeol Company, Tokyo, Japan, JSM-5600 model). The coupons with biofilms were prepared for SEM imaging by the following procedures. The coupons were washed gently twice with a sterile PBS solution to remove the dead and loosely attached cells, and fixed in a 3 vol% PBS solution of glutaradehyde for 8 h at 4 ^{o}C. Thereafter, the coupons were removed from the glutaradehyde solution and washed twice with deionized water, followed by stepwise dehydration with 25, 50, 75, 90 and 100 vol% ethanol for 10 min each. The specimens were then dried in an air-tight desiccator prior to SEM imaging. To observe the surface corrosion damage, the biofilm were removed from the coupon surface with sterile cotton swabs immediately after the coupons were taken out, followed by rinsing with deionized water thrice, dried by purging with nitrogen gas, and finally stored in an air-tight vacuum desiccator prior to analysis. Control coupons from the sterile medium were also prepared by the similar procedures of deionized water rinsing and nitrogen gas drying as mentioned above.

3.3 Results and discussion

3.3.1 Corrosion behavior of 304 SS in the sterile and *Pseudomonas*-inoculated media

3.3.1.1 Tafel polarization measurement

Tafel plots were recorded as described in the experimental section. The data were analyzed quantitatively using the GPES 4.9.5 software to obtain the Tafel slopes (β_a and β_c), the corrosion potentials (E_{corr}), the corrosion current densities (i_{corr}) and the corrosion rates. Figure 3.2 shows the Tafel plots of 304 SS after exposure to the sterile nutrient-rich medium for 7 days. This plot is used as the representative plot to illustrate the Tafel analysis. The linear portions of anodic and cathodic curves are extrapolated back to their intersections to obtain the Tafel slopes (β_a and β_c), E_{corr} and i_{corr}.

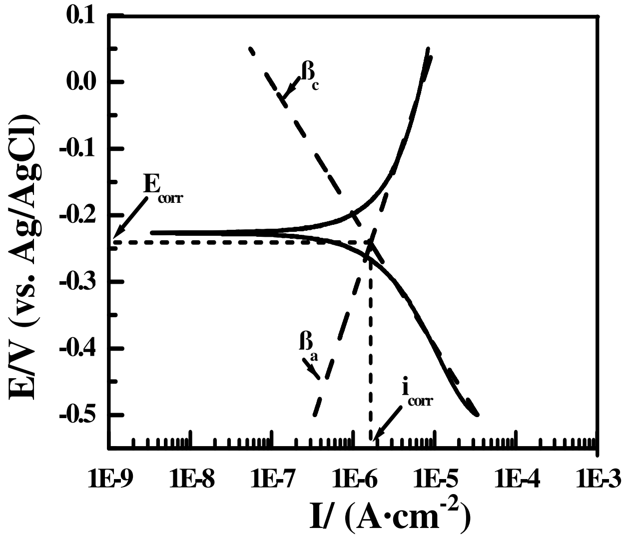

Figure 3.2 The extrapolation of representative Tafel plots to determine Tafel slopes, E_{corr} and i_{corr}. The representative Tafel plots obtained after 7 days of exposure in the sterile nutrient-rich medium.

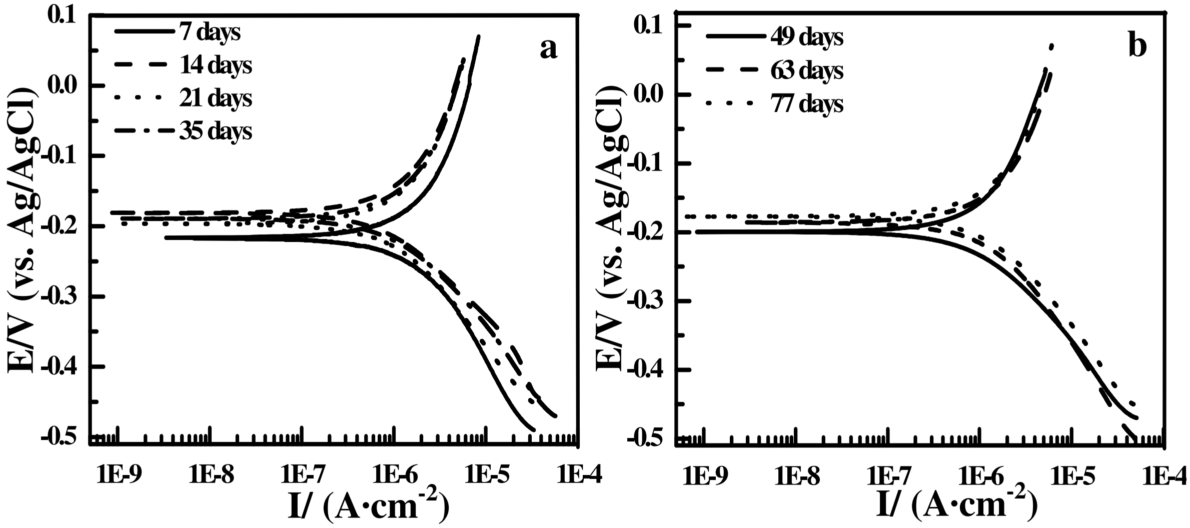

Figure 3.3 Tafel plots of 304 SS in the sterile nutrient-rich medium after (a) short-term exposure periods of 7, 14, 21 and 35 days; and (b) long-term exposure periods of 49, 63 and 77 days.

Figures 3.3a and 3.3b show the Tafel plots of 304 SS after short-term and long-term exposures in the sterile nutrient-rich medium, respectively. The Tafel analytical data are shown in the below Table 3.1. Corrosion current densities, i_{corr}, of 304 SS remain relatively constant throughout the exposure periods in the sterile medium, albeit with a slight increase after the initial exposure period of 7 days and after the long-term exposures (i.e., 63 and 77 days), indicative of no significant changes in the corrosion rates of 304 SS in the sterile nutrient-rich medium. This phenomenon is consistent with the presence of a stable passivating chromium-iron oxide/hydroxide film on the surface. The passive films on stainless steels are reported to be very thin (~1-5 nm). Their formation depends on the solution pH, chloride ion concentration in the electrolyte, anodic ageing time, and the composition of the substrate on which they are formed (Alamr et al., 2006). Corrosion potential, E_{corr}, undergoes a slightly noble shift of 50 mV with exposure time. This is probably attributable to the inhibitive effect of the passive film on the anodic oxidation reaction. The cathodic Tafel slopes, β_c, fluctuate in the range of ~ -140 to -200 $mV\cdot dec^{-1}$, indicative of a slight diffusion control. The anodic Tafel slopes, β_a, remain more than 300 $mV\cdot dec^{-1}$ throughout the exposure period, indicating that the anodic oxidation reactions are under diffusion control.

Table 3.1 Analysis parameters of Tafel plots of 304 SS in the sterile medium after different exposure times

Exposure time (days)	$\beta_c{}^a$ ($mV\cdot dec^{-1}$)	$\beta_a{}^b$ ($mV\cdot dec^{-1}$)	$E_{corr}{}^c$ (V)	i_{corr} ($\mu A\cdot cm^{-2}$)	Corrosion rate ($mm\cdot y^{-1}$)
7	-197	377	-0.241	2.08	0.0215
14	-150	322	-0.203	1.38	0.0142
21	-168	314	-0.207	1.36	0.0141
35	-143	305	-0.202	1.38	0.0143
49	-150	318	-0.206	1.29	0.0140
63	-187	331	-0.197	1.63	0.0168
77	-168	389	-0.196	1.77	0.0183

Tafel plots of 304 SS after short-term and long-term exposure periods in the *Pseudomonas*-inoculated medium are shown respectively in Figures 3.4a and 3.4b.

During the short-term exposure, the corrosion current densities, i_{corr}, increase slowly to 3.75 $\mu A \cdot cm^{-2}$ (or ~50%) after 35 days of exposure. With exposure time extending beyond 49 days, i_{corr} increases relatively fast and attains the high value of 7.38 $\mu A \cdot cm^{-2}$ after 77 days of exposure. This phenomenon is probably associated with the prolonged effect of *Pseudomonas* bacteria and aggressive chloride anions. The corrosion potential, E_{corr}, undergoes an active shift in the *Pseudomonas*-inoculated medium with exposure time. The active shift in corrosion potentials is probably associated with the colonization of the *Pseudomonas* bacteria and the subsequent biofilm formation on the surface of 304 SS. However, this phenomenon cannot be interpreted by the mixed potential theory alone, since the effect of *Pseudomonas* on the corrosion process is complicated and unpredictable. The anodic Tafel slope, β_a, remains at a relatively larger value, albeit with a slight decrease with exposure time, indicative of the diffusion control of anodic reaction. On the other hand, the cathodic Tafel slopes, β_c, show relatively higher values as compared to those of control coupons, indicative of mass transport effect of biofilm of *Pseudomonas* bacterium on the dissolved oxygen.

Comparing the Tafel plots and the corresponding electrochemical analysis results of 304 SS in the nutrient-rich medium in the presence and absence of *Pseudomonas* bacteria, several differences are apparent: (i) the anodic Tafel slopes, β_a, are relatively small in the presence of *Pseudomonas*, and gradually decrease with exposure time. These results suggest the detrimental effect of *Pseudomonas* on the integrity of the passive oxide film, probably leading to incipient pits (or metastable pits), (ii) the cathodic Tafel slopes, β_c, show a larger value in the presence *Pseudomonas* bacteria, indicating a decrease in the kinetics of the oxygen reduction reaction. This result is probably caused by the local depletion of oxygen due to respiration of aerobic *Pseudomonas* cells within the biofilms,

(iii) the corrosion current densities, i_{corr}, of 304 SS in the presence of *Pseudomonas* are higher by as much as 4.5 fold over those in the absence of *Pseudomonas* after 77 days of exposure, (iv) the corrosion potentials, E_{corr}, appear to shift to the noble direction with exposure time in the absence of *Pseudomonas*, whereas, E_{corr} undergoes a active shift with exposure time under the effect of the *Pseudomonas* bacteria. These results reveal that the stainless steel specimens undergo different corrosion processes in the nutrient-rich medium in the presence and in absence of *Pseudomonas* bacterium.

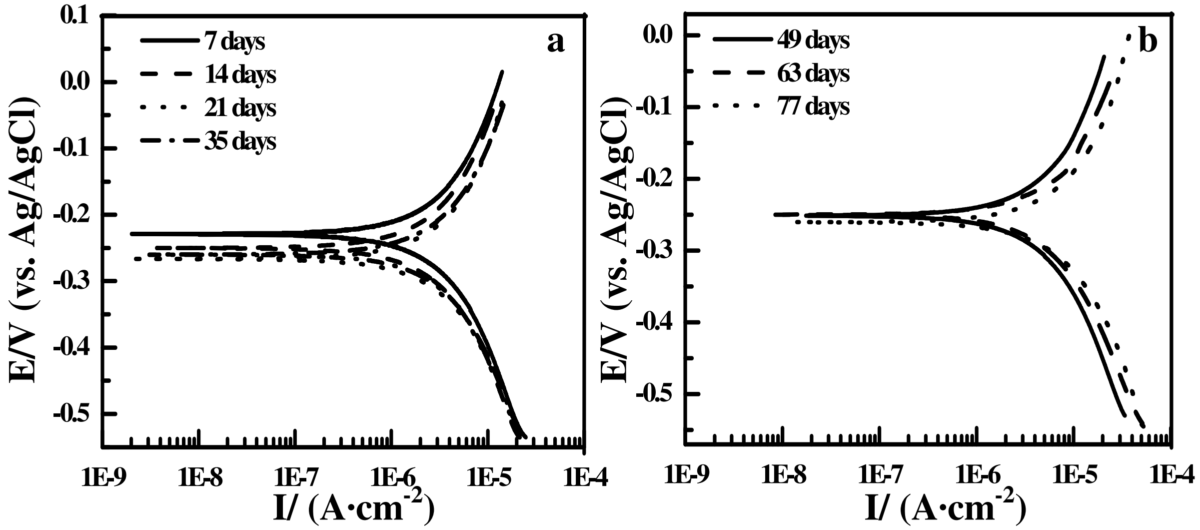

Figure 3.4 Tafel plots of 304 SS in the *Pseudomonas*-inoculated medium after (a) short-term exposure periods of 7, 14, 21 and 35 days; and (b) long-term exposure periods of 49, 63 and 77 days.

Table 3.2 Analysis parameters of Tafel plots of 304 SS in the *Pseudomonas*-inoculated medium after different exposure times

Exposure time (days)	β_c (mV·dec^{-1})	β_a (mV·dec^{-1})	E_{corr} (V)	I_{corr} (μA·cm^{-2})	Corrosion rate (mm·y^{-1})
7	-301	311	-0.224	2.58	0.0267
14	-317	287	-0.236	3.24	0.0335
21	-293	301	-0.239	3.27	0.0339
35	-312	282	-0.248	3.62	0.0375
49	-295	306	-0.244	5.45	0.0564
63	-301	286	-0.254	6.92	0.0716
77	-310	272	-0.262	7.38	0.0765

3.3.1.2 Electrochemical impedance measurements

The impedance spectra of 304 SS after short-term and long-term exposure to the sterile nutrient-rich medium are shown in Figure 3.5I and 3.5II, respectively. The Nyquist plots (Fig. 3.5Ia) reveal that the real component of the impedance spectrum slightly increases with time, and then reaches a maximum value after 35 days of exposure. During the long-term exposure, the diameter of the impedance loop undergoes a slight decrease with time (Fig. 3.5IIa). The Bode magnitude plots (Fig. 3.5Ib and 3.5IIb) also show the logarithmic values of impedance spectra oscillating over 4.5 at the lowest frequency. Both impedance spectra indicate that the protective passive film formed on the stainless steel coupon surface remains in a relatively stable state over time. The Bode phase angle plots of the short-term coupons have an apparent maximum peak angle with a small shoulder. The maxima appearing in the frequency range of 1 and 100 Hz is ascribed to the formation of a protective oxide film, the small shoulder located in the frequency range of 1 and 0.1 Hz are probably due to electrical double layer (EDL) (Fig. 3.5Ic). For the Bode phase angle plots of the long-term specimens, the maximum peaks due to the passive film appear in the same frequency range as the short-term samples. However, the smaller shoulder has almost vanished and only exhibits a weak signal (Fig. 3.5IIc). The phase maxima in the Bode phase angle plot and a slope close to -1 in the Bode magnitude plot usually provide information of the relaxation time constants (Tait, 1994).

Figures 3.6I and 3.6II show the respective impedance spectra of 304 SS after short-term and long-term exposure in the *Pseudomonas*-inoculated medium. As can be seen in the Nyquist plots (Figs. 3.6Ia and 3.6IIa), the diameter of impedance loop decreases gradually with time. The respective Bode magnitude plot (Figs. 3.6Ib and 3.6IIb) reveals that the total impedance magnitude decreases gradually from the logarithmic value of ~

4.4 to 3.9. The diameters of impedance loops and the impedance magnitude of the long-term specimens have decreased dramatically as compared to those of the short-term exposed specimens, indicative of the detrimental effect of synergistic interactions of *Pseudomonas* bacterium and aggressive anions on the passive film. The Bode phase angle plots have undergone marked changes after different exposure times due to the effect of *Pseudomonas* on the passive film. As for the short-term samples, the maximum peak angles are significantly broadened, as compared to their counterparts in the sterile nutrient-rich medium, and span a frequency range of 0.01 and 1000 Hz. Moreover, the maximum phase angles are lower than that in the sterile nutrient-rich medium (i.e., ~75^o versus 60^o, Fig. 3.6Ic). On the other hand, two maximum phase angles have appeared for the long-term coupons in the *Pseudomonas*-inoculated medium: the one in a high frequency range of 100 and 1000 Hz is attributed to the formation of a protective oxide film, while the one in a frequency range of 0.1 and 10 Hz is probably associated with the biofilm or the electrical double layer. Both of the maximum phase angles are below 55^o (Fig. 3.6IIc). These results are indicative of the enhancement in corrosion rates of stainless steel specimens in the presence of *Pseudomonas* in the nutrient-rich medium.

The impedance spectra obtained in the sterile and *Pseudomonas*-inoculated media after different exposure times are analyzed and fitted to circuit parameters using the non-linear least square method in the program EQUIVCRT by Boukamp (1986). Figure 3.7 shows the physical model and the corresponding equivalent circuits, which can be satisfactorily used to fit the EIS data as the Chi-square (χ^2) values are around 10^{-3}. The equivalent circuit (a) in Figure 6 models two relaxation time constants, and it is frequently used to represent a thin and compact protective passive film formed on the

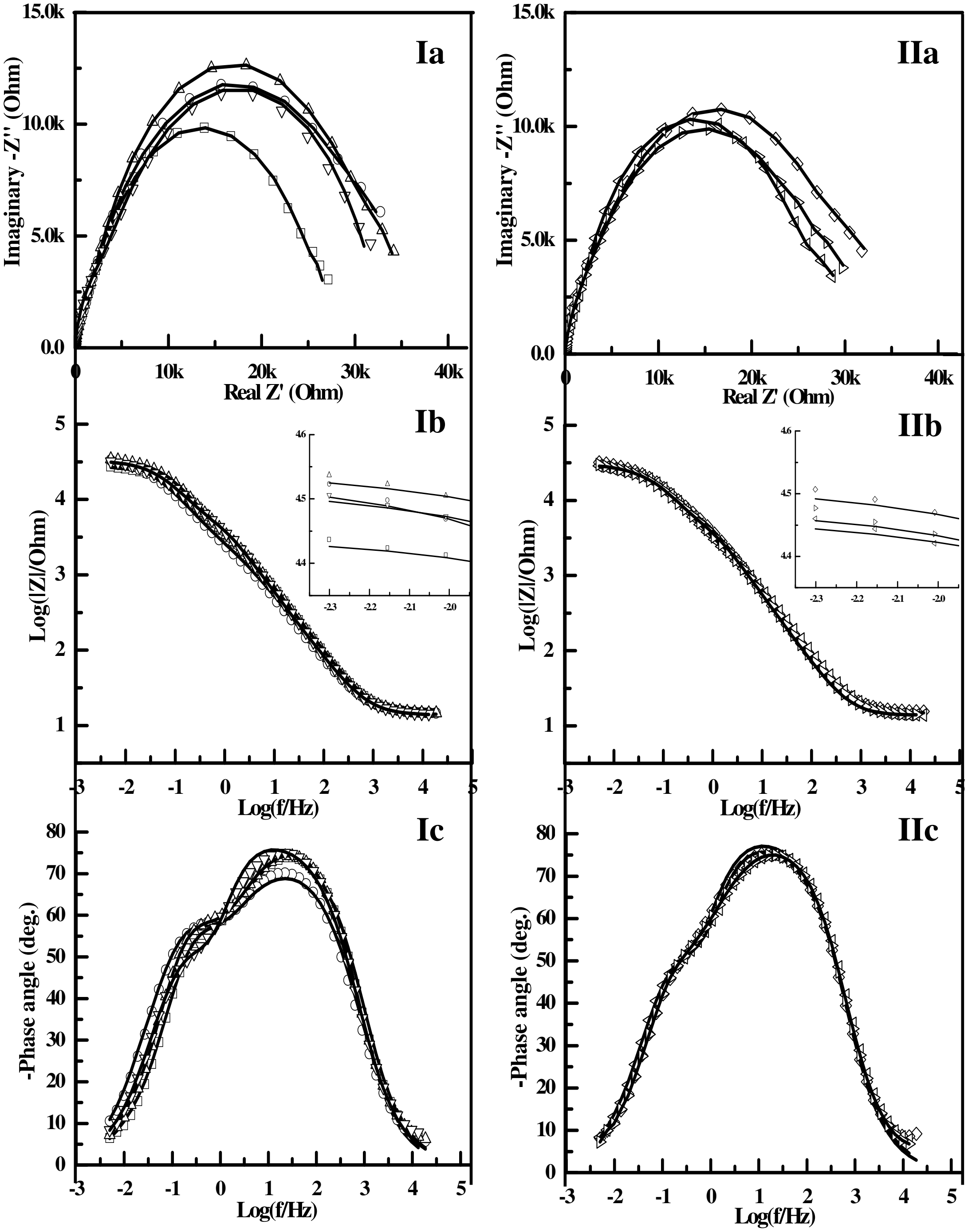

Fig. 3.5 EIS data of 304 SS recorded at the OCP in the sterile nutrient-rich medium after short-term exposure periods ((Ia), (Ib) and (Ic)) of 7 days (open squares); 14 days (open circles); 21 days (open upper triangles) and 35 days (open lower triangles); and long-term exposure periods ((IIa), (IIb) and ((IIc)) of 49 days (open diamonds); 63 days (open left triangles) and 77 days (open right triangles). Solid lines represent the fitted results based on the corresponding equivalent circuit (a); (a) Nyquist plots; (b) Total Bode magnitude plots; (c) Bode phase angle plots.

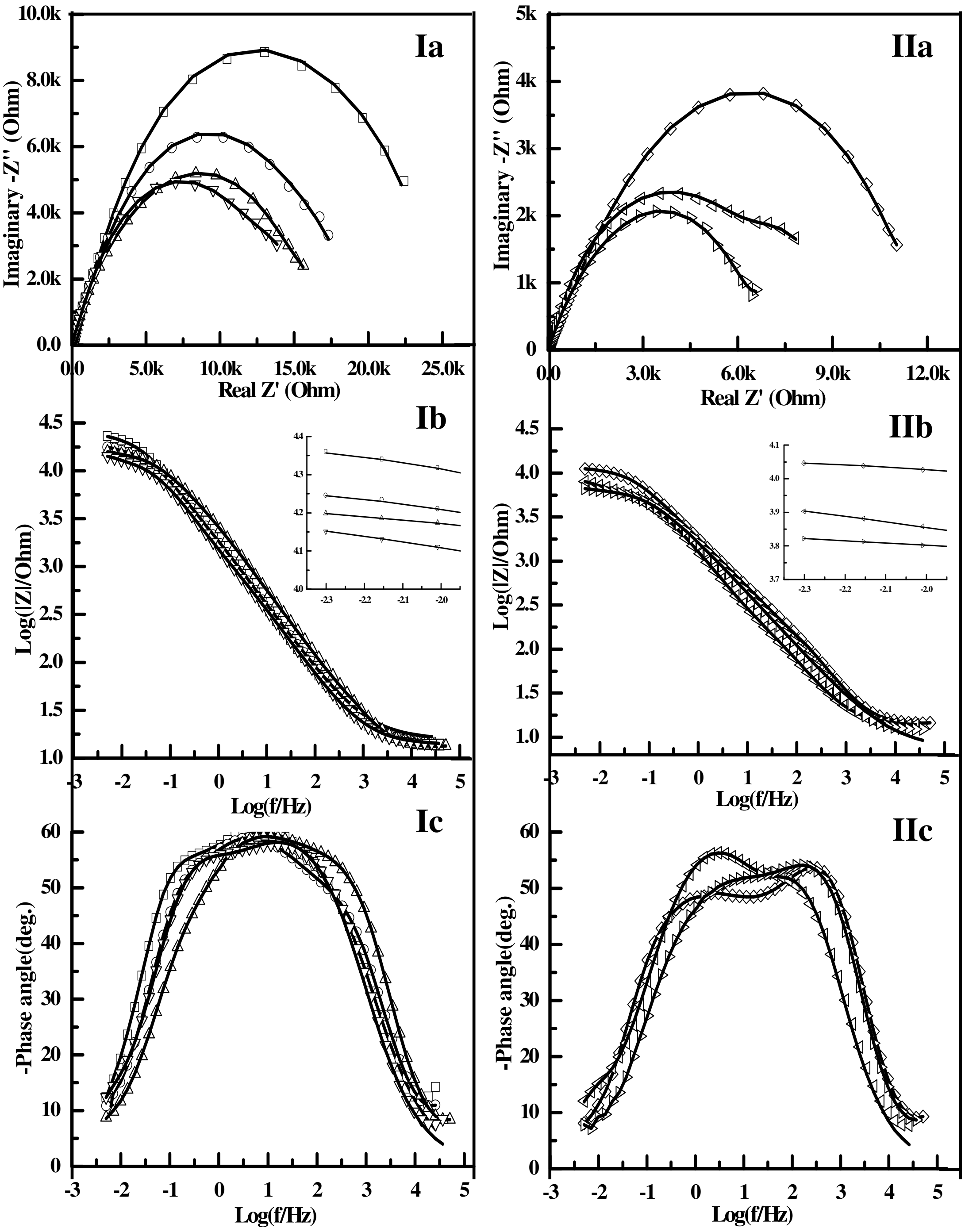

Figure 3.6 EIS data of 304 SS recorded at the OCP in the *Pseudomonas*-inoculated medium after short-term exposure periods ((Ia), (Ib) and (Ic)) of 7 days (open squares); 14 days (open circles); 21 days (open upper triangles) and 35 days (open lower triangles); and long-term exposure periods ((IIa), (IIb) and (IIc)) of 49 days (open diamonds); 63 days (open left triangles) and 77 days (open right triangles). Solid lines represent the fitted results based on the corresponding equivalent circuit (b); (a) Nyquist plots; (b) Total Bode magnitude plots; (c) Bode phase angle plots.

metal surface. "**O**" is introduced to represent the path of a finite diffusion process (Zhang et al., 2002). The cotangent hyperbolic term "**O**" is used to describe the diffusion of mobile species through a thin layer, such as an oxide layer or coating, followed by a reaction at the electrode/layer interface (Benedetti et al., 1995). It is defined by the following equation (Boukamp, 1986; Benedetti et al., 1995; Yu and Pehkonen, 2004):

$$Y = \tanh(B\sqrt{j\omega}) / Y_0\sqrt{j\omega} \tag{3-1}$$

Here, $B = \delta / \sqrt{D}$, $Y_0 = 1/\sigma\sqrt{2}$ and δ is the Nernst diffusion layer thickness, D is the average value of the diffusion coefficients of the species, and σ is the Warburg coefficient. The quotient of B divided by Y_0 is accepted as a description for the diffusion resistance of a protective film of finite length (Benedetti et al., 1995; Yu and Pehkonen, 2004). In the current study, the O_f reflects the diffusion process of metal ions through oxide film on the stainless steel surface. The equivalent circuit (b) contains three relaxation time constants, and illustrates the formation of a duplex surface film on the metal surface: the outer layer is a heterogeneous biofilm, while the inner part is a porous oxide film. According to the AC circuit theory, an impedance spectrum obtained for a given electrochemical system can be correlated with one or more equivalent circuits (Wang et al., 1986).

The depression of the semicircle with their center below the real axis is well known as the dispersing effect in Figures 3.5a and 3.6a (Mansfeld, 1981). The frequency dispersion behavior is probably related to the inherent heterogeneous nature of the solid surface (McCafferty, 1997). Due to the fact that the bulk solution/EDL and the EDL/electrode interface do not behave as an ideal capacitor in the presence of the dispersing effect, a constant phase element (CPE) is often used as a substitute for the capacitor in the equivalent circuit to fit the EIS data more accurately. The CPE defined in the usual impedance and admittance formats are as follows:

$$Z_{CPE} = 1/[Y_0(j\omega)^n] \tag{3-2}$$

$$Y_{CPE} = Y_0(j\omega)^n \tag{3-3}$$

Here, j is the imaginary root, ω (= 2πf) is the angular frequency. The factor n, defined as the CPE power, is an adjustable parameter that lies between 0 and 1, and can be used as a measure of the surface inhomogeneity. Its decrease is connected to the increase in metal surface roughening. The factor Y_0 denotes a parameter related to capacitance. The capacitance can be calculated from the experimentally determined CPE parameters using the following equation (Benedetti et al, 1995; Xu et al, 1999):

$$C = \omega^{n-1} / Y_0 \sin(n\pi/2) \tag{3-4}$$

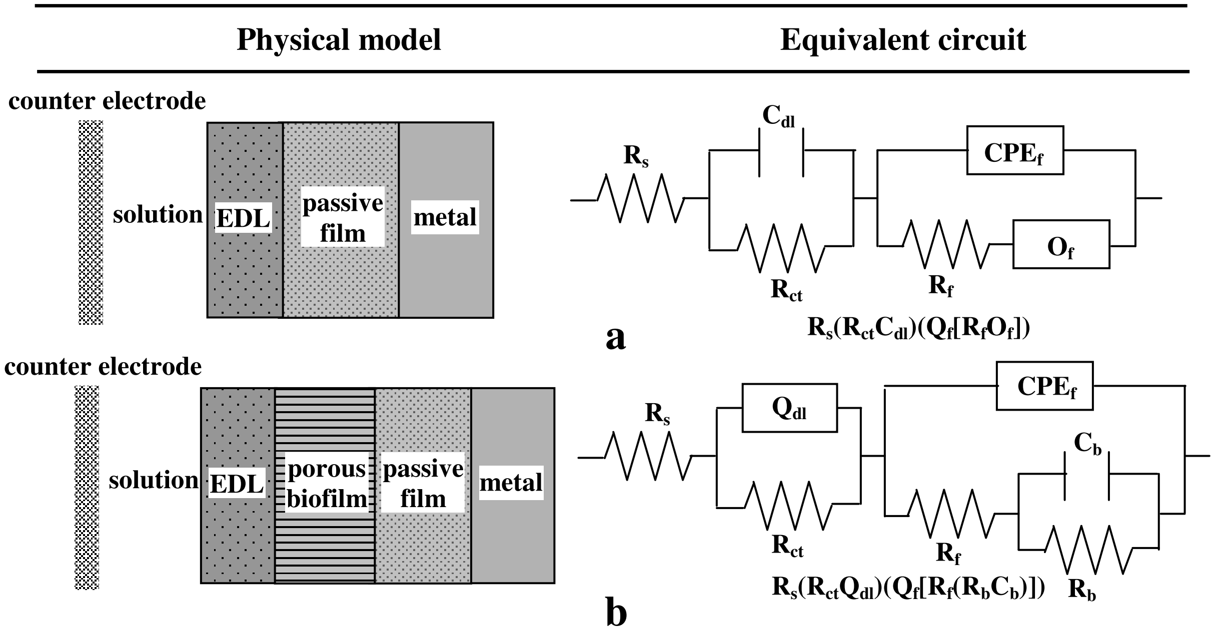

R_s, resistance of the electrolyte solution; C_{dl}, capacitance of the electrical double layer (EDL); R_{ct}, charge transfer resistance of EDL; Q_{dl}; CPE of the EDL; C_b, capacitance of the biofilm formed on 304 SS; R_b; resistance of the biofilm formed on 304 SS; Q_f, CPE of the surface passive film on 304 SS; R_f, resistance of the surface passive film on 304 SS; O_f, finite length diffusion element of the surface passive film.

Figure 3.7 Physical models and the corresponding equivalent circuits used for fitting the EIS data of the steel coupons

Table 3.3 Fitting parameters of EIS data of 304 SS in the sterile medium after different exposure times

Time (days) Parameter	7	14	21	35	49	63	77
R_{sol} (Ω)	13.29	14.33	12.63	13.64	14.56	13.76	14.14
R_{ct} (kΩ)	1.22	1.32	1.46	2.13	2.30	2.03	2.01
C_{dl} (μF)	59.58	68.90	55.69	70.61	73.12	71.17	69.23
R_f (kΩ)	24.59	26.19	30.60	30.92	27.43	25.19	24.54
Q_f $Y_0 * e^{-5}$	1.54	3.12	1.90	1.11	1.37	1.82	1.76
n_1	0.86	0.88	0.87	0.82	0.84	0.87	0.85
O_f $Y_0 * e^{-3}$	3.10	1.67	1.99	1.28	1.78	2.21	1.40
B	5.68	4.13	5.34	5.31	5.19	5.66	4.73
Z_f (kΩ)	1.83	2.47	2.68	4.25	2.92	2.56	3.38
$\sum\chi^2 * e^{-3}$	2.60	9.26	3.41	1.98	5.73	4.55	7.90

The EIS data of stainless steel coupons after the short-term and long-term exposures in the sterile nutrient-rich medium are both fitted using the equivalent circuit (a). The parameters used for fitting are given in Table 3.3. The resistance of the surface passive film, R_f, increases with exposure time during the short-term exposure, and reaches a maximum value of ~ 31 kΩ after 35 days. Thereafter, R_f decrease slightly with time, probably due to formation of conditioning layers by the adsorption of organic compounds and the related changes in composition of the passive films with time. The porous and non-protective conditioning layers adhere strongly to the underlying oxide film and probably contributed to the complexity of surface conditions (Beech et al., 2000). Abreu et al. (2006) reported that the passive film on AISI 304L SS underwent an increase in the oxidized iron content and a change in Cr distribution with increasing exposure time in a chloride solution. The charge transfer resistance, R_{ct}, undergoes similar changes to those in R_f with exposure time. The variation in R_f is, nevertheless, very small (below 20%) for all exposure periods, indicative of the stability of the passive film on the stainless steel surface in the sterile nutrient-rich medium. Another noticeable circuit element in Table 3 is Z_f (=B/Y_0), which represents the diffusion resistance of active species through the thin oxide layer. The diffusion resistance, Z_f, is dependent on the resistance of the passive film, R_f. The diffusion resistance is probably associated with one of the following diffusion processes: (i) the diffusion of metal ions (such as iron or chromium) through the oxide film, (ii) the diffusion of metal ions from the surface of the oxide film to the bulk solution, (iii) the diffusion of oxygen in the oxide film and (iv) the diffusion of dissolved oxygen from the bulk solution to the film surface. In addition, the values of the exponential term, n, in the description of Q_f remain more than 0.8 throughout, indicative of the presence of a relatively smooth and uniform surface of the coupons in the sterile nutrient-rich medium.

The temporal impedance spectra of the stainless steel coupons in the *Pseudomonas*-inoculated nutrient-rich medium are fitted with the equivalent circuit (b) to obtain the fitting parameters (Table 3.4). Both the charge transfer resistance, R_{ct}, and the passive film resistance, R_f, decrease gradually with time. At the initial 7 days of exposure, the values of R_{ct} and R_f are close to those of the corresponding specimen in the sterile nutrient-rich medium. This result suggests that the passive film retains its integrity initially, although some distinguishable *Pseudomonas* cells, either individually or in small aggregates, have colonized on the specimen surface. Upon prolonging the exposure, both the R_{ct} and R_f values decrease dramatically. This phenomenon can be attributed to the deleterious effect of *Pseudomonas* bacteria and their biofilm on the integrity of the passive film to result in, for example, pitting corrosion. The resistance of the biofilm, R_b, varies with time, consistent with the fact that the development of biofilm is a dynamic process and is accompanied by the continuous attachment, growth, detachment from the solid surface (Videla, 1996). The exponential term n of Q_f appears to decrease with time, indicating that the passive film becomes rougher in the biotic medium. This result is consistent with the on-set of the pitting corrosion under the heterogeneous biofilms, since the biofilm of the *Pseudomonas* NCIMB 2021 bacteria has been reported to induce extensive micro-pitting corrosion on the surface of stainless steel 316 (Beech et al., 2000).

Table 3.4 Fitting parameters of EIS data of 304 SS in the *Pseudomonas*-inoculated medium after different exposure times

Time (days) Parameter	7	14	21	35	49	63	77
R_{sol} (Ω)	13.45	13.38	14.07	13.57	11.88	14.01	12.52
R_{ct} (kΩ)	2.18	1.83	1.85	1.35	0.63	0.48	0.59
Q_{EDL} $Y_0 * e^{-6}$	2.77	2.56	2.59	3.02	3.16	2.86	3.14
n_1	0.66	0.64	0.67	0.66	0.64	0.68	0.58
R_f (kΩ)	20.89	16.25	14.29	13.25	9.59	7.65	8.49
Q_f $Y_0 * e^{-5}$	1.04	3.23	1.79	2.04	2.26	1.62	1.59
n_2	0.91	0.84	0.79	0.86	0.80	0.75	0.77
R_b (kΩ)	1.22	1.37	1.34	1.73	1.37	1.93	2.00
C_b (mF)	17.96	17.22	29.55	15.10	21.18	12.68	16.21
$\sum\chi^2 * e^{-3}$	4.89	1.37	0.59	0.76	0.37	2.69	1.12

3.3.1.3 Cyclic polarization curves

Cyclic polarization curves (via cyclic voltammetry) were measured for the stainless steel coupons exposed to the sterile and the *Pseudomonas*-inoculated media for 35 days, and are shown in Figure 3.8. Obviously, both the control and the inoculated coupons retained a degree of passivity, since the current density in the passive range never exceed 10 $\mu A \cdot cm^{-2}$. A negative hysteresis in the cyclic polarization curve of control coupons indicates that localized corrosion is unlikely to occur for 304 SS in the sterile medium. However, a narrow positive hysteresis occurs in the cyclic polarization curve of inoculated controls, indicative of different polarization behaviors of 304 SS under the effect of *Pseudomonas* bacteria. It has been reported that positive hysteresis occurs when a damaged passive film is not repaired and/or pits are initiated (Tait, 1978), while negative hysteresis occurs when a damaged passive film repairs itself and pits are not initiated (Tait, 1979). The positive hysteresis, as well as the slight active shift of corrosion potentials, for the inoculated coupons is indicative of an adverse effect on the passivity of 304 SS surface the presence of *Pseudomonas* bacteria.

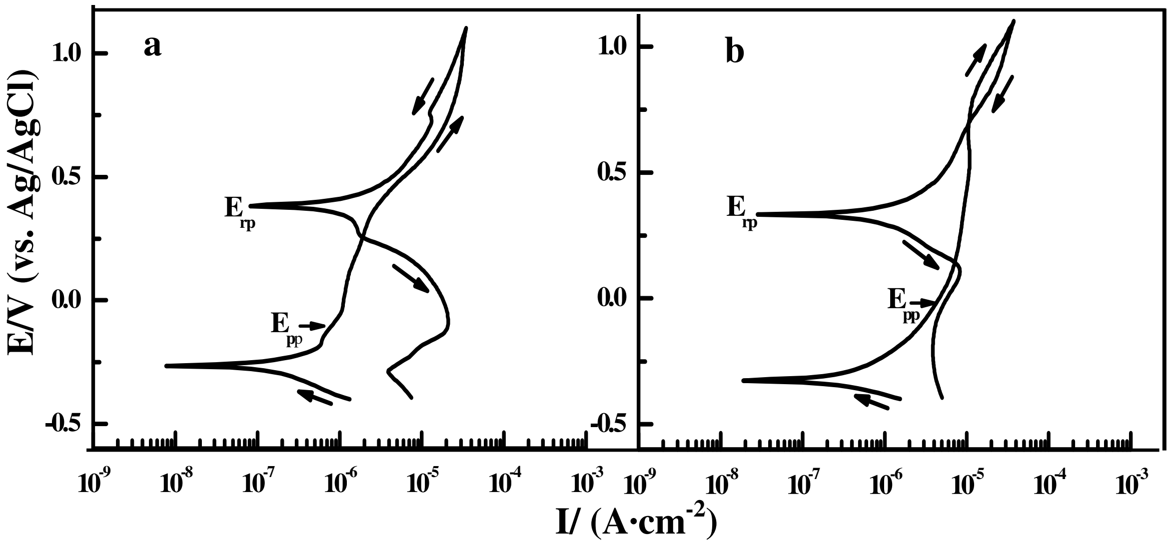

Figure 3.8 Cyclic polarization curves of 304 SS coupons in the (a) sterile and (b) the *Pseudomonas*-inoculated media for 35 days.

3.3.2 SEM and EDX studies

Representative SEM micrographs and the corresponding EDX spectra of stainless steel specimens, which are exposed to the sterile nutrient-rich medium to serve as the control samples, are shown in Figure 3.9. No localized corrosion was observed on the metal surface, except for the formation of conditioning layers by the spontaneous adsorption of organic macromolecules from the bulk solution after 14 and 35 days (Figs. 3.9a and 3.9b). The formation of conditioning layers on the solid surface is a ubiquitous phenomenon in aquatic environments, and is recognized to be the initial step of biofilm formation (Videla, 1996). Previous studies reported that the amount of organic species adsorbed increased with time and discrete or patchy films were formed after a short exposure time (Pradier et al., 2000; Compère et al., 2001). However, after 63 days of exposure, minor corrosion appears to occur on the specimen surface (Fig. 3.9c). EDX was used to quantify the chemical composition of corrosion products on the coupon surface. In the case of the short-term samples, the metallic elements of Fe, Cr and Ni are obviously predominant (Figs. 3.9a and 3.9b). For the long-term specimens, the EDX spectrum shows that a trace amount of Cl (~0.5%) is also detected (Fig. 3.9c). The presence of Cl can be used to interpret the cause of minor localized corrosion upon the long-term exposure. This result is also in good agreement with a previous study that stainless steel is susceptible to localized corrosion by chloride ions (Stott, 1993). Furthermore, the occurrence of minor localized corrosion on the long-term specimen also explains the slight decrease in resistance of the passive film, R_f.

SEM results reveal that the development of biofilms on the stainless steel surface is a dynamic process (Figs. 3.10a, 3.10c and 3.10e). The SEM image of the 14-day specimen reveals dense *Pseudomonas* cells at some localized sites. They aggregate to form bacterial colonies or clusters (Fig. 3.10a). The formation of patchy biofilms or clusters provides physicochemical conditions in localized environments to facilitate the initiation of pitting corrosion. (Hakkarainen, 2003). Some shallow pits are discernible on the 14-day coupon surface upon removal of the biofilms (Fig. 3.10b). Upon prolonging the exposure time to 35 days, bacterial cells associated with extracellular polymeric substances (EPS) are observed on the coupon surface (Fig. 3.10c). It has been reported that the bacterial cell aggregates are interspersed throughout the EPS matrix, providing pathways for the diffusion of active and nutrient species and giving rise to local gradients in metabolic products, aggressive ions (such as Cl^-), or dissolved oxygen (i.e., differential aeration cells) (Costerton, 1991). All of the above can generate active electrochemical corrosion cells to facilitate the occurrence of localized corrosion. After the removal of the biofilm, SEM image of the 35-day specimen reveals localized corrosion, visible as intense micropits and some deep macropits (Fig. 3.10d). In the case of the coupons after the long-term exposure, the coupon surface is covered by a highly porous and heterogeneous biofilm (Fig. 3.10e). Individual cells are no longer clearly visible on the biofilm, since the bacterial cells are probably embedded within the EPS matrix. After removing the biofilm, extensive micropits and macropits are present on the 63-day specimen surface (Fig. 3.10f).

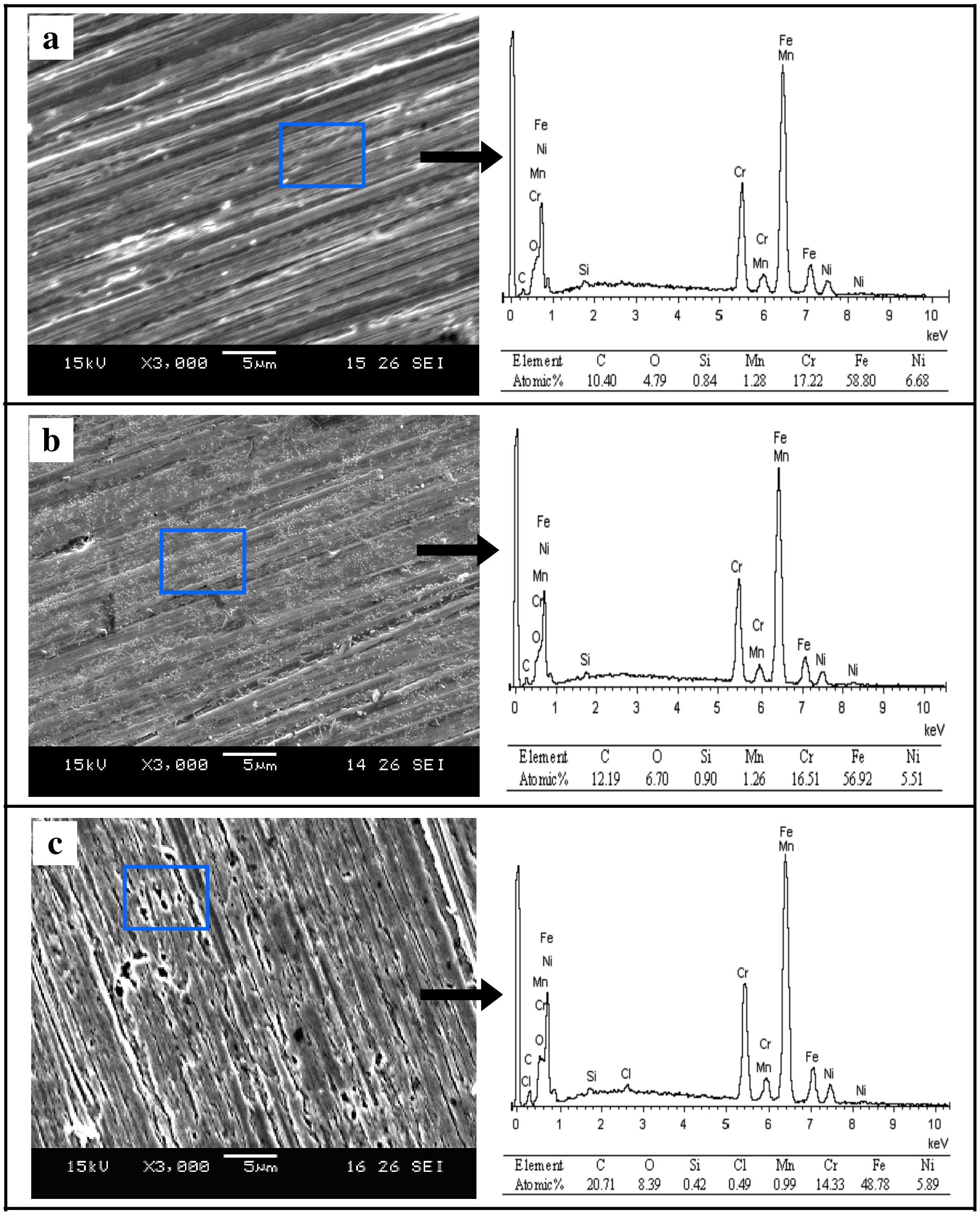

Element	C	O	Si	Mn	Cr	Fe	Ni
Atomic%	10.40	4.79	0.84	1.28	17.22	58.80	6.68

Element	C	O	Si	Mn	Cr	Fe	Ni
Atomic%	12.19	6.70	0.90	1.26	16.51	56.92	5.51

Element	C	O	Si	Cl	Mn	Cr	Fe	Ni
Atomic%	20.71	8.39	0.42	0.49	0.99	14.33	48.78	5.89

Figure 3.9 Representative SEM images and EDX of 304 SS in the sterile nutrient-rich medium after different exposure times: (a) 14; (b) 35 and (c) 63 days. The EDX spectra correspond to the rectangle area on the corresponding SEM images.

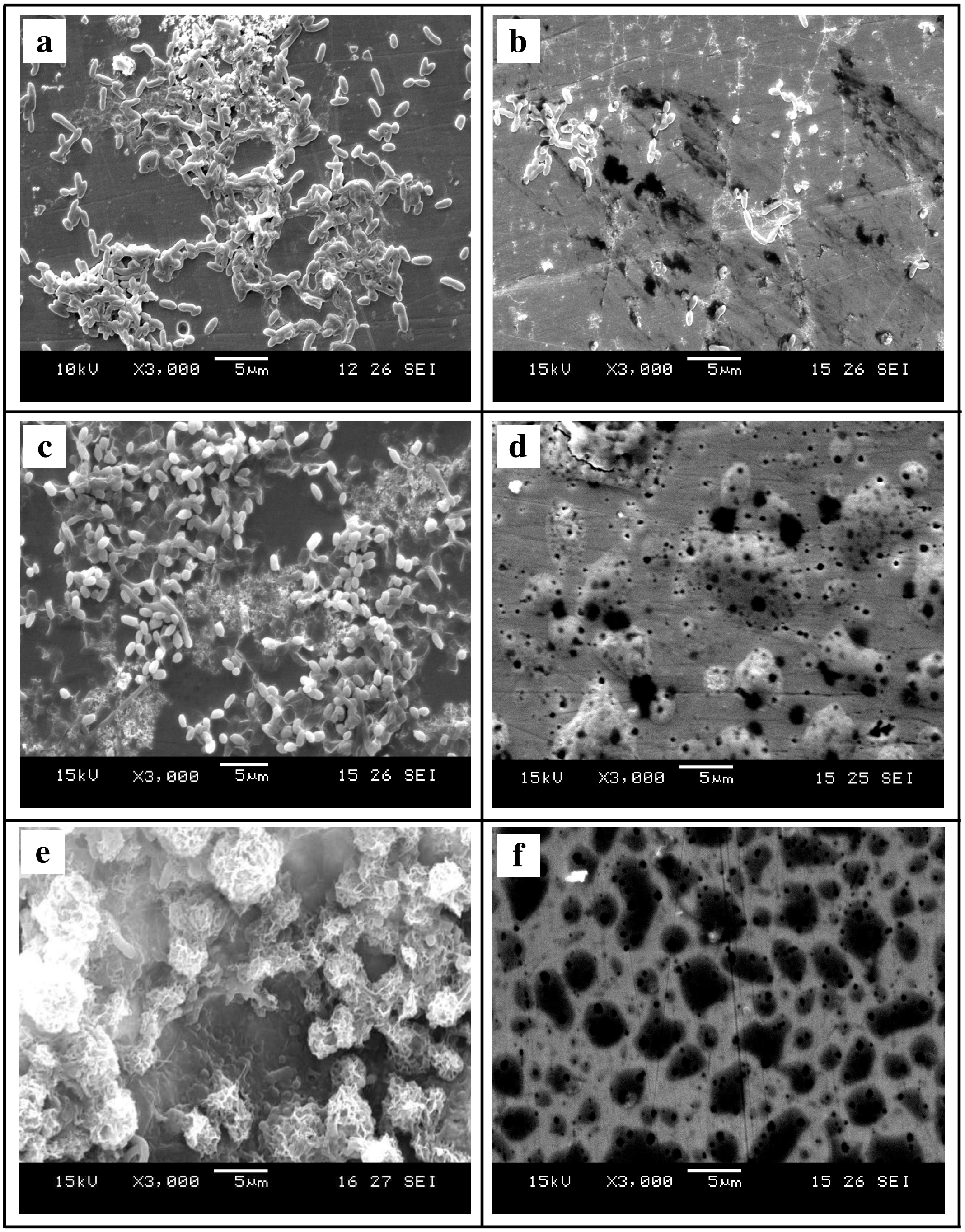

Figure 3.10 Representative SEM images of (a) 14 day-old; (c) 35 day-old; (e) 63 day-old biofilms formed on the 304 SS coupon surface. The corroded coupon surface after the removal of biofilms after different exposure times: (b) 14; (d) 35 and (f) 63 days.

To quantify the chemical compositions in the pitted areas on the metal surface, EDX analysis was carried out on representative pits of the specimen from various exposure times. Figure 3.11 shows the SEM images and the EDX spectra of the short-term coupons

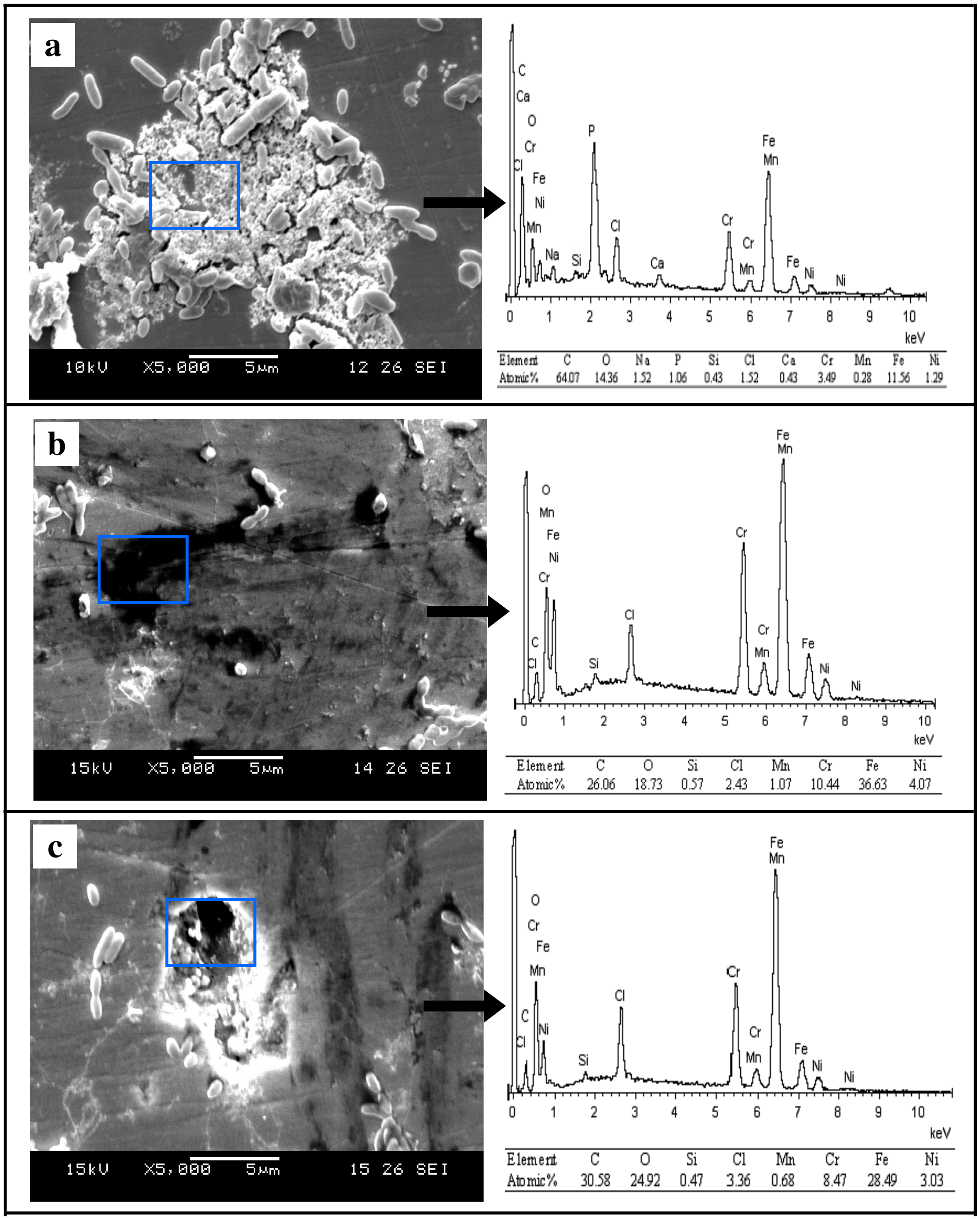

Element	C	O	Na	P	Si	Cl	Ca	Cr	Mn	Fe	Ni
Atomic%	64.07	14.36	1.52	1.06	0.43	1.52	0.43	3.49	0.28	11.56	1.29

Element	C	O	Si	Cl	Mn	Cr	Fe	Ni
Atomic%	26.06	18.73	0.57	2.43	1.07	10.44	36.63	4.07

Element	C	O	Si	Cl	Mn	Cr	Fe	Ni
Atomic%	30.58	24.92	0.47	3.36	0.68	8.47	28.49	3.03

Figure 3.11 SEM images and EDX spectra of representative pits after the biofilm removal on the coupon surface after a short-term exposure: (a, b) 14 days; (c) 35 days.

(Figs. 3.11a, 3.11b and 3.11c). Figure 3.11a shows a deteriorated site under a bacterial cluster after 14 days of exposure. The corresponding EDX spectrum shows that in addition to the metallic elements of Fe, Cr, Ni and Mn, signals associated with P, O, Cl, C and Na are also discernible, indicative of the presence of bacterial cells and their EPS and aggressive chloride species in the pitted zone. Figures 3.11b and 3.11c show respectively the macropits and the corresponding EDX spectra of the 14-day and 35-day specimen. The elemental peaks in both EDX spectra are very similar to each other, except for the variation in peak intensity. Two apparent features can be readily noticeable: i) the enrichment of C, O and Cl in the pitted areas with exposure time and ii) the depletion of metallic elements of Fe, Cr, Ni and Mn in the pitted areas. The results appear to correlate with the occurrence of localized corrosion in the presence of aggressive chloride ions (Cl^-) as well as the colonized bacteria.

To demonstrate the involvement of chloride ions in initiating and propagating pitting corrosion, EDX analysis was performed on several locations, which have different surface characteristics, on the surface of a representative 63-day specimen. Figure 3.12 shows the SEM image and three EDX spectra corresponding to the analyzed locations. Among the three EDX spectra, the most noticeable feature is the change in the amount of Cl, which is apparently correlated with pitting corrosion. As shown in Figure 3.12, the relative abundance of Cl is as high as ~9% in a deep and large pit (point A), while it is ~2.2% in a shallow and small pit (point B) and is only ~1.3% in a newly-initiated pit (point C). In addition, the enrichment of C and O, and the depletion of metallic elements of Fe, Cr and Ni appear to be associated with the pitted regions as well. Consequently, it can be concluded that both bacterial colonization of *Pseudomonas* and aggressive chloride play significant roles in the initiation and propagation of pits. This is consistent with the conclusions of Morales et al. (1993) in studying the role of *Pseudomonas aeruginosa* in the localized corrosion of stainless steel. They concluded that the presence of growing bacterial cells enhanced the breakdown of passivity by the aggressive Cl^-. However, Beech et al. (2000) emphasized that the acceleration of corrosion reactions and the occurrence of extensive pitting corrosion was caused by the biofilm and plantonic EPS rather than by the effect of aggressive Cl^-.

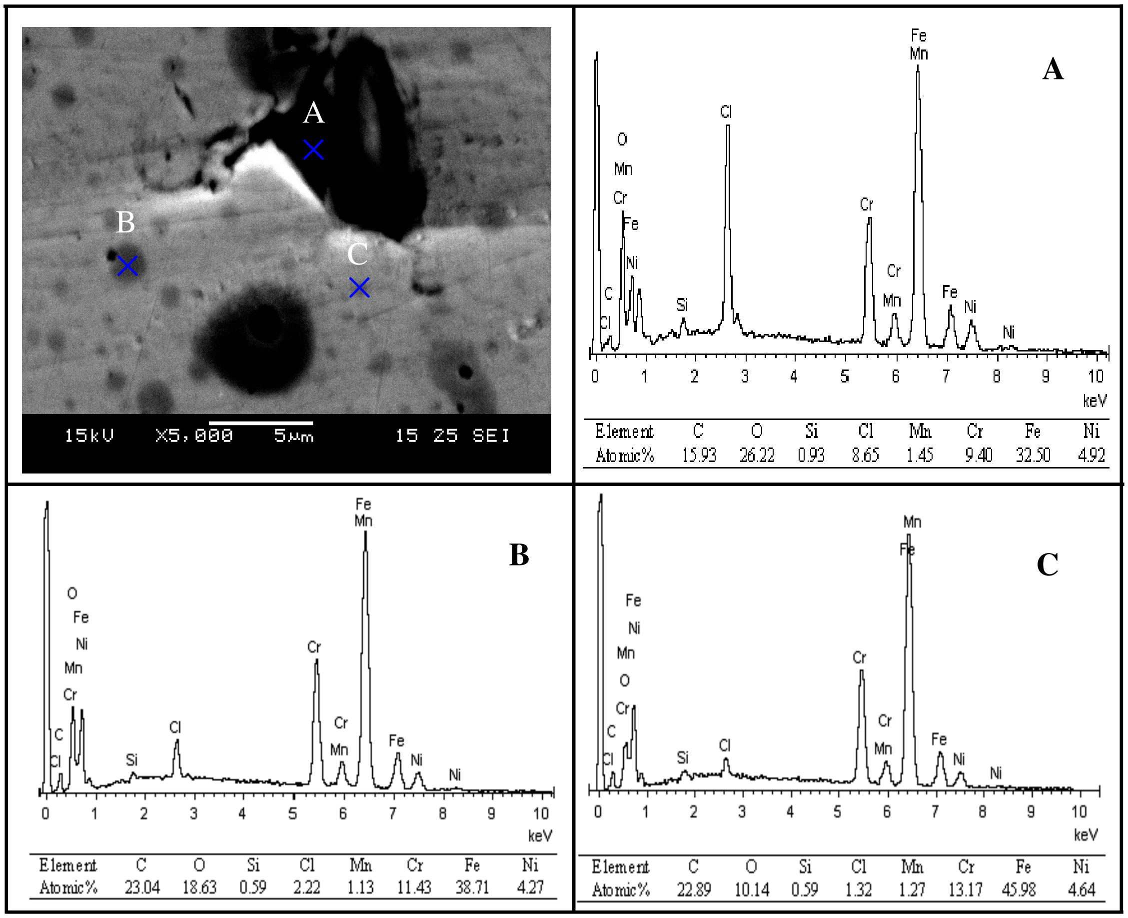

A

Element	C	O	Si	Cl	Mn	Cr	Fe	Ni
Atomic%	15.93	26.22	0.93	8.65	1.45	9.40	32.50	4.92

B

Element	C	O	Si	Cl	Mn	Cr	Fe	Ni
Atomic%	23.04	18.63	0.59	2.22	1.13	11.43	38.71	4.27

C

Element	C	O	Si	Cl	Mn	Cr	Fe	Ni
Atomic%	22.89	10.14	0.59	1.32	1.27	13.17	45.98	4.64

Figure 3.12 EDX spectra of various locations on a representative SEM image with the biofilm removed on the 63-day-exposed specimen. The symbol of × shows the regions with EDX analysis. A, B and C represents the corresponding EDX spectra.

Comparing the EDX spectra of bacteria-colonized specimens with those of sterile control specimens, the formation of heterogeneous biofilms, aided by the aggressive chloride, are believed to be responsible for the initiation and propagation of pitting corrosion on the bacteria-colonized specimen surface. It has been reported that three conditions must be fulfilled in the occurrence of pitting corrosion: i) the presence of aggressive anions (such as Cl^-) in the electrolyte, ii) the existence of potential difference between the interior of the pit and the open surface, and iii) the reaction temperature must be beyond a critical temperature (Hakkarainen, 2003). These conclusions help to explain the occurrence of extensive micropitting corrosion in the present study. The colonization of a bacterial biofilm gives rise to the potential differences between areas under the biofilm, which serve as the anodic sites, and surrounding regions, which act as the cathodic sites. The synergistic effect of aggressive chloride ions (Cl^-) and colonized bacterial cells can therefore trigger the partial loss of passivity of the stainless steel and the initiation of pitting corrosion. The initial damage to the passivation film has an important consequence to the long-term performance of stainless steel, as deep pits can cause wall penetration, leakage and failure. It has been reported that a pit, once initiated, provides a recess area that hinders mass transfer between the pit interior and the exterior bulk solution (Jones, 1996). The growth of pits has been widely recognized to be a self-propagating or autocatalytic process, since hydrolysis of the corrosion products and aggressive chloride ions can result in acidic solutions that destroy passivity locally and create an active (corroding) anode within the pit (Geiser et al., 2002).

3.4 Summary

This chapter focused mainly on the investigation of the effect of *Pseudomonas* NCIMB 2021 bacterium on the corrosion processes of 304 SS in comparison with sterile experiments. Electrochemical results demonstrated that despite of the slight decrease in the resistance of the passive film after long-term exposure, the passive film formed on SS 304 in the sterile nutrient-rich medium was relatively stable, and resulted in the anodic reaction to be under diffusion control. The colonization of *Pseudomonas* bacteria on the coupon surface resulted in the acceleration of the anodic reaction due to the deterioration of the passivity of the oxide film and the slowing down of the cathodic reaction accompanying the depletion of oxygen. SEM morphology revealed that the heterogeneity and the coverage of biofilms formed on the metal surface increased with time, and that extensive micropitting corrosion occurred under the biofilms. EDX spectra further verified that the occurrence of pitting corrosion was caused by the synergistic effect of aggressive chloride ions and the colonization of bacterial cells and their EPS.

CHAPTER 4

LOCALIZED CORROSION OF 304 STAINLESS STEEL BY AEROBIC *PSEUDOMONAS* NCIMB 2021 BACTERIUM: AFM AND XPS STUDY

4.1 General Background

In Chapter 3, 304 SS was found to be vulnerable to MIC in the presence of a marine aerobic *Pseudomonas* NCIMB 2021 bacterium. However, it still remains uncertain how large a role MIC plays in the corrosion of common stainless steel and by which mechanism it occurs. In addition, an important feature, which was reported to be correlated with the occurrence of pitting corrosion in specific areas (such as at the grain boundary), is the segregation of elements (Geesey et al. 1996; Shi et al., 2003). Attempts have been made to correlate the chemical changes in the passive film caused by microbial colonization with the localized damage or pitting corrosion of stainless steel (Beech et al., 2000; Geesey et al., 1996; Shi et al., 2003; Pendyala et al., 1996). However, there is ongoing controversy whether and to what extent the biofilms formed on the stainless steel surface promote selective depletion of elements, such as the depletion of Cr or Fe in the outermost passive oxide film. Therefore, the detection of compositional changes of the outermost layer caused by biofilm formation helps to clarify the role of bacterial colonization in localized pitting corrosion of stainless steel.

The purpose of this chapter is to investigate MIC of 304 SS by *Pseudomonas* NCIMB 2021 bacterium using AFM and XPS. AFM was used to image in situ the proliferation of sessile cells, to monitor the development of biofilms with exposure time and to assess the degree of corrosion damage by quantifying the pitting corrosion of metals underneath the biofilm at various exposure times. XPS measurements were carried out to obtain the elemental information of the outermost passive layer on stainless steel after the biofilm removal to determine the subtle changes in surface chemistry induced by the biofilm formation, since the outmost layer is where biofilm microbial processes are likely to have their greatest influence. In comparison, stainless steel coupons exposed to the same sterile medium under same conditions served as controls.

4.2. Materials and methods

4.2.1 Preparation of coupons

The 304 SS coupons and their preparation were similar to those procedures described in Section 3.2.1 of Chapter 3, except that the coupons ground with silicon carbide were further polished to a mirror-finish surface using 0.3 μm alumina powders.

4.2.2 Preparation of medium and *Pseudomonas* culture

The medium and inoculums were prepared exactly as those described in Section 3.2.2 of Chapter 3

4.2.3 Development of biofilms and corrosion in the *Pseudomonas* inoculated medium

The development of biofilms on the coupon surface as well as the corrosion of the steel coupons in the *Pseudomonas* inoculated medium is similar to those procedures described in Section 3.2.3 of Chapter 3. Both the AFM and XPS studies were repeated twice employing four coupons for each exposure time.

4.2.4 AFM study

To characterize the growth of sessile *Pseudomonas* cells on the surface of stainless steel 304, a coupon with a 7-day-old biofilm was immediately mounted on the stubs after removed from the *Pseudomonas* inoculated medium, and subsequently a series of images of a single *Pseudomonas* cell were captured in different growth stages. A Nanoscope IIIA fluid tapping mode AFM was used to image the proliferation of a sessile *Pseudomonas* cell in situ on the coupon surface. A standard fluid cell was used. The fluid flowed past the cell at a rate of 5 mL/h and stopped when capturing images with a scan rate of 0.25 Hz to minimize the interference of liquid in the fluid cell. The proliferation of sessile *Pseudomonas* cells was recorded over a period of ~ 300 min. For biofilm imaging and corrosion damage caused by bacterial colonization, the coupons are prepared similarly to those described in Section 3.2.5.

A Nanoscope IIIa AFM (Digital Instruments, Santa Barbara, CA, USA) operating in a contact mode in air was used to capture the images of biofilms and pits on the metal coupon surface. The nanoprobe cantilevers were made of silicon nitride (Si_3N_4) with a spring constant of k = 0.06 N/m (Digital Instruments, USA). The radius of curvature of the AFM tip is ~50 nm. The scan rate was varied between 1.0 and 2.0 Hz depending on the image size. The Digital Nanoscope software (Version 5.30) was used to analyze the topographic images of the coupon surface. During the AFM measurement, a 100×100 μm image was firstly captured in order to assess the exact position and the nature of bacterial cells or biofilms, with further scans being used to zoom onto any interesting features. AFM images were randomly captured on the coupons with biofilms to represent the characteristics of the entire coupon surface after various exposure times. To reveal the progression of pitting corrosion, six different areas were randomly selected on each coupon to capture representative pits.

4.2.5 XPS characterization of the outermost surface film

To better understand the elemental information of the passive film on the steel coupon surface after exposed to the sterile and inoculated media and to verify the subtle changes in the surface chemistry induced by bacterial colonization, a detailed XPS study was carried out on the outermost layers of three types of corrosion specimens: a) the coupons with biofilms after exposed to the *Pseudomonas* inoculated medium for 7 and 28 days, b) the coupon with biofilm removed after exposure to the *Pseudomonas* inoculated medium for 7 and 28 days, c) the coupon after exposure to the sterile medium for 7 and 28 days as the control samples.

At the predetermined exposure time, the steel coupons were removed from the inoculated medium, washed twice with sterile DI water, placed in liquid nitrogen for 15 min, and then lyophilized with a freeze dryer (Telstar, Spain) at -50 ℃ for 8 h. Thus, the coupons covered with biofilms were prepared and ready to be characterized with XPS. The preparation procedure of the coupons with the biofilm removed was as described previously (Beech et al., 2000): the biofilm was removed from the coupon surface with sterile cotton swabs immediately after the coupons were taken out, followed by rinsing with sterile DI water twice, dried by purging with nitrogen gas, and finally stored in an vacuum desiccator prior to analysis. Control coupons were also prepared by the procedures of DI water rinsing and nitrogen gas drying as mentioned above.

For XPS measurements, an AXIS HSi spectrometer (Kratos Analytical Ltd.) with a monochromatized Al Kα X-ray source (1486.6 eV photons) was employed at a constant dwell time of 100 ms and a pass energy of 40 eV. The anode voltage was 15 kV and the anode current was 10 mA. The pressure in the analysis chamber was maintained at 10^{-7}-10^{-9} Torr during each measurement. All the survey scans and the core-level spectra were obtained at a photoelectron take-off angle of 90^{o} without Argon ion etching. Survey scans were recorded within a range of 0-1100 eV. To compensate for the surface charging effect, all core-level spectra were referenced to the C 1s hydrocarbon peak at 284.6 eV. In spectral deconvolution, the linewidth (i.e. full width at half-maximum) of the Gaussian peaks was maintained constant for all components in a particular spectrum. The peak area ratios for the various elements were correlated with the use of experimentally determined instrumental sensitivity factors (Briggs and Seah, 1990).

4.3. Results and discussion

4.3.1 AFM study

4.3.1.1 In situ imaging the proliferation of a sessile *Pseudomonas* cell

Figure 4.1 illustrates a typical image of a *Pseudomonas* NCIMB 2021 cell on the 304 SS surface after immersion in the *Pseudomonas* inoculated medium for 7 days. The dimensions of the cell are 1.78×0.84×0.16 µm (length × width × depth). The rod-shape of the bacteria is also clearly visible.

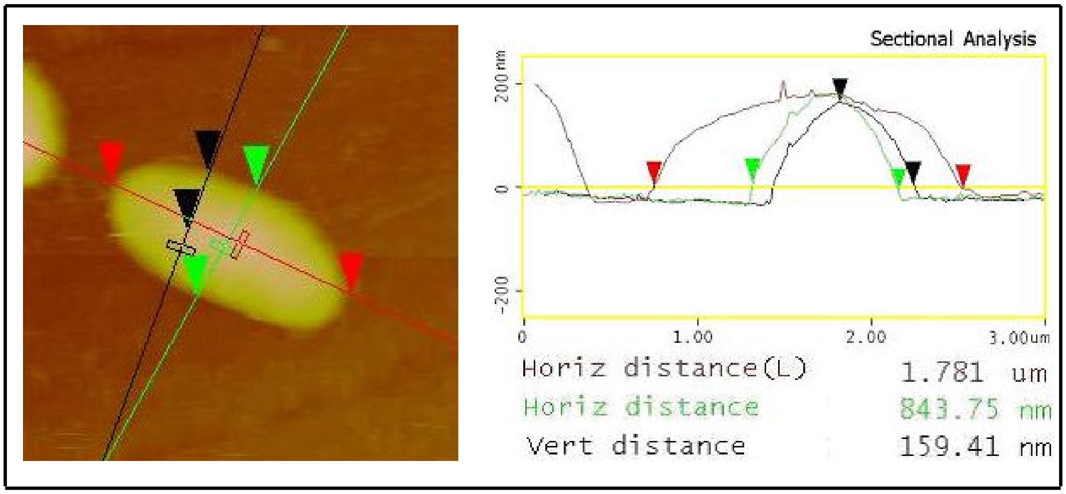

Figure 4.1 AFM images of a single *Pseudomonas* NCIMB 2021 cell on the coupon surface after 7 days of exposure

Figure 4.2 shows a series of *Pseudomonas* cell in various stages in a 7 day-old biofilm on the surface of 304 SS. It can be clearly observed that a *Pseudomonas* cell is a rod-shaped and polar flagellated cell (Fig. 4.2a). It attaches itself to the surface in a face-to-face manner, and proliferates by binary fission. The proliferation process can be depicted as follows: a mature *Pseudomonas* cell begins to divide as shown in Figure 4.2b, then two daughter cells are generated later (Fig. 4.2c), lastly, the two daughter cells proceed to migrate slowly away from each other (Fig. 4.2d). This is in good agreement with the previous reports about the proliferation of bacterial cells (Mueller et al., 1992).

The results also suggest that the repetition of binary fission of sessile *Pseudomonas* cells and the continuous attachment of *Pseudomonas* cells from the bulk solution to the metal surface are significant steps in the process of the biofilm formation, thus the biofilm development on the solid surface is ultimately dependent upon the population growth of the initial surface-colonizing bacteria and upon the copious production of EPS by the colonizing organisms (Marshall, 1994).

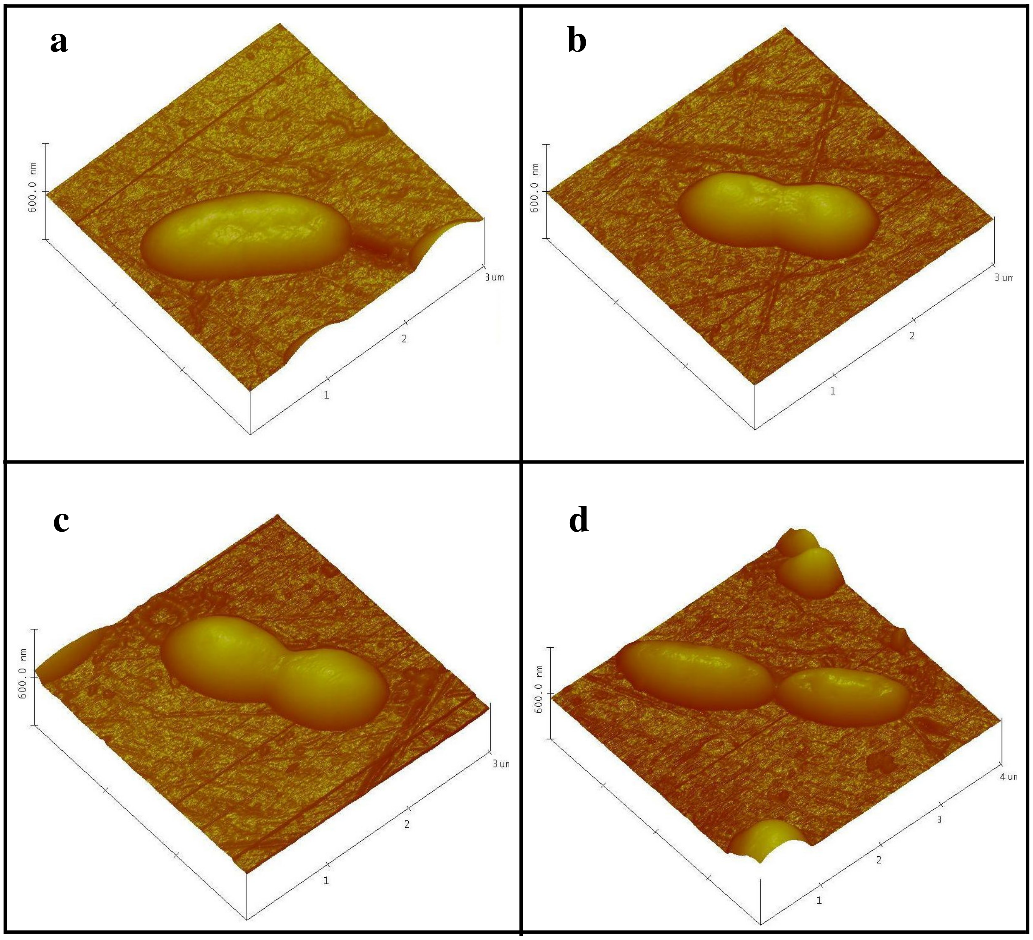

Figure 4.2 A series of AFM images of sessile cells within a 7 day-old biofilm on the steel coupon surface illustrating the binary fission process of *Pseudomonas sp.* NCIMB 2021. (a) a mature *Pseudomonas* cell, (b) a cell in the process of dividing, (c) the formation of two daughter cells, (d) the separation of two daughter cells.

It is noteworthy that the resolution of an in situ image is generally lower compared to imaging in air. Two possible factors are found to result in lower resolution of in situ

AFM images: one is the interference of fluids to the movement of the AFM tip, the other is the attachment of bacterial cells to the AFM tip. The current study alleviates the fluid interference by using a slow scan rate. Simultaneously, the present study focuses on a single sessile *Pseudomonas* cell in a discrete 7-day-old biofilm instead of the aging biofilms to circumvent the tip-fouling problem. It is conceivable that the lower resolution problem of in situ AFM images can be minimized through a proper choice of tip material and changes in the operating parameters, since relatively high-resolution in situ AFM images are captured in the current study (Figure 4.2).

4.3.1.2 The development of biofilm on the stainless steel coupon surface

A series of AFM images were captured on the steel coupons after predetermined exposure times to show a dynamic process for the biofilm formation on the surface of 304 SS coupon. Figure 4.3 demonstrates that the development of the biofilm on the coupon surface is a dynamic and continuous process. Figure 4.3a shows that a number of *Pseudomonas* cells have attached to the metal surface, but only a few bacterial clusters or a patchy biofilm generate after 7 days of exposure. When the exposure time is extended to 14 days, the patchy biofilm increases in thickness and coverage, and becomes more heterogeneous (Fig. 4.3b). A thicker and more heterogeneous biofilm is formed on the surface of stainless steel 304 (Fig. 4.3c) upon prolonging the exposure time to 21 days. It is obvious that the biofilm of a monoculture *Pseudomonas* bacterium not only changes from discrete bacterial clusters to biofilms, but also increases in thickness and heterogeneity with increasing exposure time. The patchiness and heterogeneity of the biofilm are reported to be very important to the initiation of localized corrosion and the acceleration of corrosion rates, since they can give rise to local differences in metabolic

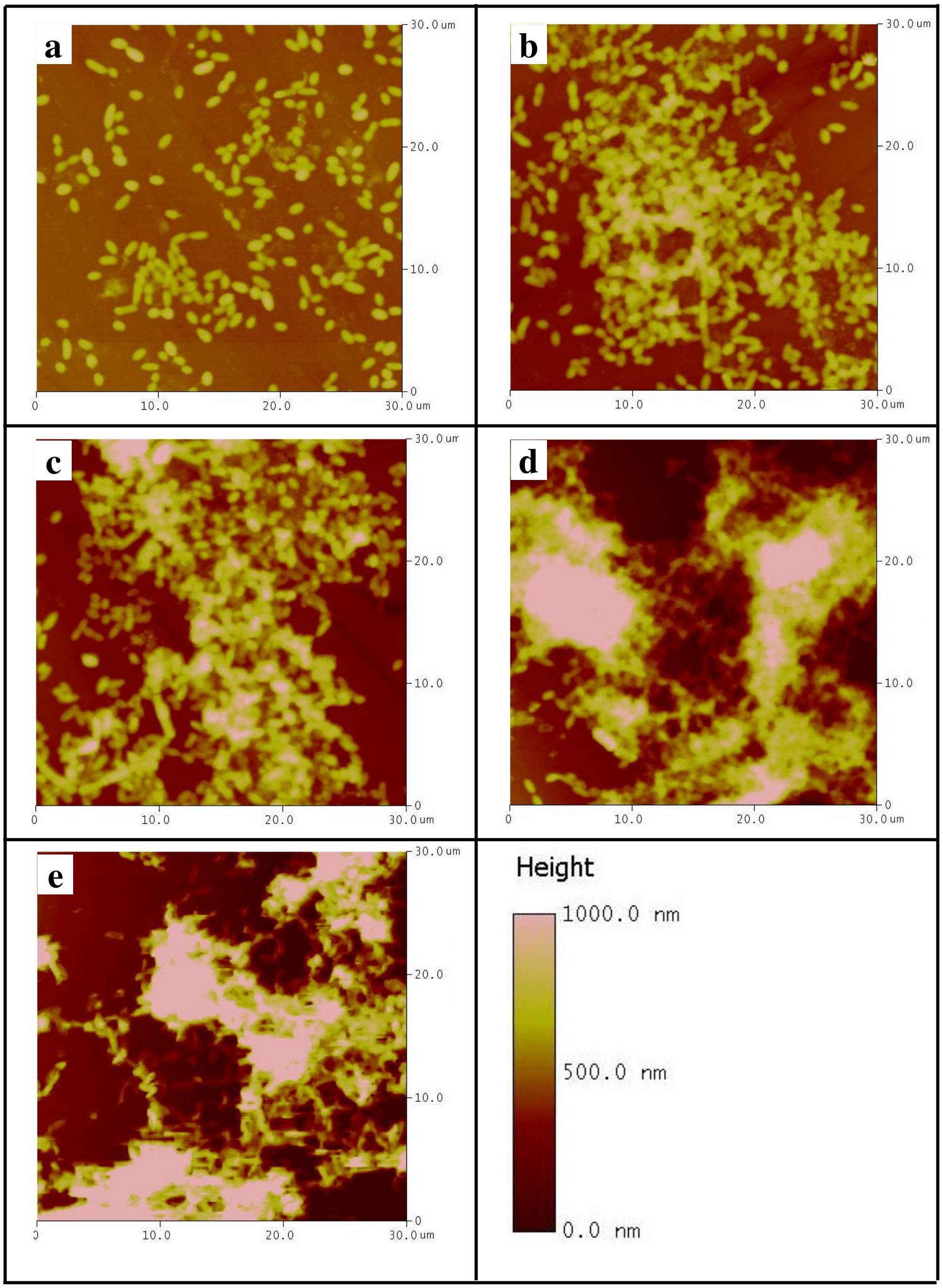

Figure 4.3 AFM images of (a) 7 day-old, (b) 14 day-old, (c) 21 day-old, (d) 35 day-old, (e) 49 day-old biofilms formed by pure cultures of *Pseudomonas sp.* NCIMB 2021 on the surfaces of 304 SS coupons.

products, pH, or DO (differential aeration cells), all of which can generate active electrochemical corrosion cells (Beech et al., 2002; Fang et al., 2000; Hamilton, 1994). Figures 4.3d and 4.3e show the aging biofilm formed on the coupon surface, exhibiting a high level of heterogeneity, after a long exposure time. Patches of cell aggregates (not monolayer) are interspersed throughout an exopolysaccharide matrix that varies in its density, creating open areas, where water channels are formed. A recent study using nondestructive confocal scanning laser microscope (CSLM) to investigate the hydrated biofilms has shown that the volume of bacterial biofilms is occupied more by the glycocalyx matrix (75 to 95%) than by bacterial cells (5 to 25%), and that these cells may be concentrated either in the lower or the upper regions of the biofilm (Caldwell et al., 1992; Costerton et al., 1995). The current results confirm previous findings of the structure and the characteristics of the biofilm. In addition to its structure, the composition of the biofilm may also play an important role in MIC. It is reported that biofilms are composed of clusters of microbial cells, EPS and interstitial voids (Xu et al., 1999). The EPS secreted by SRB was recognized to accelerate the corrosion rate of mild steel by as much as 5-fold in the presence of 1% (w/w) EPS solution, as compared to in the absence of SRB (Chan et al., 2002).

4.3.1.3 Imaging pitting corrosion of stainless steel 304 in *Pseudomonas* culture

The extent of corrosion damage caused by the bacterial colonization was assessed by profiling the pits on the coupon surface after the removal of biofilms and deposits. Figure 4.4 shows the AFM images (100×100 µm) after various exposure times. As shown in Figure 4.4a, a newly-prepared coupon exhibits a smooth and pit-free surface. The initiation of pitting corrosion is found on a 14-day coupon surface, and the number of pits and their sizes seems to increase with exposure time (Figs. 4.4b, 4.4c and 4.4d). The occurrence of micro-pitting corrosion on the coupon surface after 49 days of exposure indicates the failure of the passive film of stainless steel 304 under the attack of *Pseudomonas* bacteria and aggressive anions.

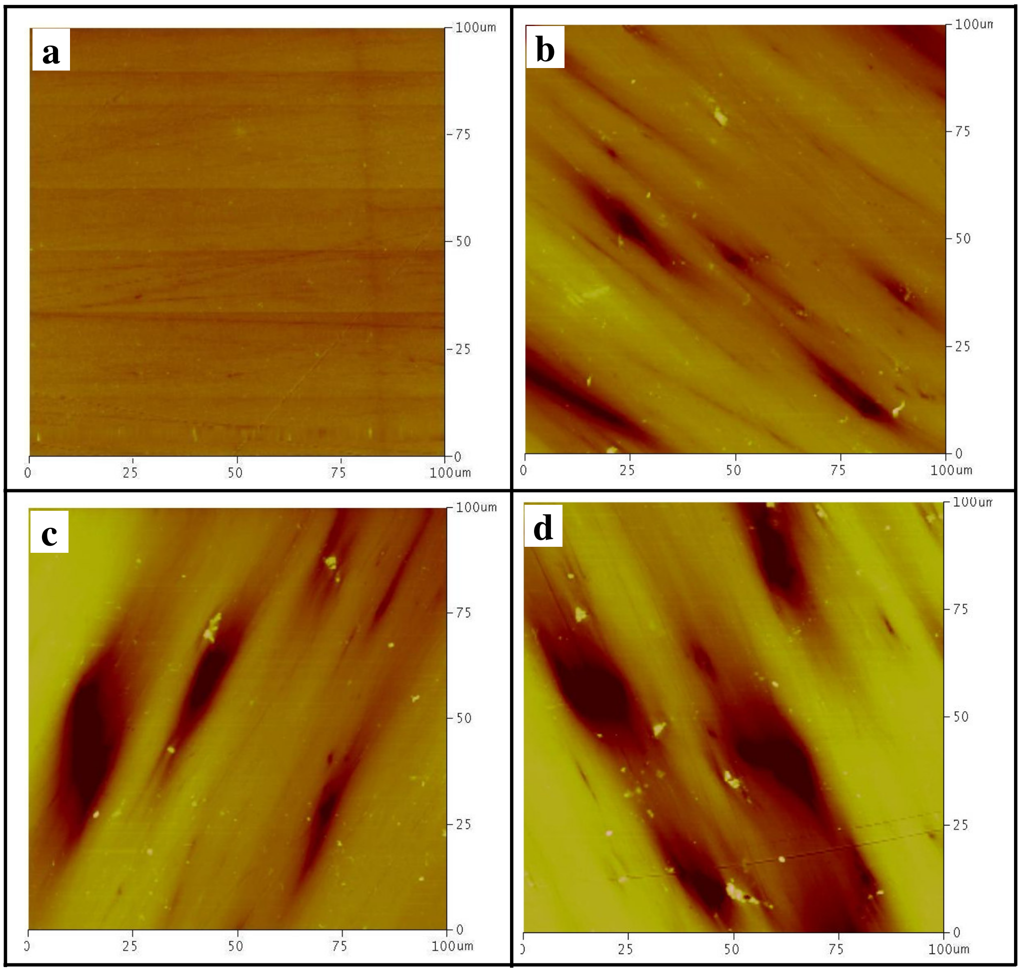

Figure 4.4 AFM images of a newly-prepared coupon (a) and coupons with the biofilm removed after various exposure times: (b) 14, (c) 28, (d) 49 days.

Table 4.1 The mean depth of pits for MIC and control coupons (mean ± SD[*], nm)

Exposure time (days)	14	21	28	35	49
MIC	144.24 ± 28.67	304.78 ± 23.68	397.02 ± 48.40	520.46 ± 27.98	696.41 ± 40.52
Control	ND[†]	ND	ND	30.82 ± 1.58	35.28 ± 3.94

[*] SD denotes standard deviation, [†] ND refers to not detected.

To evaluate the changes in the depth and the width of pits with exposure time, it is particularly useful to probe the morphological changes of individual pits. AFM has been widely recognized to have a higher resolution and accuracy in the vertical dimension compared to other microscopic techniques, and this offers an opportunity to quantify localized corrosion (Beech et al., 2002, Fang et al., 2000). The depth and the width of a

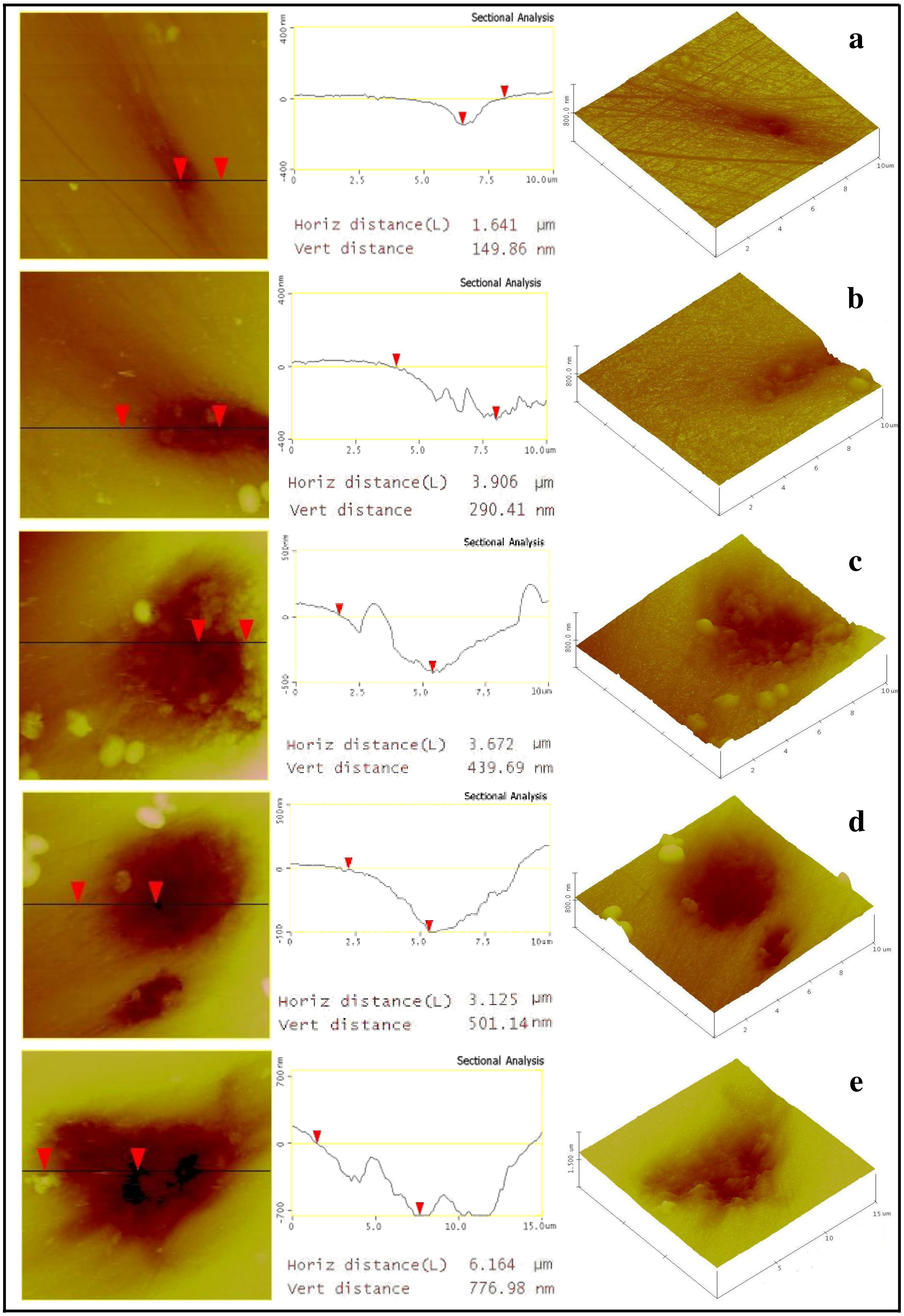

Figure 4.5 AFM images of the presence of pits on the corroded surfaces of the stainless steel 304 coupon after different exposure times: (a) 14, (b) 21, (c) 28, (d) 35, (e) 49 days.

pit can be obtained by the sectional analysis provided by the AFM software. Figure 4.5 shows a series of AFM images of representative pits on the corroded coupons after various exposure times. The two-dimensional and the corresponding three-dimensional renditions are shown together with the sectional analysis for each AFM image. After 14 days of exposure, a relatively shallow pit with a depth of ~150 nm is generated on the surface of steel coupons, indicative of the initiation of micro-pitting corrosion (Fig. 4.5a). As the corrosion proceeded, the width and the depth of pits propagate (Figs. 4.5b-4.5d), and thus much deeper and wider pits are present on the SS coupon surface. The depth of pits reaches as high as ~770 nm after 49 days of exposure in the *Pseudomonas* inoculated medium (Fig. 4.5e). In light of all the pits captured at each predetermined time, the mean depth of pits on the coupon surface is calculated and shown in Table 4.1. It is clearly observed that the mean depth of the pits increases with exposure time in this study.

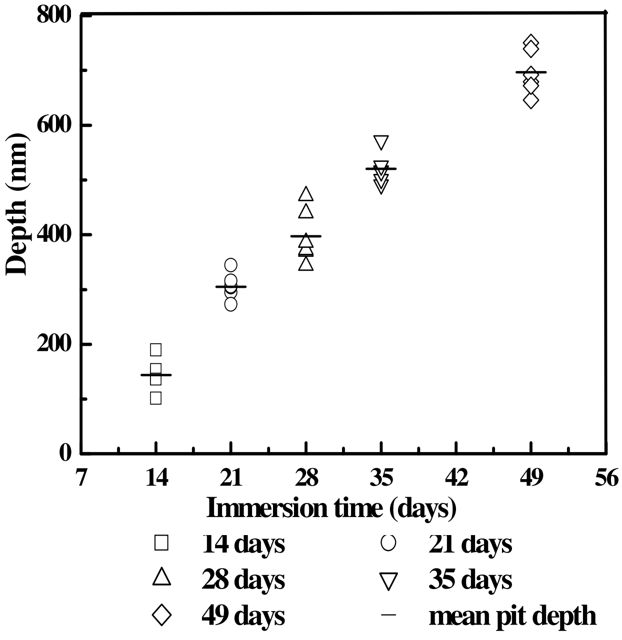

Figure 4.6 A scattergram showing the relationship of pit depth with exposure time. Six representative pit depths measured with sectional analysis are shown for each corroded coupon surface. The symbol bar denotes the mean depth of pits.

A scattergram is also plotted in Figure 4.6 to show the relationship of pit depth with exposure time. The depth of pits apparently increases linearly with exposure time. This is consistent with the conclusions of Xu et al. (1999) in studying MIC of mild steel. Interestingly, the shape of the corroded pits is neither triangular nor cylindrical, rather it is of irregular cones. This probably indicates that the shape of the pits generated on the coupons with biofilms mainly depends on the shape and the thickness of the biofilms.

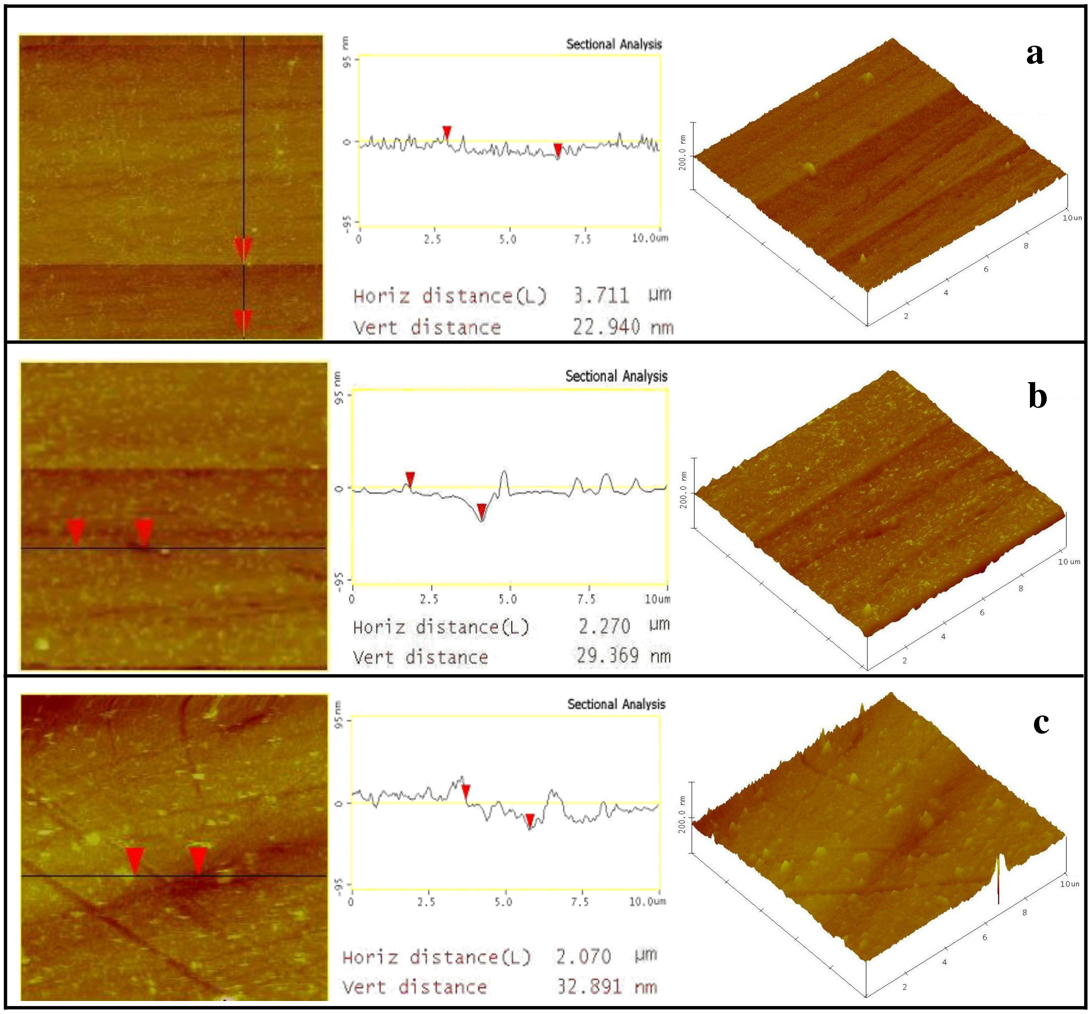

Figure 4.7 AFM images of the surface of control coupons after different exposure times: (a) 14 days, (b) 35 days, (c) 49 days.

Figure 4.7 shows AFM images of the control coupon surface after exposed to the sterile medium for 14 and 49 days. No pits can be observed on the control coupons after

14 days of exposure (Fig. 4.7a). Furthermore, no evidence of the occurrence of pitting corrosion is found on the coupon surface even after 35 and 49 days of exposure (Figs. 4.7b and 4.7c). The depth of a shallow pit is 35.28 ± 3.94 nm on the 49-day control coupon surface, which is smaller as much as ~25-fold than the corresponding MIC coupons. When comparing the deterioration of the MIC coupon surface with the corresponding control coupon surface, it is easy to conclude that the corrosion damage of stainless steel 304 is mainly caused by the biological effect under heterogeneous biofilms. As described before (Xu et al., 1999; Steele et al., 1994), the microorganisms probably do not participate in the corrosion process directly, but actively change the interfacial environment by creating concentration cells to facilitate the corrosion process.

4.3.2 Surface characterization with XPS

4.3.2.1 Surface elemental analysis with a wide scan

Survey scans were carried out to identify all detectable elements in the outermost layers of the surface film on all three types of coupons. The relative atomic concentrations of elements (i.e. RACE) and their ratios are calculated using the peak areas normalized on the basis of data acquisition and sensitivity factors. The elements of C, O, N, Fe, Cr, Ni and Si are recorded on all coupons (Figure 4.8). The RACE of the outermost layers of the surface film is shown in Table 4.2. For the coupons with biofilms, the main constituents are C, O and N, and the elements of Fe and Cr decrease in RACE with increasing biofilm accumulation. The surface film contains ~70% of C after 28 days of exposure as well as no Fe and Cr detectable, indicating that the biofilm was thick enough at that location to exceed the XPS detection limit. This is in good agreement with the above AFM measurements (Fig. 4.3c). It is noteworthy that the conditioning layers, formed by the adsorption of organic compounds from the bulk solution, probably make a small contribution to the C, O and N peaks in the inoculated medium. However, they are negligible in comparison with the bacterial cells and EPS in the biofilm as described in previous studies (Johansson and Saastamoinen, 1999). As for the coupons with the biofilm removed, the main constituents are C, O, N, Fe and Cr. Traces of Ni and Si can also be detected. The high content of C, O and N is believed to arise from the EPS and the conditioning layers, which probably bound to the metal so tightly that the brief scraping treatment with cotton swabs fails to strip them off. Among them, the most noticeable change in the outermost layers is the increase in the Cr content with exposure time, which reaches as high as ~ 5.5% after 28 days of exposure. It has reported that the enrichment of Cr in the surface film is accompanied with the depletion of Fe due to the effect of surface-harboring biofilm (Beech et al., 2000; Pendyala et al., 1996). For the control coupons, the chemistry of the surface film consists mainly of C, O, N, Fe and Cr and remains relatively constant throughout, indicative of the stability of passive film in the sterile medium. Another significant feature of all three types of coupon surface is the weakness of Ni signal in the surface film. The result has been widely reported by previous investigators in studying on the passive film of stainless steels (Abreu et al., 2006; Varga et al., 1997; Li et al., 2001). Olefjord and Wegrelius (1990) reported that the Ni^{2+} content was low in the passive film of stainless steel. Varga et al. (1997) found that Ni was detected with poor signal-to-noise ratio in the passive film of stainless steel, and so it appeared to play a minor role in the structure of the surface oxide film. The major reason for the phenomenon is probably: (i) the selective dissolution of Ni from the oxide film (Abreu et al., 2006), (ii) Ni has the slowest reaction rate with O_2^- among the alloy elements of Fe, Cr and Ni on stainless steel 304, thus leading to Ni close to the oxide/metal interface (Li et al., 2001).

Table 4.2 Relative atomic concentrations of the main constituents on the coupon surface in the sterile and *Pseudomonas* inoculated media after different exposure times.

Atomic concentration (%)	7 days			28 days		
	A_1[a]	B_1[b]	C_1[c]	A_2[d]	B_2[e]	C_2[f]
C	57.27 ± 2.86	50.72 ± 3.80	48.19 ± 4.82	69.72 ± 5.23	47.32 ± 2.37	47.61 ± 1.19
O	33.52 ± 0.84	39.11 ± 1.37	37.71 ± 1.86	30.11 ± 2.26	40.75 ± 3.06	38.64 ± 2.94
N	4.92 ± 0.37	2.11 ± 0.26	2.93 ± 0.15	4.63 ± 0.38	1.93 ± 0.17	2.65 ± 0.20
Fe	1.94 ± 0.19	3.97 ± 0.49	9.15 ± 0.67	0.17 ± 0.03	3.96 ± 0.59	9.15 ± 0.82
Cr	1.63 ± 0.20	2.95 ± 0.22	1.33 ± 0.17	b.d.l.	5.52 ± 0.42	1.95 ± 0.24
Ni	b.d.l.[†]	0.72 ± 0.11	0.69 ± 0.09	b.d.l.	b.d.l.	b.d.l.
Si	0.72 ± 0.14	0.42 ± 0.08	b.d.1	1.12 ± 0.17	0.53 ± 0.06	b.d.l.

a). A_1 refers to the coupon with biofilms after 7 days of exposure;
b). B_1 refers to 7-day coupon with the biofilm removed;
c). C_1 refers to the control coupon after 7 days of exposure;
d). A_2 refers to the coupon with biofilms after 28 days of exposure;
e). B_2 refers to the 28-day coupon with the biofilm removed;
f).C_2 refers to the control coupon after 28 days of exposure;
† b.d.l. denotes below detection limit.

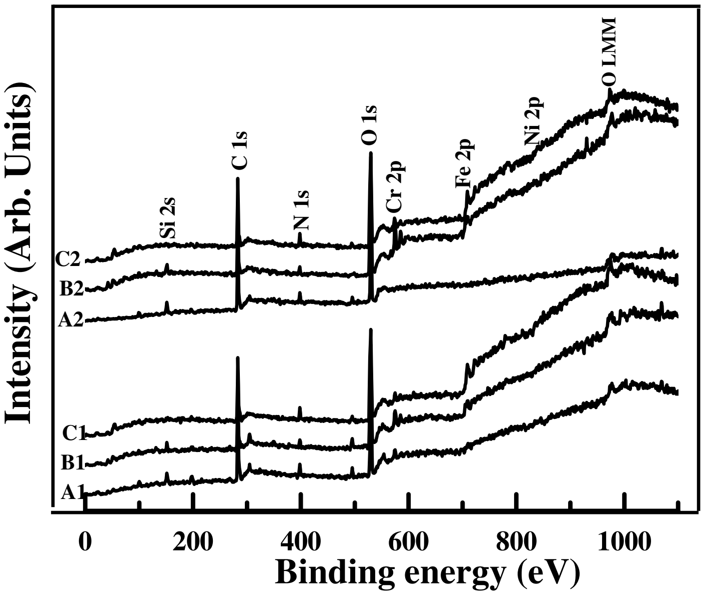

Figure 4.8 Wide XPS spectra of the surface film on the coupon surface in the sterile and *Pseudomonas* inoculated media at different exposure times. Number 1 and 2 respectively corresponds to 7 and 28 days of exposure.

To clarify the subtle changes in the surface chemistry caused by the bacterial colonization, the RACE of the coupons with the biofilm removed is compared with that of the control coupons. Two main features can be highlighted: (i) More Fe is depleted from the passive film on the coupons with the biofilm removed than on the control samples, (ii) The coupons with the biofilm removed are enriched in the Cr content in the outermost layer and the enrichment of Cr increased with exposure time. Hence, the colonization of biofilms is believed to result in an increase of Cr and a decrease of Fe in the outmost layer. However, Cr (presumably in an ionized state) is reported to often accumulate in areas, where the localized corrosion has already occurred (Geesey et al., 1996). Beech et al. (2000) proposed that the increased concentration of Cr usually occurred within the micropits as a result of Fe loss. Consequently, the enrichment of Cr may be the result of micropitting beneath the biofilms in this study.

3.2.2 Chemical analysis of the outermost layers on the surface of stainless steel 304

The study on the microbially-induced changes of the passive film mainly focuses on identifying or validating the changes in the relative abundance of constituents, such as the depletion of Cr or Fe, in previously-published research (Beech et al., 2000; Geesey et al., 1996; Shi et al., 2003; Pendyala et al., 1996). No investigators have studied the changes in the chemical composition and the valence state of metals in the outermost layers of the passive film. To better understand the differences in the chemical composition of the passive film on different types of coupon surfaces, comparative studies are carried out herein by XPS to acquire the Fe 2p, Cr 2p and O 1s high-resolution spectra of the 28-day coupon surfaces.

The core-level Fe $2p_{3/2}$ spectrum obtained from the passive film of the control coupons after 28 days of exposure in the sterile medium is shown in Figure 4.9a, and it can be curve-fitted with six peak components at binding energies (B.E.s) of 706.5, 708.3, 709.5, 710.7, 712.2 and 713.5 eV, corresponding to metallic Fe, Fe_3O_4, FeO, Fe_2O_3, FeOOH and $Fe_2(SO_4)_3$, respectively (Abreu et al., 2006; Varga et al., 1997; Wagner et al.,

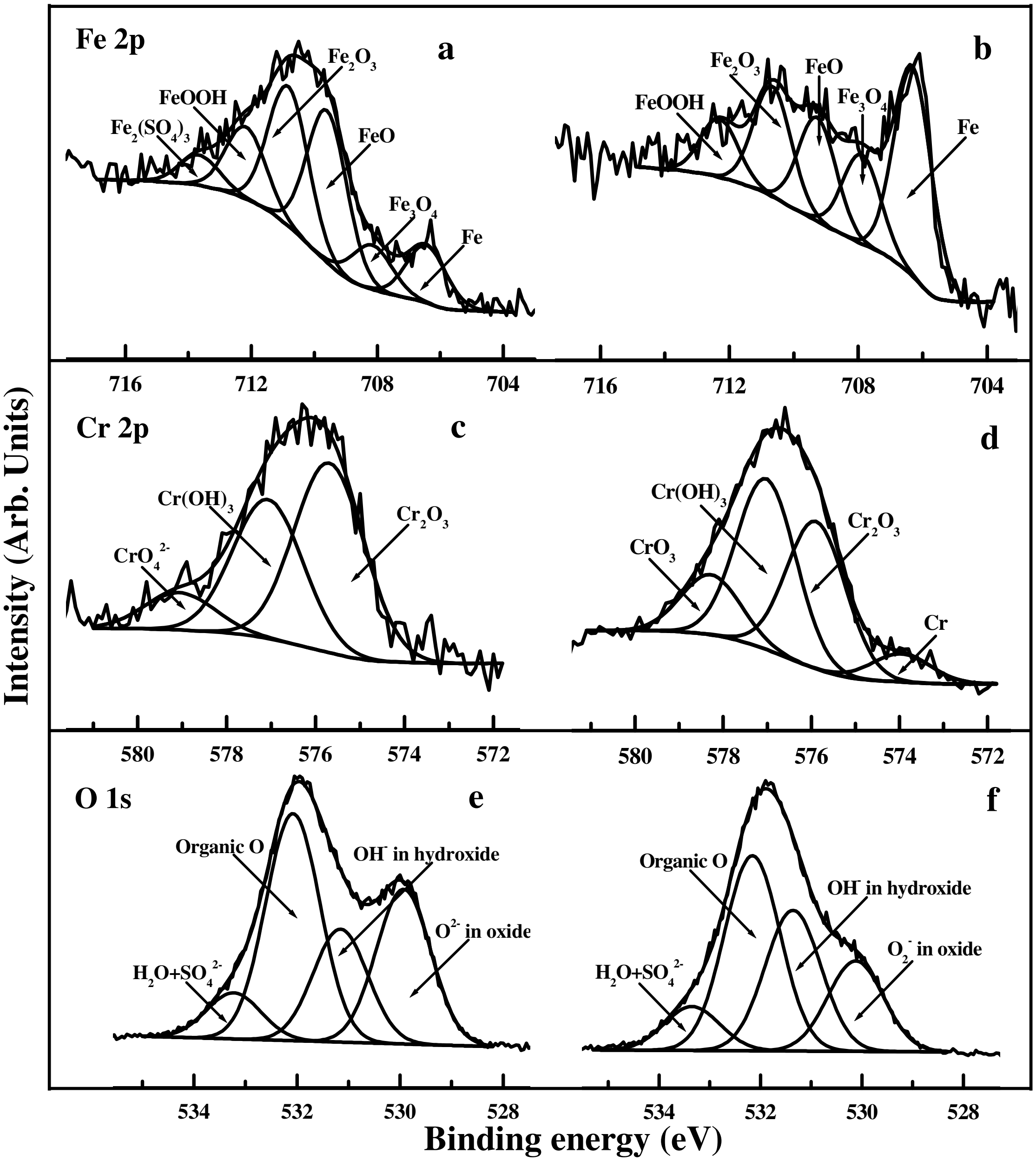

Figure 4.9 High-resolution Fe 2p, Cr 2p and O 1s core-level spectra of the surface film on 304 SS surface after 28 days of exposure in the sterile and *Pseudomonas* inoculated media. (a), (c) and (e) correspond to coupons in the sterile medium, (b), (d) and (f) correspond to coupons with the biofilm removed.

1992). The intensity of each component is used to calculate its relative abundance in the passive film as shown in Table 4.3. It is clearly observed that FeO, Fe_2O_3 and FeOOH are the predominant species. The relative amount of metallic Fe is ~12% in the passive film on the control samples, indicating that the passive film formed on stainless steel 304 is a very thin oxide film as XPS can only detect elemental information from the top ~ 1-6 nm of the metal surface (Varga et al., 1997). It has been reported that the thickness of spontaneously formed passive films for most of metals and alloys was less than several nanometers (Sato, 1990), and that the thickness of the oxide layer for stainless steel was less than 2 nm in a chloride-containing solution at room temperature (Olsson and Hürnström, 1994). Moreover, a small amount of Fe_3O_4 is also detected in the passive film. The Fe_3O_4, an inverse spinel, is structurally similar to a mixture of FeO and Fe_2O_3.

Figure 4.9b shows the core-level Fe $2p_{3/2}$ spectrum acquired from the corroded coupon surface with the biofilm removed after exposed to the *Pseudomonas* inoculated medium for 28 days. Deconvolution of the core-level Fe $2p_{3/2}$ spectrum yields five peak components at B.E.s of 706.8, 708.3, 709.6, 711.0 and 712.3 eV, attributable to metallic Fe, Fe_3O_4, FeO, Fe_2O_3 and FeOOH, respectively. The relative abundance of each component is also shown in Table 4.3. In comparison with the results on the control samples, the relative abundance of each component undergoes a significant change for the coupons with the biofilm removed, one is the large increase in the relative amount of metallic Fe from 12% to 39%, and the other is the apparent decrease in the relative amount of Fe^{2+} species, Fe^{3+} oxides and oxyhydroxides. These results probably indicate that the thickness of passive film on the coupon surface becomes thinner under the attack of *Pseudomonas* bacteria and aggressive anions. Moreover, the difference in the ratio of Fe^{2+}/Fe^{3+} is notable between the control coupons and the coupons with the biofilm removed, implying that the *Pseudomonas* bacteria is possibly involved in the oxidation/reduction reactions of iron (Beech and Sunner, 2004). Chan et al. (2003) reported that bacterial exopolymers, and most likely acidic polysaccharides, might act as a template for the assembly of akaganeite (β-FeOOH) pseudo-single crystals. They further proposed that the oxidation of ferrous ions and the subsequent precipitation of iron oxyhydroxides on the biofilm exopolymers would release protons, thus leading to a decrease in the pH outside the cell membrane (Chan et al., 2003). In the present study, it is believed that the thinning of the passive film and the valence state change of Fe in the oxide film are both caused by the presence of the *Pseudomonas* biofilm and its EPS.

Figures 4.9c and 4.9d respectively illustrate the core-level Cr $2p_{3/2}$ spectra obtained from the surfaces of the control coupons and the coupons with the biofilm removed after 28 days of exposure. The Cr $2p_{3/2}$ spectrum of the control samples can be curve-fitted with three peak components at B.E.s of 575.7, 577.1 and 579.3 eV. The peak at the B.E. of 575.7 eV is reported to be due to Cr_2O_3. The other two contributions at the B.E. of 577.1 and 579.3 eV are due to $Cr(OH)_3$ and CrO_4^{2-} in the oxide layer (Abreu et al., 2006; Varga et al., 1997; Wagner et al., 1992). The core-level Cr $2p_{3/2}$ spectrum of the coupons with the biofilm removed is deconvoluted into four peak components at B.E.s of 574, 575.7, 577.1 and 578.3 eV, corresponding to the metallic Cr, Cr_2O_3, $Cr(OH)_3$ and CrO_3, respectively. The relative amount of each component for both coupons is also shown in Table 4.3. Three main differences of the core-level Cr $2p_{3/2}$ spectra between the control coupons and the coupons with the bioiflm removed can be distinguished: (i) the appearance of metallic Cr on the surface of the coupons with the biofilm removed is ascribed to the thinning of the passive film as well, (ii) the relative amount of Cr(III) species (mainly Cr_2O_3 and $Cr(OH)_3$) is very different from each other, since it is mainly Cr_2O_3 on the control coupons, and $Cr(OH)_3$ is more significant on the coupons with the biofilm removed. It is reported that Cr directly reacted with water to form Cr_2O_3, followed by the formation of $Cr(OH)_3$ at the oxide-solution interface, and that Cr_2O_3 is probably more corrosion-resistant than $Cr(OH)_3$ (Hermas et al., 2007). This probably explains why the enrichment of Cr in the surface film on the coupons with the biofilm removed does not increase the resistance of the passive film, (iii) the Cr(VI) species are in different states on both coupon surfaces, existing on the control coupons as CrO_4^- and on the coupon with the biofilm removed as CrO_3.

Table 4.3 Fitting parameters for the core-level Fe $2p_{3/2}$, Cr $2p_{3/2}$ and O 1s XPS spectra and the relative quantity of compounds in the outermost passive film on 304 SS after 28 days of exposure in the sterile and *Pseudomonas* inoculated media

Valence state	Sample surface	Proposed Components	Binding energy (eV)	Intensity (counts/s)	Relative quantity	FWHM* (eV)	$\sum \chi^2$
Fe 2p	Control	Fe	706.5	540.8	0.12	1.49	1.05
		Fe_3O_4	708.3	415.4	0.09	1.49	1.05
		FeO	709.5	1425.6	0.31	1.49	1.05
		Fe_2O_3	710.7	1312.6	0.27	1.49	1.05
		FeOOH	712.2	676.2	0.15	1.49	1.05
		$Fe_2(SO_4)_3$	713.5	284.2	0.06	1.49	1.05
	After biofilm removal	Fe	706.8	1570.2	0.39	1.31	1.18
		Fe_3O_4	708.3	634.8	0.15	1.31	1.18
		FeO	709.6	731.8	0.18	1.31	1.18
		Fe_2O_3	711.0	770.6	0.19	1.31	1.18
		FeOOH	712.3	362.0	0.09	1.31	1.18
Cr 2p	Control	Cr_2O_3	575.7	1013.7	0.52	1.58	0.72
		$Cr(OH)_3$	577.1	743.2	0.38	1.58	0.72
		CrO_4^{2-}	579.3	199.2	0.10	1.58	0.72
	After biofilm removal	Cr	574	322.4	0.07	1.58	0.70
		Cr_2O_3	575.7	1689.1	0.36	1.58	0.70
		$Cr(OH)_3$	577.1	1956.3	0.42	1.58	0.70
		CrO_3	578.3	687.7	0.15	1.58	0.70
O 1s	Control	O_2^-	529.9	1953.4	0.29	1.24	0.80
		OH^-	531.3	1426.5	0.21	1.24	0.80
		Organic O	532.1	2865.2	0.42	1.24	0.80
		H_2O/SO_4^{2-}	533.2	581.9	0.08	1.24	0.80
	After biofilm removal	O_2^-	529.9	1439.3	0.19	1.29	1.26
		OH^-	531.3	2242.2	0.30	1.29	1.26
		Organic O	532.2	3105.8	0.42	1.29	1.26
		H_2O/SO_4^{2-}	533.2	699.4	0.09	1.29	1.26

[*] FWHM is the abbreviation of full width at half maximum, and denotes the peak width.

The core-level O 1s spectra recorded to correlate with the Fe 2p and Cr 2p spectra for the two types of coupons are shown in Figures 4.9e and 4.9f. The core-level O 1s spectrum of the control coupons is curve-fitted with four contributions at B.E.s of 529.9, 531.3, 532.1 and 533.2 eV. The peak components at B.E.s of 529.9 and 531.3 eV correspond to O_2^- in oxides and OH^- in hydroxides, respectively (Abreu et al., 2006; Varga et al., 1997; Wagner et al., 1992; Hermas et al., 2007). The peak component at the B.E. of 532.1 eV is most likely due to organic oxygen in the porous and heterogeneous conditioning layers (Gubner and Beech, 2000). The contribution at the B.E. of 533.2 eV may be attributed to oxygen in water or sulfate species (Hermas et al., 2007). In the case of the coupons with the biofilm removed, the deconvolution of the core-level O 1s spectrum yields four peak components at the B.E. of 529.9, 531.3, 532.2 and 533.2 eV, attributable to oxides, hydroxides, organic oxygen and oxygen in water or sulfate species, respectively. Oxides are more abundant than hydroxides in the surface film of the control coupons, while the relative abundance of hydroxides is higher than that of oxide in the surface film of the coupons with the biofilm removed. This is in good agreement with the aforementioned Fe 2p and Cr 2p spectra.

4.4 Summary

In this chapter, the power and versatility of AFM in investigating the corrosion of stainless steels induced by microorganisms was verified. The growth of attached *Pseudomonas* cells via binary fission could be observed, and that the development of biofilms was a dynamic and continuous process with an increase in the heterogeneity and the thickness on the 304 SS surface. The deterioration of the SS coupon surface gradually increased with exposure time under the localized attack of the *Pseudomonas* bacteria. The depth of pits increased linearly with exposure time. XPS results revealed that the elemental composition in the outermost layer of the surface films underwent a substantial change induced by the bacterial colonization with an enrichment of Cr and a depletion of Fe.

CHAPTER 5

THE INFLUENCE OF AEROBIC *PSEUDOMONAS* NCIMB 2021 BACTERIUM ON THE CORROSION OF 70/30 CU-NI ALLOY IN SIMULATED SEAWATER

5.1 General Background

Cu-Ni alloys are used extensively as pipelines, heat exchangers, and offshore oil structures in seawater due to their corrosion resistance, machinability, and thermal and electrical conductivity (Mansfeld et al., 1992). The good corrosion resistance of Cu-Ni alloy has been attributed to the formation of a duplex oxide film comprising an outer layer of cupric hydroxyl chloride, $Cu_2(OH)_3Cl$, overlaying a compact inner layer of cuprous oxide, Cu_2O (Kato et al., 1980, Druska et al., 1996). However, Cu-Ni alloys are found to be susceptible to MIC (Wagner and Little, 1993). Originally, the toxicity of copper to microorganisms had led to the belief that Cu-Ni alloys have excellent anti-fouling properties. Thereby MIC of copper and its alloys is insignificant (Iverson, 1987). Subsequently, Cu-Ni alloys have been found only to prevent or retard the settlement of macrofouling species, such as barnacles, mussels and tubeworms. Other organisms, including bacteria, microalgae and fungi, can readily attach themselves to the surface of Cu-Ni alloys by excreting EPS to form a slime layer (Little et al., 1993). Extensive investigations have been carried out to determine the involvement and the contributions of microorganisms in the corrosion processes of Cu-Ni alloys (Blunn, 1986; Geesey et al., 1986, Pope et al., 1984, 1986, 1987, Bremer and Geesey, 1991, Huang, et al., 2004, Videla, 2001). However, most of these studies focused on the effect of SRB, only a few studies have devoted to the MIC of Cu-Ni alloys by aerobic bacteria (Rao and Nair, 1998; Busalmen et al., 2002; Valcarce et al., 2005, 2006).

This chapter aims to gain a better understanding on the effect of the *Pseudomonas* NCIMB 2021 bacteria on the corrosion behavior of 70/30 Cu-Ni alloys as a function of time in the nutrient-rich simulated seawater. Electrochemical studies were performed to evaluate the alternation of corrosion behavior of the alloy coupons in the presence of

Pseudomonas cells as compared to the sterile control coupons. SEM was used to assess the surface topography and the degree of corrosion damage underneath the biofilms and corrosion products. The evolution of the passive films with exposure time in the presence and the absence of the *Pseudomonas* bacterium were monitored by XPS, which allowed an evaluation of the effect of the *Pseudomonas* bacteria on the passive film formation as well as to determine the influence of the bacterial cells and the EPS on the protective oxide film.

5. 2 Experimental methods

5.2.1 Test coupons and preparation

70/30 Cu-Ni alloys (CDA 715), with the nominal composition of 67.84% Cu, 30.6% Ni, 0.63% Fe, 0.6% Mn, 0.02% Zn, 0.018% C and 0.002% S and other trace elements, was purchased from Metal Samples company (Alabama, USA). The procedure for polishing test coupons is similar to those described in Section 3.2.1. The polished coupons were first rinsed with DI water thrice, then immersed in 15% HCl for 3 min to remove the oxide film (Jones, 1996), followed by successive rinsing with DI water until no residual acid remained, and then degreased with acetone, sterilized by immersion in 70% ethanol for 8h, and finally dried in a laminar flow cabinet.

5.2.2 Medium and inoculum cultivation

The medium and inoculums were prepared similarly to those described in Section 3.2.2.

5.2.3 Corrosion experiment with *Pseudomonas* culture

The corrosion experiments and medium replacement was similar to those described in Section 3.2.3.

5.2.4 Electrochemical measurements

The measurement of Tafel plots and EIS was performed similarly as described in Section 3.2.4. The cyclic polarization curves were also recorded in a potential range of -0.75 to 0.75 V vs. reference electrode after 3, 7 and 28 days of exposure in the sterile and *Pseudomonas*-inoculated media.

.

5.2.5 Surface topography analysis with SEM

The coupons with biofilms underwent fixation and dehydration according to the procedures described in Section 3.2.5. To assess the degree of corrosion damage under the biofilms, ultrasonic treatment was used. The coupons were immersed in a beaker with 100 ml of a 0.1 M EDTA solution (Zhang et al., 2002, Feng et al., 1996), and then ultrasonicated for 15 min in a sonication bath (Cole-Parmer, USA) with a frequency of 40-50 KHz to remove the corrosion products and the biofilms. SEM imaging sites were randomly chosen on the coupon surface to be representative of the entire surface of the alloy coupons.

5.2.6 The chemical analysis of surface film with XPS

To better understand the evolution of the surface film with exposure time, to evaluate the influence of the *Pseudomonas bacteria* on the formation process of surface film and to verify the difference in the chelating functional groups between the conditioning layers and the bacterial cells and its EPS, XPS studies were undertaken as follows: 1) control coupons in the sterile medium for 3, 7 and 28 days, respectively, 2) coupons in the *Pseudomonas*-inoculated medium for 3, 7 and 28 days, respectively.

For the coupons with biofilms, they were retrieved from the *Pseudomonas*-inoculated medium, washed thrice with sterile DI water to remove the dead and loosely attached cells, placed in a liquid nitrogen tank for 15 min, followed by lyophilizing with a freeze dryer (Telstar, Spain) at -50℃ for 8 h, and stored in a vacuum desiccator prior to the analysis. For the coupons with biofilms, two types of analysis sites were selected depending on different surface features: one is the bacterial cluster area (BCA), the other is the void area (VA) without the coverage of the biofilms. For control coupons, the analysis sites were randomly chosen on the coupon surfaces. The procedures for XPS analysis as well as the control coupon preparation were similar to those described in Section 4.2.5.

5.3. Results and discussion

5.3.1 Corrosion behavior of Cu-Ni alloy coupons in the sterile and *Pseudomonas*-inoculated media

5.3.1.1 Tafel plot measurement

Figure 5.1 shows Tafel plots of the alloy coupons in the sterile nutrient-rich medium at various exposure times. The quantitative analysis of Tafel plots are similar to those described in Section 3.3.1.1, and the results are shown in Table 5.1. Corrosion current densities, i_{corr}, decrease with exposure time, and dramatically reduce from initially ~10 $\mu A \cdot cm^{-2}$ to ~1.5 $\mu A \cdot cm^{-2}$ after 42 days of exposure, indicative of the decrease in the corrosion rate of the alloy with exposure time owing to the formation of the protective oxide film (Mansfeld et al., 1994, Kato et al., 1980, Druska et al., 1996). Corrosion potentials, E_{corr}, undergo a slightly noble shift from ~-0.2 to ~-0.18 V after 42 days of immersion. This may be caused by the inhibition effect of the protective oxide film on the electrode reactions. The cathodic Tafel slopes, β_c, show no visible trends, fluctuating between -200 and -240 $mV \cdot dec^{-1}$ with exposure time, whereas anodic Tafel slopes, β_a appear to increase with exposure time from ~230 to 270 $mV \cdot dec^{-1}$, indicative of the

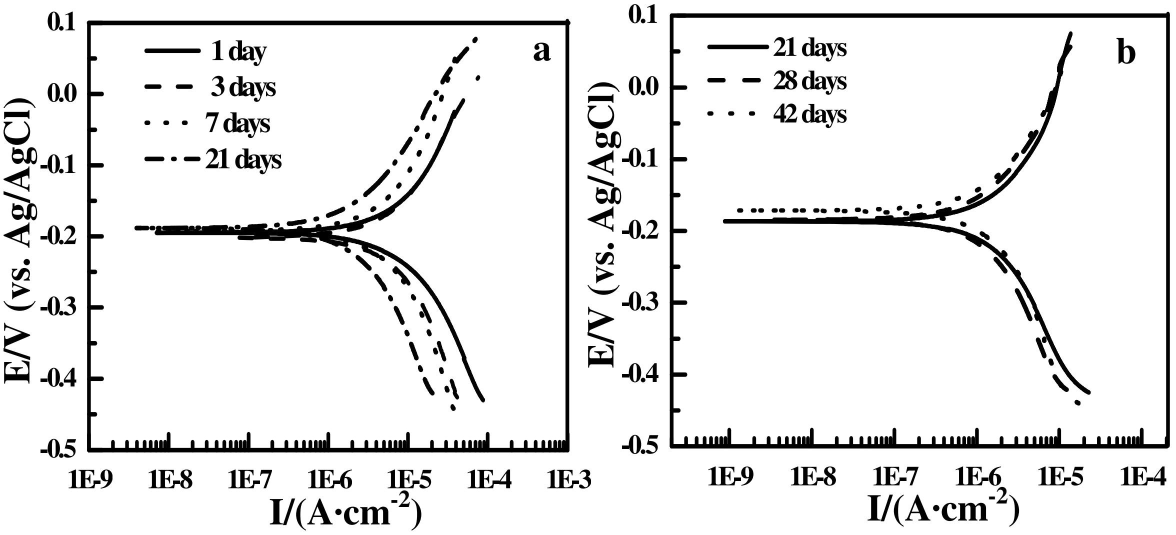

Figure 5.1 Tafel plots of the alloy coupons in the sterile nutrient-rich medium after different exposure times: (a) 1, 3, 7 and 14 days, (b) 21, 28 and 42 days.

Table 5.1 Tafel analysis of polarization curves of the 70/30 Cu-Ni alloy in the sterile medium after different exposure times

Exposure time (days)	β_c (mV·dec^{-1})	β_a (mV·dec^{-1})	E_{corr} (V)	i_{corr} (μA·cm^{-2})
1	-220	233	-0.194	10.03
3	-232	237	-0.195	9.83
7	-243	258	-0.192	5.78
14	-189	262	-0.188	2.98
21	-217	272	-0.187	2.05
28	-236	250	-0.184	1.58
42	-220	274	-0.177	1.49

diffusion control at the anodic site. This is in good agreement with previous conclusions that the protective oxide film on the Cu-Ni alloys made the diffusion of a reactant or a product to be the rate-determining step (Kato et al., 1980). However, the Tafel slopes of anodic reactions are inconsistent with those reported previously (Kear et al., 2004), which often quote values in the order of 60 mV·dec^{-1} for a single electron reaction and in the order of 120 mV·dec^{-1} for a double-electron reaction of freshly polished copper alloys in simulated seawater. The currently observed deviation of the anodic Tafel slopes probably results from the anodic concentration polarization due to the presence of rich organic chelators of copper ions in the nutrient-rich medium. A similar result has been reported in studying the corrosion behavior of 70/30 Cu-Ni alloys in sulfide-containing seawater (Al-Hajji and Reda, 1994, 1995).

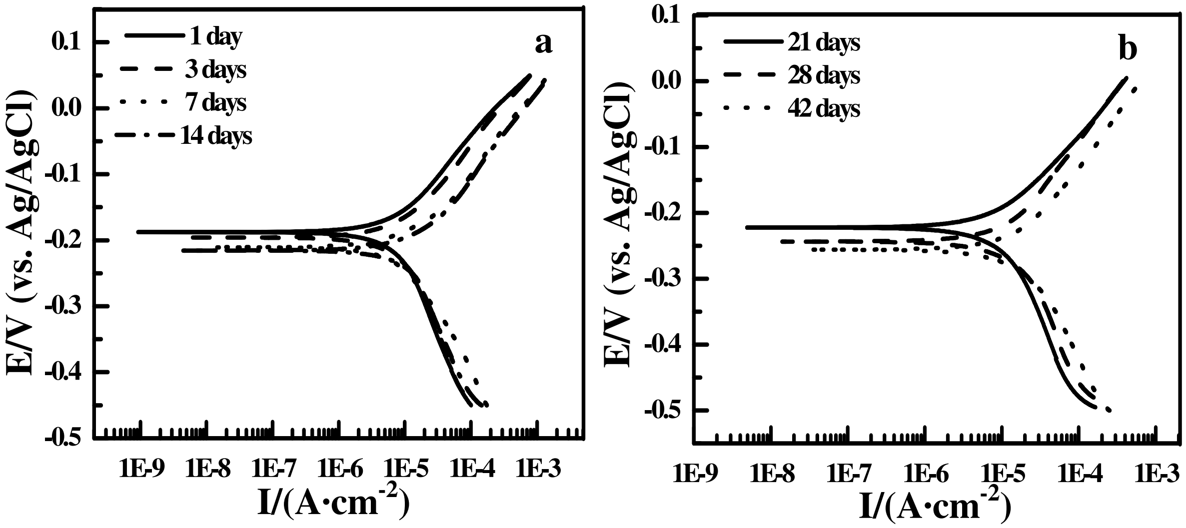

Figure 5.2 Tafel plots of the alloy coupons in the *Pseudomonas*-inoculated nutrient-rich medium after different exposure times: (a) 1, 3, 7 and 14 days, (b) 21, 28 and 42 days.

Table 5.2 Tafel analysis of polarization curves of the 70/30 Cu-Ni alloy in the *Pseudomonas*-inoculated medium of after different exposure times

Exposure time (days)	β_c (mV·dec^{-1})	β_a (mV·dec^{-1})	E_{corr} (V)	i_{corr} (μA·cm^{-2})
1	-247	117	-0.186	10.08
3	-245	122	-0.196	10.79
7	-220	125	-0.211	11.77
14	-224	128	-0.215	13.86
21	-212	125	-0.237	13.03
28	-215	124	-0.243	15.30
42	-176	131	-0.256	20.53

Tafel plots of the alloy coupons in the *Pseudomonas*-inoculated medium as a function of time are illustrated in Figure 5.2. The quantitative analysis results are summarized in Table 5.2. The presence of *Pseudomonas* bacteria obviously results in different corrosion behaviors of the alloy coupons as compared to the control experiments. Corrosion current densities, i_{corr}, gradually increase with exposure time, and become as high as ~20.5 μA·cm^{-2} after 42 days in the *Pseudomonas*-inoculated medium. The apparent active shift in the corrosion potentials, E_{corr}, is observed from ~-0.20 to ~-0.26 V after 42 days of exposure, which is associated with the increase in the anodic dissolution reactions. The anodic Tafel slopes, β_a, fluctuate with exposure time within a range of ~120 and ~130 mV·dec^{-1}, indicative of the activation control of anodic reactions. The cathodic Tafel slopes, β_c, remain relatively stable in a range of ~-250 to ~-175 mV·dec^{-1}, indicative of mass transfer effect (or partial diffusion control) of the cathodic reaction.

To compare the Tafel plots and the corresponding electrochemical analysis results of the alloy coupons in the *Pseudomonas*-inoculated medium with those in the sterile medium, several apparent features are highlighted as follows: a) At the initial stage of exposure period (1 and 3 days), i_{corr}, E_{corr}, and the cathodic Tafel slopes, $\beta_{c,}$ of the alloy coupons in the biotic and abiotic media are very similar to each other, except for the notable decrease in the anodic Tafel slopes, β_a, which is ascribed to the structure of passive films on the coupon surface, b) Upon prolonging exposure time beyond 7 days, the differences in the corrosion behavior are discerned between the coupons with biofilms and control coupons. i_{corr} increases gradually with exposure time in the presence of *Pseudomonas*, while they decrease with exposure time in the sterile medium. Thereby, i_{corr} of the alloy coupons in the presence of *Pseudomonas* is higher by as much as 14-fold than those of the control coupons after 42 days of exposure. E_{corr} in both media shows opposite trends. The inhibition effect of the protective oxide film interpreted the noble shift of corrosion potentials of the control coupons (Kato et al., 1980). However, the active shift of E_{corr} of the coupons with biofilms is associated with the anodic dissolution of the alloy coupons under the effect of *Pseudomonas* bacteria.

5.3.1.2 EIS measurement

The EIS data of the alloy coupons in the sterile medium after different exposure times are illustrated in Figure 5.3. In the Nyquist plots (Figs. 5.3Ia and 5.3IIa), the diameters of impedance loops markedly increase with exposure time, indicative of the decrease in the corrosion rates of the alloy coupon. The Bode magnitude plots show that the total impedance magnitudes at the lowest frequency increase with exposure time (the logarithmic value of impedance from ~3.4 to ~4.5), implying the increase in the corrosion resistance due to the formation of a protective oxide film (Figs. 5.3Ib and 5.3IIb). From the respective Bode phase angle plot (Figs.5.3Ic and 5.3IIc), two peak maxima were distinguished except for the 1-day coupon (which displays only one peak maximum): the peak maximum in the high frequency range is attributed to the protective oxide film, while the peak maximum at the low frequency range probably derives from EDL. Another peak maximum is supposed to exist owing to the formation of the conditioning layers on the metal surface by the adsorption of organic compounds, but it is invisible due to being overlaid by the wide peak angle of the compact oxide film.

Figure 5.4 shows the temporal EIS data of the alloy coupons in the *Pseudomonas*-inoculated medium. The diameters of impedance loops in the Nyquist plots (Figs. 5.4Ia 5.4IIa) decrease gradually with exposure time, indicative of the increase in the corrosion rates of the alloy coupons with exposure time. The respective Bode magnitude plot shows that the total impedance magnitude also decreases with exposure time (the logarithmic value changed from ~3.25 to ~3.1) (Figs. 5.4Ib and 5.4IIb). In the case of the phase angel Bode plots (Figs. 5.4Ic and 5.4IIc), a weak phase angle maximum appear at the lowest frequency range except for the 1-day coupon, implying active pit growth (Mansfeld et al., 1993). Other two peak maxima arise when exposure time increasing to more than 7 days in the *Pseudomonas*-inoculated medium: the one in the higher frequency range is attributed to the passive film, the other in the lower frequency range is related to the EDL. As a matter of fact, the formation of the *Pseudomonas* biofilms on the coupon surface also gives rise to another peak maximum, which is difficult to detect due to its close proximity to the peak maximum of passive films. Furthermore, the maximum phase angles in the high frequency range gradually decrease from ~57° to ~44.5° with exposure time, indicating that the passive film became less protective with exposure time under the attack of *Pseudomonas* bacteria.

Taking into account the contribution of each phenomenon, such as EDL, oxide film formation, biofilms and others, the physical models and their corresponding equivalent circuits shown in Figure 5.5 are used to analyze and fit the EIS data of the alloy coupons in the sterile and *Pseudomonas*-inoculated media. Equivalent circuit (a) includes two time constants and is frequently used to represent the formation of a layer of oxide film on the metal surface, equivalent circuit (b) models three relaxation time constants and is used to show the formation of a duplex surface film on the coupon surface: an outer layer of the heterogeneous biofilm and an inner layer of porous oxide film, equivalent circuit (c) also models three time constants, and represents a duplex layer of surface film consisting of an outer layer of the non-protective conditioning layer and an inner layer of the compact and protective oxide film. In Figures 5.3a and 5.4a, the depression of the capacitance semicircle, whose center lied below the real axis, is due to an inhomogeneous surface. Therefore, it is necessary to introduce a constant phase element (i.e. CPE) into the equivalent circuits for the EIS data fitting instead of an ideal capacitor. Many studies (Mansfeld et al., 1981, 1993; Zhang and Pehkonen, 2002) have used a CPE to model frequency dispersion behavior corresponding to different physical phenomena, such as surface heterogeneity and surface impurity. The physical meanings and formula of the CPE have been described in detail in Section 3.3.1.2.

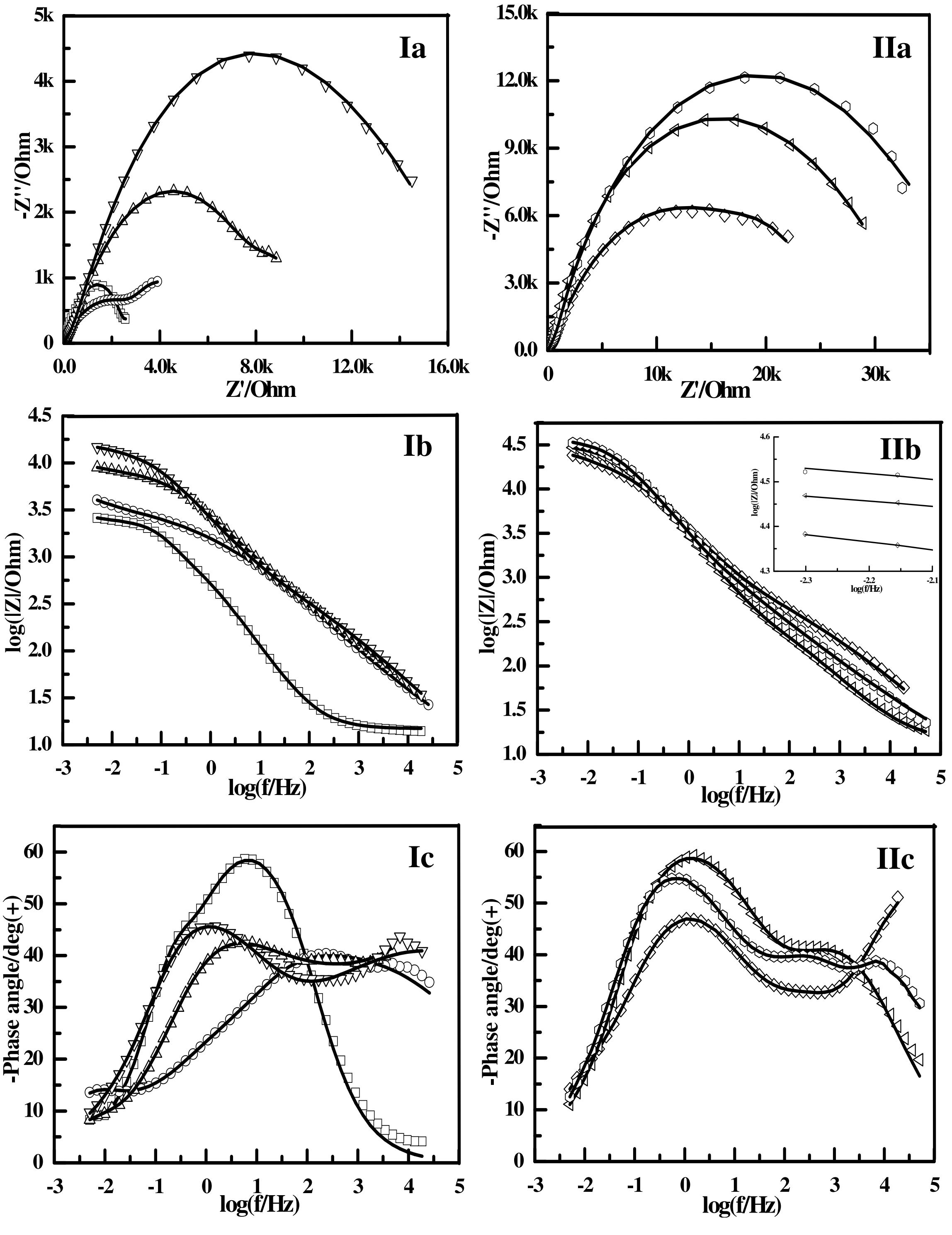

Figure 5.3 EIS data of the alloy coupons recorded at the OCP in the sterile nutrient-rich medium after different exposure times: (I) 1 day (open squares), 3 days (open circles), 7 days (open upper triangles) and 14 days (open lower triangles), (II) 21 days (open diamonds), 28 days (open left triangles) and 42 days (open hexagon). Solid lines represent the fitted results based on the corresponding equivalent circuits. (a) Nyquist plots, (b) Bode magnitude plots and (c) Bode phase angle plots.

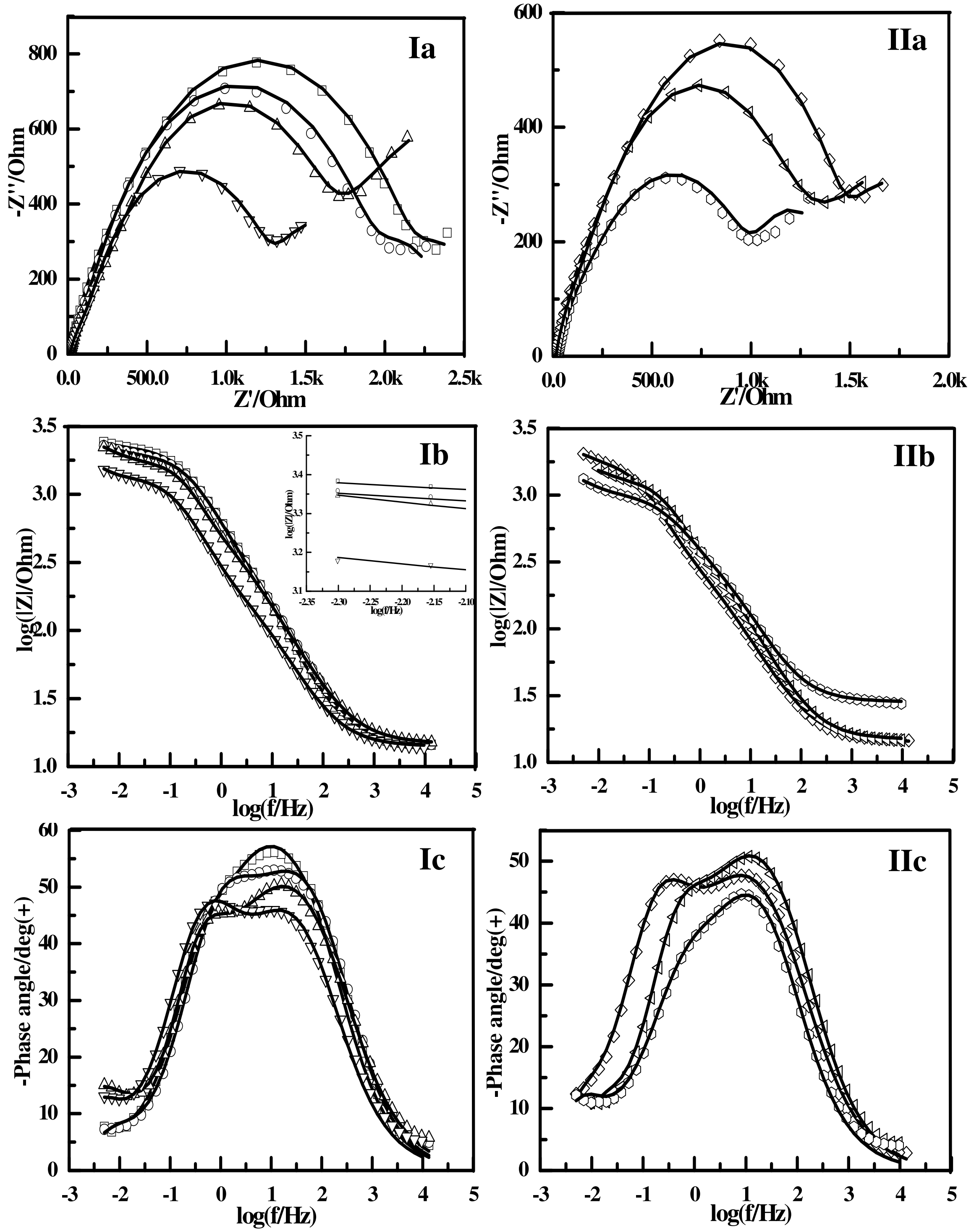

Figure 5.4 EIS data of the alloy coupons recorded at the OCP in the *Pseudomonas*-inoculated medium after different exposure times: (I) 1 day (open squares), 3 days (open circles),7 days (open upper triangles) and 14 days (open lower triangles), (II) 21 days (open diamonds), 28 days (open left triangles) and 42 days (open hexagons). Solid lines represent the fitted results based on the equivalent circuits. (a) Nyquist plots, (b) Bode magnitude plots and (c) Bode phase angle plots.

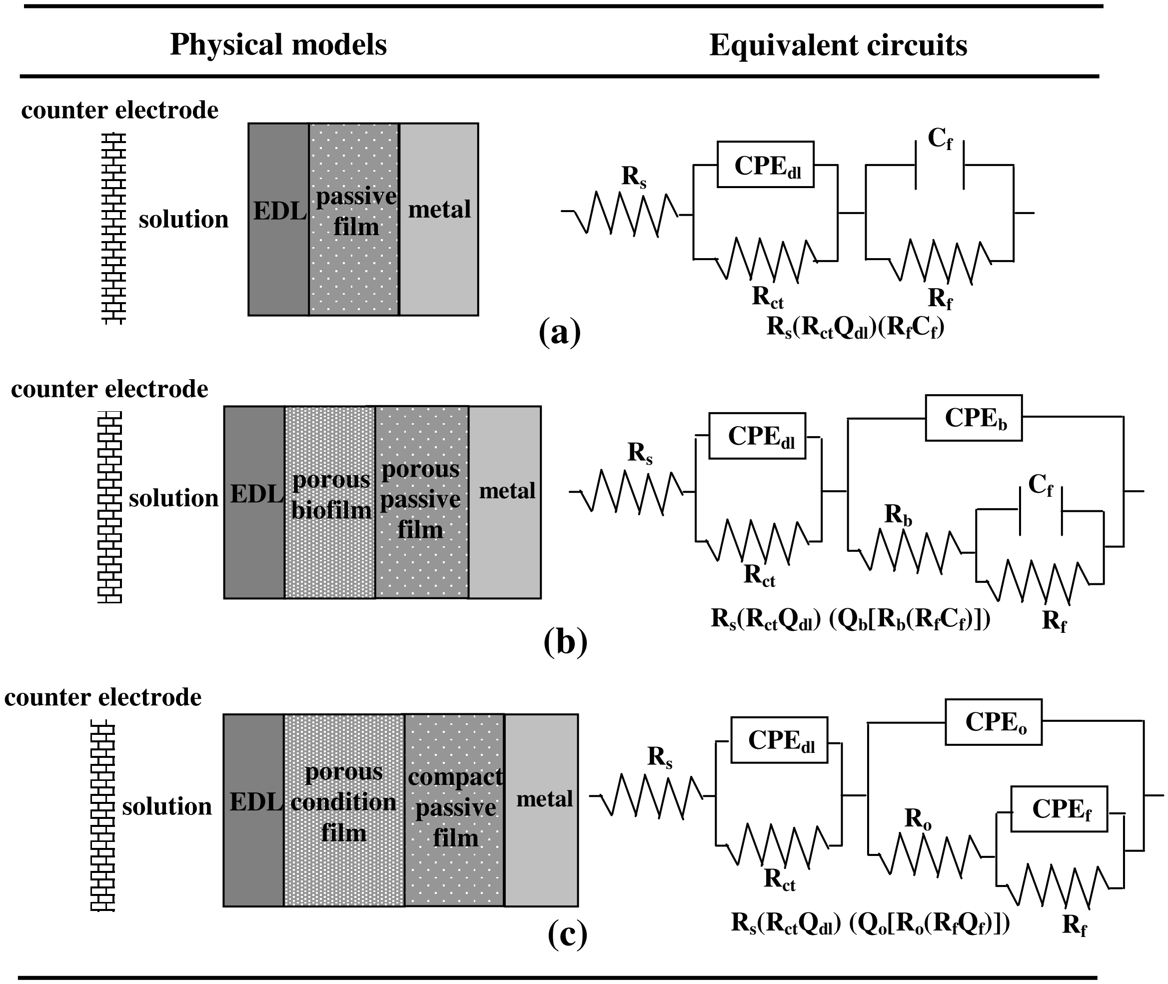

R_s, resistance of the solution, Q_{dl}, CPE of the electrical double layer (EDL), R_{ct}, charge transfer resistance of EDL, Q_b, CPE of the biofilm of *Pseudomonas* bacterium, R_b, resistance of the biofilm of *Pseudomonas* bacterium, Q_o, CPE of the conditioning layer of organic compounds, R_o, resistance of the conditioning layer of organic compounds, C_f, capacitance of the surface passive film, Q_f, CPE of the surface passive film, R_f, resistance of the passive film.

Figure 5.5 Three physical models and the corresponding equivalent circuits (a, b, c) used for fitting the EIS data of the alloy coupons in the sterile and *Pseudomonas*-inoculated media.

The EIS data of the alloys coupons in the sterile medium are fitted with equivalent circuits (a) (applicable to 1-day coupon) and (c). The values of Chi-Square χ^2 are all less than 10^{-3}, exhibiting the goodness of the fits. The fitted parameters of the electrical components are listed in Table 5.3. The charge transfer resistance, R_{ct}, of the alloy coupons increases with exposure time, indicative of the decrease in the corrosion rate. It has been widely recognized that the corrosion rate is inversely proportional to the change transfer resistance on the basis of the Stern-Geary equation, $R_p = B / i_{corr}$, where B is a parameter related to the Tafel slopes (Jones, 1996). Moreover, the increasing rate in the charge transfer resistance, R_{ct}, slows down after a long exposure period. During the initial stage of the coupons in the sterile medium, the charge transfer resistance, R_{ct}, dramatically increases by ~3.8-fold from 1 to 7 days. However, it only increases ~30% from 28 to 42 days. The resistance of the conditioning layers, R_o, generated by the adsorption of organic compounds, remains relatively small throughout, indicating that the conditioning layer on the coupon surface was non-protective and porous. Furthermore, the n_2 values are all below 0.55, indicative of the high heterogeneity of the conditioning layers, since the adsorption of organic compounds on the metal surface is not a uniform process (Thompson and Campbell, 1994; Beech et al., 2000). Another noticeable circuit element is the resistance of oxide films, R_f. The increase in R_f with exposure time reveals that the oxide film grows gradually in the thickness and compactness with exposure time. The n_3 values remain above 0.8, indicative of the relatively homogeneity and compactness of the inner oxide film.

Table 5.3 Fitting parameters of EIS data of the alloy coupons in the sterile medium after different exposure times

Exposure time (days) / Parameters	1	3	7	14	21	28	42
R_s (Ω)	15.20	13.14	14.50	13.88	14.56	13.75	15.51
R_{ct} (kΩ)	1.97	3.23	7.66	10.09	16.99	21.12	27.30
Q_{EDL} Y_{dl} ($\Omega^{-1}s^n$)	$2.94*10^{-4}$	$7.42*10^{-6}$	$9.63*10^{-6}$	6.1_5*10^{-6}	$7.38*10^{-7}$	$9.48*10^{-7}$	$1.09*10^{-7}$
n_1	0.88	0.46	0.66	0.52	0.66	0.79	0.79
R_o (kΩ)	-	0.16	0.84	0.58	0.54	0.64	1.42
Q_o Y_o ($\Omega^{-1}s^n$)	-	$1.19*10^{-5}$	$2.61*10^{-8}$	$6.08*10^{-8}$	$1.04*10^{-9}$	$1.70*10^{-9}$	$2.20*10^{-9}$
n_2	-	0.75	0.46	0.49	0.54	0.51	0.42
R_f (kΩ)	1.06	1.99	2.30	6.85	8.70	12.73	14.86
Q_f Y_f ($\Omega^{-1}s^n$)	-	$3.12*10^{-3}$	$4.91*10^{-3}$	$1.97*10^{-3}$	$1.77*10^{-3}$	$1.18*10^{-4}$	$4.17*10^{-5}$
n_3	-	0.80	0.87	0.77	0.94	0.81	0.95
C_f (mF)	78.8	-	-	-	-	-	-
$\sum\chi^2*10^{-3}$	1.25	0.59	5.40	1.93	1.51	6.57	9.68

The fitted circuit parameters of the alloy coupons obtained in the *Pseudomonas*-inoculated medium are listed in Table 5.4. Obviously, the charge transfer resistance, R_{ct}, decreases gradually with exposure time, indicative of an increase in the corrosion rate of the coupons with biofilms. The resistance of the biofilm, R_b, has no clear trend due to its variation in magnitude with exposure time. This is consistent with the conclusions that the development of biofilms is a dynamic process accompanied by the continuous attachment, growth, detachment on the solid metal surface (Costerton et al., 1999). The resistance of the oxide film, R_f, shows an initial increase, and then a decrease with exposure time after attaining the maximum value after 7 days. The complexity is caused by the presence of the *Pseudomonas* bacteria on the coupon surface. Based on the change in the values of R_{ct} and R_f with exposure time, it is readily concluded that the presence of the *Pseudomonas* cells and its EPS on the coupon surface might retard or change the process of the oxide film formation, or to facilitate the localized breakdown of the oxide film. The bacterial colonization on the metal surface has been widely recognized to result in the loss of the passivity of the surface film, since the passive film becomes more porous and heterogeneous with exposure time by the implication of the microbial activities in the corrosion processes, and posed no barrier to the diffusion of active ions and product ions (Caldwell et al., 1992, Xu et al., 1999).

Table 5.4 Fitting parameters of EIS data of the alloy coupons in the *Pseudomonas* medium inoculated after different exposure times

Exposure time (days) / Parameters	1	3	7	14	21	28	42
R_s (Ω)	13.83	14.60	16.00	14.09	15.18	14.84	18.36
R_{ct} (kΩ)	1.91	1.88	1.58	1.21	1.17	1.04	0.90
Q_{EDL} Y_{dl} ($\Omega^{-1}s^n$)	$8.98 * 10^{-5}$	$6.08 * 10^{-5}$	$1.56 * 10^{-4}$	$2.39 * 10^{-4}$	$4.42 * 10^{-4}$	$3.32 * 10^{-4}$	$6.72 * 10^{-4}$
n_1	0.83	0.82	0.85	0.84	0.89	0.89	0.74
R_b (kΩ)	-	0.12	0.23	0.12	0.34	0.24	0.14
Q_b Y_b ($\Omega^{-1}s^n$)	-	$3.30 * 10^{-5}$	$2.31 * 10^{-5}$	$3.70 * 10^{-5}$	$3.91 * 10^{-5}$	$3.04 * 10^{-5}$	$5.76 * 10^{-5}$
n_2	-	0.74	0.74	0.71	0.72	0.72	0.76
R_f (kΩ)	0.71	0.39	1.04	0.59	0.49	0.40	0.41
C_f (mF)	87.2	61.2	39.0	79.4	89.9	71.33	71.4
$\sum\chi^2 * 10^{-3}$	6.81	1.42	4.34	8.07	3.85	4.21	9.76

5.3.1.3 Cyclic polarization curves

Figure 5.6 shows the cyclic polarization curves of the alloy coupons after 3, 7 and 28 days of exposure in the sterile and *Pseudomonas*-inoculated media. For the sterile control coupons, corrosion current densities in the forward scan remain less than 0.1 mA·cm^{-2} throughout the exposure densities (Figs. 5.6a, 5.6c and 5.6e), indicative of high passivity of oxide films on the control coupons (ASTM G61, 2003). The negative hysteresis loops in the cyclic polarization curves indicates that localized corrosion is unlikely to occur on the control coupons. The current initially increased exponentially with potential, which is characteristic of an activation-controlled electrochemical reaction rather than an autocatalytic process such as pitting. The inoculated alloy coupons also retain a degree of passivity due to current densities never exceeding 0.1 mA·cm^{-2} in the forward scan, whereas, the reverse polarization curves shift to more active values of current densities with exposure time (Figs. 5.6b, 5.6d and 5.6f), thus a positive hysteresis loop in cyclic polarization curve is clearly observed on the inoculated coupons after 28 days of exposure. It has been reported that an alloy that is resistant to pitting corrosion show no hysteresis (or negative), whereas susceptible alloys show increasing hysteresis (Jones, 1996). The positive hysteresis and active shift in corrosion potential in cyclic polarization curves for the inoculated coupons indicate the anodic dissolution reaction is enhanced under the effect of *Pseudomonas* bacterium.

5.3.2 Surface topography analysis with SEM

Figure 5.7 shows the SEM images of the alloy coupons in the sterile and *Pseudomonas*-inoculated media for 7 and 42 days of exposure. A layer of oxide film is clearly observed on the coupon surface after 7 days of exposure (Fig. 5.7a). After 42 days of exposure, a thick duplex layer is discerned on the alloy surface, comprising of a porous

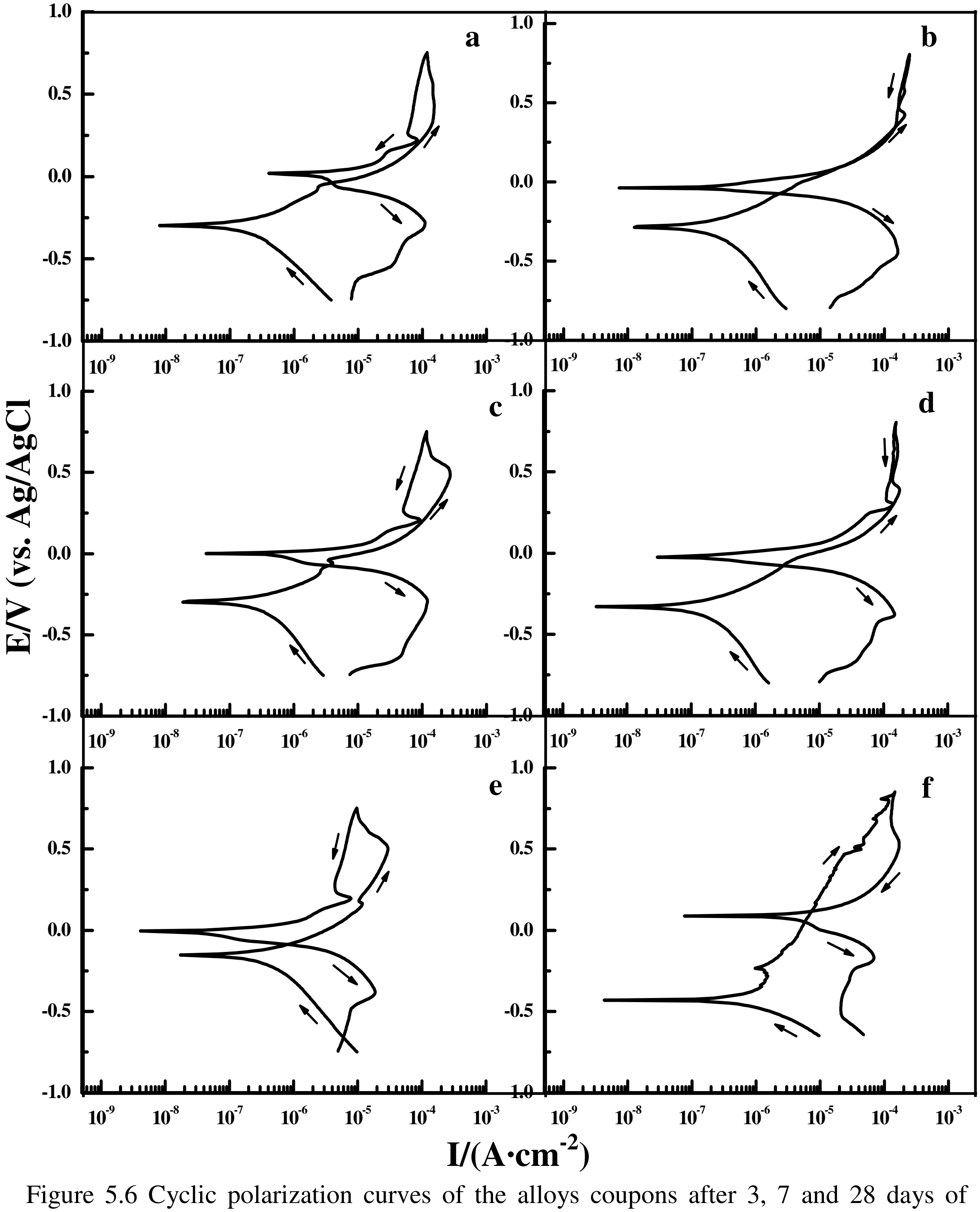

Figure 5.6 Cyclic polarization curves of the alloys coupons after 3, 7 and 28 days of exposure in the sterile (a, c, e) and the *Pseudomonas*-inoculated (b, d, f) media. (a, b) for 3 days, (c, d) for 7 days and (e, f) for 28 days.

outer layer with cracks and a compact inner layer (Fig. 5.7b). The outer layer was probably a combination of the conditioning layer and the cupric oxide film, while the

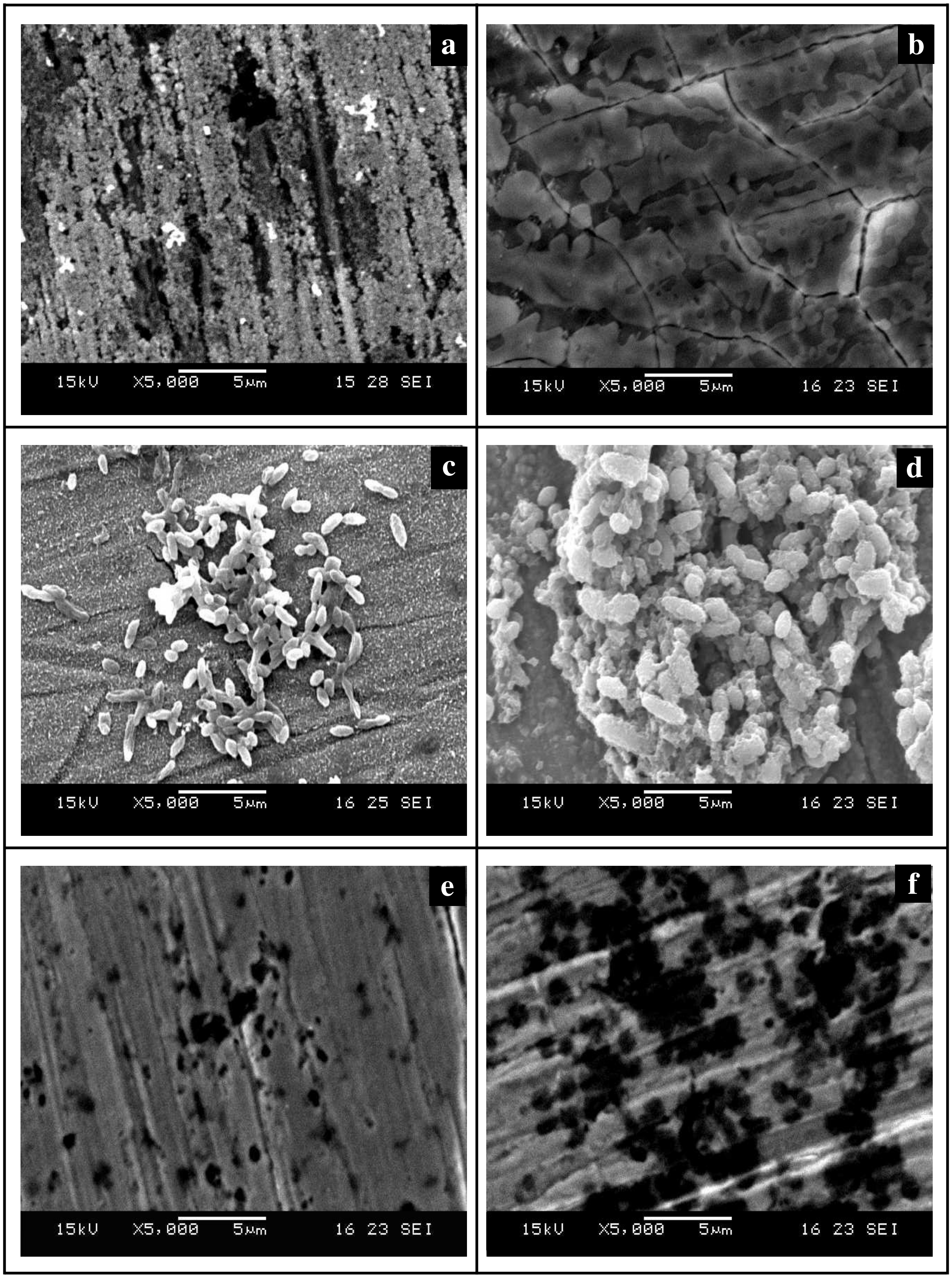

Figure 5.7 SEM images of the alloy coupons in the sterile (a, b) and *Pseudomonas*-inoculated media (c, d) for 7 days and 42 days, the corroded surface after the biofilm removal shown as (e) and (f). (a), (c), (e) for 7 days, (b), (d) (f) for 42 days.

inner layer was mainly composed of cuprous oxide (Cu_2O) (Mansfeld et al, 1994, Kato et al., 1980). An aggregation of bacterial cells would result in a patchy biofilm on the coupon surface after 7 days of exposure to the *Pseudomonas*-inoculated medium (Fig. 5.7c). After the removal of the biofilms, some micropits are found on the coupon surface (Fig. 5.7e). With increasing time to 42 days, the *Pseudomonas* cells become dense at localized sites, and are embedded into the corrosion products to form the clusters (Fig. 5.7d). The formation of the bacterial clusters or discrete biofilms has been reported to provide the physicochemical conditions in localized environments to facilitate the attack of microorganisms, thus leading to pitting corrosion on the metal surface (Borenstein, 1996). Extensive micro-pits are clearly observed on the 42-day coupon surface with the biofilm removal, indicative of micro-pitting corrosion on the coupon surface (Fig. 5.7f).

5.3.3 Surface elemental analysis with XPS survey scan

Survey scans were performed to identify all detectable elements on the surface film of the control and the coupons with biofilms. As described in the experimental section, the coupons with biofilms were further characterized at the VA and BCA sites. The RACE and their ratios are calculated using the peak areas normalized on the basis of acquisition parameters and sensitivity factors. Figure 5.8 shows that the elements of C, O, N, Cu, Ni and Cl are all detected on both types of coupons. The RACE of the surface film is shown in Table 5.5.

For the control coupons, the surface film is composed mainly of C, O and Cu, accompanied by trace elements of Cu, Ni, Cl and O. The chemistry of the surface film shows the occurrence of denickelefication, as the [Cu]/[Ni] ratio is much less than the original value (7:3). Previous studies have proposed that the organic macromolecular compounds, such as proteins and carbohydrates, would spontaneously adsorb on the solid surface to form a discrete or patchy conditioning layer after a short exposure period (Pradier et al., 2000). In this study, the presence of copious C, O and N on the alloy surface reveals the formation of the conditioning layers (Fig. 5.8(a)). It is noteworthy that the metallic elements of Cu and Ni are also detectable in spite of the presence of the conditioning layers on the alloy coupons. This is probably ascribed to the following reasons: i) the conditioning layer is thin, or porous and heterogeneous, thus insufficient to prevent the penetration of the electrons originating from the passive layer of the metal, ii) the conditioning layers might be a mixture of metal oxide/hydroxides originating from the surface film and the organic compounds (Beech et al., 2000), iii) the metal ions are probably chelated by the organic functional groups in conditioning layers.

For the coupons with biofilms, the survey scan XPS spectra of the VA are illustrated in Figure 5.8(b). It can be clearly observed that the main constituents of the surface film at the void areas are the elements of C, O, N and Cu. In addition, traces of Ni and Cl are detected. The increase in the relative proportion of C and N is clearly observed in relative to the control coupons. This is believed to result from the adsorption of the free EPS, which is released by the free bacterial cells into the bulk solution, and the organic compounds. Another significant feature is the decrease in the relative abundance of Cu and O at the VA on the coupons with biofilms. It has been reported that the free EPS released into the bulk solution can compete with the bacterial cells for binding sites on the metal surface, thus, further contributing to the biocorrosion process (Breur et al., 2002). In the case of the BCA on the coupons with biofilms (Fig. 5.8(c), the relative abundance of C and N are much higher than those in the conditioning layers, as well as the VA on the same samples, indicative of the presence of the biofilm and their EPS. It should be emphasized that the conditioning layers probably make a small contribution to

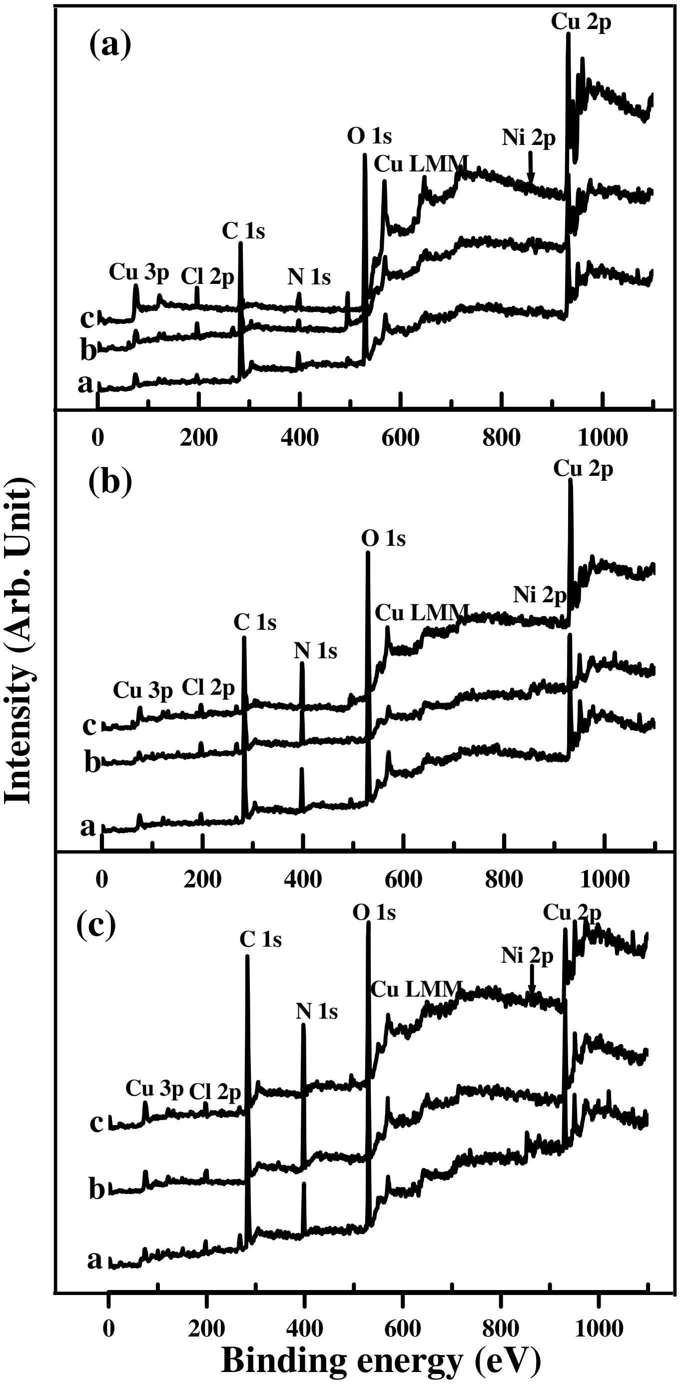

Figure 5.8 Wide scan XPS spectra recorded on of the alloy coupon surface after exposure to the sterile and the *Pseudomonas*-inoculated nutrient-rich media for 3, 7 and 28 days: (a) the control coupons, (b) the void areas on the coupon surface with biofilms, (c) the bacterial cluster areas on the coupon surface with biofilms. The spectra a, b and c correspond to 3, 7 and 28 days, respectively.

Table 5.5 Relative elemental concentrations of the surface film on the alloy coupon surface in the sterile and *Pseudomonas*-inoculated media for different exposure times

Samples	Exposure time/days	Atomic concentration (%)						
		C	O	N	Cu	Ni	Cl	[Cu]:[Ni]
Sterile[a]	3	47.17	33.13	2.87	14.83	1.13	0.87	7 : 0.6
	7	47.23	32.91	2.54	14.92	0.65	1.75	7 : 0.3
	28	49.91	30.02	2.78	15.15	0.32	1.82	7 : 0.1
VA[b]	3	58.39	27.08	5.86.	6.80	1.30	0.73	7 : 1.4
	7	63.49	23.61	6.26	4.90	0.74	1.00	7 : 1.0
	28	63.04	26.28	5.64	4.07	0.31	0.66	7 : 0.6
BCA[c]	3	65.25	22.37	6.85	2.99	1.56	0.98	7 : 3.5
	7	65.19	22.04	8.26	3.12	0.31	1.08	7 : 0.7
	28	65.24	22.18	8.64	2.17	0.54	1.23	7 : 1.8

a) Sterile refers to the alloy coupon exposed to the abiotic nutrient-rich medium,
b)VA refers to the void area without the coverage of the biofilms on the coupons with biofilms,
c) BCA refers to the bacterial cluster area on the coupons with biofilms.

the C, O and N peaks for the coupon surface with biofilms. However, they are negligible in comparison with the bacteria and EPS in the biofilm according to previous findings (Johansson and Saastamoinen, 1999). On the other hand, the bacterial cluster area is different in its thickness and coverage with time, hence, the RACE of the surface films undergoes a slight change. The metallic elements of Cu and Ni were still detectable at the BCA after 28 days of exposure, which is due to the combination of biofilms and corrosion products to form a porous surface film (Mansfeld and Little, 1999). The denickelefication phenomenon can also be observed on the alloy coupons with biofilms (Table 5.5).

5.3.4 The nature of the outermost layers

Figure 5.9 shows the high resolution Cu 2p, $\mathrm{Cu_{LMM}}$, Cu $2p_{3/2}$, O 1s and C 1s core-level spectra of the surface film on the control coupons after 3, 7 and 28 days of exposure, respectively. The major component of Cu 2p spectra undergo a positive shift in BE on the main Cu 2p lines with exposure time, which reveals the growth of the oxide film on the alloy coupon surface (Fig. 5.9I). Another remarkable feature is the increase in the intensity of the shakeup satellite between 938 and 945 eV with time. These characteristic satellites have been widely recognized to arise from Cu^{2+} species, since they are caused by the presence of the unfilled (d9) valence level of the Cu^{2+} ions (Whelan et al., 2004, Tan et al., 2006). The intense shakeup feature on the 28-day control coupons indicates the presence of copious Cu^{2+} compounds in the surface film. The phenomenon is further confirmed by the Cu_{LMM} Auger spectra of a peak at B.E. of 569.4 eV (Fig. 5.9II). Deconvolution of the core-level Cu $2p_{3/2}$ spectra of the control coupons for 3 and 7 days of exposure yields four peaks (Figs. 5.9a and 5.9b). The peaks at the B.E. of 930.8, 932.1, 933.8 and 935.5 eV correspond to CuCl, Cu and Cu_2O, CuO and $Cu(OH)_2$, respectively (Wang et al., 1994, Briggs and Seah, 1993, Wagner et al., 1992). However, there are only three curve-fitted peak components of the core-level Cu $2p_{3/2}$ spectrum for 28-day coupons at B.E. of 932.1, 933.8 and 935.5 eV, attributable to Cu_2O, CuO and $Cu(OH)_2$, respectively. It is noteworthy that the $Cu2p_{3/2}$ component observed at 932.1 eV is not readily assigned, because the metallic Cu and Cu^+ have identical BE value (~0.1 eV difference). However, the BE of the Cu_{LMM} Auger line decreases by 2.6 eV for Cu_2O (570.5 eV) relative to Cu metal (567.8 eV) due to differences in relaxation energies in these materials, and can therefore be used to clearly distinguish between the two components (Tobin et al., 1983). The Cu_{LMM} Auger spectra of the control coupons after 3, 7 and 28 days of exposure are shown in Figure 5.9II. The relatively small Auger peak at 567.8 eV in relative to the peak at 570.5 eV indicates that only traces of the metallic Cu is present on the control alloy. The intensity of each deconvoluted component is used to calculate their relative quantity in the Cu 2p spectra in the oxide layers on the control coupon surface, and the results are shown in Table 5.6. The relative amount of CuCl is ~ 6 % in the product layer on the 3-day control coupons, and disappears after 28 days of exposure. On the contrary, the of the oxide film undergo a conversion from Cu_2O into CuO upon prolonging exposure time, while the relative amount of $Cu(OH)_2$ gradually increases from ~7% to ~27% after 28 days of exposure. These are indications of the formation of a duplex corrosion product layer on the alloy coupon surface, which is composed of an inner cuprous oxide layer (Cu_2O) and an outer cupric oxide layer (including CuO and $Cu(OH)_2$).

Figures 5.9d, 5.9e and 5.9f show the C 1s core-level spectra in the surface film on the control coupons after 3, 7 and 28 days of exposure, respectively, which is believed to arise from the conditioning layer. The C 1s core-level spectra are curve-fitted into four peak components at B.E. of 284.6, 285.5, 286.2 and 288.2 eV. The peak at 284.6 eV is reported to be due to the C-C/C-H bond, which is generally considered as the main component of carbohydrates, the peaks at 285.5 and 286.2 are attributed to the C-N and C-O bonds, respectively, which possibly corresponded to the functional groups of proteins, the component at 277.8 eV is ascribed to the presence of the C=O/O-C-O bond (Chan et al., 2002, Beech et al., 2000, Rouxhet et al., 1994). The relative quantity of each component of C 1s spectra is listed in Table 5.6 as well. It is clearly observed that the C-C/C-H bond is predominant in the conditioning layers for all the three control coupons (above ~ 65 %), the proteinic functional groups of C-O and C-N are also significant components in the conditioning layers, total amount of which is ~ 15 % for 3-day control coupons and reached as high as ~ 20 % beyond 7 days of exposure. It is, therefore, easily concluded that the conditioning layer consisted mainly of carbohydrates and proteins. This is consistent with the conclusions by Compère et al. (2001). The O 1s core-level spectra are further recorded to correlate with the Cu 2p and C 1s spectra, which can be combined with Cu 2p and C 1s spectra to certify the existence of certain species. The O 1s core-level spectra of the control coupons after 3, 7 and 28 days of exposure are illustrated in Figures 5.9g, 5.9h, and 5.9i, respectively. Deconvolution of the O 1s core- l

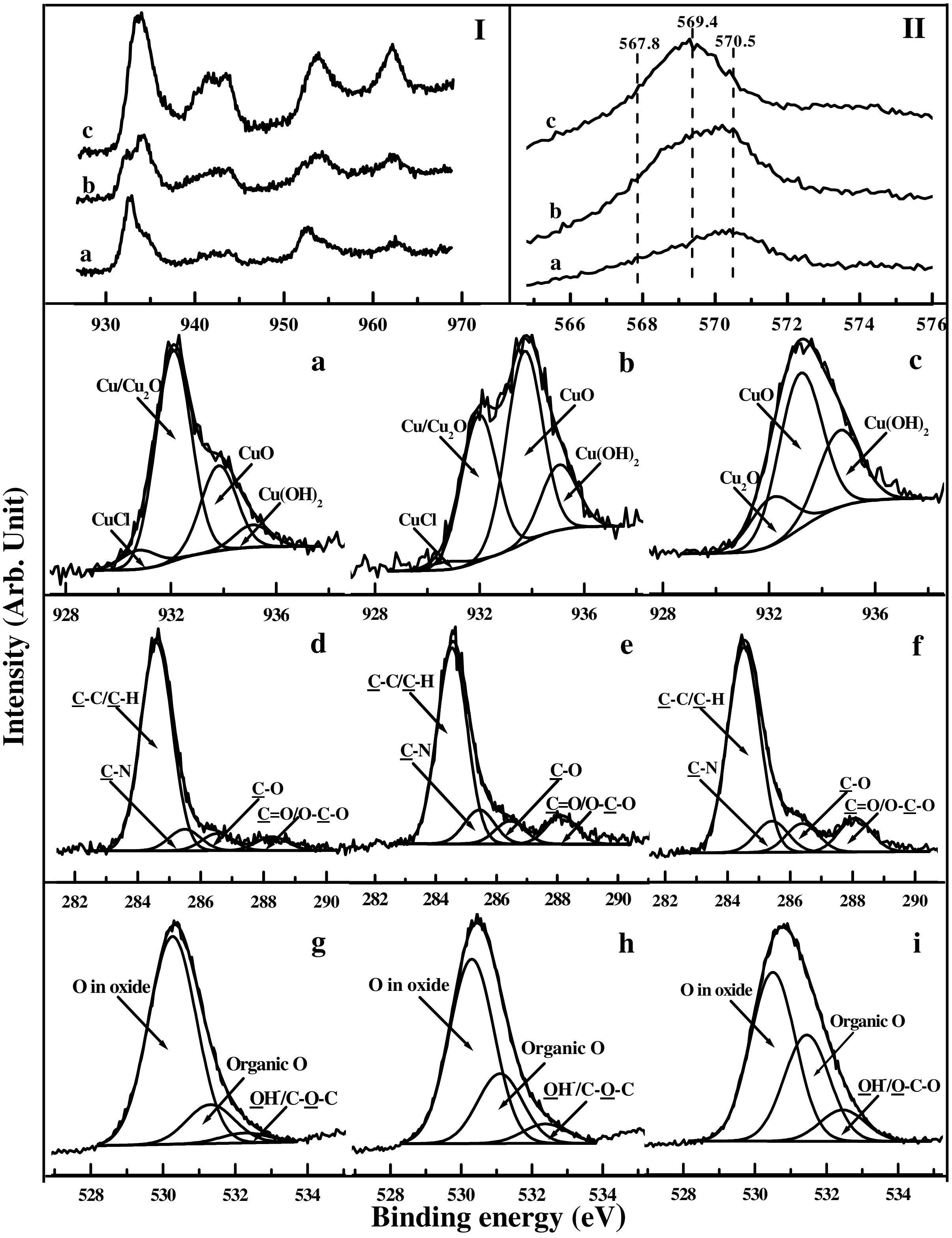

Figure 5.9 High-resolution XPS spectra of the control coupons after exposure to the sterile nutrient-rich medium for (a, d, g) 3, (b, e, h) 7 and (c, f, i) 28 days, (I) Cu 2p, (II) Cu_{LMM}, Cu $2p_{3/2}$ spectra (a, b, c), C 1s spectra (d, e, f), O 1s spectra (g, h, i).

Table 5.6 Fitting parameters of the Cu 2p, O 1s and C 1s core-level spectra and the relative quantity of compounds in the surface film of the control coupons after exposure to the sterile medium for various times

Valence state	Exposure time (days)	Proposed Components	Binding energy (eV)	Intensity (counts/s)	Relative quantity	FWHM (eV)	$\sum \chi^2$
Cu 2p	3 days	CuCl	930.8	205.0	5.6%	1.58	0.76
		Cu, Cu_2O	932.1	2282.9	62.5%	1.58	0.76
		CuO	933.8	923.8	25.3%	1.58	0.76
		$Cu(OH)_2$	935.5	242.7	6.6%	1.58	0.76
	7 days	CuCl	930.8	74.9	1.9%	1.60	0.98
		Cu, Cu_2O	932.1	1377.5	35.5%	1.60	0.98
		CuO	933.8	1807.2	46.6%	1.60	0.98
		$Cu(OH)_2$	935.5	615.8	15.9%	1.60	0.98
	28 days	Cu_2O	932.1	1271.3	17.1%	1.62	1.03
		CuO	933.8	4112.1	55.5%	1.62	1.03
		$Cu(OH)_2$	935.5	2030.3	27.4%	1.62	1.03
O 1s	3 days	O in oxide	530.3	5051.6	81.0%	1.55	1.08
		Organic O	531.4	946.0	15.2%	1.55	1.08
		OH^-, C-O-O	532.5	238.3	3.8%	1.55	1.08
	7 days	O in oxide	530.3	4362.3	67.4%	1.60	0.98
		Organic O	531.3	1649.3	25.5%	1.60	0.98
		OH^-, C-O-C	532.6	458.8	7.1%	1.60	0.98
	28 days	O in oxide	530.2	4497.3	55.1%	1.48	0.92
		Organic O	531.2	2826.5	34.7%	1.48	0.92
		OH^-, C-O-C	532.6	833.5	10.2%	1.48	0.92
C 1s	3 days	C-C, C-H	284.6	1443.0	79.9%	1.17	1.05
		C-N	285.5	148.6	8.2%	1.17	1.05
		C-O	286.2	118.8	6.6%	1.17	1.05
		C=O, O-C-O	287.8	95.1	5.3%	1.17	1.05
	7 days	C-C, C-H	284.6	1174.9	69.6%	1.15	1.30
		C-N	285.5	203.9	12.1%	1.15	1.30
		C-O	286.2	137.8	8.2%	1.15	1.30
		C=O, O-C-O	287.9	170.6	10.1%	1.15	1.30
	28 days	C-C, C-H	284.6	1568.3	65.1%	1.24	1.39
		C-N	285.5	241.8	10.0%	1.24	1.39
		C-O	286.2	346.7	14.4%	1.24	1.39
		C=O, O-C-O	287.8	253.5	10.5%	1.24	1.39

level spectra yields three peak components: i) a component at 530.3 eV, attributed to metal oxides, ii) a component at 531.3 eV attributable to the organic O (including C=O and C-O), which is mainly from carboxylic acid, carboxylate, ester, carbonyl or amide, iii) a component at 532.6 eV is ascribed to the hydroxyl group, OH^-, originating from the metal and organic (C-OH) hydroxide, or hemiacetal and acetal C-O-C (Compère et al., 2001, Rouxhet and Genet, 1991). Although it decreases with exposure time, the relative quantity of the copper oxide remains as the major component of the surface film on the control coupons (Table 5.6).

Figure 5.10 illustrates the Cu 2p, Cu_{LMM}, Cu $2p_{3/2}$, C 1s and O 1s core-level spectra of the VA on the coupons with biofilms after 3, 7 and 28 days of exposure, respectively. The Cu 2p spectra on the main Cu 2p line also undergo the B.E. shift similarly to those of control coupons, but they are somewhat different from each other due to the major peak component appearing at 932.1 eV for the Cu $2p_{3/2}$ of the 28-day coupon with biofilms (Fig. 5.10I). The characteristic shakeup satellite between 938 and 945 eV is only noticeable on the 7-day Cu 2p spectra, implying the presence of relatively high quantity of Cu^{2+} compounds at the VA on the 7-day coupons with biofilms. The broad peaks at B.E. 569.4 eV in the Cu_{LMM} spectra further confirm the formation of Cu^{2+} compounds (Fig. 5.10II). The Cu $2p_{3/2}$ core-level spectra of the 3-day, 7-day and 28-day coupons at 930.8, 932.1, 933.8 and 935.5 eV are attributed to CuCl, Cu and Cu_2O, CuO and $Cu(OH)_2$, respectively (Figs. 5.10a, 5.10b, and 5.10c). The intense peaks at 570.5 eV in the Cu_{LMM} Auger lines for all three coupons reveal the predominance of Cu_2O over the metallic Cu (Fig. 5.10II). The quantitative analysis results of the curve- fitted components are shown in Table 5.7. The evolution of the oxide film at the VA on the coupon surface with biofilms is somewhat similar to that of the control coupons at the initial 3 and 7 days, since the major constituents of the Cu 2p spectra are also Cu_2O and CuO, and the relative amount of CuO increases with exposure time from 3 to 7 days. However, the formation of CuO of the samples with biofilms appears to be slower than that of the control coupons, indicating that the process of the oxide film formation is slightly altered by the effect of the free *Pseudomonas* cells and the free EPS. The Cu $2p_{3/2}$ core-level spectra of 28-day coupons further confirm the detrimental effect of the free bacterial cells and the free EPS

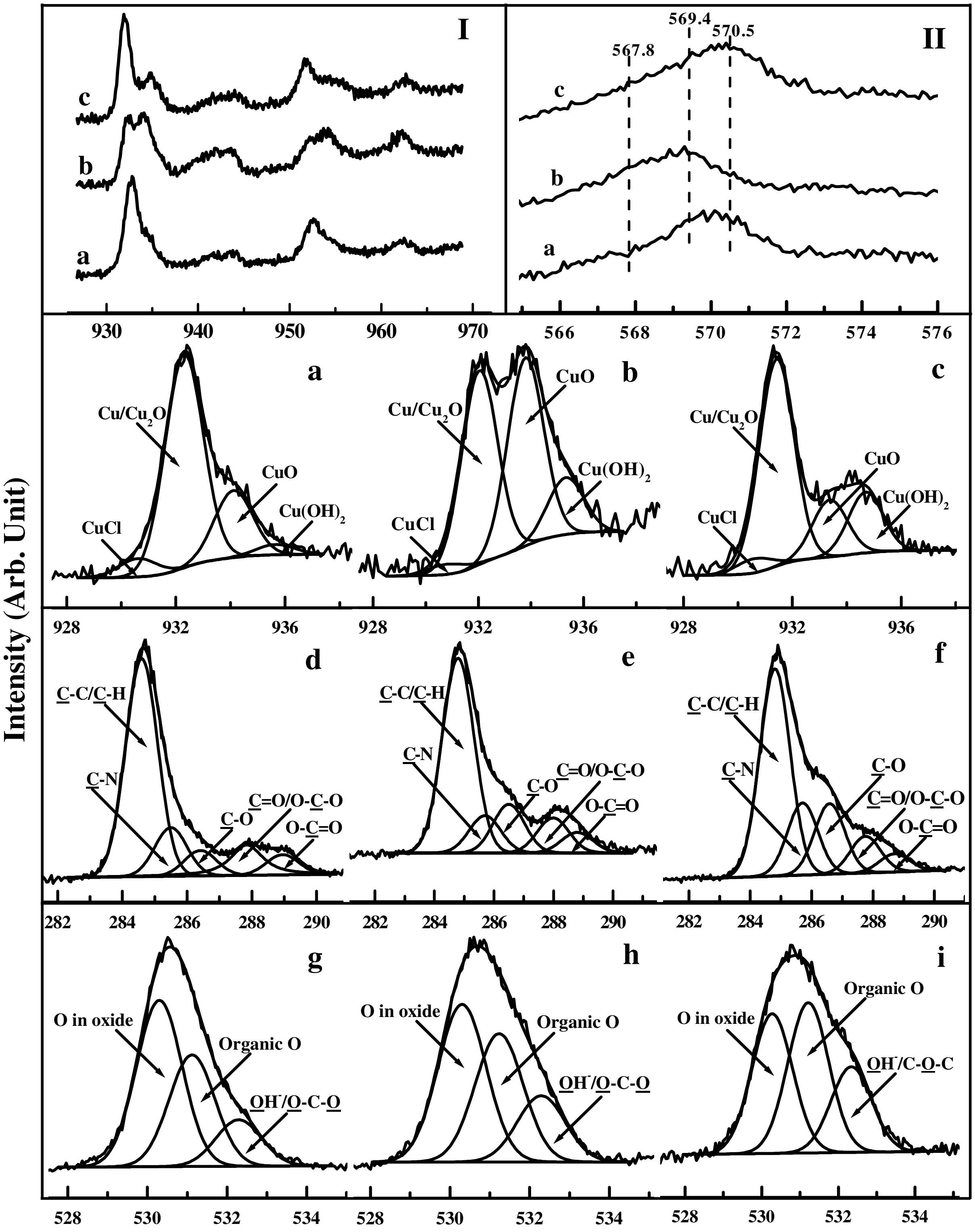

Figure 5.10 High-resolution XPS spectra of the void areas without the coverage of biofilms on the coupons with biofilms after exposure to the *Pseudomonas*-inoculated medium for (a, d, g) 3, (b, e, h) 7 and (c, f, i) 28 days, (I) Cu 2p, (II) Cu$_{LMM}$, Cu 2p$_{3/2}$ spectra (a, b, c), C 1s spectra (d, e, f), O 1s spectra (g, h, i).

Table 5.7 Fitting parameters of the Cu 2p, O 1s and C 1s core-level spectra and the relative quantity of each compound at the VA sites on the coupons with biofilms after various exposure times

Valence state	Exposure time (days)	Proposed Components	Binding energy (eV)	Intensity (counts/s)	Relative quantity	FWHM* (eV)	$\sum \chi^2$
Cu 2p	3 days	CuCl	930.8	224.4	5.9%	1.64	0.80
		Cu, Cu_2O	932.1	2619.3	69.1%	1.64	0.80
		CuO	933.8	823.7	21.7%	1.64	0.80
		$Cu(OH)_2$	935.5	125.8	3.3%	1.64	0.80
	7 days	CuCl	930.8	94.0	2.3%	1.61	0.97
		Cu, Cu_2O	932.1	1755.4	43.1%	1.61	0.97
		CuO	933.8	1708.4	42.0%	1.61	0.97
		$Cu(OH)_2$	935.5	514.3	12.6%	1.61	0.97
	28 days	CuCl	930.8	94.5	2.2%	1.57	1.05
		Cu, Cu_2O	932.1	2734.1	62.6%	1.57	1.05
		CuO	933.8	724.5	16.5%	1.57	1.05
		$Cu(OH)_2$	935.5	816.0	18.7%	1.57	1.05
O 1s	3 days	O in oxide	530.3	2740.5	52.0%	1.53	0.94
		Organic O	531.2	1718.1	32.6%	1.53	0.94
		OH^-, C-O-O	532.6	811.5	15.4%	1.53	0.94
	7 days	O in oxide	530.3	2274.4	44.8%	1.42	1.13
		Organic O	531.2	1851.1	36.4%	1.42	1.13
		OH^-, C-O-C	532.5	955.0	18.8%	1.42	1.13
	28 days	O in oxide	530.3	1153.3	37.2%	1.25	1.09
		Organic O	531.2	1240.3	40.0%	1.25	1.09
		OH^-, C-O-C	532.5	706.9	22.8%	1.25	1.09
C 1s	3 days	C-C, C-H	284.6	2364.8	60.6%	1.15	0.79
		C-N	285.5	580.4	14.9%	1.15	0.79
		C-O	286.2	274.8	7.0%	1.15	0.79
		C=O, O-C-O	287.9	460.9	11.8%	1.15	0.79
		O-C=O	289.0	221.3	5.7%	1.15	0.79
	7 days	C-C, C-H	284.6	2259.6	57.9%	1.25	1.09
		C-N	285.5	433.6	11.1%	1.25	1.09
		C-O	286.2	564.8	14.5%	1.25	1.09
		C=O, O-C-O	288.0	407.0	10.4%	1.25	1.09
		O-C=O	289.0	238.1	6.1%	1.25	1.09
	28 days	C-C, C-H	284.6	2708.9	51.2%	1.17	0.98
		C-N	285.5	944.4	17.8%	1.17	0.98
		C-O	286.2	922.6	17.4%	1.17	0.98
		C=O, O-C-O	288.0	478.5	9.1%	1.17	0.98
		O-C=O	289.0	236.9	4.5%	1.17	0.98

on the surface film (Fig. 10c). The relative abundance of CuO decreases from ~ 42 % to ~ 16.5 % upon exposure time increasing from 7 to 28 days, at the same time, a small amount of CuCl (~ 2 %) is still detectable on the 28-day coupons, indicative of the corrosion reaction being proceeded. The presence of CuCl has been widely considered as the first step in the corrosion reaction of copper alloys (Kear et al., 2004, Wang et al., 1994). These results imply that the oxide film loses the integrity of its structure due to the localized damage of the oxide film.

The C1s core-level spectra of the VA ascertain the presence of the free EPS on the coupons with biofilms. Figures 5.10d, 5.10e, and 5.10f correspond to the C 1s core-level spectra of the 3-, 7- and 28-day coupons, respectively. All of them can be curve-fitted into five peak components at B.E. of 284.6, 285.5, 286.2, 287.9 and 289.0 eV, attributable to the functional groups of C-C/C-H, C-N, C-O, C=O/O-C-O and O=C-O, respectively. The most remarkable feature is the presence of O=C-O functionalities on the coupons with biofilms with the relative abundance of ~5 % in the C 1s spectra (Table 5.7). The functional groups of C-N and C-O appear to increase with exposure time, and reach by ~17 % after 28 days. The relative amount of C=O and O-C-O was constant at ~10 % (Table 5.7). These functional groups originate mainly from the adsorption of the organic compounds and the free EPS in bulk solution. However, the appearance of carboxylic groups of O=C-O is ascribed to the free EPS as compared with the C 1s spectra of the control coupons. In light of the previous analysis results of the free EPS excreted by the *Pseudomonas* NCIMB 2021 bacterium, the carboxylic groups of O=C-O originate from the uronic acid residues (Beech et al., 1999). The O 1s spectra at the VA on the coupons with biofilms are also correlated with the Cu 2p and the C 1s core-level spectra to further validate the influence of *Pseudomonas* bacteria on the oxide film formation. Three peak components are similarly curve-fitted to O in the metal oxide, organic O, OH^-/O-C-O as that of the control coupons (Figs. 5.10g-5.10i), whereas, the relative abundance of each component is much different from those of the control coupons (Table 5.7). The O in metal oxides decreases with exposure time, and is only

~37% left in the surface film after 28 days of exposure, which is much less than that of the corresponding control coupon. On the contrary, the organic O and OH^-/O-C-O appear to increase with exposure time, and reach up to 40 % and 23 %, respectively. The results of Cu 2p, C 1s and O 1s core-level spectra reveal the involvement of the *Pseudomonas* cells and its free EPS in the process of the oxide film formation.

The bacterial cluster areas on the metal coupon have been widely recognized to induce the occurrence of the localized corrosion (Borenstein, 1994, Videla, 1996). The Cu 2p, Cu_{LMM}, Cu $2p_{3/2}$, C 1s and O 1s spectra at the BCA on the coupons with biofilms after 3, 7 and 28 days of exposure are presented as Figure 5.11. The colonization of the bacterial clusters on the coupon surface makes the composition of the oxide layers much different from the VA on the same coupons with biofilms and control coupons. The Cu 2p spectra at the BCA after 3, 7 and 28 days of exposure show the major components of Cu 2p spectra at BE of 932.1 eV, indicative of the presence of metallic Cu or Cu^+ at the bacterial cluster areas (Fig. 5.11I). In addition, there is little evidence of the shakeup features in the range of 938 and 945 eV and the weak signal of the peak at 933.8 eV, indicating that the Cu^{2+} compounds act as the minor components in the Cu 2p spectra. This is further corroborated by the weak signal of the peak at 569.4 eV in the Cu_{LMM} Auger spectra in Figure 5.11II. These results are consistent with the conclusions by Siedlarek et al (1994) that there are only Cu^+ compounds formed on the copper substrate covered with EPS. The Cu $2p_{3/2}$ core-level spectrum of the 3-day coupons is curve-fitted into two peak components at 930.8 and 932.1 eV, attributable to CuCl and Cu/Cu_2O, respectively (Fig. 5.11a). The Cu $2p_{3/2}$ core-level spectrum of the 7-day coupons is curve-fitted into three peak components at 930.8, 932.2 and 933.8 eV, corresponding to CuCl, Cu/CuO and CuO, respectively (Fig. 5.11b). For the 28-day coupons, an additional peak arising from the Cu $2p_{3/2}$ core-level spectrum at 935.5 eV is ascribed to $Cu(OH)_2$ in

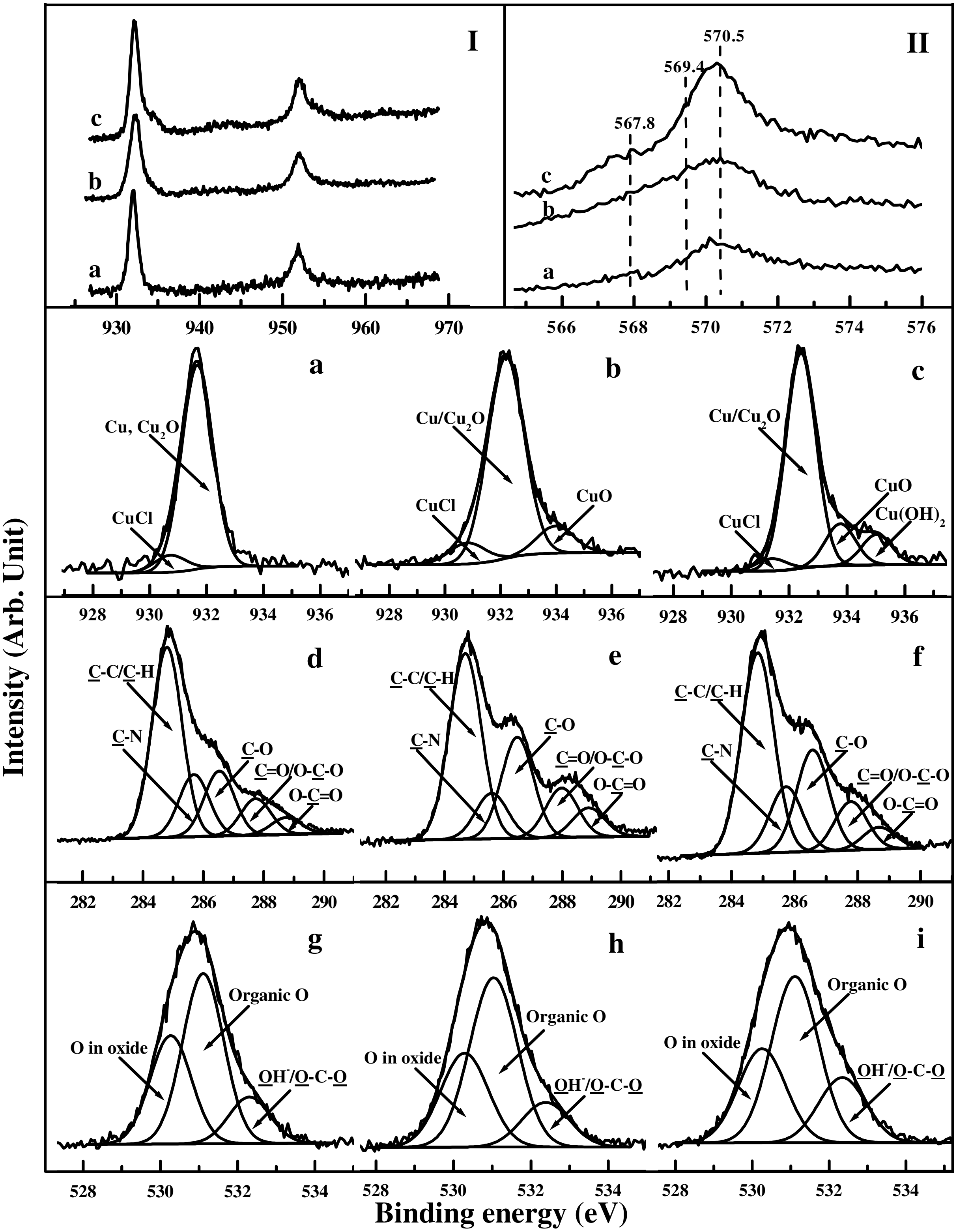

Figure 5.11 High-resolution XPS spectra of the bacterial cluster areas on the coupons with biofilms after exposure to the *Pseudomonas*-inoculated medium for (a, d, g) 3, (b, e, h) 7 and (c, f, i) 28 days, (I) Cu 2p, (II) Cu_{LMM}, Cu $2p_{3/2}$ spectra (a, b, c), C 1s spectra (d, e, f), O 1s spectra (g, h, i).

5.8 Fitting parameters of the Cu 2p, O 1s and C 1s spectra and the relative quantity of compounds of the BCA on the coupons with biofilms after various exposure times

Valence state	Exposure time (days)	Proposed Components	Binding energy (eV)	Intensity (counts/s)	Relative quantity	FWHM* (eV)	$\sum\chi^2$
Cu 2p	3 days	CuCl	930.8	181.9	5.7%	1.33	1.23
		Cu, Cu_2O	932.1	3007.6	94.3%	1.33	1.23
	7 days	CuCl	930.8	296.9	3.4%	1.32	1.65
		Cu, Cu_2O	932.2	7348.7	84.6%	1.32	1.65
		CuO	933.8	1040.5	12.0%	1.32	1.65
	28 days	CuCl	930.8	181.8	4.1%	1.22	1.24
		Cu, Cu_2O	932.2	3199.5	71.9%	1.22	1.24
		CuO	933.8	619.8	13.9%	1.22	1.24
		$Cu(OH)_2$	935.5	450.1	10.1%	1.22	1.24
O 1s	3 days	O in oxide	530.2	971.2	33.3%	1.25	1.29
		Organic O	531.2	1526.5	52.4%	1.25	1.29
		OH^-, C-O-O	532.6	417.0	14.3%	1.25	1.29
	7 days	O in oxide	530.2	1320.8	30.5%	1.35	1.64
		Organic O	531.2	2380.5	55.0%	1.35	1.64
		OH^-, C-O-C	532.5	626.8	14.5%	1.35	1.64
	28 days	O in oxide	530.3	1322.1	28.9%	1.45	1.25
		Organic O	531.3	2337.7	51.1%	1.45	1.25
		OH^-, C-O-C	532.5	915.5	20.0%	1.45	1.25
C 1s	3 days	C-C, C-H	284.6	2737.1	51.2%	1.17	1.42
		C-N	285.5	895.0	16.8%	1.17	1.42
		C-O	286.2	938.1	17.5%	1.17	1.42
		C=O, O-C-O	288.0	526.2	9.9%	1.17	1.42
		O-C=O	289.1	243.7	4.6%	1.17	1.42
	7 days	C-C, C-H	284.6	2298.8	45.2%	1.28	1.31
		C-N	285.5	563.7	11.1%	1.28	1.31
		C-O	286.2	1251.2	24.6%	1.28	1.31
		C=O, O-C-O	287.9	613.8	12.0%	1.28	1.31
		O-C=O	289.0	362.1	7.1%	1.28	1.31
	28 days	C-C, C-H	284.6	1963.6	45.7%	1.21	0.91
		C-N	285.5	642.4	15.0%	1.21	0.91
		C-O	286.2	994.2	23.1%	1.21	0.91
		C=O, O-C-O	288.0	476.0	11.1%	1.21	0.91
		O-C=O	289.1	216.3	5.1%	1.21	0.91

relative to the 7-day coupon (Fig. 5.11c). Based on the relative quantity of each component for the Cu 2p spectra in Table 5.8, several apparent features can be distinguished: i) the relative amount of Cu_2O remains predominant in the Cu 2p spectra throughout the exposure period, although it decreases from ~94 % to ~72 % with exposure time, ii) only after 7 days of exposure can the Cu^{2+} compounds be detectable, and they act as the minor components in the Cu 2p spectra, iii) a small amount of CuCl

(~5 %) is always detectable at the BCA on the coupons with biofilms. The results imply that the patchy biofilm and the biofilm EPS probably retard the formation of the duplex oxide film, and thus induce the corrosion reactions to proceed.

The C 1s core-level spectra are recorded at the BCA to substantiate the contribution of the biofilm and its EPS to the corrosion process. The C 1s core-level spectra of the BCA on the coupons with biofilms after 3, 7 and 28 days of exposure are respectively shown in Figures 5.11d, 5.11e and 5.11f. Similar to the VA on the coupons with biofilms, the C 1s core-level spectra of the BCA are also curve-fitted into five peak components of C-C/C-H (284.6 eV), C-N (285.5 eV), C-O (286.2 eV), C=O/O-C-O (280.0 eV) and O=C-O (289.1 eV). However, the relative abundance of each functional group is much different from those of the VA and the control coupons. As shown in Table 5.8, the relative quantity of the chelating functional groups of C-N, C-O, C=O/O-C-O and O=C-O increases sharply to ~55 %, accompanied with an apparent decrease in the relative amount of C-C/C-H functionality. Bacterial cells were reported to occupy ~5-25 % of the biofilm volume (Caldwell et al., 1992). EPS, as a matrix of the biofilm, is widely recognized to be the major component of the biofilm. On the other hand, microorganisms would excrete more EPS under the adverse circumstances, such as toxic metal ions of Cu^{2+}, Cr^{3+} and Cd^{2+} etc, to protect them from damage (Fang et al., 2002). It is therefore reasonable to believe that the increase in the chelating functionalities at the BCA originates mainly from the bacterial cells and the biofilm EPS. The O 1s core-level spectra of the BCA on the coupons with biofilms are also recorded to correlate with the Cu 2p and C 1s spectra as shown in Figures 5.11g-5.11i. O 1s core-level spectra of the BCA are similarly curve-fitted into three peak components to those of the VA at the coupons with biofilms and control coupons. Based on the quantitative analysis results in

Table 5.8, the noticeable feature is the sharp increase in the relative amount of the organic O, which remains more than 50 %, which are mainly associated with the presence of the biofilm EPS and the bacterial cells at the BCA sites.

The capacity of EPS to bind metal ions is important to MIC, and depends on both bacterial species and the type of metal ions (Beech and Sunner, 2004). Multivalent ions, such as Cu^{2+}, Mg^{2+} and Fe^{3+} etc, can be strongly coupled to the multi-dentate anodic ligands, such as carboxyl, glycerate, pyruvate and succinate groups (Kinzler et al., 2003). The *Pseudomonas* NCIMB 2021 bacterium in this study has been reported as a slime-producing bacterium, and can excrete the free, capsular and biofilm EPS (Beech et al., 1999). The chelating functional groups of the bacterial EPS, such as C=O, O-C-O, C-N and O-C=O, can react with metallic ions via weak electrostatic forces with hydroxyl groups on neutral polymers or via a salt bridge with carboxyl groups on acid polymers (Schreiber et al., 1990). The involvement of the bacterial EPS in the MIC of copper has been proposed in two ways: i) the EPS generated during microbial activity creates the preferential cathodic sites through the cation-selective nature of the EPS (Siedlarek et al., 1994, Wagner et al., 1997), ii) the binding of copper by microbially-produced EPS leads to a development of copper ion concentration cells, thereby, a weakly acidic environment is generated (Geesey et al., 1986). In the current study, the influences of the *Pseudomonas* cells and its EPS on the oxide film are as follows: i) the localized decrease in pH by concentrating the acidic functional groups, such as uronic acid, in the heterogeneous biofilms can impair the existing oxide film at localized sites, This has been proposed to interpret the MIC of copper in potable water systems (Webster et al., 2000), ii) the copious chelating functional groups bound with copper cations to form Cu-EPS complexes, thus, the bacterial EPS is implicated in the corrosion reactions by opening up a unique redox reaction pathway in the biofilm/metal system.

5.4 Summary

The influence of aerobic *Pseudomonas* NCIMB 2021 bacterium on the corrosion behaviors of the 70/30 Cu-Ni alloy were investigated using electrochemical and surface analytical methods. Electrochemical results revealed that the corrosion rate of the alloy coupons gradually decreased with exposure time in the sterile medium due to the formation of a protective duplex oxide layer, while, it underwent a notable increase with exposure time under the effect of the bacterial cells and its EPS. SEM images revealed extensive micro-pitting corrosion occurring underneath the bacterial clusters or the discrete biofilms on the alloy coupon surface. XPS results confirmed the correlation of the corrosion behavior of the alloy coupons with the oxide film formation on the alloy surface. The structure of the surface film was altered by the implication of the bacterial cells and the EPS in the formation process of the oxide films.

CHAPTER 6

MODIFICATION OF SURFACE-OXIDIZED COPPER ALLOY BY COUPLING OF VIOLOGENS FOR INHIBITING MICROBIOLOGICALLY INFLUENCED CORROSION

6.1 General background

In chapter 5, Cu-Ni alloys have been verified to be particularly susceptible to MIC. MIC is a serious problem in the marine environment, because it is estimated that 20~30% of all corrosion is caused by MIC, at a direct cost of 30-50 billion dollars per year (Walsh et al., 1993). Inhibiting the occurrence of MIC on various materials has therefore become very crucial to many industries, and has attracted considerable research effect.

The most widely accepted approach in combating MIC is "to keep the system clean". As a result, the use of biocides has been the most extensively used method in aquatic environments (Videla, 2002). Traditional biocides include oxidizing biocides, such as chlorine and bromine, and non-oxidizing biocides, such as glutaradehyde, formaldehyde and isothiazolones (Videla, 2002). Unfortunately, most of these biocides are inherently toxic and difficult to degrade. They could have negative impacts on the environment, if they were applied without a proper environmental risk assessment. Furthermore, the method of adding biocides to bulk solutions to reduce microbial counts is generally effective only in enclosed environments, such as the chlorine used in distribution systems. For open environments, like in seawater, the method becomes infeasible and uneconomical (Metosh-dickey et al., 2004). Another strategy devoted to inhibit or prevent the biofilm formation on the substrate surfaces has been developed to tackle the problem of MIC in recent years. Introducing antibacterial properties on the substrate surfaces to avoid or minimize the development of the unwanted biofilm is a direct way to control MIC. Various methods, such as ion exchange, adsorption, sol-gel and covalent binding, have been employed to immobilize bactericidal agents on the substrate surfaces to inactivate the bacteria during their initial attachment (Guiamet et al., 1999; Al-Darbi et al., 2002; Copello et al., 2006; Nakagawa et al., 1984; Advincula et al., 2007; Cen et al., 2003). The functional groups are usually covalently bound to the substrate surface; thus the environmental problems are minimized (Tiller et al., 2002; Cen et al., 2003; Shi et al., 2005.

The study in this chapter seeks to immobilize a thin layer of viologens on a surface-oxidized metallic substrate to impart the desirable bactericidal and corrosion-inhibitive properties for combating MIC. Viologens are the parent compounds of one of the most exciting type of herbicides (the 'paraquate' family), discovered for many years, and bactericidal action of this compound has been widely studied (Monk, 1998; Shi et al., 2005; Kawabata, 1992). Pioneering work also revealed that pyridium and its derivatives can reduce the corrosion rate of copper and steel in aggressive environments (Ma et al., 2001; El Daha et al., 1999; Vasudevan et al., 1995). To realize this, a polymeric precursor, 4-(chloromethyl) phenyl tricholorosilane (CTS), was firstly immobilized on the surface-oxidized alloy surface. This silane coupling agent has been immobilized on SiO_2 and Fe_3O_4 particles to render these surfaces active and functional in previous studies (Fu et al., 2005; Hu et al., 2006). The viologen moieties were then introduced onto the metallic substrate surface via covalent interactions between the immobilized CTS and bipyridine. Finally, the terminal pyridine groups were quaternized by coupling with benzyl chloride. The chemical composition and the topography of the viologen-modified substrate were determined by X-ray photoelectron spectroscopy (XPS) and atomic force microscopy (AFM), respectively. Thus, the antibacterial and corrosion-inhibition properties of the modified metallic surfaces were assessed with microscopic and electrochemical techniques, and by comparison with the pristine surface-oxidized coupons, in a seawater-based suspension inoculated with an aerobic *Pseudomonas* bacterium.

6.2 Experimental Section

6.2.1 Materials

70:30 Cu-Ni alloys was purchased from Metal Samples Co. of Alabama, USA as those used in chapter 5. 4-(chloromethyl)-phenyl tricholorosilane (CTS, 97%), 4,4'-bipyridine (98%) and benzyl chloride were obtained from Aldrich Chemical Co. and were used as received. Peptone, yeast extract and agar were purchased from Oxoid Chemical Co. *Pseudomonas sp.* NCIMB 2021 bacterium was obtained from the National Collection of Marine Bacteria (Sussex, UK) as that used in chapter 3, 4 and 5. Solvents, such as acetone, carbon tetrachloride (CCl_4), *N,N'*-dimethylformamide (DMF, >99%), and other chemicals were of reagent grade and were used as received from Aldrich Chemical Co.

6.2.2 Preparation of surface-oxidized Cu-Ni alloys

The Cu-Ni alloy coupons for electrochemical studies and surface characterization were prepared similarly to those described in Section 4.2.1. A chemical oxide layer was grown by placing the coupons in a hydrogen peroxide solution (37%) at 100℃ for 15 min, as reported previously (Sung et al., 2000). After that, the surface-oxidized coupons were rinsed thoroughly with DI water, and blown dry with a stream of nitrogen.

6.2.3 Immobilization of the functional silane and coupling of viologen moieties on the surface-oxidized substrate

The procedures for functionalizing the surface-oxidized alloy substrate with viologens consisted of three steps, as shown in Figure 6.1. These steps are described in detail below.

4-(chloromethyl)-phenyl tricholorosilane (CTS) was first immobilized on the surface-oxidized substrate by self-assembly. The surface-oxidized sheet coupons were immersed in 40 mL of anhydrous carbon tetrachloride solution containing 100 μL of CTS. The reaction mixture was stirred for 2 h at room temperature. The resulting CTS-immobilized metal coupons were washed with carbon tetrachloride thrice to remove the residual silane, followed by rinsing with acetone and DI water twice. They were dried by pumping under reduced pressure.

The formation of viologens on the CTS-immobilized oxidized metal surface was carried out according to the Menshutkin reaction (Monk, 1998). The method involved a two-step reaction: (i) the chemical reaction of CTS-immobilized surface with 4,4'-bipyridine; and (ii) the pyridine groups were quaternized by reaction with benzyl chloride to form the viologen moieties. The CTS-immobilized coupons were introduced into 30-mL DMF solutions containing 1 wt% 4,4'-bipyridine in a Pyrex glass tube. The reaction with 4,4'-bipyridine could be carried out at temperatures between 40 and 90℃ for various periods of time (Ng et al., 2001). The reaction was carried out at 50℃ for 24 and 48 h in this study. After the prescribed reaction time, the bipyridine-modified (CTS-BP) coupon surface was rinsed with copious amounts of DMF and DI water to remove physically adsorbed residual reactant, before being dried under reduced pressure. The coupons with immobilized bipyridine groups were then placed in 30 mL of DMF solutions containing 10 vol.% benzyl chlorides for 24 h at 70℃. At the end of the reaction period, the surface-quaternized coupons were washed thrice with DMF and DI water. The viologens-coupled coupons were finally dried under a reduced pressure and stored in air-tight desiccators for further studies (Monk, 1998; Ng et al., 2001).

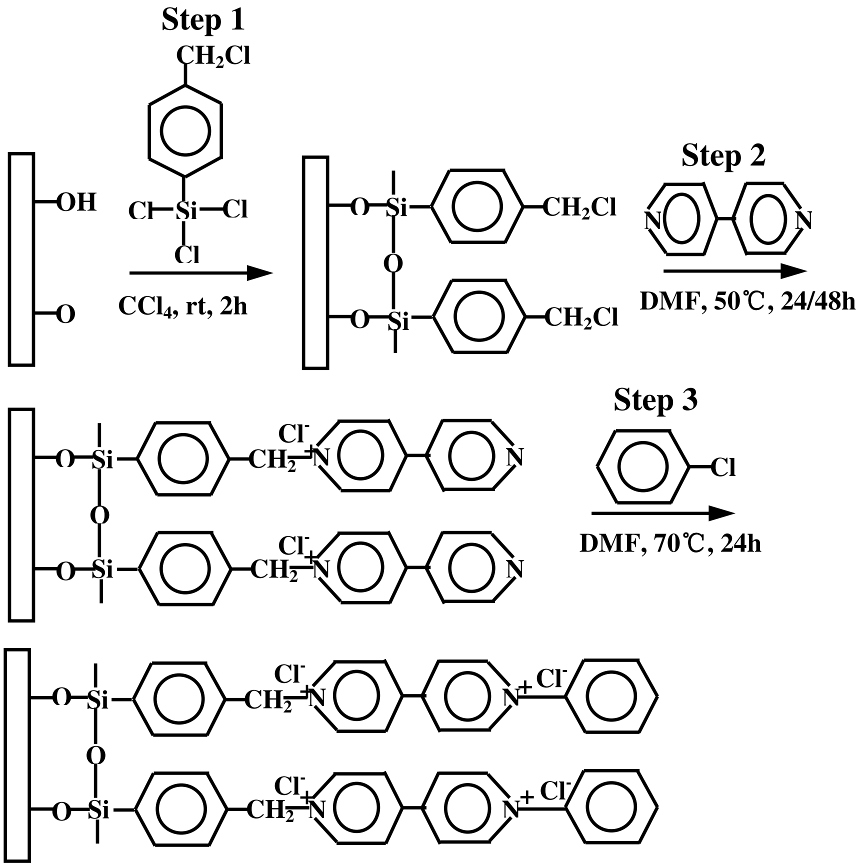

Figure 6.1 Schematic illustration of the processes for the preparation of the SOM-CTS-DBV surface; the formation of a Si-O bonded CTS monolayer (the SOM-CTS surface) in Step 1, followed by the chemical reaction of the immobilized CTS with 4, 4'-bipyradine (the SOM-CTS-BP surface) in Step 2, and the subsequent quaternization reaction to produce the viologen-functionalized surface (the SOM-CTS-DBV surface) in Step 3.

6.2.4 Surface characterization

The chemical compositions of the pristine and the functionalized substrates were determined by XPS as those described in Section 4.2.5 of chapter 4. The surface topography of the pristine and the modified substrates was studied by AFM as those described in Section 4.2.4 of chapter 4. In each case, an area of 2×2 μm^2 was scanned using the tapping mode. The Digital Nanoscope software (Version 5.30) was used to determine the arithmetic mean of the surface roughness (R_a). Static water contact angles of the pristine and functionalized substrates were measured at 25 ℃ and 60% relative humidity, using the sessile drop method with a 3 μL water droplet, in a telescopic goniometer (Rame-Hart model 100-00-(230), Rame-Hart, Inc., NJ). The telescope with a magnification power of 23× was equipped with a protractor of 1° graduation. For each angle reported, at least three measurements from different surface locations were averaged. The reported angle was accurate to ±3°.

6.2.5 Preparation of medium and medium inoculation

The preparation of medium and the inoculum cultivation were exactly same as those described in Section 3.2.2 of chapter 3.

6.2.6 Assessment of antibacterial activity against aerobic *Pseudomonas* strain.

The antibacterial characteristics of the surface-modified coupons were assessed by SEM imaging. The preparation of SEM samples was similar to those described in Section 3.2.5 of chapter 3. To assess the degree of corrosion damage under the biofilms on the pristine and surface-modified alloy coupons, the bacterial clusters and the colonized bacterial cells were gently removed from the coupon surface with sterile cotton swabs immediately after the coupons were removed from the culture, followed by rising with DI water thrice, dried by purging with nitrogen gas, and finally stored in vacuum desiccators prior to analysis. The SEM imaging sites were randomly chosen on the specimen surface to be representative of the entire surface.

6.2.7 Determination of the corrosion-inhibition properties of the surface-modified coupons

The pristine and surface-modified coupons were exposed to the *Pseudomonas* inoculated medium for 7, 14, 21 and 35 days using the semi-continuous mode of culture growth. To evaluate the corrosion-inhibition properties of the surface-modified coupons, to substantiate the occurrence of pitting corrosion, and to find out the structure of corrosion layers on the substrate surface, the measurement of Tafel plots, cyclic polarization curves and EIS data were performed as those described in Section 3.2.4 of chapter 3. From the analytical parameters of Tafel plots, the inhibition efficiency (IE) could be calculated from the following equation (Tebbji et al., 2005):

$$IE\% = \frac{i_p - i_{corr}}{i_p} \qquad (6.1)$$

Here, i_p and i_{corr} are the corrosion current densities of the pristine and surface-modified coupons, respectively, determined by an extrapolation of cathodic and anodic Tafel lines to the corrosion potential, $E_{corr.}$

6.3 Results and Discussion

6.3.1 Characterization of the surface- oxidized metal: the SOM surface

XPS and Auger spectra for the surface-oxidized 70:30 Cu-Ni alloys are shown in Figure 6.2. The photoelectron lines at binding energies (B.E.) of ~ 77, 123, 285, 530, 570, and 930 eV, which are attributed to Cu 3p, Cu 3s, C 1s, O 1s, Cu LMM, and Cu 2p, respectively, are observed in the wide scan spectrum of the pristine surface-oxidized 70:30 Cu-Ni alloys (Fig. 6.2a). A large O 1s peak is observed at 530 eV, indicative of the formation of an oxide layer on the pristine copper alloys. The intense Cu 2p and Cu $L_3M_{45}M_{45}$ Auger lines and the absence of Ni 2p line indicate that the oxide layer is only associated with copper. The high-resolution Cu $L_3M_{45}M_{45}$ Auger spectrum clearly shows that the broad peak at the B.E. of 569.6 eV associated with the Cu^{2+} species, in comparison with to a very weak signal of Cu^+ at the B.E. of 570.1 eV and Cu^0 at 567.3

eV (Fig. 6.2d). The deconvolution of the Cu $2p_{3/2}$ core-level spectrum yields two peak components at B.E. of 933.8 and 935.5 eV, attributable to CuO and $Cu(OH)_2$, respectively (Fig. 6.2c) (Whelan et al., 2004). Earlier XPS results indicated that a layer of CuO and $Cu(OH)_2$ could be grown by H_2O_2 treatment, and the thickness was reported to be about 500 Å, as measured by ellipsometry (Sung et al., 2000). The C 1s core-level spectrum can be curve-fitted with three peak components having B.E. at 284.6, 286.2 and 288.5 eV, corresponding to C-C/C-H, C-O and COO- species, respectively (Fig. 6.2b). The peak component at 284.6 eV is attributed to adventitious carbon or hydrocarbons adsorbed during sample handling (Tan et al., 2006).

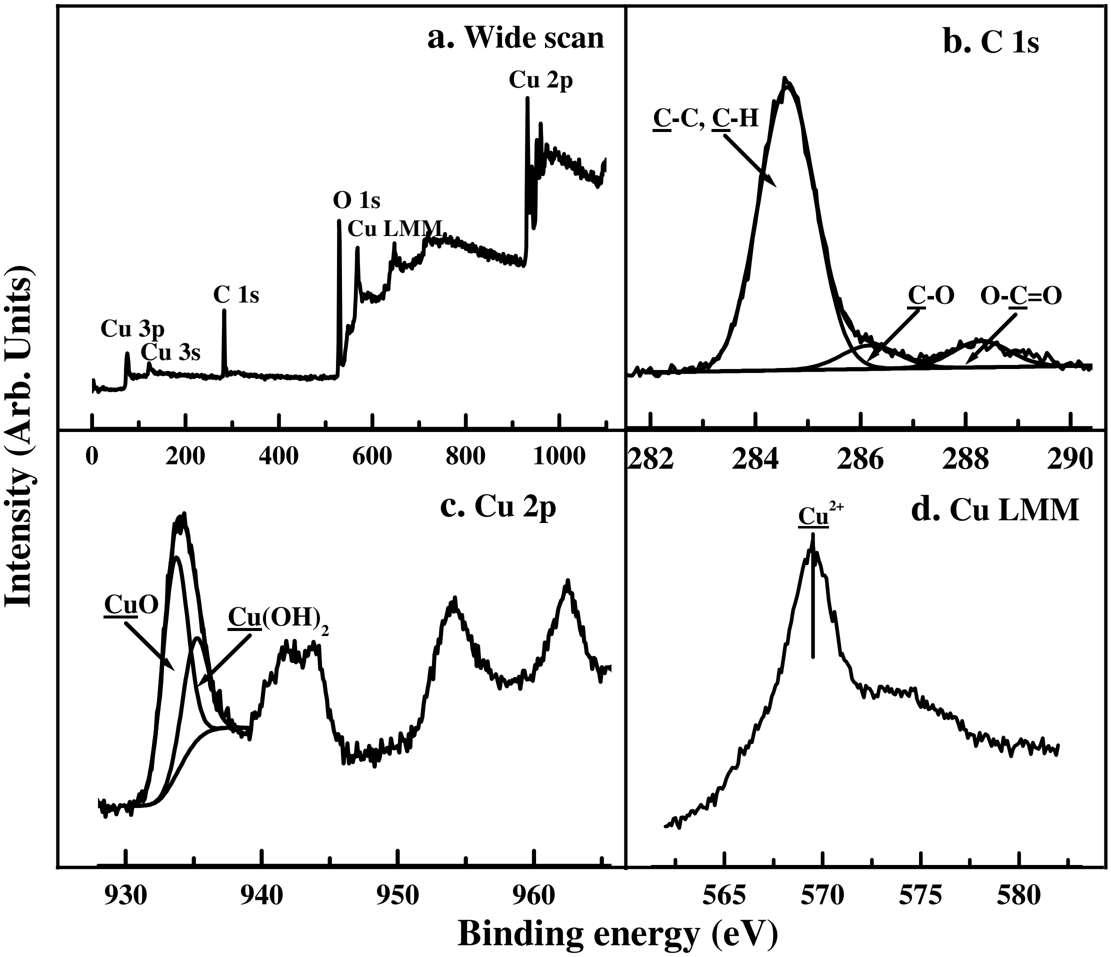

Figure 6.2 XPS wide scan (a), C 1s (b), Cu 2p (c) and Cu LMM (d) spectra of the pristine surface-oxidized metals (SOM)

6.3.2 Immobilization of functional silane on the surface-oxidized alloys: the SOM-CTS surface

The successful immobilization of 4-(chloromethyl)phenyl tricholorosilane (CTS) on the oxidized metal surface was ascertained by the XPS spectra. In comparison with the photoelectron lines of the pristine metal surface in Figure 6.2a, four additional photoelectron lines at B.E. of ~ 99, 151, 197 and 230 eV, corresponding to Si 2p, Si 2s, Cl 2p, and Cl 2s species, respectively, can be clearly observed in the wide scan spectrum of the CTS-immobilized substrate surface in Figure 6.3a. The C 1s core-level spectrum of this surface can be deconvoluted into three peak components with B.E. at 283.9, 284.6,

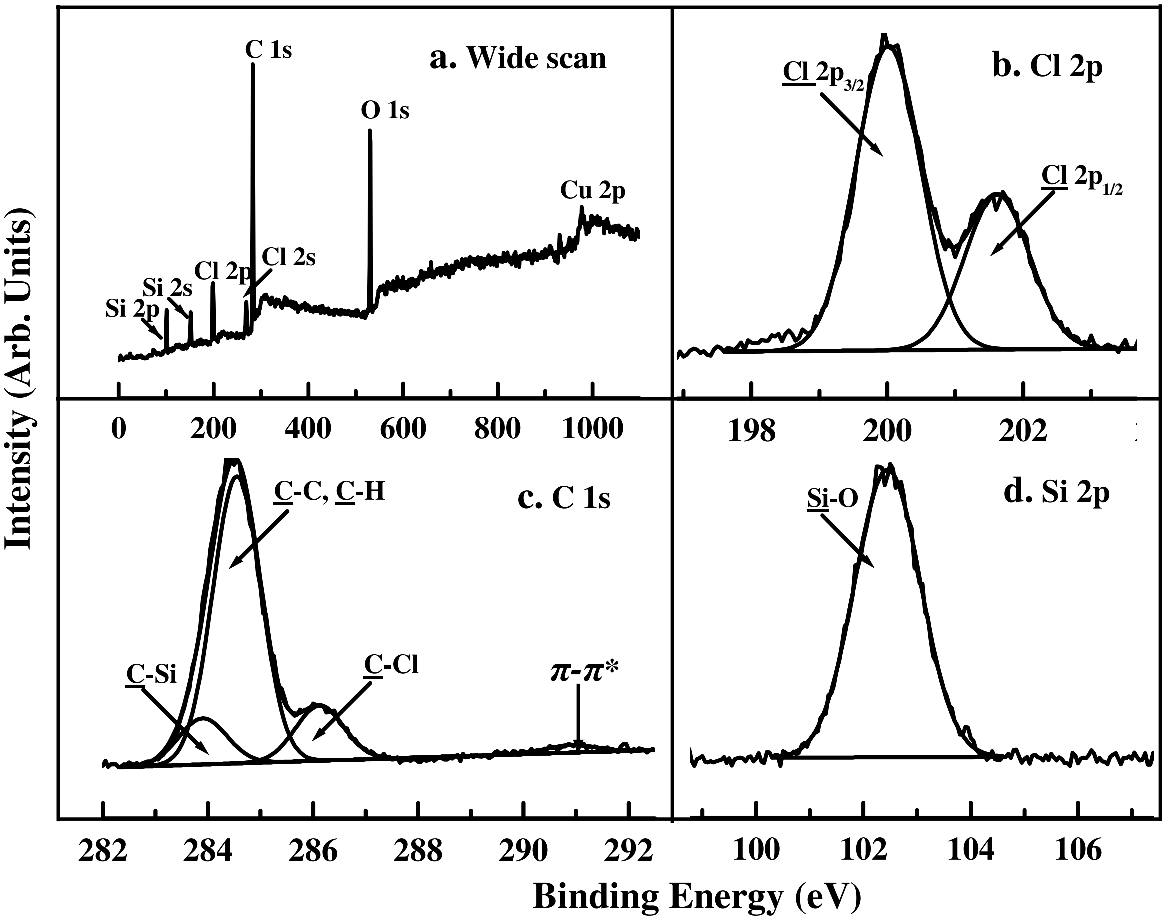

Figure 6.3 XPS wide scan (a), Cl 2p (b), C 1s (c) and Si 2p (d) spectra of the SOM-CTS surface.

and 286.2 eV,attributable to the C-Si, C-C/C-H, and C-Cl species, respectively (Wagner et al., 1992). The area ratio of the three peak components is 0.87:5.0:1.0. The π– π* shake-up satellite associated with the aromatic ring of CTS is also discernible at a B.E. of ~ 291 eV (Fig. 6.3c). The appearance of Si and Cl signals in the wide scan spectrum, as well as C-Si and C-Cl species and the π– π* shake-up satellite in the C 1s core-level spectrum, are consistent with immobilization of CTS on the surface-oxidized metallic substrates (Fu et al., 2005). Figure 6.3b shows the Cl 2p spectrum of the SOM-CTS surface. The Cl $2p_{3/2}$ and Cl $2p_{1/2}$ spin-orbit split doublet at ~200 and 201.6 eV are attributed to the covalently bonded chlorine. The Si 2p spectrum of the SOM-CTS surface is shown in Figure 6.3d. The [Si]:[C] ratio, as determined from the Si 2p and C 1s core-level spectral area ratio, is about 1:7.1, which is in good agreement with the theoretical value of 1:7 for CTS (Hu et al., 2006).

6.3.3 Covalent coupling of bipyridine onto the CTS-immobilized coupons: the SOM-CTS-BP surface

The coupling reactions between the SOM-CTS surface and 4,4'-bipyridine generated the SOM-CTS-BP surface. The successful coupling of 4,4'-bipyridine onto the SOM-CTS surface can be deduced by comparing the XPS wide scan spectra of the surface before and after the coupling process. Figure 6.4a shows the XPS wide scan spectrum of the SOM-CTS-BP surface. In comparison with the corresponding SOM-CTS surface in Figure 6.3a, an apparent difference can be distinguished is that the presence of N signal is clearly visible, indicating that the bipyridine groups have been successfully coupled to the metal surface. The corresponding N 1s core-level spectra of the modified surface for reaction time of 24 and 48 h are shown respectively in Figures 6.4d and 6.4f. Both of them can be curve-fitted with three peak components. The peak component at 401.8 eV is assigned to the positively charged nitrogen (N^+); the one at 399.6 eV is due to the radical cation (N^*) of the pyridine rings during X-ray excitation in the analysis chamber of the XPS instrument, and finally the peak component at 398.6 eV is attributed to the unreacted imine nitrogen (-N=) of the pyridine rings (Liu et al., 2002). The $[N^+]/[N_T]$ ratio, as determined on the basis of the positively charged nitrogen (N^+) and total nitrogen spectral area ratio within the sampling depth of the XPS technique, is about 0.44 and 0.40 after reaction time of 24 and 48 h, respectively (Figs. 6.4d and 6.4f). The ratios are both close to the theoretical value 0.5. Thus, most of the bipyridine groups stay affixed to the substrate via covalent interaction. The small deviation probably has resulted, at least in part, from the physisorption of 4,4'-bipyridine. Figures 6.4c and 6.4e show the corresponding Cl 2p core-level spectra of the surface-modified substrate for reaction time of 24 and 48 h, respectively. The Cl 2p core-level spectrum of the SOM-CTS-BP surface can be deconvoluted into two spin-orbit-split doublets with B.E. values for the Cl $2p_{3/2}$ peak components located at about 197.2 and 199.7 eV (Figs. 6.4c and 6.4e), attributable to ionic chloride (Cl^-) and covalent chlorine (-Cl) species, respectively (Briggs and Seah, 1990). The ratio of $[Cl^-]/[Cl_T]$, as determined on the basis of the ionic chlorine and total chlorine spectral area ratio within the sampling depth of XPS technique, can be used to assess the progress of coupling reaction. Approximate half of active methyl-chlorine groups were coupled with bipyridine groups after 24 h of reaction. With the extension of reaction time to 48 h, the ratio of $[Cl^-]/[Cl_T]$ reached to as high as 89%, indicating that most of the methyl-chlorine groups have reacted with 4,4'-bipyridine. The C 1s core-level spectra of both SOM-CTS-BP surface are very similar, and include a peak at 285.5 eV, attributed to the C-N species of the coupled bipyridine groups, in addition to the C-C/C-H peak component at 284.6 eV, and the $C\text{-}N^+$ peak component at 286.2 eV (Fig. 6.4b).

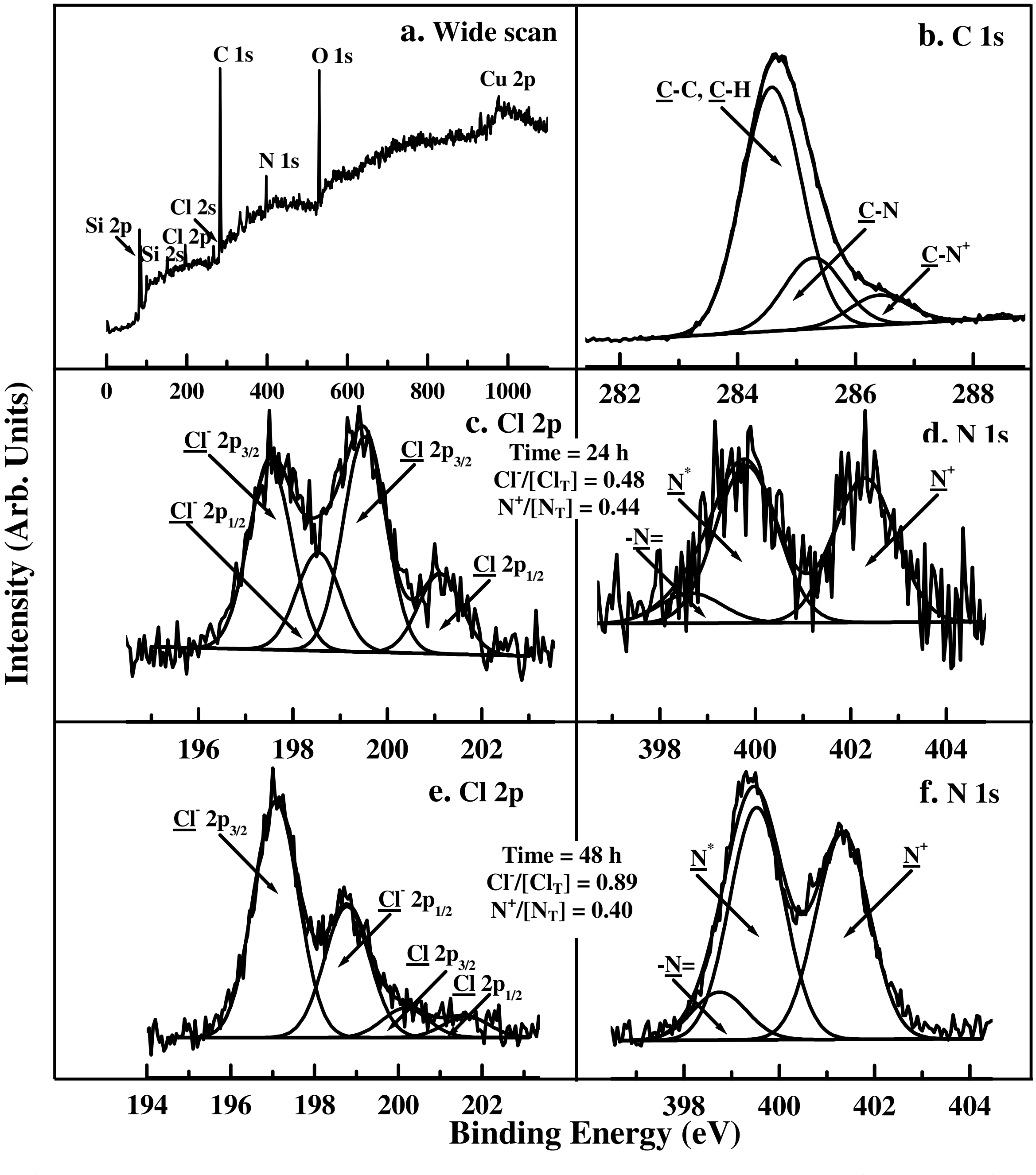

Figure 6.4 XPS wide scan (a), C 1s (b), Cl 2p (c) and (e), N 1s (d) and (f) spectra of the SOM-CTS-BP surface. (c) and (d) for the 24-hour functionalized substrate surface; (e) and (f) for the 48-hour functionalized substrate surface.

6.3.4 Quaternization of the end pyridine groups to form the viologen moieties: the SOM-CTS-DBV surface

The end pyridine groups of the SOM-CTS-BP surface were quaternized by benzyl chloride to form the viologen moieties on the alloy surface. Figure 6.5 shows the XPS spectra of the SOM-CTS-DBV surface. No significant difference can be observed in the XPS wide scan spectrum before and after the quaternization process except for minor changes in the relative intensity of C and Cl signals (Fig. 6.5a). The C 1s core-level spectra of the SOM-CTS-BP and the SOM-CTS-DBV surfaces are similar to each other, except for the disappearance of the peak component at the B.E. of 285.5 eV, which is ascribed to the C-N species, indicative of a high degree of quaternization of the pyridine groups (Fig. 6.5b). The corresponding N 1s core-level spectrum in Figure 6.5d shows a predominant peak component at the higher B.E. of 401.8 eV, attributable to positively charged nitrogen (N^+) of the di-quaternized molecules. The other two minor peak components are ascribed to the radical cation (N^*) and the imine nitrogen (-N=) species,

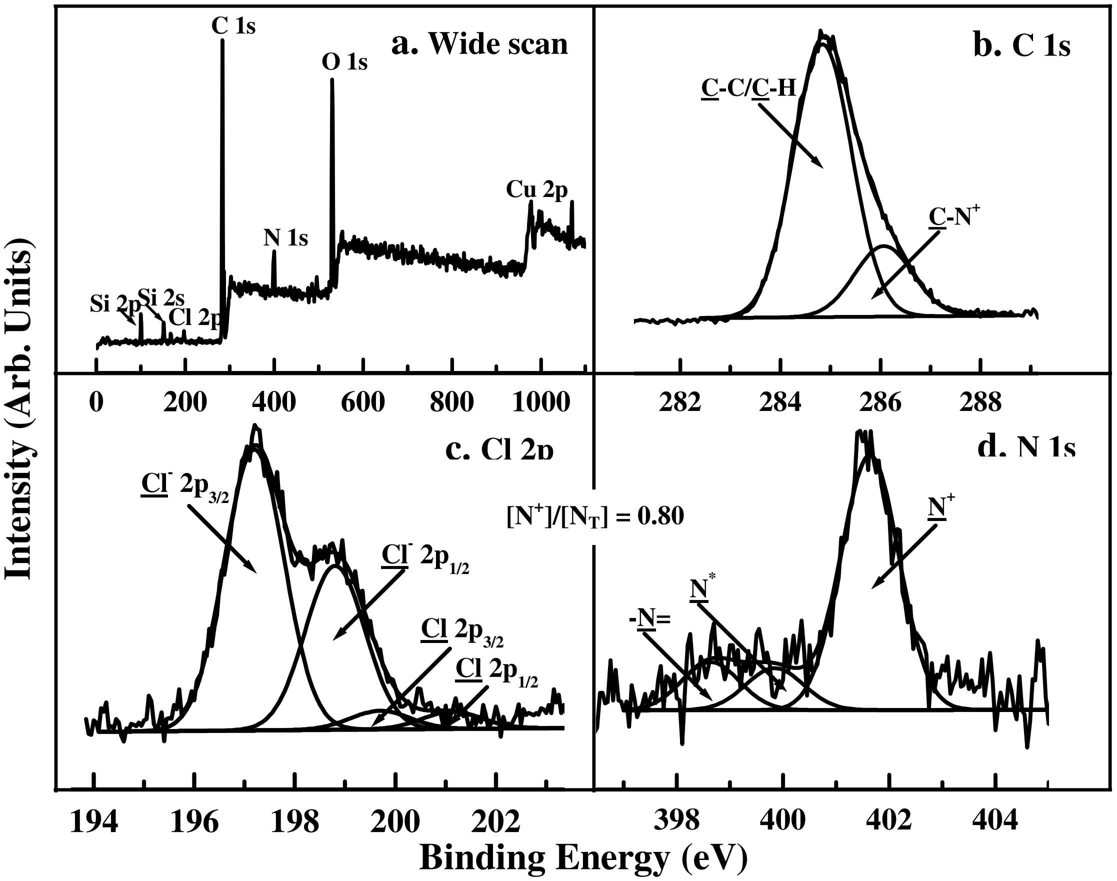

Figure 6.5 XPS wide scan (a), C 1s (b), Cl 2p (c) and N 1s (d) spectra of the SOM-CTS-DBV surface.

as described in Figures 6.4d and 6.4f (Liu et al., 2002). The N 1s line shape confirms the derivatization of the –N= groups by benzyl chloride. On the basis of the $[N^+]/[N_T]$ ratio, the degree of quaternization of the pyridine rings is ~ 80%. The Cl 2p core-level spectra of the SOM-CTS-DBV surface also shows two spin-orbit-split doublets of ionic chlorine (Cl^-) and covalent chlorine (-Cl) species. A high $[Cl^-]/[Cl_T]$ ratio would imply that the immobilized pyridine groups have reacted extensively with the benzyl chloride to result in the formation of viologen-functionalized surface. The $[Cl^-]/[Cl_T]$ and $[N^+]/[N_T]$ ratios are in good agreement with each other and are consistent with the viologen-functionalized surface depicted in Figure 6.1. The presence of a small amount of covalent chlorine (-Cl) on the SOM-CTS-BDV surface can be attributed to the residual chlorine of CTS, which have failed to react completely in step 2, or the physisorption of benzyl chloride on the substrate surface.

6.3.5 Surface morphology and wettability measurements

The changes in the surface morphology of the surface-oxidized alloy substrate before and after each step of modification were investigated by AFM. Representative AFM images of the pristine and stepwise functionalized surfaces are shown in Figure 6.6. The root mean square surface roughness (R_a) of the pristine OM surface is about 11.9 nm (Fig. 6.6a). The R_a value of the SOM-CTS surface is about 6.7 nm (Fig. 6.6b). Hence, there is a small decrease in surface roughness after the CTS immobilized. Although ellipsometry is not used to determine the thickness of CTS coupled on the substrates, the average thickness of a similarly self-assembled silane monolayer on a reflective mica surface was determined by ellipsometry to be ~ 2.6 nm ((Nakagawa and Ogawa, 1994). On the other hand, the surface shows distinct features after coupling of bipyridine and viologen moieties. The surface roughness, R_a, increases to about 22.5 and 63.4 nm, respectively (Figs. 6.6c and 6.6d). The large increase in surface roughness of the surface-modified coupons suggests agglomeration of the quaternized viologen moieties on the substrate surface. As the size of *Pseudomonas* NCIMB 2021 used in the present study is about 1.0 to 2.5 µm in length and 0.4 to 0.6µm in diameter (Beech et al., 2000), the increase in surface nano-roughness, arising from viologen immobilization, probably will not have any significant effect on the bacterial adhesion (Hilberta et al., 2003; Barnes et al., 1999; Tide et al., 1999; Verran and Boyd, 2001). The viologen-immobilized surface exhibits good antibacterial and anticorrosion properties, with sparsely adhered bacterial cells and absence of pitting and other forms of corrosion (see Figures 6.7 and 6.8 below).

The hydrophilicity of each substrate surface was evaluated by contact-angle measurements. As shown in Table 6.1, the variation in static water contact angles of functionalized substrate surface from that of the pristine coupon surface suggests changes in surface wettability introduced by the coupled functional groups. The contact angle increases from ~44° to 93° due to the immobilization of CTS on the surface-oxidized coupon, indicating an increase in the hydrophobicity of the surface. On the other hand, when the SOM-CTS surface was coupled with bipyridine via covalent interactions, the water contact angles decrease to about 72° due to the formation of a thin positively-charged layer of pyridinium groups. However, as the quaternization reaction proceeds to form a layer of viologen moieties on the substrate surface, the water contact angle does not decease further as initially expected. Instead, it increases slightly to ~74°, as compared to that on the SOM-CTS-BP surface. This result is probably caused by surface phenomena that are related to the wetting or contact angle hysteresis, such as interfacial tension, surface roughness, chemical heterogeneity, sorption layers, molecular orientation and/or swelling (Kwok et al., 1997).

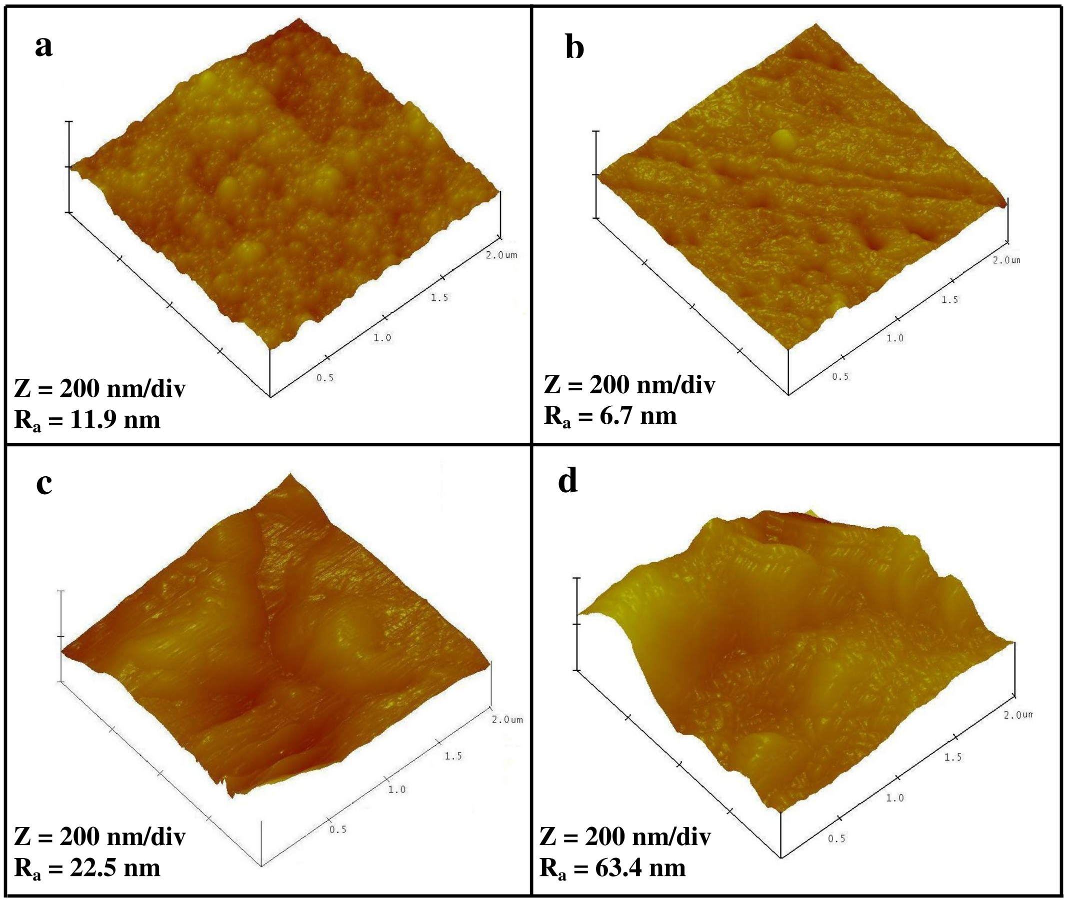

Figure 6.6 AFM images of the (a) pristine SOM surface, (b) SOM-CTS surface, (c) SOM-CTS-BP surface and (d) SOM-CTS-DBV surface.

Table 6.1 Static water contact angles of different substrate surfaces

Sample surface	Static water contact angles (±3°)
Pristine SOM[a]	44
SOM-CTS[b]	93
SOM-CTS-BP[c]	72
SOM-CTS-DBV[d]	74

a) SOM corresponds to the surface-oxidized Cu-Ni alloy
b) SOM-CTS corresponds to the surface-oxidized Cu-Ni alloy immobilized with CTS
c) SOM-CTS-BP corresponds to the SOM-CTS surface coupled with 4,4'-bipyridine
d) SOM-CTS-DBV corresponds to the vilogen-functionalized surface

6.3.6 Antibacterial Characteristics of the functionalized SOM-CTS-DBV surface

The pristine and the surface-modified coupons were exposed to the *Pseudomonas* inoculated medium as described in the experimental section to simulate the natural attachment of marine aerobic bacteria on the solid substrates. Figures 6.7a, 6.7c, 6.7e and 6.7g correspond to the bacterial incubation of the pristine metal surface in the *Pseudomonas* inoculated medium for 7, 14, 21 and 35 days, respectively. These SEM images are representative of the entire surface of the respective substrates. Some distinguishable *Pseudomonas* cells, either individually or in small bacterial clusters, attach to the pristine SOM surface. Active cell growth, as well as division, is also observed after 7 days of incubation (Figure 6.7a). With the increase in exposure time, the cultures of *Pseudomonas* cells become dense, and aggregate to form bacterial microcolonies on the pristine substrate as shown in Figures 6.7c, 6.7e and 6.7g. It is reported that microorganisms tended to settle preferentially on the metal surface in the form of discrete colonies or at least in a spotty manner rather than in a continuous biofilm in order to reduce the total surface area in contact with the toxic substrates (Fang et al., 2002). The formation of patchy biofilm provides the physicochemical conditions in localized environments to facilitate the attack of *Pseudomonas* on the surface-oxidized coupon, leading to the occurrence of pitting corrosion. As shown in Figures 6.8 a, 6.8c and 6.8e, pitting corrosion can be clearly observed on the pristine coupon surface after removal of the biofilms. The depth and size of the pits both appear to increase with the exposure time. It has been reported that the occurrence of pitting corrosion underneath the bacterial clusters was mainly caused by the differential aeration cells, resulting from respiration of the colonized obligate aerobic *Pseudomonas* strains on the metallic substrates (Little and Wagner, 1994; Fang et al., 2002; Valcarce et al., 2005, 2006). The cuprous or cupric oxide layers formed on the copper alloys are widely recognized to inhibit corrosion in abiotic aggressive aqueous environments due to their excellent corrosion resistance (Palit and Pehkonen, 2000). However, this study reveals that they can be broken down under the attack of *Pseudomonas* bacteria, and lose their passivity. These results also confirm the previous conclusion that normal material surfaces, including toxic copper or nickel alloys, are good templates for the proliferation of microorganisms and that biofilm formation will occur readily on such materials in contact with bacteria (Costerton et al., 1999; Mueller et al, 2002). The interactions between bacteria with solid substrates can arise from electrostatic forces, Lifshitz-van der Waals force, hydrophobic-hydrophobic interaction and receptor-ligand interactive forces (Gristina et al., 1987; Hermansson, 1999; Schweinsberg and Ashworth, 1988).

In the case of functionalized coupons, the attachment of *Pseudomonas* cells is much different from the pristine coupons. Figures 6.7b, 6.7d, 6.7f and 6.7h show the modified SOM-CTS-DBV surface after exposure in the *Pseudomonas* inoculated mediums for 7, 14, 21 and 35 days, respectively. A significant reduction in the number of attached bacterial cells is clearly observed on the functionalized SOM-CTS-DBV surface in relative to the corresponding pristine alloy substrate. After 7 days of incubation, only few *Pseudomonas* cells can be spotted over the rough surface of the functionalized substrate (Fig. 6.7b). Aggregation and cell division are indiscernible on this substrate. Upon prolonging the exposure time to 21 days, there are still only some single, and apparently smaller, *Pseudomonas* cells sparsely distributed on the functionalized substrate (Figs. 6.7d and 6.7f). Little evidence of growth or proliferation can be observed. Hence, most of the cells observed on the modified substrate probably have originated from the initial seeding of the *Pseudomonas* cells rather than from cell division. These results confirm that the functionalized SOM-CTS-DBV surface has a desired antibacterial activity and that biofilm formation is inhibited on such a functionalized surface in contact with bacteria. Undoubtedly, the antibacterial activity of the modified surface results from high

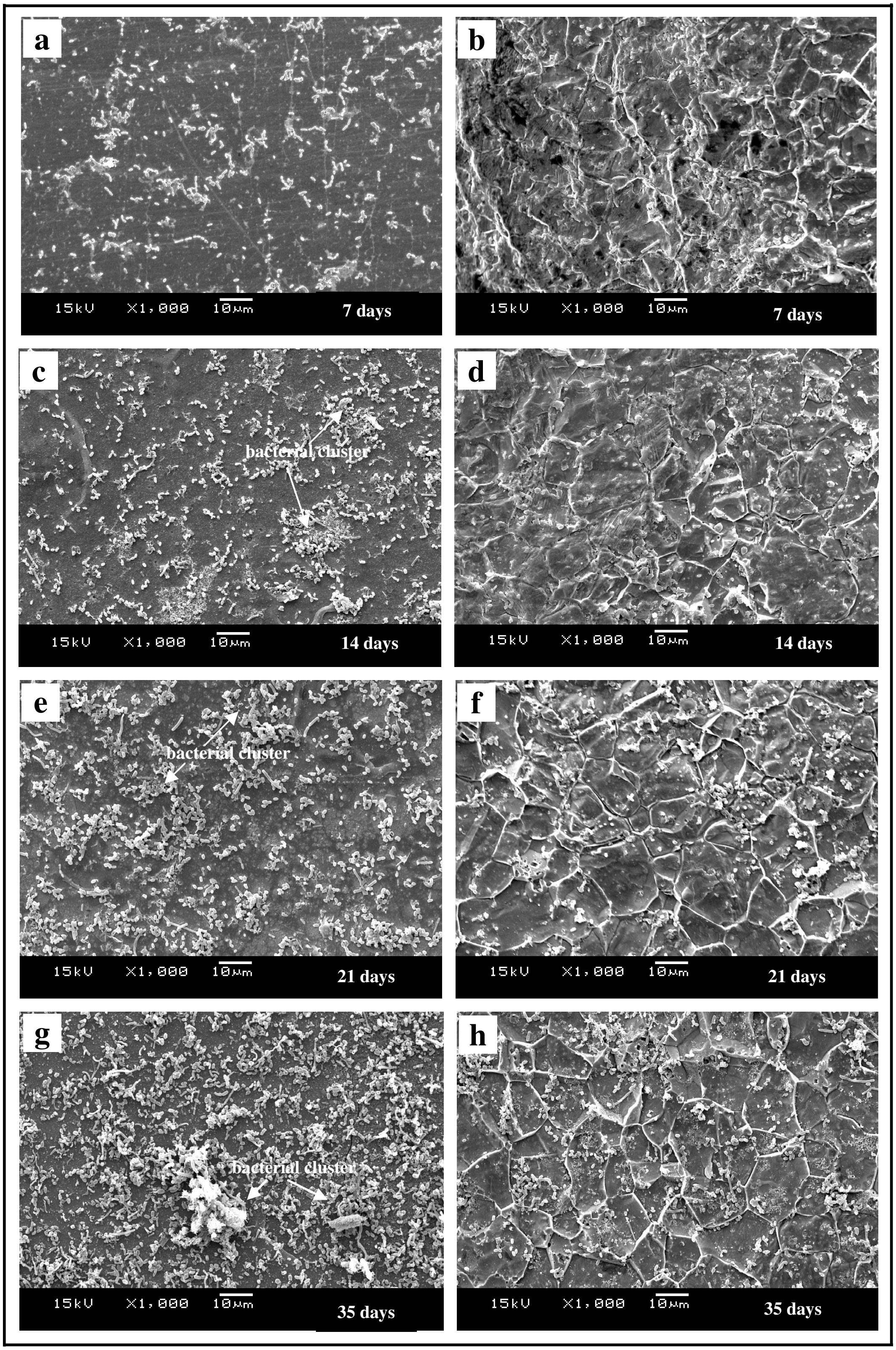

Figure 6.7 SEM images of the pristine SOM surface (a, c, e and g) and the SOM-CTS-DBV surface (b, d, f and h) after incubation in the *Pseudomonas* inoculated medium for 7, 14, 21 and 35 days, respectively.

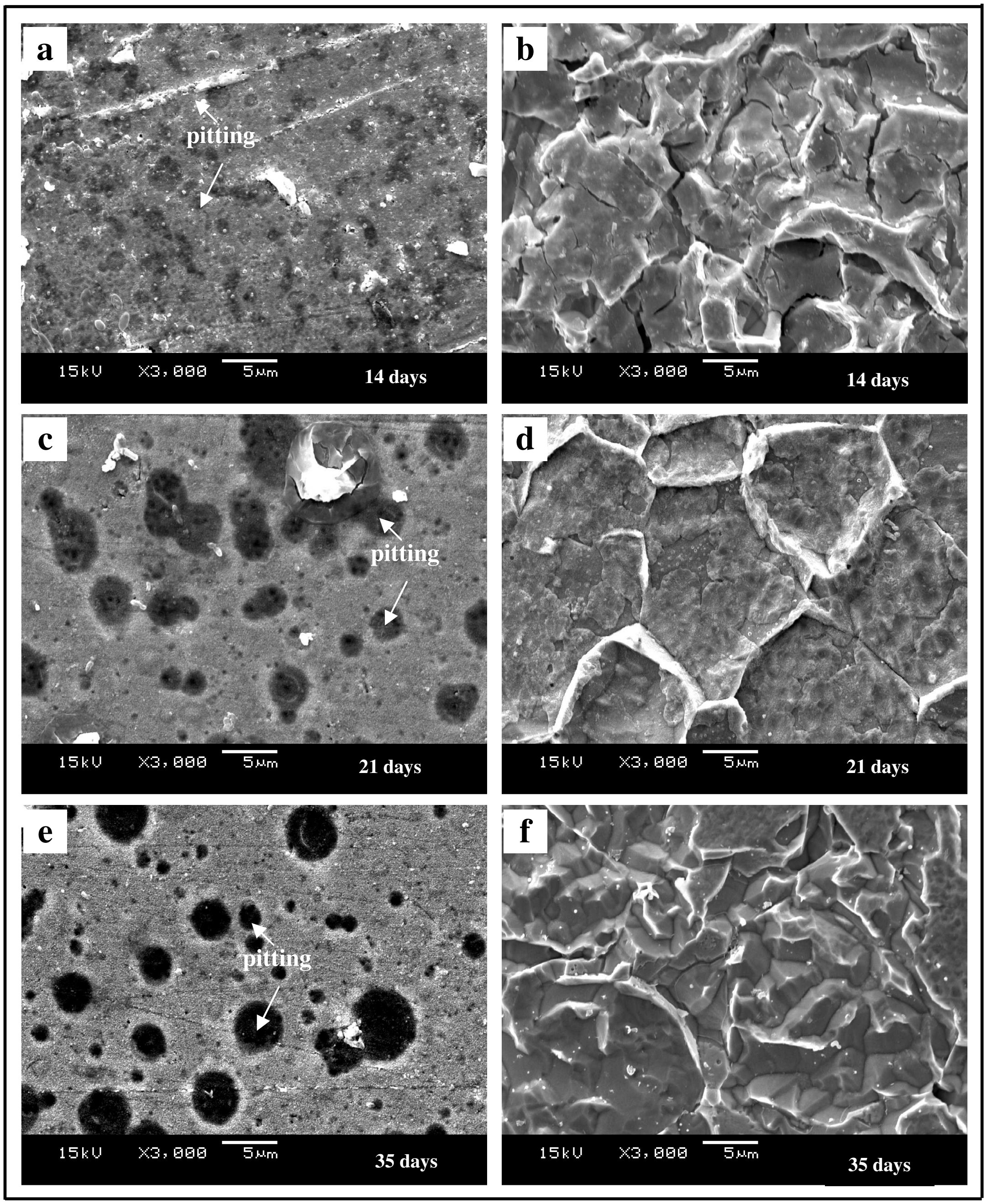

Figure 6.8 SEM images of the pristine SOM surface (a, c and e) and the SOM-CTS-DBV surface (b, d and f) after exposure to the *Pseudomonas* inoculated medium for 14, 21 and 35 days, respectively, followed by removal of the biofilms.

densities of quaternary ammonium groups (N^+) of the coupled viologens. The surface-bearing poly-cationic groups can penetrate the bacterial membrane, resulting in the bacterial cell damage and death (Tiller et al., 2002; Cen et al., 2003; Lin et al., 2002). The following sequential steps have been proposed for the antibacterial mechanism involving polycations: (i) adsorption onto the bacterial cell surface; (ii) diffusion through the cell wall; (iii) binding to the cytoplasmic membrane; (iv) disruption of the cytoplasmic membrane; (v) release of K^+ ion and other cytoplasmic constituents; (vi) precipitation of cell contents and death of the cell (McDonnell and Russell, 1999; Franklin and Snow, 1981). This study further confirms that viologens, as pyridinium-type polymers with polycationic groups, can be used to functionalize surface-oxidized metal coupons and to induce good antibacterial effects, not unlike the effects produced when they are applied on the polymeric substrates (Nakagawa et al., 1982; Lin et al., 2002).

The durability of the modified SOM-CTS-DBV surface is crucial in evaluating the surface modification technique for controlling MIC. It is clearly observed that after 35 days of incubation, the attachment of *Pseudomonas* cells becomes relatively dense along the interstitial space on the functionalized substrate, and that cell division seems to have resumed as well (Fig. 6.7h). This phenomenon is probably caused by partial spalling of the coupled organic layer from the substrate. The partial spalling on the functionalized substrate would be accompanied by the partial loss of antibacterial properties at some sites. Hence, *Pseudomonas* cells can begin to attach to or proliferate on the functionalized surface. However, the amount of *Pseudomonas* cells on the modified substrate is still much smaller than that on the surface-oxidized pristine coupon. It was also observed that no pitting corrosion or other localized corrosion (such as crevice corrosion), had occurred on the SOM-CTS-DBV surfaces throughout the incubation periods (Figs. 6.8b, 6.8d and 6.8f). The rough surface of the 35-day-incubated coupon shows the results of the partial spalling of the coupled organic layer (Fig. 6.8f). All these results indicate that the functionalized substrate still retains an antibacterial and corrosion-inhibition abilities after a relatively long periods of exposure.

6.3.7 Characterizing the corrosion-inhibition properties of the modified SOM-CTS-DBV surface

Tafel measurements were carried out to determine the change in the inhibitive efficiency (IE) with exposure time. Figures 6.9a, 6.9b, 6.9c and 6.9d show the Tafel plots

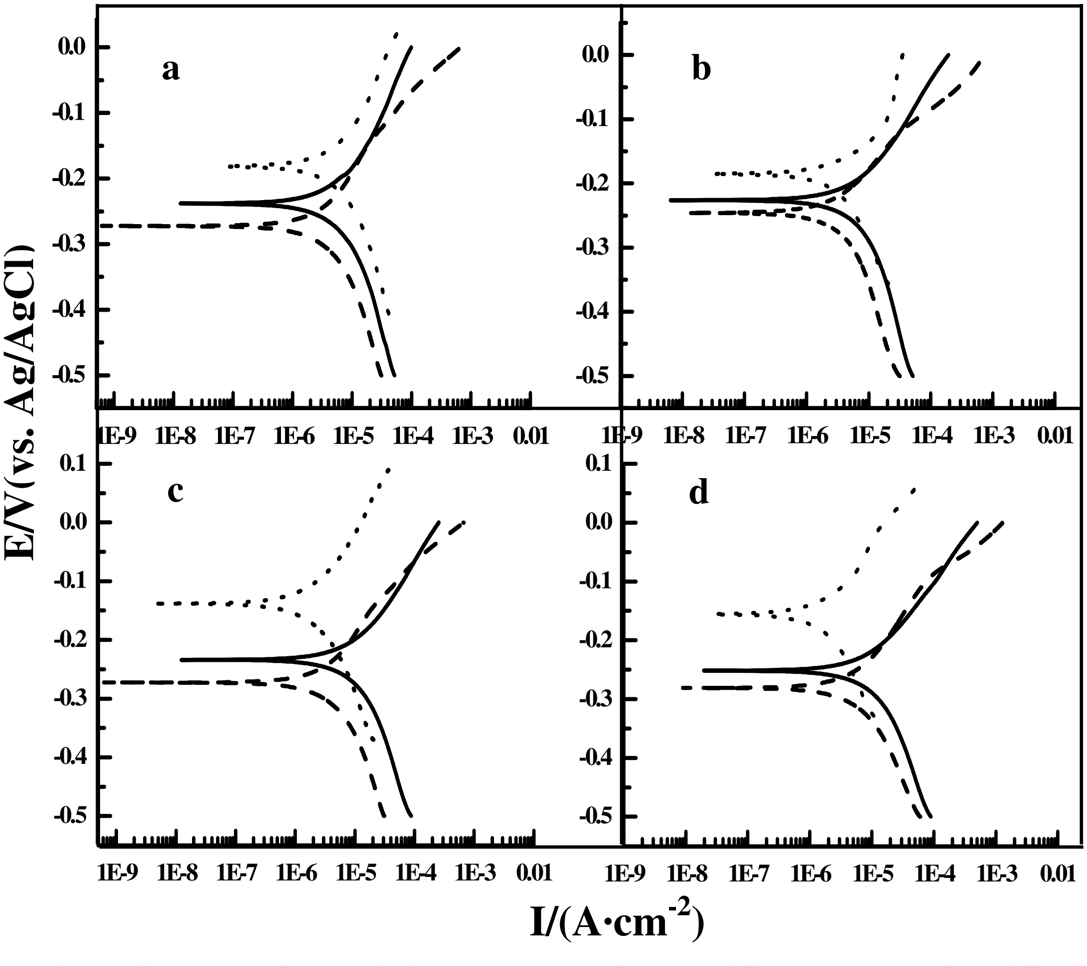

Figure 6.9 Tafel plots of the pristine and the surface-modified coupons after different exposure times: 7 days (a), 14 days (b), 21 days (c) and 35 days (d). Solid lines represent the experimental results of the pristine coupons in the *Pseudomonas* inoculated medium; dashed lines correspond to the experimental data of the surface-modified coupons in the *Pseudomonas* inoculated medium; dotted lines represent the experimental results of the pristine coupons in the sterile medium.

of the pristine and the modified coupons after exposure to the sterile and the *Pseudomonas* inoculated media for 7, 14, 21 and 35 days, respectively. It can be observed that the cathodic Tafel lines of the functionalized coupons all shift to lower current values as relative to the pristine coupons, while the anodic Tafel lines do not change appreciably, indicating that the coupled organic layer predominates as a cathodic inhibitor. This result is in good agreement with the previous reports on the quaternary ammonium salts acting as cathodic inhibitors (Elachouri et al., 1995). The Tafel plots were analyzed more quantitatively with the GPES software to obtain the values of the Tafel slopes (β_a and β_c), corrosion potentials (E_{corr}), corrosion current densities ($i_{corr.}$), inhibition efficiency (IE) and the corrosion rates, as shown in Table 6.2. It is obvious that E_{corr} of the modified coupons undergoes a slight active shift in comparison to the corresponding pristine coupon in the *Pseudomonas* inoculated medium throughout the exposure period. This phenomenon can probably be attributed to the decrease in the cathodic process of the surface-modified coupons in terms of the mixed potential theory. i_{corr} values of the modified coupons are smaller than those of the corresponding pristine coupons, indicating that the coupled organic layer has a desirable corrosion-inhibition activity as compared with the pristine oxide layer in the *Pseudomonas* inoculated medium. Therefore, the inhibition efficiency (IE), calculated with Equation 6.1, is as high as approximately 62% after 7 days of exposure, and still remains close to 50% after a long-term incubation. This result is consistent with the previous reports on the inhibition efficiency of quaternary ammonium salts (Ma et al., 2001; El Dahan et al., 1999). The relatively high inhibition efficiency throughout the exposure period confirms that the functionalized coupons have a desirable corrosion-inhibition activity to protect the underlying metallic substrate from the effect of microorganisms and other aggressive species. It is also important to note that the inhibition efficiency decreased gradually with exposure time due to the partial spalling of the coupled organic layer at some sites on the functionalized coupons. This result is consistent with the aforementioned SEM results.

Table 6.2 Analysis of Tafel plots of the pristine and the modified coupons after different exposure times in the sterile and the *Pseudomonas* inoculated media

Time (days)	**Medium**	**Samples**	**β_c ($mV\cdot dec^{-1}$)**	**β_a ($mV\cdot dec^{-1}$)**	**$E_{corr.}$ (V)**	**$i_{corr.}$ ($\mu A\cdot cm^{-2}$)**	**IE (%)**	**Corrosion rate ($mm\cdot y^{-1}$)**
7	sterile	pristine	-177	163	-0.176	5.18	-	0.059
	inoculated	pristine	-310	188	-0.225	8.58	61.66	0.097
		modified	-225	111	-0.244	3.29		0.037
14	sterile	pristine	-297	191	-0.164	4.05	-	0.043
	inoculated	pristine	-347	172	-0.226	10.35	59.53	0.116
		modified	-278	110	-0.230	4.19		0.048
21	sterile	pristine	-247	172	-0.152	2.61	-	0.030
	inoculated	pristine	-299	159	-0.221	12.87	50.27	0.146
		modified	-264	113	-0.252	6.40		0.073
35	sterile	pristine	-224	181	-0.154	2.18	-	0.025
	inoculated	pristine	-285	149	-0.240	13.31	48.99	0.151
		modified	-218	139	-0.271	6.79		0.077

For the pristine coupons exposed to the *Pseudomonas* inoculated medium, the corrosion rate obviously increases with exposure time and reaches as high as 0.15 $mm\cdot y^{-1}$ after 35 days of incubation (Table 6.2), indicating that the oxide layer on the metal surface gradually loses its protective properties under the attack of *Pseudomonas* bacteria. On the contrary, the corrosion rate of the pristine coupons gradually decreases with time in the sterile medium, and only remains 0.025 $mm\cdot y^{-1}$ after 35 days of exposure (Table 6.2), which is ascribed to the increase in the thickness and the compactness of the protective oxide films. It has reported that the high corrosion resistance of the oxide films mainly arises from the inner layer of cuprous oxide (Cu_2O) in a duplex oxide layers (Kato et al., 1980; Mansfeld et al., 1994). These results confirm that the corrosion rate of pristine coupons is accelerated by the effect of *Pseudomonas* bacteria. Another feature is a noticeable active shift of the values of E_{corr} for the pristine coupons in the *Pseudomonas* inoculated medium as compared with that in the sterile medium. This is mainly attributed to the acceleration of anodic reactions under the attack of *Pseudomonas* bacteria in light of the mixed potential theory.

EIS measurements were conducted on the pristine and the modified coupons after different exposure times in the sterile and the *Pseudomonas* inoculated medium. Nyquist plots and Bode phase angle plots of the pristine and the surface-modified coupons after different exposure times in the sterile and the *Pseudomonas* inoculated medium are shown in Figure 6.10. It can be seen that the diameters of the semicircles of the surface-modified coupons are somewhat larger than those of the corresponding pristine coupons in the *Pseudomonas* medium, indicative of the good corrosion resistance of the functionalized coupons. At the same time, the diameters of the semicircles of the pristine coupons in the sterile medium are also much larger than those in the *Pseudomonas* medium, implying an enhancement of corrosion of the pristine coupons in the presence of *Pseudomonas* bacteria (Figs. 6.10a, 6.10c, 6.10e and 6.10g). Another distinct feature is that the impedance loops of three types of coupons are depressed semicircles with their centers below the real axis. This phenomenon is known as the dispersing effect (Mansfeld, 1981). This effect may have resulted from the roughness of a solid metal electrode, the non-uniform reaction rate on the electrode surface (Xu et al., 1999); or the varying thickness and the composition of the coating (Schiller and Strunz, 2001). The surface heterogeneity results mainly from the oxide layer, the organic conditioning layers, or the biofilm formation on the pristine coupon surface; while it arises mainly from the rough organic layer on the surface-modified substrate surface.

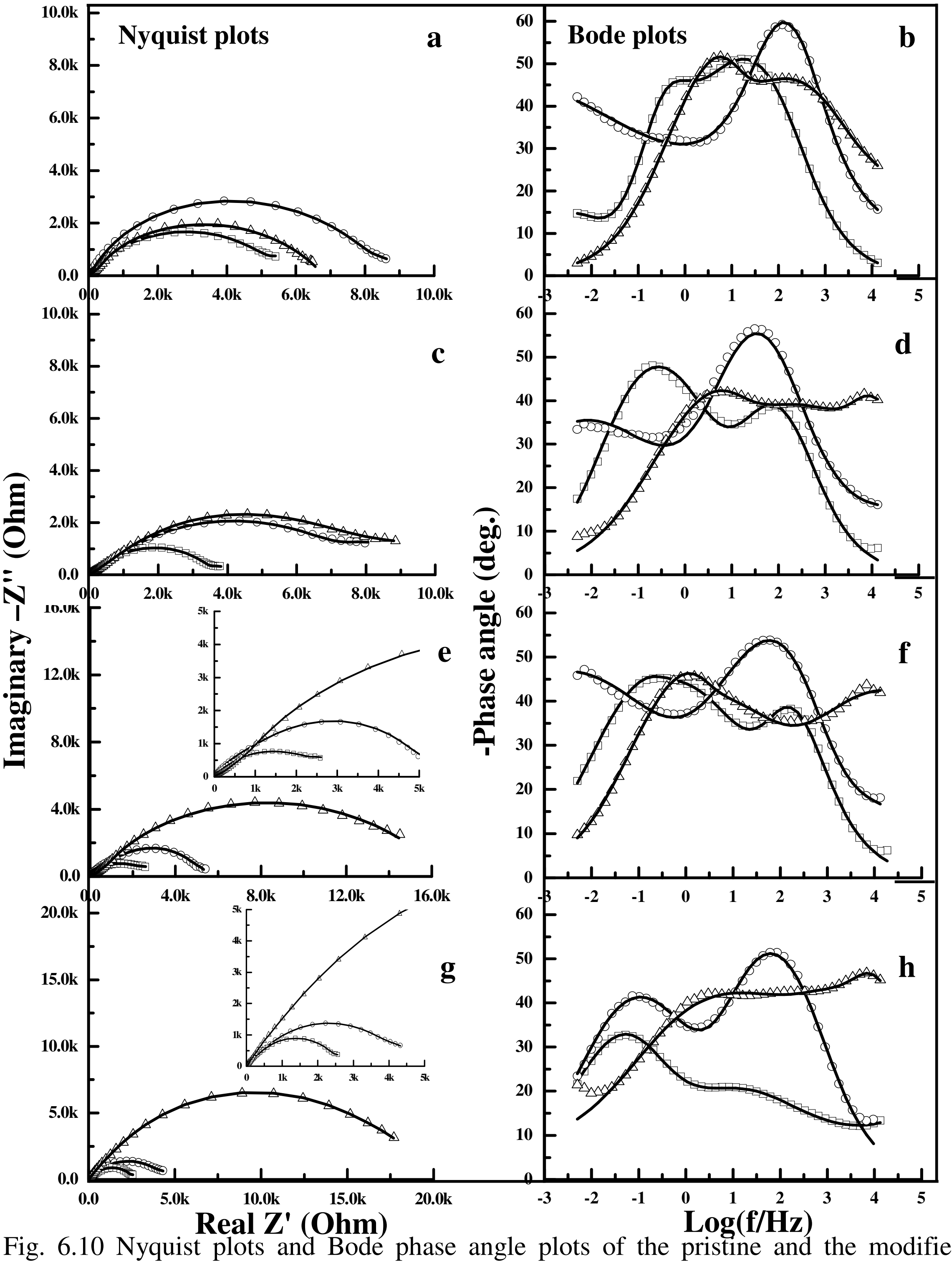

Fig. 6.10 Nyquist plots and Bode phase angle plots of the pristine and the modified coupons after different exposure times: 7 days (a, b), 14 days (c, d), 21 days (e, f) and 35 days (g, h). Open squares correspond to the EIS data of the pristine coupons in the *Pseudomonas* inoculated medium; open circles represent the EIS data of the surface-modified coupons in the *Pseudomonas* inoculated medium; open upper triangles correspond to the EIS data of the pristine coupons in the sterile medium. The solid lines show the fitted results based on the corresponding equivalent circuits.

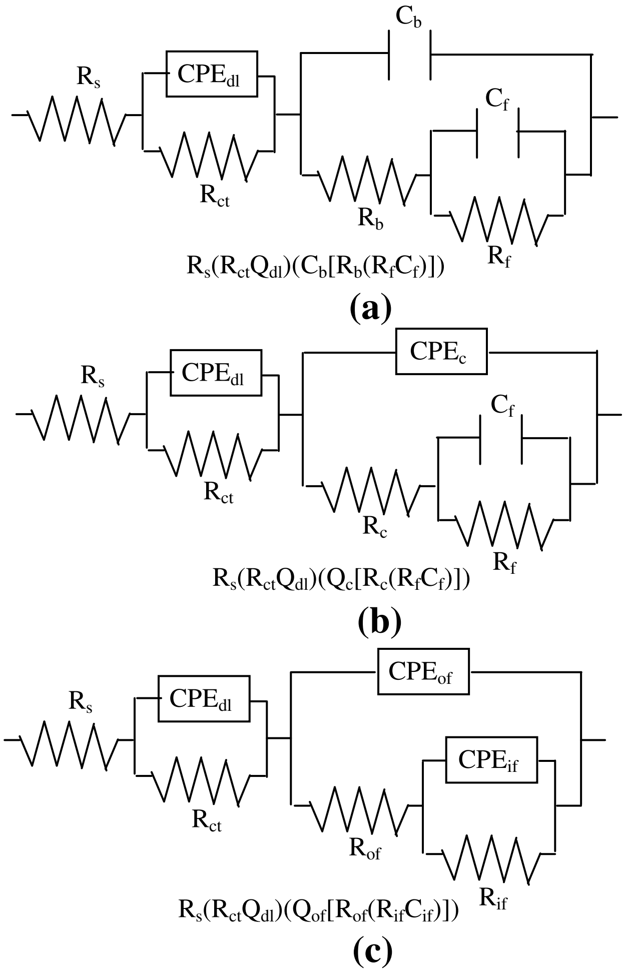

R_s, resistance of the electrolyte solution; Q_{dl}, constant phase element (CPE) of the electrical double layer (EDL); R_{ct}, charge transfer resistance of EDL; Q_c, CPE of the coupled organic layer; R_c, resistance of the coupled organic layer; C_b, capacitance of the biofilm; R_b, resistance of the biofilm; C_f, capacitance of the oxide film; R_f, resistance of the oxide film; Q_{of}, CPE of the outer surface film consisting of the outer oxide layer and the conditioning layer; R_{of}, resistance of the outer surface film; Q_{if}, CPE of the inner oxide film; R_{if}, resistance of the inner oxide film.

Figure 6.11 Equivalent electrical circuits used for fitting the EIS data of the pristine and the surface-modified coupons after different exposure times in the sterile and the *Pseudomonas* inoculated media.

As aforementioned in Section 3.3.1.2, EIS data are analyzed by a proper equivalent circuit. The phase maxima on Bode phase angle plots usually provide information on the relaxation time constants (Tait, 1994). The maxima located in the high frequency regions are commonly attributed to coatings or the compact oxide layers; the peak appearing at low frequency regions usually arises from the charge transfer process, the mass transfer (diffusion or migration) processes, or other relaxation processes taking place at the film/electrolyte interface (Mansfeld et al., 1993). Based on the characteristics of the Bode phase angle plots shown in Figure 6.10, equivalent circuits containing three time constants are used to fit the EIS data of the pristine and the surface-modified coupons. Figure 6.11 shows three equivalent circuits that can be satisfactorily used to fit the impedance data in this study. Table 6.3 show the The values of Chi-Square are all in the order of ~10^{-3} (Table 6.3), indicative of the good fitness of the EIS data with the proposed equivalent circuits.

Table 6.3 shows the parameters used for fitting the EIS data of the pristine and the modified coupons after different exposure times in the sterile and the *Pseudomonas* inoculated media. For the pristine coupons in the *Pseudomonas* inoculated medium, both the charge transfer resistance, R_{ct}, and the resistance of the oxide layer, R_f, decrease with exposure time, indicating an increase in the corrosion rate of the pristine coupons under the attack of aerobic *Pseudomonas*. The variation in the biofilm resistance, R_b, is consistent with the conclusion that the development of biofilm is a dynamic process (Videla, 1996). Whereas, the values of R_{ct} of the pristine coupons in the sterile medium appear to increase slightly with exposure time, accompanying with the dramatically increase in the values of the resistance of the inner oxide layers, R_{if}, indicative of the decrease in corrosion rate owing to the inhibition effect of the oxide films. The resistance of the outer oxide layers, R_{of}, which probably originates from a combination of the organic conditioning layers and the outer porous oxide layers, also increase with exposure time. It has been reported that a duplex oxide layer, consisting of an inner cuprous oxide (Cu_2O) and an outer cupric oxide (CuO) are rapidly formed on the Cu-Ni alloy surface after a short period of immersion in abiotic aerated seawater or artificial

Table 6.3 Parameters for fitting EIS spectra of the pristine and the modified coupons after different exposure periods in the sterile and the *Pseudomonas* inoculated media

Time (days)	**7**			**14**			**21**			**35**		
	sterile	inoculated		sterile	inoculated		sterile	inoculated		sterile	inoculated	
Parameters	pristine[a]	pristine[b]	modified[c]	pristine	pristine	modified	pristine	pristine	modified	pristine	pristine	modified
R_{sol} (Ω)	12.02	12.73	11.09	13.19	12.89	11.99	13.01	16.42	15.07	15.45	20.09	13.37
R_{ct} (kΩ)	5.68	5.20	6.37	6.34	3.51	6.06	7.31	2.53	3.93	6.92	2.34	3.83
Q_{EDL} $Y_{0*}e^{-5}(\Omega^{-1}s^{n})$	9.23	0.66	0.30	6.87	1.32	0.33	1.95	1.94	0.44	4.35	4.35	0.50
n_1	0.75	0.71	0.71	0.69	0.68	0.73	0.70	0.68	0.71	0.74	0.76	0.61
R_c (kΩ)	–	–	2.44	–	–	2.19	–	–	1.76	–	–	1.32
Q_c $Y_{0\,*}\,e^{-5}\,(\Omega^{-1}s^{n})$	–	–	4.13	–	–	5.81	–	–	5.16	–	–	3.29
n_2	–	–	0.87	–	–	0.84	–	–	0.83	–	–	0.76
R_b (kΩ)	–	0.026	–	–	0.122	–	–	0.064	–	–	0.195	–
C_b (mF)	–	2.40	–	–	0.78	–	–	1.18	–	–	0.56	–
R_f (kΩ)	–	1.35	0.59	–	0.44	0.55	–	0.57	0.51	–	0.52	0.41
C_f (mF)	–	73.2	55.4	–	70.9	57.4	–	85.9	44.8	–	140.8	56.6
R_{of} (Ω)	79.6	–	–	303.7	–	–	938.0	–	–	1240.4	–	–
Q_{of} $Y_{0\,*}\,e^{-4}\,(\Omega^{-1}s^{n})$	13.9	–	–	3.07	–	–	2.09	–	–	1.52	–	–
n_3	0.58	–	–	0.41	–	–	0.50	–	–	0.54	–	–
R_{if} (kΩ)	2.36	–	–	4.45	–	–	8.06	–	–	11.40	–	–
Q_{if} $Y_{0\,*}\,e^{-5}\,(\Omega^{-1}s^{n})$	1.06	–	–	8.23	–	–	2.14	–	–	4.64	–	–
n_4	0.81	–	–	0.74	–	–	0.77	–	–	0.77	–	–
$\sum\chi^{2}\,*\,e^{-3}$	3.90	6.78	0.35	1.13	5.52	2.00	4.98	4.24	9.80	5.21	6.35	1.46

a). Equivalent circuit (c) is used to fit the EIS data of the pristine coupons in the sterile medium;

b). Equivalent circuit (a) is used to fit the EIS data of the pristine coupons in the *Pseudomonas* inoculated medium;

c). Equivalent circuit (b) is used to fit the EIS data of the surface-modified coupons in the *Pseudomonas* inoculated medium.

seawter (Mansfeld et al., 1994; Kato et al., 1980). These results further confirm that the oxide layer formed on the copper alloys, consisting mainly of CuO and $Cu(OH)_2$, is susceptible to MIC under the attack of microorganisms. In the case of the surface-modified coupons in the *Pseudomonas* inoculated medium, the charge transfer resistance, R_{ct}, and the resistance of the coupled organic layer, R_c, remain almost unchanged during first 14 days. Thereafter they undergo an apparent decrease upon prolonging the exposure time. The eventual decrease in R_{ct} and R_c of the surface-modified coupons is ascribed to the spalling of the organic layer from the coupon surface. The fact that the R_{ct} of the surface-modified coupon is always larger than that of the corresponding pristine coupon is consistent with a lower corrosion rate for the modified coupon. Thus, the expected corrosion-inhibition property of the coupled organic layer has been ascertained. In the light of earlier studies (Ma et al., 2001; El Dahan et al., 1999; Vasudevan et al., 1995; Vaidya et al., 1999), the corrosion-inhibition activity of the coupled organic layer probably arises from both the self-assembled silane monolayer and the viologen layer. Furthermore, based on the electrochemical results, the thin layer of viologens, with its quaternary ammonium salt and pyridinium moieties, maybe played a significant role in rendering the good corrosion-inhibition property to the alloy coupons.

6.3.8 Stability of the modified SOM-CTS-DBV surface and its improvement

Based on the above results of surface analyses and electrochemical studies, it is appropriate to emphasize the significance of the stability and durability of the coupled organic layer on the surface-oxidized substrate for controlling MIC. As described earlier, the surface-functioned coupons exhibit excellent antibacterial and corrosion-inhibition properties at the initial stages of exposure (~14 days). Thereafter, the bactericidal and corrosion-inhibition abilities undergo an obvious deterioration due to partial spalling of the coupled organic layer. The mechanism of partial spalling of the coupled organic layer has not been fully understood. The following conditions might have contributed to its occurrence: (i) the bonding strength between the oxide layer and the underlying metal substrate might have weak end, (ii) the bonding strength between the CTS and the oxide layer might also have been weakened, and (iii) the compactness of the coupled organic layer, or the density of the immobilized viologens, might have been lower than initially expected.

To eliminate the factors that can probably cause the instability of the organic layer, further studies focused on using an argon-plasma pretreated metal surface instead of the oxidized metal surface as the substrate for immobilizing the organic layer are in progress. The argon-plasma pretreated substrate is believed to be able to circumvent the problem of the spalling of the grafted organic films, because various material substrates, including glass, fiber, paper and stainless steel (Cen et al., 2003; Lin et al., 2002; Ng et al., 2001; Liu et al., 2002; Dong et al., 2005), have been extensively functionalized with various polymers, and the grafted organic and polymer layers have been shown to remain unchanged under harsh environments.

6.3.9 Summary

In this chapter, modification of the surface-oxidized Cu-Ni alloy was achieved in three steps: (i) silanization of the substrate surface by a self-assembled silane coupling agent (CTS) to act as initiators, (ii) immobilization of pyridine groups by chemical reactions between methyl-chloride groups and 4,4'-bipyridine, (iii) the quaternization of the terminal pyridine groups into pyridinium groups by coupling with benzyl chloride. The successful build-up of the viologen layer was confirmed by XPS analysis and static contact angles. Effective inhibition of bacterial growth was achieved using the so-functionalized substrate during the initial exposure periods. On the other hand, electrochemical analysis results showed that the coupled organic layer had a desirable resistance to MIC during the initial 14-day incubation in the *Pseudomonas* inoculated medium. However, both the bactericidal activity and the corrosion-inhibition ability were reduced due to the occurrence of partial spalling of the coupled organic layer on the functionalized coupons after a long-term exposure. In addition, the oxidized layer formed on the surface of Cu-Ni alloy was found to be ineffective in protecting the substrate from the microbially induced corrosion, although it could dramatically decrease corrosion rate of the Cu-Ni alloy in the sterile medium.

CHAPTER 7

ANAEROBIC CORROSION OF 304 STAINLESS STEEL BY *DESULFOVIBRIO DESULFURICANS* BACTERIA AND ITS INHIBITION WITH TITANIUM OXIDE/BUTOXIDE COATINGS FROM SOL-GEL PROGRESS IN SIMULATED SEAWATER-BASED MEDIUM

7.1 Anaerobic corrosion of 304 SS in the biotic SSMB medium containing *D. desulfuricans* bacteria

7.1.1 General background

MIC of stainless steel can be considered in two categories: aerobic and anaerobic. For anaerobic bacteria, sulfate-reducing bacteria (SRB) are widely recognized to be the most destructive microorganisms in biocorrosion, and they are the principal causative organisms to induce the MIC of stainless steel (Jack et al., 1992, Beech, 2003, Hamilton, 1985, Lee et al., 1995, Coetser and Cloete, 2005, Videla, 2000; Dexter et al., 1991). SRB are abundant in natural habitats, such as marine and fresh water sediments or sludges, and play a key role in the biogeochemical sulfur cycle (Little et al., 1999, 2000). The cathodic depolarization theory (Von wolzogen Kuehr and Van der Vlugt, 1934), the production of aggressive sulfide ions (Lee et al., 1995), the binding of metal ions by EPS (Beech et al., 1998), and the formation of aggressive ferrous sulfide (King and Wakerley, 1973) are the main mechanisms used for interpreting the involvement of SRB in the corrosion processes of stainless steels.

The purpose of Section 7.1 is to investigate the effect of a marine anaerobic sulfate-reducing bacterium, *Desulfovibrio desulfuricans* (ATCC, No 27774), on the corrosion of 304 SS in a simulated seawater-based modified Barr's medium as a function of exposure time using microscopy techniques. AFM was used to monitor the development of biofilms on the coupon surface. SEM was used to assess the degree of corrosion damage after the removal of biofilms at various stages of exposure. XPS was used to evaluate the nature of corrosion products on the coupon surface. For comparison purpose, the 304 SS coupons were also exposed to the same SSMB medium without the *D. desulfuricans* bacteria under the same conditions.

7.1.2 Experimental section

7.1.2.1 Metal samples preparation

The SS 304 coupons were prepared using procedures similarly to those described in Section 3.2.1 of Chapter 3.

7.1.2.2 Medium preparation

All tests were performed using a simulated seawater-based Modified Baar's medium (SSMB medium). Each liter of the medium consisted of 23.476 g NaCl, 3.917 g Na_2SO_4, 0.192 g $NaHCO_3$, 0.664 g KCl, 0.096 g KBr, 10.61 g $MgCl_2 \cdot 6H_2O$, 1.469 g $CaCl_2 \cdot 6H_2O$, 0.026 g H_3BO_3, 0.04 g $SrCl_2 \cdot 6H_2O$, 0.41 g $MgSO_4 \cdot 7H_2O$, 0.1 g NH_4Cl, 0.1 g $CaSO_4$, 0.05 g K_2HPO_4, 0.5 g tri-sodium citrate, 3.5 g sodium lactate, 1g yeast extract. The pH was adjusted to 7.5 ± 0.1 using a 5 M NaOH solution, and sterilized by autoclaving at 121^{o}C for 20 min at a pressure of15 psi. After cooling, 5 ml of the $(NH_4)_2Fe(SO_4)_2$ solution (containing 0.1 g $(NH_4)_2Fe(SO_4)_2$), sterilized by filtration using a syringe filter (0.45 μm in pore size), was introduced to 1000 ml of the experimental medium to act as an indicator and the iron trace element for the growth of *D. desulfuricans.*

7.1.2.3 Microorganisms cultivation and inoculation

A gram-negative anaerobic sulfate-reducing bacterium, *D. desulfuricans* (ATCC, No. 27774), was obtained from American Type Culture Collection (Manassas, VA, USA). A new culture was resuscitated from a freeze-dried ampoule, and subcultured twice in 5 ml of the Modified Baar's (MB) medium before use. The composition of the MB medium is as follows (per liter DI water): $MgSO_4 \cdot 7H_2O$ 4.1 g, NH_4Cl 1.0 g, $CaSO_4$ 1.0 g, K_2HPO_4 0.05 g, tri-sodium citrate 5 g, sodium lactate 3.5 g, yeast extract 1.0 g and $(NH_4)_2$ $FeSO_4 \cdot 6H_2O$ 1.38 g. The resuscitated bacteria were further cultured in a 125 ml

Erlenmeyer flask containing 20 ml of the fresh MB medium for 3 days at 30°C. All the bacterial cultivations were performed in an anaerobic chamber (Bactron IV Shel lab anaerobic environmental chamber, Sheldon Manufacturing, Inc., Cornelius, OR, USA), and maintained under an atmosphere containing 5% H_2, 5% CO_2 and 90% N_2. The 20 ml of 3-day-old *D. desulfuricans* bacterium were kept in a -20°C refrigerator to serve as the bacterial seedings in all the experiments to ensure its purity.

For the inoculation medium, a 1 ml aliquot of the 3-day-old *D. desulfuricans* was introduced into 1000 ml of the SSMB medium in each Duran bottle (2.5 L) and incubated at 30°C in the anaerobic chamber. The bacterial cell number was determined using the most probable number (MPN) method (3-tube) as described in the literature (Oblinger et al., 1975). At the same time, the metal coupons, which was sterilized in 70% ethanol solution for 8 h and dried by purging with a stream of purified N_2, were aseptically introduced into the *D. desulfuricans* inoculated medium for the assay of the corrosion behavior.

7.1.2.4 Determination of viable SRB number and sulfide concentration

The growth curve of *D. desulfuricans* was determined by monitoring the active SRB number in the *D. desulfuricans* inoculated SSMB medium after 0.5, 1, 2, 3, 5, 7, 10, 14, 17 and 21 days using the 3-tube MPN method. Simultaneously, the pH value of the bulk solution were monitored with high-precision pH meters (780 pH meter, Metrohm, Switz.), and the concentration of the biogenic sulfide ions was detected with the polarographic method using the 757 Voltammetry Computrace (Metrohm, Switz.). This method has been described in detail in the VA application bulletin (No. 199/3e). Briefly, 10 mL of diluted sodium hydroxide solution (0.1 M) was transferred into a measuring vessel, and purged for 5 min with pure N_2, followed by addition of 10 mL of the diluted sample solution, and mixed by purging with pure N_2. The polarogram was recorded with the hanging mercury drop electrode (HMDE) method. The sulfide concentration was determined by standard addition. All the reagents used in the polarogramic method were of ultrapure grade. Both the SRB enumeration and the sulfide determination were repeated twice for each incubation time. In comparison with the commonly-used Methylene Blue method, as described by American Public Health Association (APHA) (1992), the novel polarographic method used in this study has the several advantages in detecting the sulfide concentration: i) all measurements are performed under anaerobic conditions, hence the unwanted depletion of sulfide by oxygen is avoided, ii) the measured concentration limit can be down to ppb level, and iii) the operation is relatively simple.

7.1.2.5 Surface characterization

The preparation and measurement of the coupons with biofilms were performed by AFM using procedures similar to those described in Section 4.2.4 of Chapter 4. The coupons after the removal of biofilm were imaged by SEM using procedures as those described Section 3.2.5 of Chapter 3. The nature of surface film was characterized by XPS using procedures similarly as those described Section 4.2.5 of Chapter 4.

7.1.3 Results and discussion

7.1.3.1 Growth process of *D.desulfuricans* and the determination of pH value and sulfide concentration

SRB have been widely recognized to promote corrosion as a consequence of the formation of adherent biofilms on the substrate surface, as well as the generation of abundant corrosive hydrogen sulfide from their activities (Borenstein, 1994, Hamilton, 1985, Lee et al., 1995). The viable SRB cell density, the biogenic sulfide concentration and pH value in the bulk solution are therefore of great significance in interpreting the effect of *D. desulfuricans* on the corrosion behavior of 304 SS coupons.

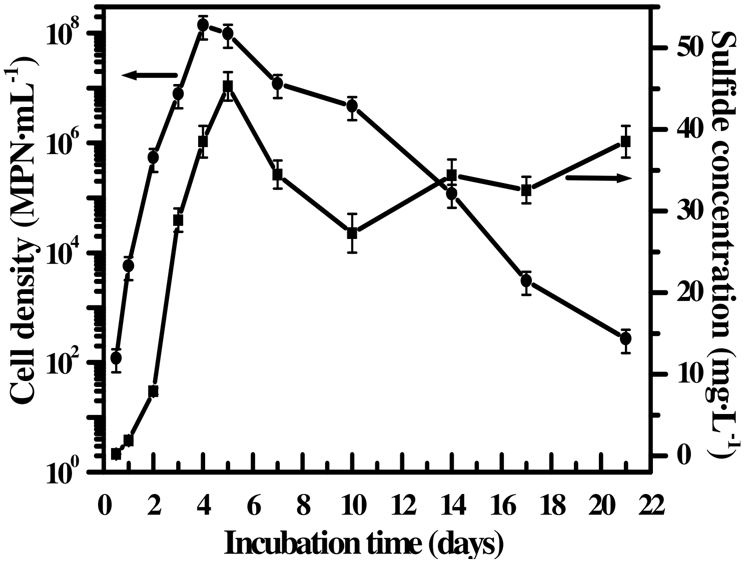

Figure 7.1 The growth curve of *D. desulfuricans* and the concentration of the biogenic sulfide in the SSMB medium as a function of incubation times.

Figure 7.1 illustrates the growing process of *D. desulfuricans* in 1000 mL of SSMB medium, which has been inoculated by 1 mL of 3-day-old SRB seeds. The results indicate that the growing process of SRB can be divided into three stages. The initial 4 days are termed the exponential phase. During this phase, the number of viable *D. desulfuricans* cells increase rapidly and achieve the maximum value after 4 days of incubation. Thereafter, the growing process of *D. desulfuricans* enters the stationary phase (from 4 to 10 days). The active *D. desulfuricans* remains at a relatively high concentration (around 10^8 MPN·mL^{-1}) in this stage. After 10 days, the number of viable *D. desulfuricans* decreases rapidly since the death rate of the bacterial cells now exceeds it regeneration rate. This stage is, thus, called the death phase.

During the growing process of *D. desulfuricans*, hydrogen sulfide (H_2S) is generated concomitantly as the metabolic product in the SSMB medium. Figure 7.1 also shows the concentration of biogenic sulfide ions in the bulk solution as a function of exposure time. Interestingly, the concentration of biogenic sulfide ions is related to the number of the viable bacterial cells in the exponential phase. The concentration of sulfide ions increases rapidly to around 45 $mg \cdot L^{-1}$ after 5 days of incubation. Thereafter, the concentration of biogenic sulfide ions becomes independent of the number of the active bacterial cells, and fluctuates with time in a range of about 30 and 40 $mg \cdot L^{-1}$. It has been reported that hydrogen sulfide is a very strong reducing agent and also inhibits the growth of most microorganisms. SRB, with a viable bacterial density of 10^3 to 10^{10} $MPN \cdot mL^{-1}$, can produce sulfide ions with concentrations ranging from 0.1 to 10 mM (about 3.2 to 320 ppm) (Seed, 1990). In this study, the concentration of sulfide ions produced by the SRB strain *D. desulfuricans* is in ranges from 0.3 to 45 ppm, as the viable bacterial density is within a range of 10^2 to 10^8 $MPN \cdot mL^{-1}$. In general, about one third of the total sulfide produced by SRB remains as the undissociated acid and about two thirds as the HS^- ions.

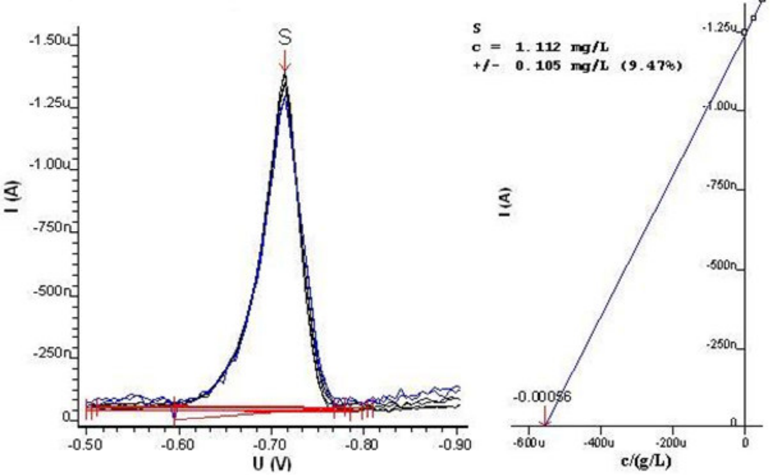

Determination of sulfide with HMDE. AB199 method

Figure 7.2 A typical polarogram and the corresponding internal standard curve illustrating the determination of the concentration of biogenic sulfide ions in the SSMB medium

The undissociated H_2S in solution will be in dynamic equilibrium at the water/air interface with H_2S gas (Gibson, 1990). A typical polarogram and the corresponding internal standard curve are shown in Figure 7.2 to illustrate the determination process of biogenic sulfide ions in the biotic SSMB medium.

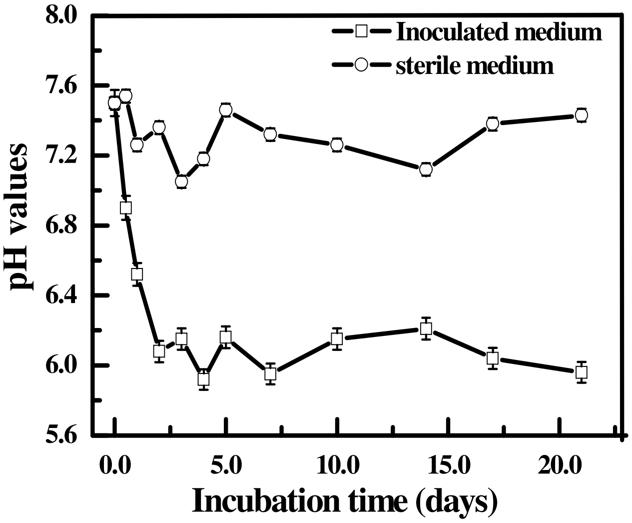

Figure 7.3 pH value of the sterile and the *D. desulfuricans* inoculated SSMB medium as a function of incubation time

Figure 7.3 shows the change in pH value of the sterile and the *D. desulfuricans* inoculated SSMB media with incubation time. It is clearly observed that the pH value of the sterile SSMB medium remains almost unchanged, fluctuating with incubation time within a narrow range of about 7.6 to around 7.2. On the contrary, the pH value of the biotic SSMB medium undergoes a rapidly decrease to about 5.8 during the exponential phase, which appears to be dependant of the concentration of biogenic sulfide ions. Thereafter, the change in pH value of the biotic medium shows a similar trend to that of sulfide ions, fluctuating at a lower value around 5.9.

7.1.3.2 AFM images of bacteria and biofilm on the coupon surface

Figure 7.4a shows a typical image of an anaerobic *D. desulfuricans* cell attached on the SS coupon surface after exposure to the biotic SSMB medium for 7 days. The dimensions of the cell are 2.97×0.74×0.39 μm (length × width × depth). The shape of the bacteria, as well as corrosion products, is clearly visible. EPS secreted by SRB facilitates irreversible cell attachment leading to colonization on the coupon surface. As cells multiply in the nutrient-rich SSMB medium, they grow and aggregate to form the bacterial clusters as shown in Figure 7.4b. The activity of *D. desulfuricans* usually leads to the localized corrosion of 304 SS. Figure 7.4c illustrates the pits generated on the coupons in the biotic SSMB medium after 14 days of exposure. The pits induced by the synergistic effect of biofilms and biogenic sulfide ions will be discussed in detail in the following SEM studies.

Under anaerobic conditions, biofilms are formed on the coupon surface in the absence of dissolved oxygen within days in the SSMB medium sustaining the SRB culture. The biofilm consists of clusters of microbial cells, EPS and interstitial voids (Xu et al., 2002). AFM images of the coupons with a biofilm of *D. desulfuricans* over different periods of exposure are shown as Figure 7.5. Some bacterial cells, either individually or in micro-colonies, are discernible on the coupon surface after 3 days of exposure (Fig. 7.5a). The initial attachment of bacteria to a solid surface is a crucial step in the process of biofilm formation (Fang et al., 2000). Bacterial cells begin to form patchy biofilm or large-size bacterial clusters after 7 days of exposure (Fig. 7.5b). It has been estimated that bacterial cells occupy only 5-25% of the biofilm volume (Caldwell et al., 1992). Upon prolonging the exposure time, the biofilms increase in coverage, thickness and heterogeneity (Fig. 7.5c, 7.5d and 7.5e). It has been widely accepted that the heterogeneous biofilm acts as a barrier to diffusion, leading to the generation of pH, sulfide and chloride concentration gradients, and thus initiating the pitting corrosion (Lee and Beer, 1995). The accumulation of bacterial cells, EPS or corrosion products on the coupon surface virtually results in the integration of corrosion deposits and bacterial cells, leading to the formation of a thick and porous layer, as shown in Figure 7.5e.

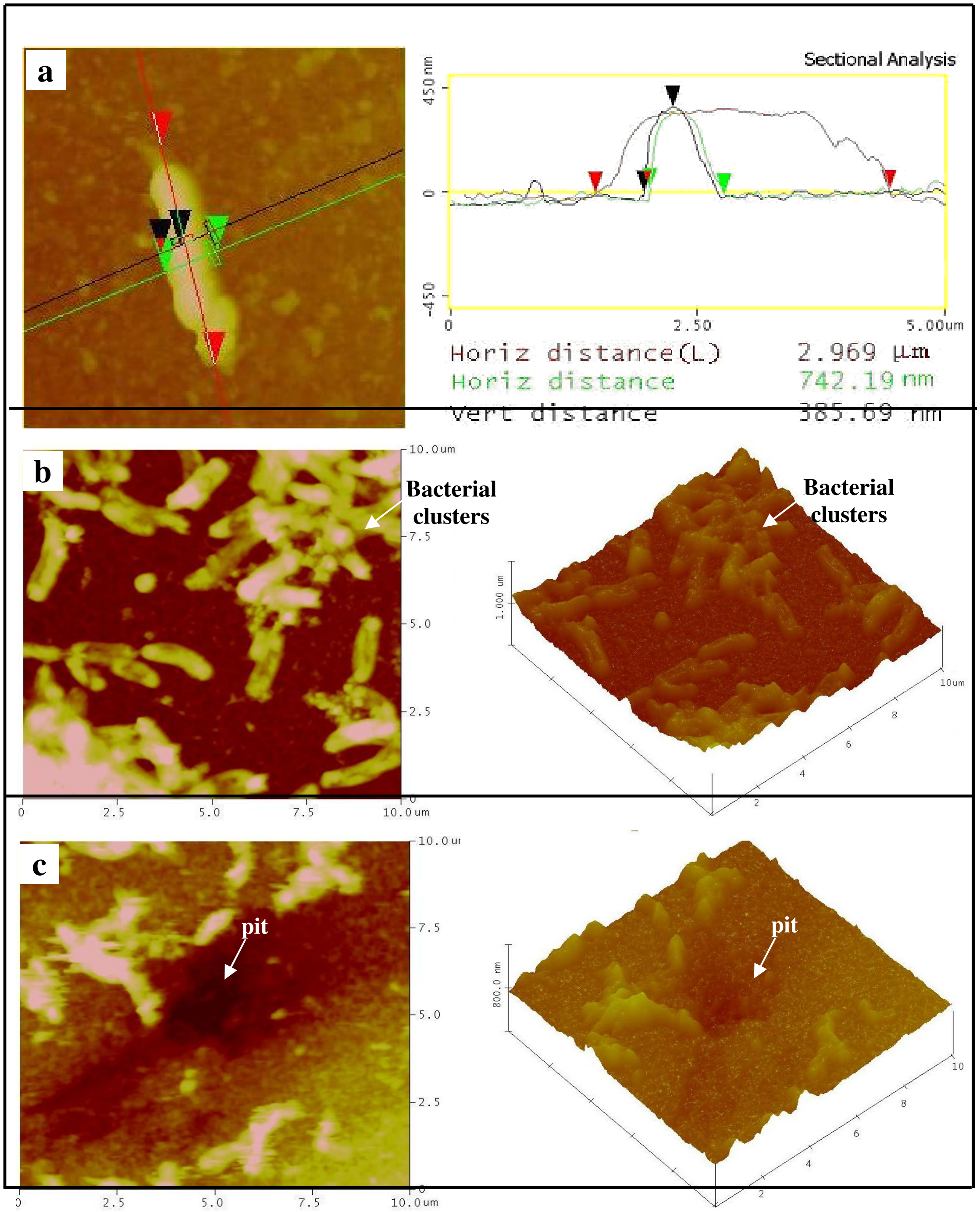

Figure 7.4 AFM images of (a) a single SRB cell, (b) SRB clusters on the 7-day-exposed coupons, and (c) a corrosion pit on the coupon surface after 14 days of exposure.

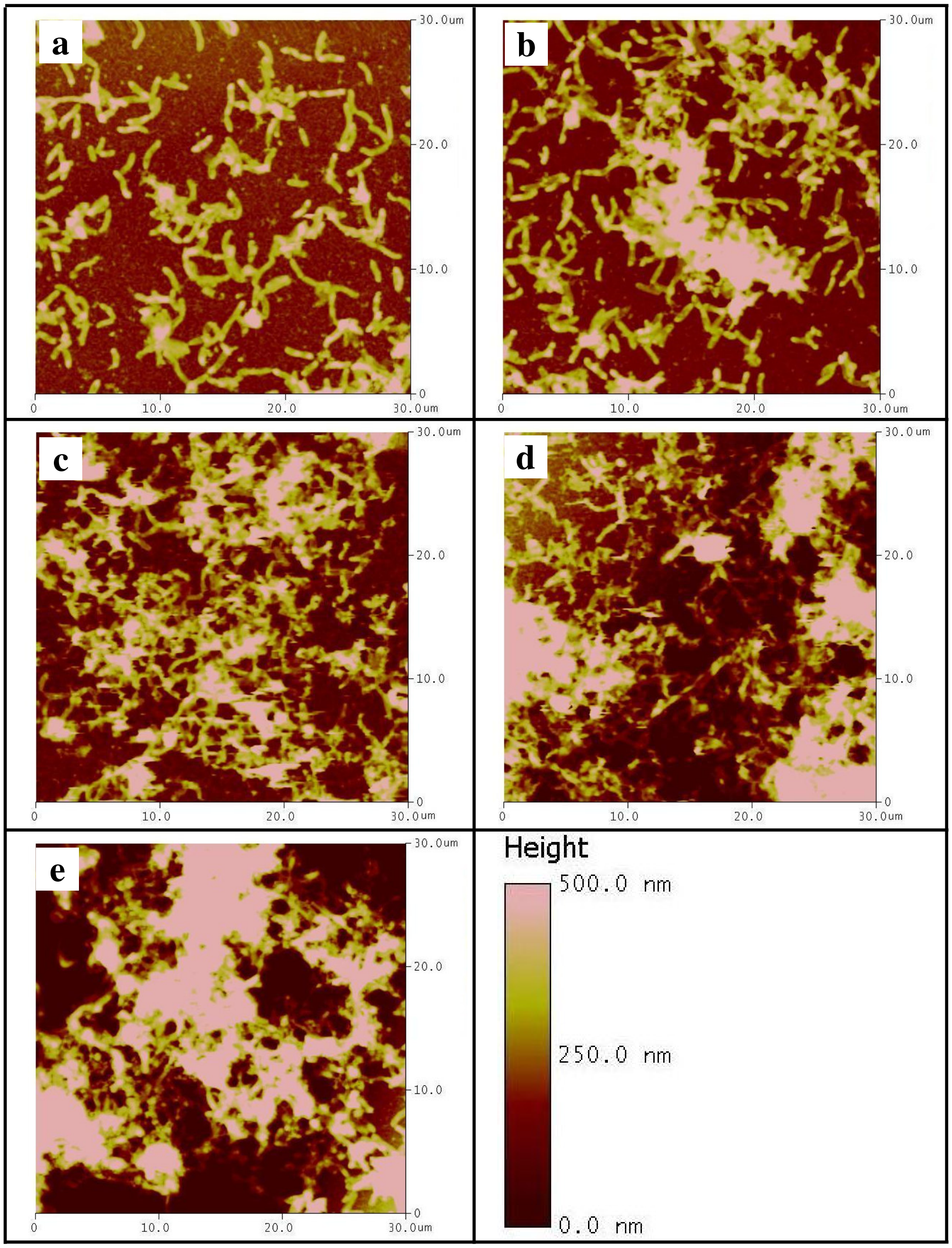

Figure 7.5 Representative AFM images of 304 SS coupons with *D. desulfuricans* biofilm after (a) 3 days, (b) 7 days, (c) 14 days, (d) 28 days and (e) 42 days of exposure in the *D. desulfuricans* inoculated SSMB medium.

Figure 7.6 shows the AFM images of the control coupons after various exposure times in the sterile SSMB medium. No evidence of pitting corrosion can be observed on the coupon surface, indicating that the coupon surface remains stable in the absence of *D. desulfuricans* bacteria (Figs. 7.6a, 7.6b and 7.6c).

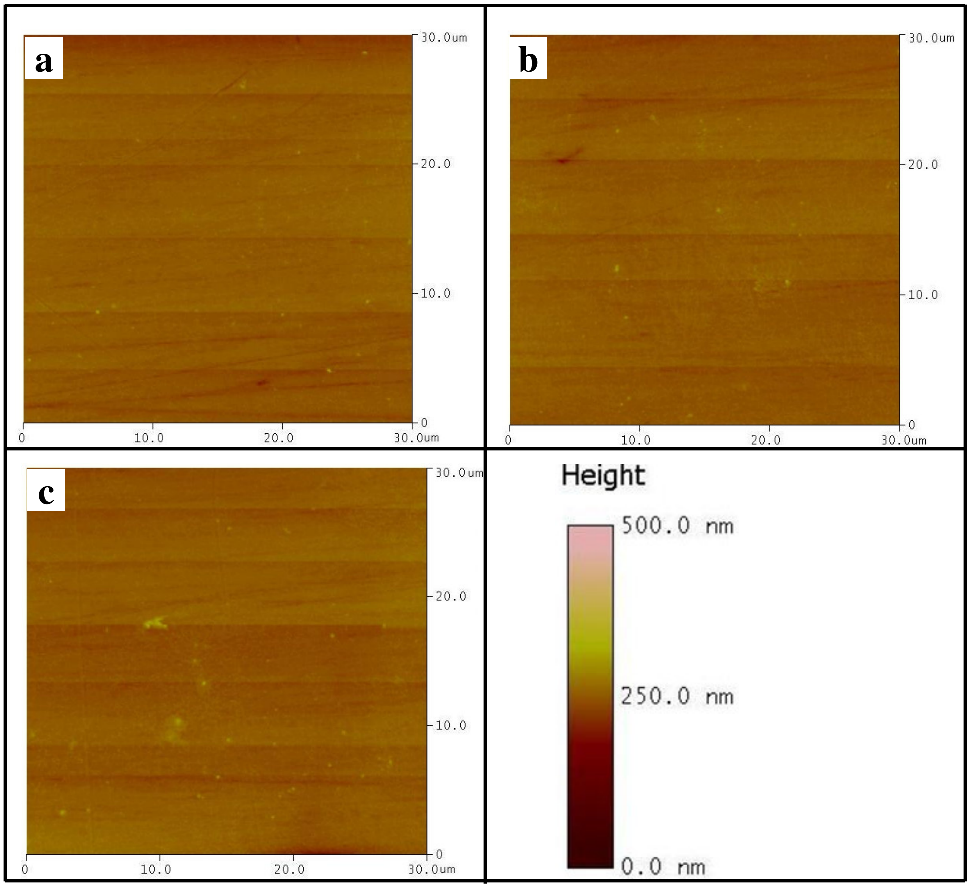

Figure 7.6 AFM images of 304 SS coupons surface after (a) 3 days, (b) 14 days and (c) 28 days of exposure in the sterile SSMB medium.

7.1.3.3 Evaluation of localized corrosion under the tubercles by SEM-EDX

Figure 7.7 shows the typical SEM images of tubercles and underneath corrosion damages after various exposure periods in the *D. desulfuricans* inoculated SSMB medium. It has been reported that tubercles result mainly from nonuniform accumulation of bacterial cells and corrosion products, and are usually associated with localized corrosion, such as pitting or crevice corrosion (Borenstein, 1994). As shown in Figures 7.7a and 7.7c, tubercles consist of the elliptical black corrosion products (probably iron

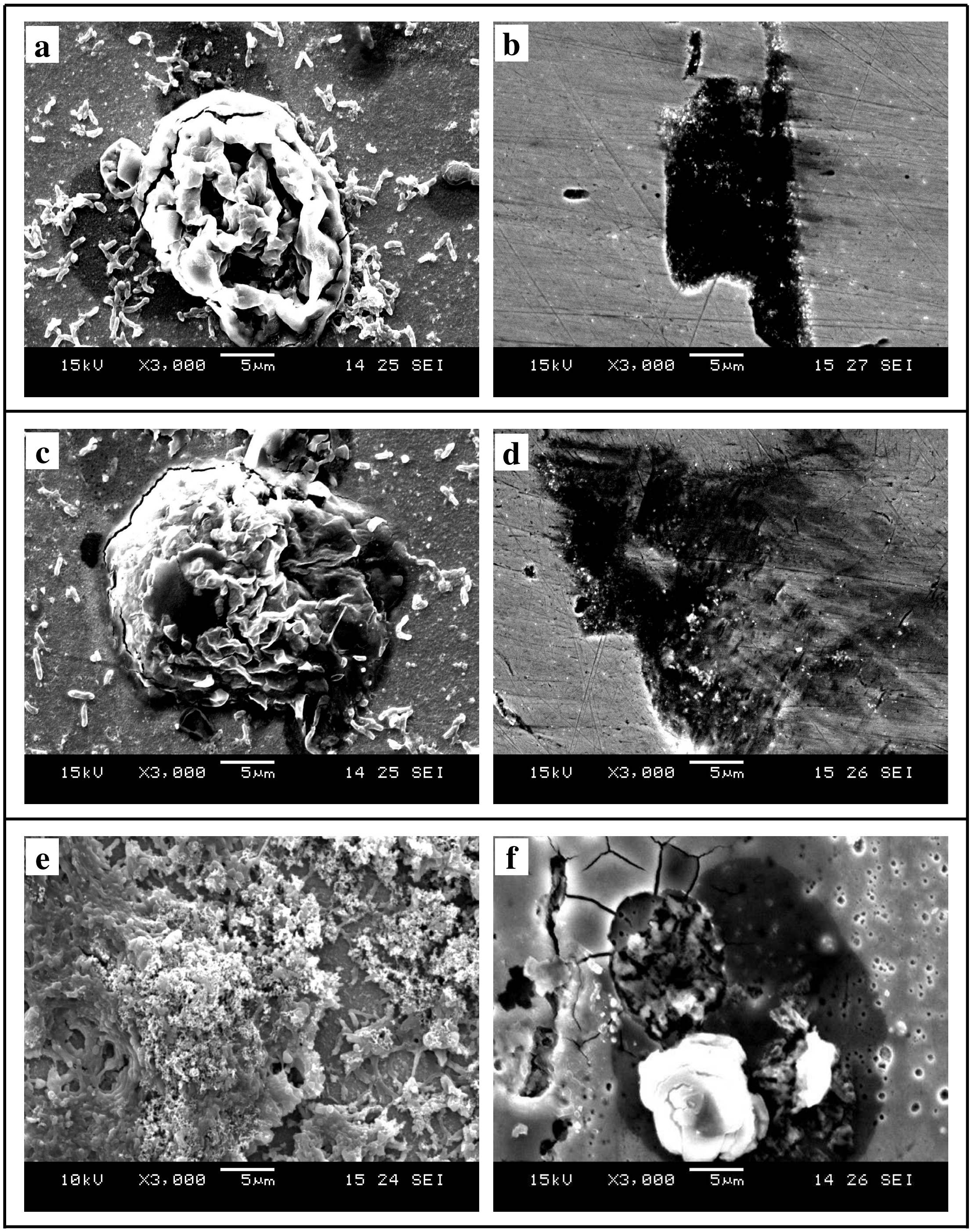

Figure 7.7 Representative SEM images of tubercles and underneath localized corrosion on the coupon surface after (a, b) 14 days, (c, d) 21 days and (e, f) 42 days of exposure in the *D. desulfuricans* inoculated SSMB medium.

sulfide) with embedded bacterial cells. The combination of bacterial cells with the corrosion deposits usually results in a porous and non-protective corrosion product layers.

It has been reported that the area underneath tubercles acts as the anode under anaerobic condition, while the region around tubercles serves as the cathode (Little, et al., 1992). If the cathodic and anodic sites are separated from one another, the pH at the anode will decrease and that at the cathode will increase. The pH within the anodic pit depends on specific hydrolysis reactions (Hoar, 1947). Lowest pH value are expected for alloys containing chromium and molybdenum, since Cl^- ions from the electrolyte will migrate to the anode to neutralize any build-up of charges (Hoar, 1947), forming heavy metal chlorides that are extremely corrosive. Under these circumstances, pitting corrosion is induced by the synergistic interactions of bacterial cells, biogenic sulfide anions and local acidity created by metallic chloride. Hence, large-size pits are clearly visible on the coupon surface (Figs. 7.7b and 7.7d). In addition, extensive micro-pits are also observed on the coupon surface after 42 days of exposure (Fig. 7.7f). Pitting corrosion is a complex but important problem, which is main cause of many corrosion failure (Sukamto et al., 1995). Majority of biocorrosion is seen as pitting type corrosion, the microbes at the metal/biofilm interface create conditions in which, incipient pitting leads to localized corrosion driven predominantly by microbiological activities (Rao et al., 2005). For the SRB-induced corrosion, Sanders and Hamilton (1986) defined two distinct forms: (i) pitting caused by SRB growing in the biofilm on metal surfaces, and (ii) sulfide-induced stress corrosion cracking and hydrogen-induced cracking or blistering caused by hydrogen permeation under a high concentration of dissolved sulfide.

Coupling with the SEM observation, EDX spectra were also recorded on the tubercle sites for the 21-day-exposed coupons. As shown in Figure 7.8, the corrosion deposits constitute mainly of iron and chromium sulfide compounds. In addition, the ingress of chloride ions can also be clearly observed inside the pits (Fig. 7.8a). The physical and chemical properties of sulfide products have been reported to affect the corrosion rate of the metal coupons due to the catalytic effect on the oxygen reduction reaction (Syrett, 1981). The iron and chromium sulfide compound can play a significant role in the SRB-induced corrosion (Lee et al., 1995). A galvanic cell is established with steel behaving as the anode and the solution/iron sulfide interface as the cathode.

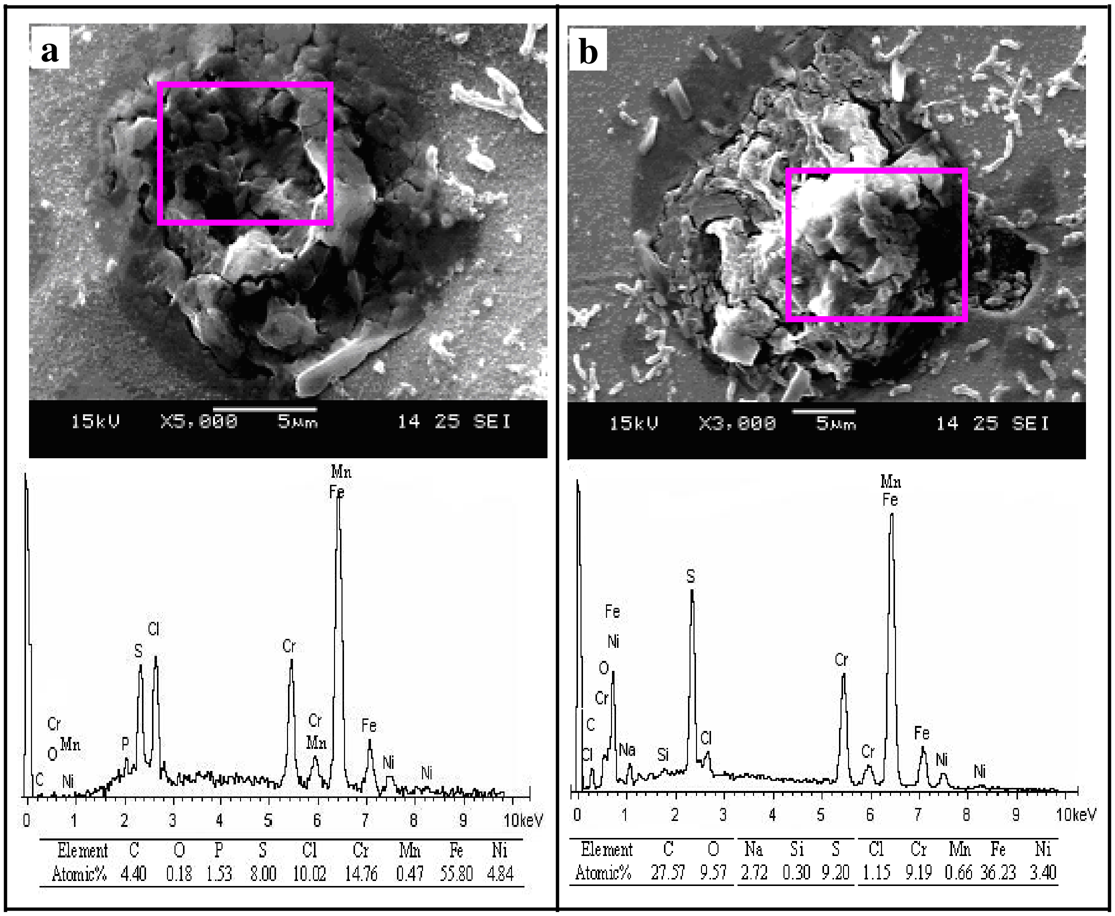

Element	C	O	P	S	Cl	Cr	Mn	Fe	Ni
Atomic%	4.40	0.18	1.53	8.00	10.02	14.76	0.47	55.80	4.84

Element	C	O	Na	Si	S	Cl	Cr	Mn	Fe	Ni
Atomic%	27.57	9.57	2.72	0.30	9.20	1.15	9.19	0.66	36.23	3.40

Figure 7.8 Representative SEM images of different tubercles on the coupon surface and the corresponding EDX spectra after (a, b) 21 days of exposure in the *D. desulfuricans* inoculated SSMB medium

7.1.3.4 Characterizing the nature of sulfide films with XPS

The nature and structure of sulfide films play significant role in the corrosion of stainless steel. It has been reported that thin adherent films of iron sulfide are protective, whereas bulky and loosely adherent precipitates enhance corrosion rates (Videla, 1996). Lee and Characklis (1993) attributed the acceleration of corrosion to the synergistic effect of biogenic sulfide and other aggressive anions, such as chloride within microbial consortia. However, little attention has been paid to the nature of the iron sulfides due to a variety of iron sulfides being detected in a biotic system containing SRB. To clarify the composition of the biotic sulfide precipitates on the coupon surface, as well to understand the evolution of sulfide films with time, XPS was used to characterize the precipitated biogenic sulfide layers after exposure to the biotic SSMB medium for 3, 14 and 42 days.

Figure 7.9 shows the high-resolution S 2p, Fe 2p and Cr 2p core-level spectra of sulfide films formed on the coupon surface after various exposure times in the *D. desulfuricans* inoculated SSMB medium The S 2p core-level spectra are fitted with doublets that characterize the spin-orbital splitting of the S $2p_{1/2}$ and S $2p_{3/2}$ peaks. Thereby, the S 2p core-level spectra are all curve-fitted into four doublets with $2p_{3/2}$ components at the BEs of around 161.1, 163.2, 165.3 and 166.9 eV (Figs. 7.9a, 7.9c and 7.9e). The peak component at the BE of 161.0 eV is attributed to the monosulfides (Wagner et al., 1992), the one at the BE of 163.2 eV is due to disulfides (Pratt et al., 1996), and the peak component appearing at the BE of 165.2 eV is attributed to S^0 (Mullet et al., 2000). In addition, the peak component at the BE of 166.9 eV is probably due to sulfate, sulfite or organic sulfur (Xu, 2001). The relative abundance of each component can be quantitatively calculated on the basis of their area ratios in the S 2p spectra, as shown in Table 7.1. The distinguishing feature is gradual decrease in the relative abundance of monosulfides (mainly including pyrrhotie ($Fe_{1-x}S$), mackinawite ($Fe_{1+x}S$) and Cr_2S_3) with exposure time, accompanied by the apparent increase in the relative amount of disulfide (mainly pyrite).

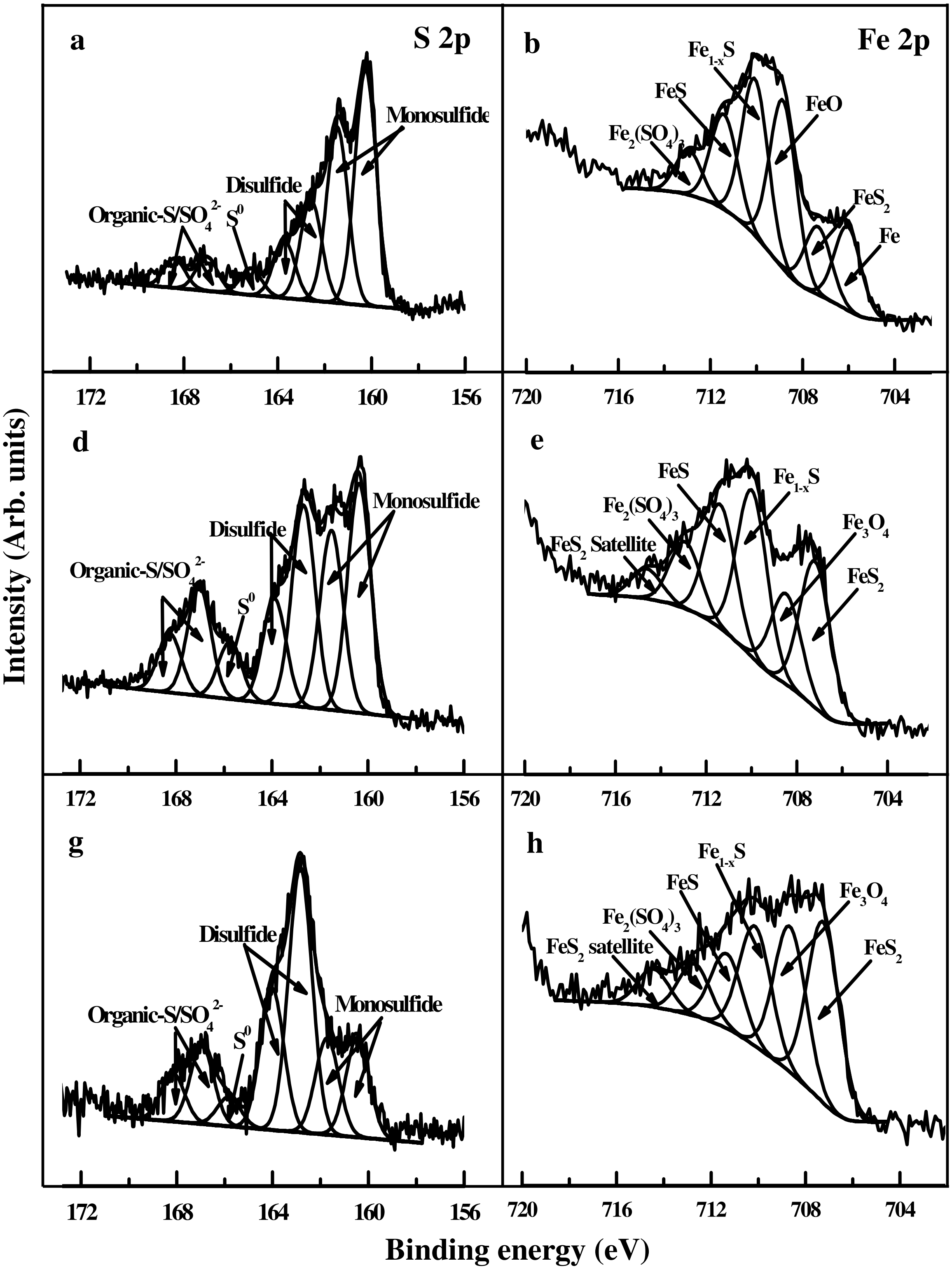

a
S 2p
Monosulfide
Disulfide
Organic-S/SO$_4^{2-}$
S^0
b
Fe 2p
Fe$_{1-x}$S
FeS
FeO
Fe$_2$(SO$_4$)$_3$
FeS$_2$
Fe
d
Monosulfide
Disulfide
Organic-S/SO$_4^{2-}$
S^0
e
FeS
Fe$_{1-x}$S
Fe$_2$(SO$_4$)$_3$
Fe$_3$O$_4$
FeS$_2$ Satellite
FeS$_2$
g
Disulfide
Monosulfide
Organic-S/SO$_4^{2-}$
S^0
h
Fe$_{1-x}$S
FeS
Fe$_3$O$_4$
Fe$_2$(SO$_4$)$_3$
FeS$_2$ satellite
FeS$_2$
172
168
164
160
156
720
716
712
708
704
Intensity (Arb. units)
Binding energy (eV)

(Continued)

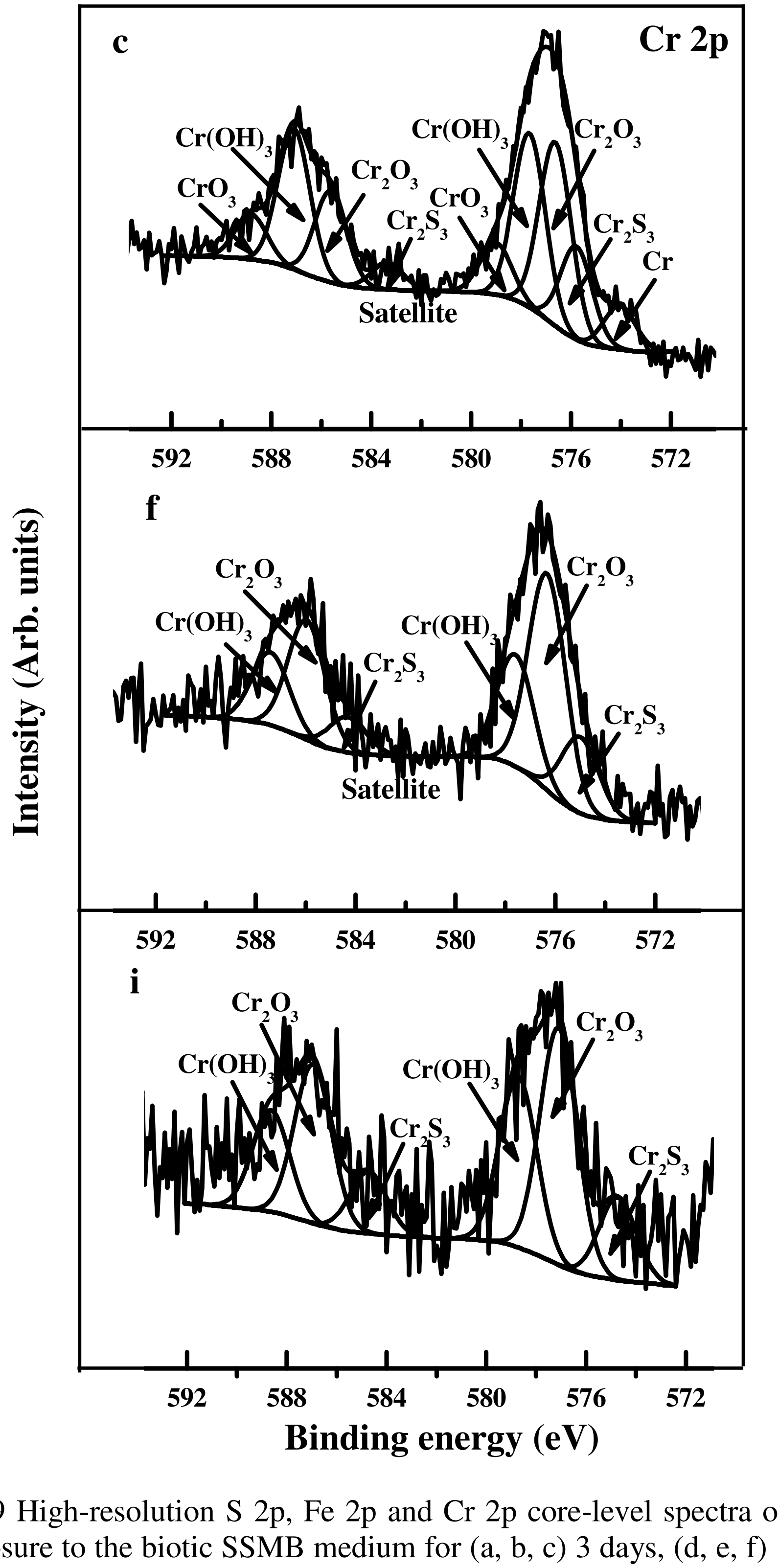

Figure 7.9 High-resolution S 2p, Fe 2p and Cr 2p core-level spectra of the surface film after exposure to the biotic SSMB medium for (a, b, c) 3 days, (d, e, f) 14 days and (g, h, i) 42 days.

Table 7.1 Fitting parameters for the S 2p, Fe 2p and Cr 2p core-level spectra and the relative abundance of various ironic and sulfide species in sulfide film on 304 SS after various exposure times in the *D. desulfuricans* inoculated SSMB medium

Exposure time (days)	Element	Compounds	Binding energy (ev)	Relative amount (100%)
3	Fe 2p	Fe	706.4	0.136
		FeS_2	707.4	0.110
		FeO	709.5	0.273
		Fe_{1-x} S	710.0	0.254
		FeS	711.4	0.154
		$Fe_2(SO_4)_3$	713.1	0.072
	S 2p	Monosulfide	161.0	0.624
		Disulfide	163.2	0.240
		S^0	165.2	0.040
		Organic-S/SO_4^{2-}	166.9	0.096
	Cr 2p	Cr	574.1	0.079
		Cr_2S_3	575.0	0.171
		Cr_2O_3	576.3	0.337
		$Cr(OH)_3$	577.1	0.318
		CrO_3	578.3	0.095
14	Fe 2p	FeS_2	707.2	0.246
		Fe_3O_4	708.3	0.153
		$Fe_{1-x}S$	710.0	0.280
		FeS	711.4	0.208
		$Fe_2(SO_4)_3$	713.1	0.113
		Satellite-pyrite	714.0	-
	S 2p	Monosulfide	161.0	0.434
		Disulfide	163.2	0.326
		S^0	165.3	0.061
		Organic-S/SO_4^{2-}	166.9	0.179
	Cr 2p	Cr_2S_3	575.0	0.189
		Cr_2O_3	576.2	0.534
		$Cr(OH)_3$	577.3	0.277
42	Fe 2p	FeS_2	707.2	0.316
		Fe_3O_4	708.3	0.254
		$Fe_{1-x}S$	710.0	0.209
		FeS	711.4	0.130
		$Fe_2(SO_4)_3$	713.1	0.091
		Satellite-pyrite	714.0	-
	S 2p	Monosulfide	161.0	0.259
		Disulfide	163.3	0.537
		S^0	165.3	0.038
		Organic-S/SO_4^{2-}	166.9	0.166
	Cr 2p	Cr_2S_3	575.0	0.168
		Cr_2O_3	576.3	0.483
		$Cr(OH)_3$	577.2	0.349

A significant amount of iron sulfides was formed on the 304 SS surface after various exposure periods in the *D. desulfuricans* inoculated SSMB medium, including FeS, FeS_2 and $Fe_{1-x}S$ (Figs. 7.9b, 7.9e, and 7.9h). Due to the formation of these sulfides, the relative portion of iron oxides was far less compared with those usually seen in the passive film in abiotic corrosion (Becdelievre et al, 1994, Wagner et al., 1992, Mustin et al., 1993). In light of the relative abundance of curve-fitted peak components in Table 7.1, two features can be highlighted in the evolution of sulfide films with exposure time: a). the appearance of the signal of metallic Fe on the 3-day-exposed coupons indicates that the layer of exposure products is rather thin, b) ferrous and ferric oxides also contribute a considerable portion of the surface iron compounds, c) the decrease in monosulfides and the increase of disulfides with exposure time is in good agreement with the change in the S 2p spectra, consistent with the appearance of pyrite satellites. It is therefore readily concludes that monosulfides (mainly pyrrhotie and mackinawite) forms in the initial stage of corrosion process of 304 SS in the biotic sulfide medium, and pyrite appears with the progress of corrosion. Mackinawite and pyrite are two common types of iron sulfides, but their roles in the sulfide corrosion of stainless steel remain controversial. Several investigators have proposed that a pyrite film is more protective to steel and less active in depolarization than a mackinawite film (Mara and Williams, 1972, Wikjord et al., 1980), whereas King and Wakerly (1973) has suggested that the corrosiveness of iron sulfides increases with the S/Fe ratio. Indeed, it is widely accepted that the evolution of iron sulfide from mackinawite to pyrite results in a large volume change. The compressive stress associated with this change further disrupts the sulfide film. Once the iron sulfide film is ruptured, a galvanic corrosion cell is established, where iron sulfides act as an excellent cathode due to their high conductivity, lower reduction potential and lower over-voltage for hydrogen evolution. Meanwhile, aggressive anions, such as Cl^-, penetrate and accumulate underneath the sulfide deposits, resulting in a decrease in local pH.

A comparison of Cr 2p spectra at various exposure periods also reveals the surface chemistry involved in changes in the outer layer of the passive film. At the initially 3 days of exposure, a small elemental Fe peak indicates that only a thin layer of passive film on the coupon surface (Fig. 7.9c). A curve-fitted peak component at B.E. of 575.0 eV is attributed to chromic sulfide (Cr_2S_3), indicative a limited sulfidation of Cr (Fig. 7.9c, 7.9f, and 7.9i). As shown in Table 7.1, the relative amount of chromic sulfide appears to increase upon prolonging exposure time, suggesting a susceptibility of the passive film to bacterial sulfate reduction. However, the major species comprising the passive film are chromic oxide (Cr_2O_3) and hydroxide ($Cr(OH)_3$) throughout the exposure periods. It is noteworthy that the Cr(VI) species (CrO_3) is detected on the 3-day-exposed coupon, but it disappears with the increase in exposure time due to the reduction of Cr^{6+} by *D. desulfuricans* (Smillie et al., 1981; Li et al., 1994).

Iron sulfide film is formed by the reaction of H_2S with either the metallic iron or the iron oxides, which in turn are formed immediately after the coupon surface have exposed to air. The anodic behavior of iron in a neutral or alkaline sulfide solution can be described by the following sequence of reactions (Shoesmith et al., 1980):

$$Fe + H_2S \rightarrow FeSH^-_{ads} + H^+ \tag{7.1}$$

$$FeSH^-_{ads} \rightarrow FeSH^+ + 2e^- \tag{7.2}$$

$$FeSH^+ \rightarrow FeS_{1-x} + xHS^- + (1-x)H^+ \tag{7.3}$$

In the marine environments, anodic metal dissolution can also proceed as the follows (Schmitt, 1991):

$$Fe + 2Cl^- + H_2O \rightarrow [Fe(OH)^+Cl^-] + HCl + 2e^- \tag{7.4}$$

Iron sulfide is formed through the following reactions:

$$[Fe(OH)^+Cl^-] + HS^- \rightarrow FeS + H_2O + Cl^- \tag{7.5}$$

The cathodic reaction may be the reduction reaction of H_2S as follows (Costello, 1974):

$$2H_2S + 2e^- \rightarrow H_2 + 2HS^- \tag{7.6}$$

Previous studies have found that a thin tarnished layer of mackinawite was initially formed initially on the SS coupon surface in the presence of SRB. This layer becomes less adherent, non-protective and heterogeneous as it thickened (McNeil and Little, 1990). In the presence of a low concentration of ferrous ion, mackinawite will transfer to pyrite (Lewandowski et al., 1997). However, this change is not observed in the abiotic medium (McNeil and Little, 1990). This result indicates that the biogenic sulfurous compounds may act as the catalyst in the transformation of iron sulfide to pyrite in a biotic medium containing SRB.

7.2 Biocorroison behavior of Ti oxide/butoxide coatings on 304 SS surface from layer-by-layer sol-gel deposition process

7.2.1 General background

The layer-by-layer sol-gel deposition technique has also been used to deposit TiO_2, SiO_2 and SiO_2-CaO oxides on metals, such as stainless steel, nickel-Ti and Ti alloys, to improve their corrosion resistance (Liu et al., 2003, Vallet-Regi et al., 2003, Drews et al., 2000, Gallardo et al., 2004, Ichinose et al., 1996; Advincula et al., 2007). The Ti oxide/ Ti (IV) butoxide coatings have been found to protect the underlying metal from localized corrosion under the attack of aggressive ions, such as chloride and sulfide (Liu et al., 2003, Gallardo et al., 2004), as well as minimizing the release of Ti ions in biological fluids (Advincula et al., 2007, Vallet-Regi et al., 2003). [24] SiO_2-CaO oxide coatings have also been used to inhibit the localized corrosion of stainless steel in biological fluids (Vallet-Regi et al., 2003). In addition, Ti oxide/butoxide coatings are bioactive coatings, as the abundant hydroxyl (OH) groups generated via hydrolysis of metal alkoxides can provide nucleation sites for the deposition of calcium and phosphate compounds. (Ichinose et al., 1996, Li et al., 1994). They also provide a bioactive surface for further re-activation via calcium phosphate deposition. The Ti oxide/butoxide coatings therefore provide an alternative to minimizing biocorrosion of stainless steel over the environmentally less friendly biocide treatment and antibacterial coatings.

Section 7.2 is devoted to the preparation of well-defined multilayers of Ti oxide/butoxide on stainless steel via the layer-by-layer sol-gel deposition. The pristine, the hydroxylated, the nitric acid-passivated and the Ti oxide/butoxide-coated surfaces were exposed to the *D. desulfuricans* inoculated simulated seawater-based modified Baar's (SSMB) medium to evaluate their biocorrosion resistance to sulfate-reducing bacteria. The corrosion behavior of various coupons was evaluated by Tafel plots, cyclic polarization curves and electrochemical impedance spectroscopy (EIS). The bacterial adhesion and the biofilm development on the pristine, the hydroxylated, the passivated and the Ti oxide/butoxide-coated coupons were monitored by SEM. SEM was also used to assess the degree of corrosion damage on the coupon surface after the removal of biofilms. Furthermore, energy dispersive X-ray spectroscopy (EDX) analysis was performed to analyze the corrosion products and to identify the deposition of calcium and phosphate on the Ti oxide/butoxide-coated surface during the process of biocorrosion.

7.2.2 Experiment section

7.2.2.1 Metal coupon preparation and Ti oxide/butoxide coatings

The 304 SS coupons and their preparation are similar to those procedures described in Section 3.2.1 of Chapter 3. The newly-polished specimens were immersed in a 30/70% (v/v) solution of H_2O_2 and H_2SO_4 for 30 min. This solution, also known as the *piranha* solution, removes the native oxides and forms a fresh OH-rich oxide on the stainless steel surface (Nanci et al., 1998). These substrates were rinsed thoroughly with copious amounts of DI water and then washed in methanol thrice being dried by a stream of purified N_2. The treated substrates were denoted as the "hydroxylated" coupons. The pristine coupons were also passivated by exposure to 30% HNO_3 for 1h as, per ASTM F86 protocol, and denoted as the "passivated" coupons. The above three types of coupons, i.e., the pristine, the hydroxylated and the passivated coupons were served as the uncoated control coupons.

The well-defined multilayers of titanium oxide were deposited on the surface of stainless steel using the layer-by-layer sol-gel processing method, as shown schematically in Figure 7.10. The sol-gel reaction first occurs between titanium butoxide and the hydroxyl (OH) groups on the surface of hydroxylated substrates. Thereafter, the Ti-OH hydroxyl groups are regenerated to form a monolayer of titanium oxide (TiO_2). Repetition of the entire process results in multilayers of titanium oxide film. The coating process has been described in detail in previous studies (Nanci et al., 1998). Briefly, the surface hydroxylated coupons were immersed in a100 mM toluene and ethanol (1:1, v:v) solution of titanium butoxide for 10 min in a sealed Pyrex glass tube. The solution was purged a prior with pure N_2 gas. Titanium butoxide reacted readily with the negatively-charged hydroxyl-functionalized stainless steel during this process. After rinsing with copious amounts of toluene to remove the unbound alkoxides, the coupon were immersed in DI water for 2 min to regenerate the hydroxyl groups and then dried by airflow. The chemisorption, rinsing, hydrolysis, and drying steps were repeated 5 times to result in the nanostructured multilayers of titanium oxide affixed on the stainless steel. The Ti oxide/butoxide coatings from the sol-gel process remained in alkoxide form on the substrate surface, and were stored in a vacuum dessicator prior to analysis. Each layer of the deposited titanium oxide has been reported to be of nanometers in thickness, as determined by ellipsometry (Nanci et al., 1998).

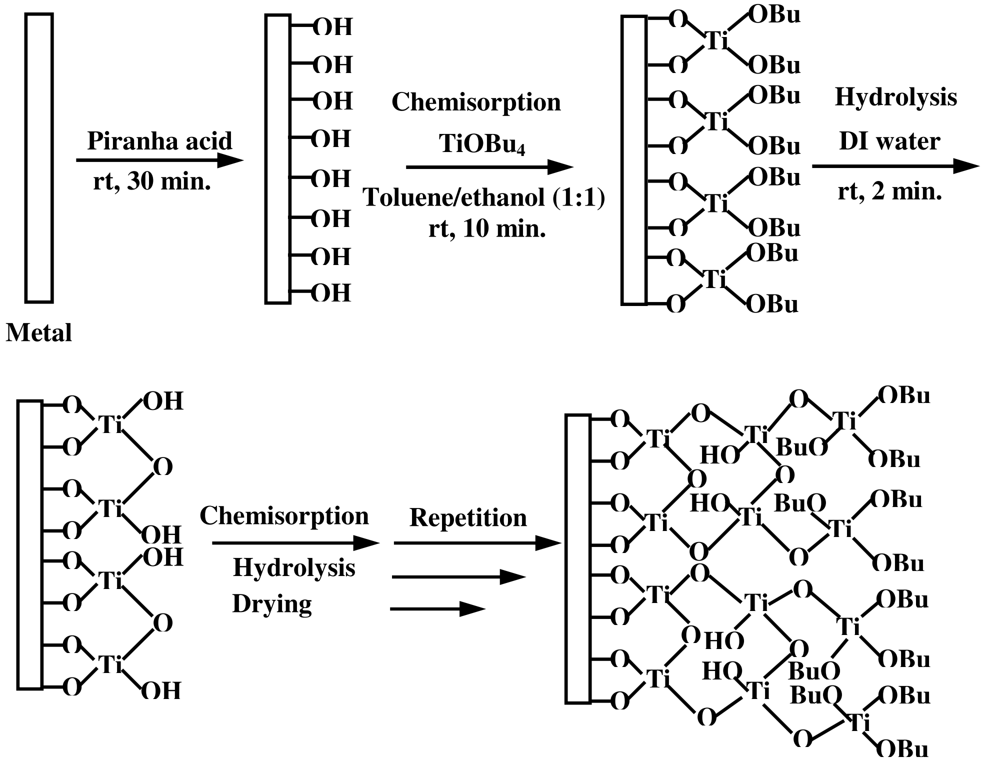

Figure 7.10 A schematic diagram illustrating the layer-by-layer sol-gel deposition process on the hydroxylated coupon surface

7.2.2.2 Medium preparation and inoculation

The preparation of SSMB medium and its inoculation was performed similarly using procedures as those described in detail in Section 7.1.2.2 and 7.1.2.3 of Chapter 7.

7.2.2.3 Surface characterization

The Ti oxide/butoxide-coated and uncoated test coupons were characterized with XPS and static water contact angles. The XPS measurement is similar to those described in Section 4.2.5 of Chapter 4, whilst the measurement of static water contact angles is similar to those described in Section 6.2.4 of Chapter 6.

7.2.2.4 Electrochemical studies

The Tafel plots, cyclic polarization curves and EIS of the Ti oxide/butoxide-coated and three types of uncoated coupons were obtained similarly using procedures as those described in Section 3.2.4 of Chapter 3.

7.2.2.5 Surface analysis with SEM-EDX

The SEM imaging coupons was similar to procedures as those described in Section 3.2.5 of Chapter 3.

7.2.3 Results and discussion

7.2.3.1 Surface characterization of Ti oxide/butoxide-coated and uncoated coupons

The surface composition of the pristine, the hydroxylated, the passivated and the Ti oxide/butoxide-coated stainless steel coupons were characterized by XPS. Figure 7.11 shows the XPS wide scan and O 1s core-level spectra of the test coupons prior to exposure to the culture medium. The normalized composition (atomic percentage) of the corresponding coupon surfaces is also summarized in Table 7.2. The photoelectron lines at binding energies (BE) of about 285, 530, 577, 711, 854 and 978 eV, attributable to C 1s, O 1s, Cr 2p, Fe 2p, Ni 2p and O KLL components, respectively, are observed in the wide scan spectra of the hydroxylated and the passivated coupons (Figs. 7.11a and 7.11b). The intense O 1s peak at 530 eV is indicative of the formation of an oxide or hydroxide layer on the hydroxylated and the passivated coupon surfaces. The corresponding high-resolution O 1s core-level spectra of the two coupons in Figure 7.11c and 7.11d consist of three peak components at the BE of about 529.9, 531.7 and 533.1 eV, attributable to the oxide (Atrens and Jin, 1987, 1990), hydroxide (Beccaria et al., 1995) and other oxygen (which is probably organic oxygen or oxygen from vapor deposition) (Varga et al., 1997; Hermas et al., 2005), respectively. In spite of the similarity in wide scan spectrum between the hydroxylated and the passivated coupons, the surface composition is different from each other, as revealed by the O 1s, Fe 2p and Cr 2p core-level XPS spectra (Figs. 7.11b, 7.11d, 7.11e, 7.11f, 7.11g and 7.11h) and static water contact angles (Table 7.3). Based on the O 1s core-level XPS spectra, the hydroxide is the predominant peak component on the hydroxylated coupon surface, indicative of the generation of a high concentration of hydroxyl groups on the pristine coupon surface upon treatment with the *Piranha* acid (Fig. 7.11c). It has been reported that the *Piranha* acid, as a strong oxidizer, regenerates a fresh oxidized/hydroxylated surface on most metals, e.g. oxides of Si-wafers and titanium substrates (Advincula et al., 2007, Nanci et al., 1998). This point is further confirmed by the sharp decrease in the static water contact angle from about 60^{o} to 18^{o} (Table 7.3) due to the presence of abundant hydroxyl groups on the hydroxylated coupon surface. Whereas, the sharp rise in intensity of oxide species of the passivated coupon surface is observed relative to that of the hydroxylated coupons, and the oxides become another dominant component, besides the hydroxides, on the passivated coupon surface (Figure 7.11d). The passive oxide and hydroxide layer formed on the passivated coupon surface results in the decrease in the static water contact angle from about 60^{o} to about 49^{o} (Table 7.3).

To correlate with the O 1s core-level XPS spectra, the Fe 2p and Cr 2p core-level XPS spectra were obtained to quantitatively evaluate the nature of surface film on the hydroxylated and the passivated coupons (Figs. 7.11e, 7.11f, 7.11g and 7.11h). For the

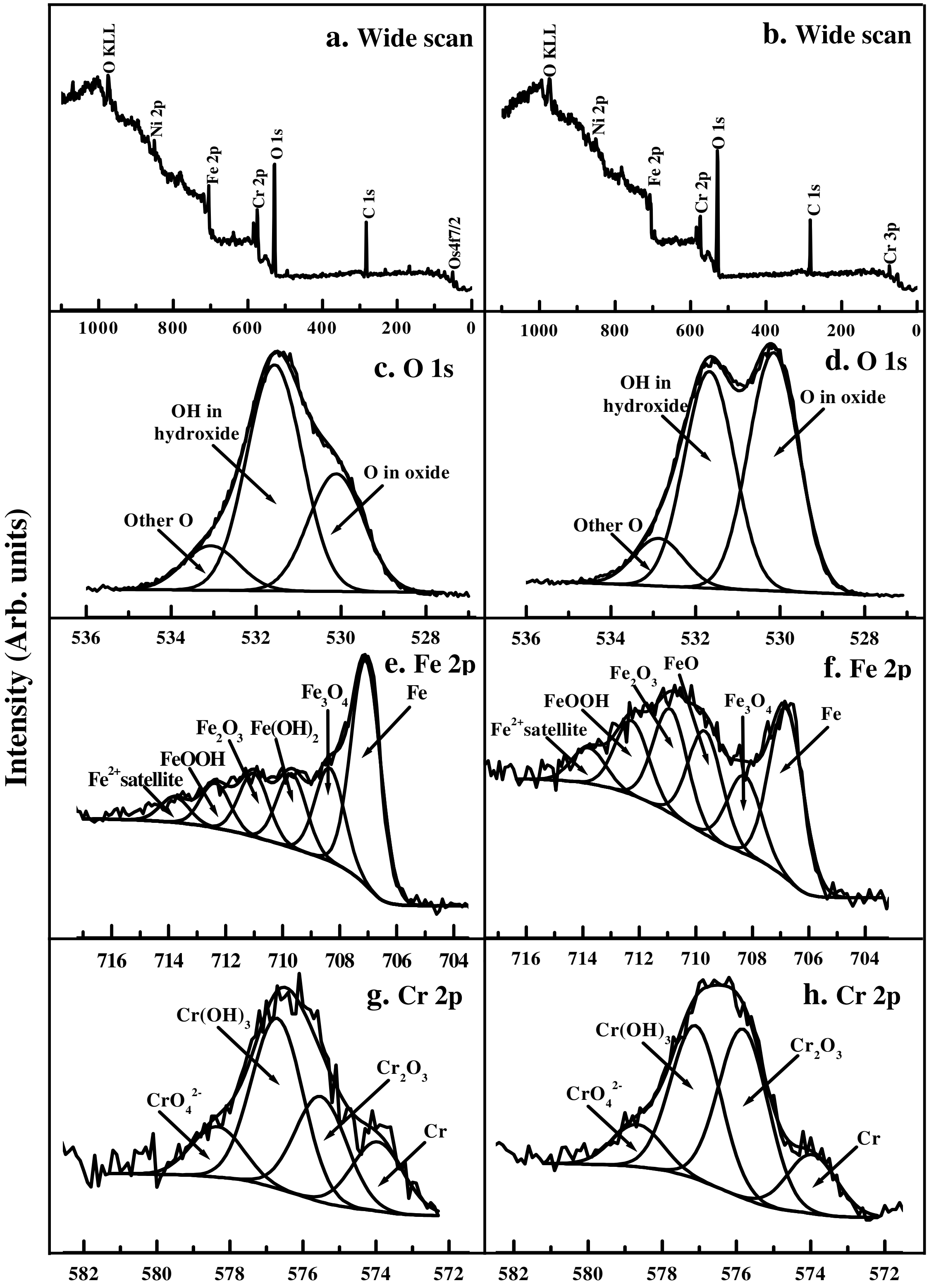

Figure 7.11 Wide scan , O 1s, Fe 2p and Cr 2p XPS core-level spectra of (a, c, e, g) the hydroxylated coupon surface and (b, d, f, h) the passivated coupon surface.

Table 7.2 Normalized atomic percentage composition of different coupon surfaces

Samples \ Elements	C 1s	O 1s	Ti 2p	Fe 2p	Cr 2p	Ni 2p
Pristine[a]	21.32	7.50	–	49.28	14.81	7.09
Passivated[b]	23.05	41.72	–	20.17	12.48	2.58
Hydroxylated[c]	21.46	50.13	–	20.31	6.36	1.74
Ti oxide/butoxide-coated[d]	49.76	39.64	10.60	b.d.l.[c]	b.d.l.	b.d.l.

a) Pristine corresponds to the surface of a newly-polished steel specimen,
b) Passivated corresponds to the steel surface treated with 30% nitric acid,
c) Hydroxylated corresponds to the steel surface treated with Piranha acid,
d) Ti oxide/butoxide-coated corresponds to the hydroxylated steel surface treated with titanium butoxide,
e) b.d.l. denotes below detection limit.

hydroxylated coupons, the Fe 2p core-level XPS spectrum is curve-fitted into six peak components with the BE of 706.8, 708.3, 709.5, 710.6, 711.8 and 714.4 eV, corresponding to the metallic Fe, Fe_3O_4, $Fe(OH)_2$, Fe_2O_3, FeOOH and Fe^{2+} satellite, respectively (Fig. 7.11e) (Varga et al., 1997). The corresponding Cr 2p core-level spectrum consists of four peak components at the BEs of about 574, 575.8, 577 and 579.3 eV, attributable to the metallic Cr, Cr_2O_3, $Cr(OH)_3$ and CrO_4^{2-}, respectively. The Fe 2p and Cr 2p core-level XPS spectra of the passivated coupons are similarly curve-fitted into components as the hydroxylated coupons, except for the presence of FeO (at the BE of about 709.3 eV) in the Fe 2p spectra (Figs. 7.11f and 7.11h). To compare the relative intensity of oxides and hydroxides in the Fe 2p and Cr 2p core-level spectra of the hydroxylated coupons with those of the passivated coupons, two distinct differences can be distinguished: (i) the relative abundance of hydroxides on the hydroxylated coupon surface is higher than that on the passivated coupon surface, which is in good agreement of that of the corresponding O 1s spectrum, and (ii) the relative abundance of the metallic iron and chromium on the hydroxylated coupons is significantly higher than that on the passivated coupons, indicative of a relatively thicker passive film formed on the passivated coupon surface than on the hydroxylated coupons. Moreover, the presence of metallic elements on the hydroxylated and the passivated coupons suggests that the passive layer on both coupon surfaces are very thin films due to the sampling depth of the XPS technique being within around 10 nm (Wagner et al., 1992). The passive films on stainless steels are reported to be very thin (around 1-10 nm) (Alamr et al., 2006). Based on the quantitative data in Table 7.2, another noticeable difference between the hydroxylated and the passivated coupon surface is the relative abundance of chromium (Cr). The enrichment of chromium in the outermost passive film after nitric acid treatment has been widely reported in the literatures (Wallinder et al., 1999, O′Laire et al., 2006). It has been also reported that the outermost passive layer on the nitric acid treated 304 stainless steel consists mainly of Fe_3O_4, Fe_2O_3, Cr_2O_3 and FeOOH ((Wallinder et al., 1999, O′Laire et al., 2006). The compositions of the passive layer in this study are in good agreement with the previous findings. In addition, the relative abundance of carbon (C1s) for the three uncoated coupons are around 20% (Table 2), due to the trace amount of carbon in stainless steel, the adsorption of adventitious carbon and hydrocarbon during sample handling (Tan et al., 2006; Wagner et al., 1992).

The successful development of the Ti oxide/butoxide coatings via the sol-gel process on the hydroxylated coupon surface was ascertained by the XPS and the static water contact angle measurements. In comparison with the photoelectron lines of the hydroxylated coupons in Figure 7.11a, the signals of the metallic elements of Cr 2p (577 eV), Fe 2p (711 eV) and Ni 2p (854 eV) are no longer discernible in the wide scan spectrum of the Ti oxide/butoxide-coated coupon surface, while two additional photo-electron lines at the BE of about 33 and 458.8 eV, attributable to Ti 3p and Ti 2p species, respectively, have appeared in Figure 7.12a. The masking of the metallic elements on the Ti oxide/butoxide-coated coupons implies that the Ti oxide/butoxide coating is thicker

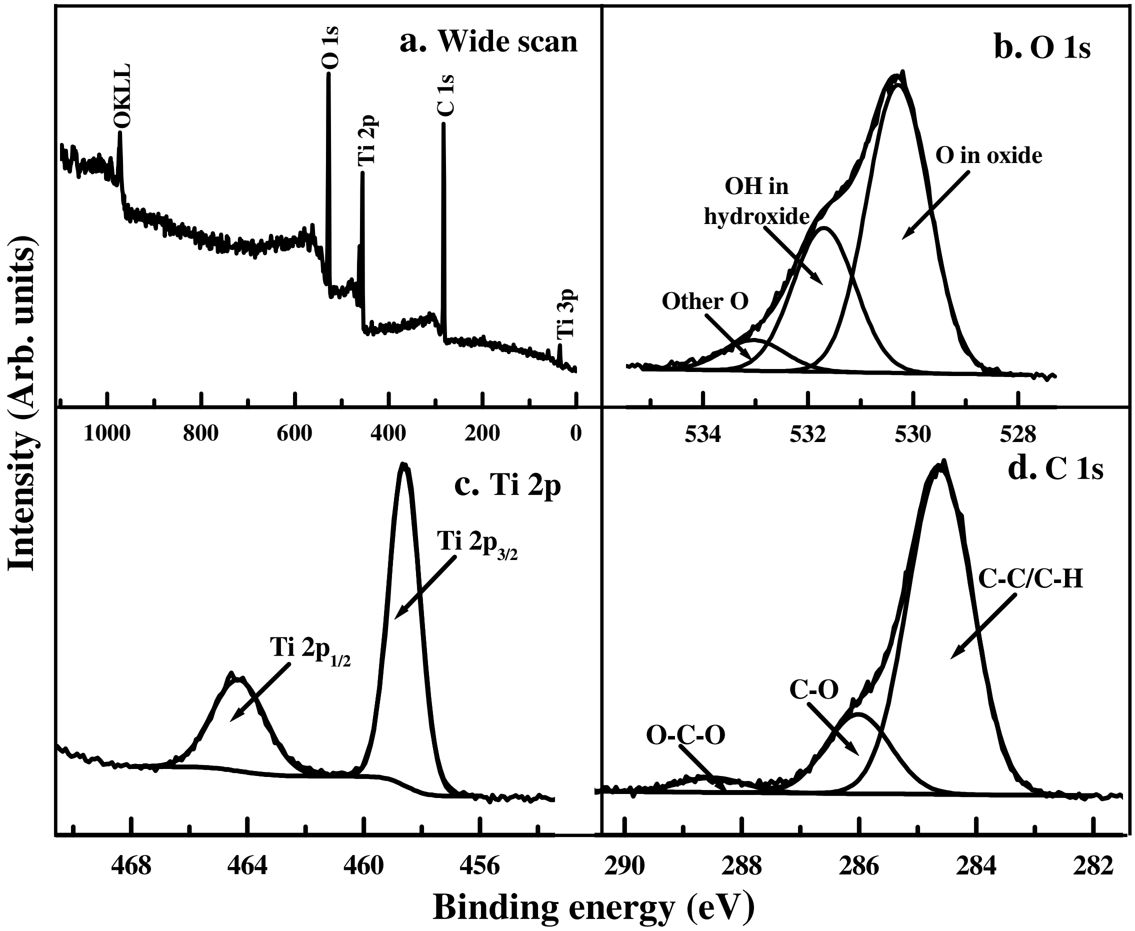

Figure 7.12 XPS spectra of the Ti oxide/butoxide-coated coupon surface (a) wide scan, (b) O 1s core-level spectra, (c) Ti 2p core-level spectra and (d) C 1s core-level spectra.

than the probing depth of the XPS technique (about 8 nm) (Wagner et al., 1992). Previous investigations have reported that the thickness of a five-layer sol-gel coating is about 22 nm (Advincula et al., 2007, Nanci et al., 1998). Table 7.2 shows the dramatic increase in the relative quantity of C from about 20% to about 50%, due to the formation of multiple Ti oxide/butoxide layers, and the relative amount of titanium (Ti) in the sol-gel coatings is about 10.5%. Simultaneously, the substrate surface becomes more hydrophobic, as the static water contact angle increases sharply from about 18° to 78° (Table 7.3). The high-resolution O 1s core-level spectrum of the Ti oxide/butoxide-coated coupons shows a predominant component peak at the BE of 529.9 eV, attributable to the titanium dioxide (TiO_2) or the nonstoichiometric oxides (Ti_xO_y), the component peak at a BE of 531.7 eV, attributable to the hydroxyl groups (Fig. 7.11f). It is reported that the titanium oxide is predominantly in the form of TiO_2, together with a small amount of Ti_xO_y (Fang et al., 1999). The Ti 2p spectrum of the corresponding surface in Figure 3c shows a spin-orbit-split doublet with BE values of 458.8 and 464.3 eV, attributable to the respective Ti $2p_{3/2}$ the Ti $2p_{1/2}$ component peaks. The Ti 2p core-level XPS spectrum at the BE of 458.8 eV indicates that the dominant component of Ti compounds is titanium oxide (TiO_2) (Wagner et al., 1992; Borgmann et al., 1993). The high-resolution C 1s core-level spectrum of the sol-gel coatings is curve-fitted into three component peaks at BEs of 284.6, 286.2 and 287.8 eV, attributable to the C-C/C-H, C-O, and O-C-O species, respectively (Wagner et al., 1992).

The change in static water contact angles during the course of layer-by-layer deposition of metal alkoxide on the substrate surface was investigated to further confirm the formation of Ti oxide multilayers via the sol-gel process. The hydroxylated coupon surface has a static water contact angle of 18^o. The contact angle of the deposited titanium butoxide layer is determined to be about 78^o. Upon hydrolysis of the alkoxide layers, the contact angle decreases to about 29^o. As shown in Figure 7.13, the fluctuation in static water contact angle during the layer-by-layer deposition process follows the adsorption and hydrolysis cycles closely. This obvious alternating trend in the static water contact angle data verifies the progressive formation of the multilayer on the metal surface via the sol-gel process.

Table 7.3 Static water contact angles of different substrate surfaces

Sample surface	Static water contact angles (±3°)
Pristine	60
Hydroxylated	18
Passivated	49
Ti oxide/butoxide-coated	78

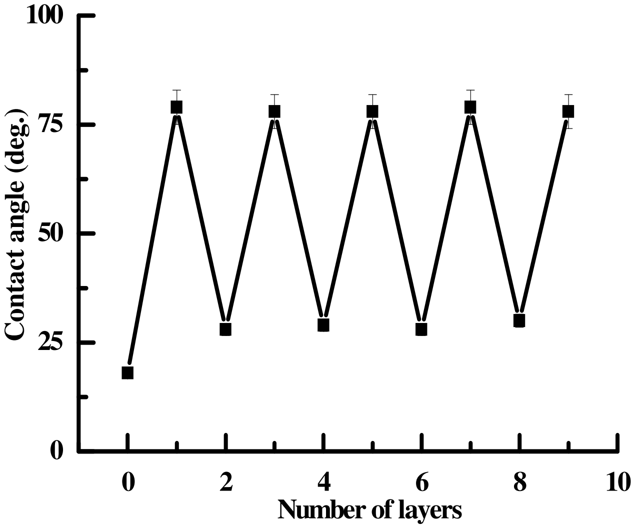

Figure 7.13 Static water contact angle of sol-gel multilayer films as a function of the number layers deposited on the coupon surface, even numbers represent films with the hydrolyzed coatings as the outermost layer whereas odd number films represent films with the non-hydrolyzed coatings.

7.2.3.2 Tafel plots

Figure 7.14 shows the Tafel plots of a Ti oxide/butoxide-coated and three types of uncoated coupons after 3, 7, 14, and 21 days of exposure in the *D. desulfuricans* inoculated SSMB medium. The data were further quantitatively analyzed with GPES software to obtain Tafel slopes (β_a and β_c), E_{corr} and i_{corr} as described in detail in Section 3.3.1.1, and the analysis results are shown in Table 7.4.

For the pristine and the hydroxylated coupons, the corrosion potential, E_{corr}, undergoes an apparent active shift with exposure time in the *D. desulfuricans* inoculated

SSMB medium. It decreases rapidly to less than -0.5 V after 3 days of exposure. The phenomenon is usually attributed to the enhancement of the anodic dissolution process in terms of the mixed potential theory (Peng and Park, 1994, Huang et al., 2004). An active shift in corrosion potentials, albeit of a smaller degree, is also observed for the passivated coupons, indicating that the passivated coupons are more resistant to biocorrosion of *D. desulfuricans* than the pristine and the hydroxylated coupons. This is further confirmed by the comparatively smaller corrosion current densities, i_{corr}, of the passivated coupons (Table 7.4). The corrosion current density of the pristine coupon increases with exposure time, and reaches as high as about 130 $\mu A \cdot cm^{-2}$ after 21 days of exposure. Similarly, the high values of i_{corr} of more than 60 $\mu A \cdot cm^{-2}$ are observed for the hydroxylated and the passivated coupons after 21 days of exposure. These results suggest that the compact oxide/hydroxide layer formed on the stainless steel surface is vulnerable to the synergistic effect of the *D. desulfuricans* and biogenic sulfide anions. The Tafel slopes of the anodic branches, β_a, of the pristine and the hydroxylated coupons increase rapidly with exposure time, which is usually ascribed to the anodic concentration polarization due to the presence of copious amounts of sulfide ions near the metal surface (Al-Hajji and Reda, 1995, Syrett, 1981). On the other hand, their cathodic Tafel slopes, β_c, fluctuate within a narrow potential range of -180 and -210 mV/decade throughout the exposure period, indicative of a diffusion control at the cathodic sites. The minor deviation in the Tafel slopes of the passivated coupons, as compared to those of the pristine and the hydroxylated coupons, are believed to be related to the presence of a comparatively thick and compact oxide/hydroxide layer on the coupon surface.

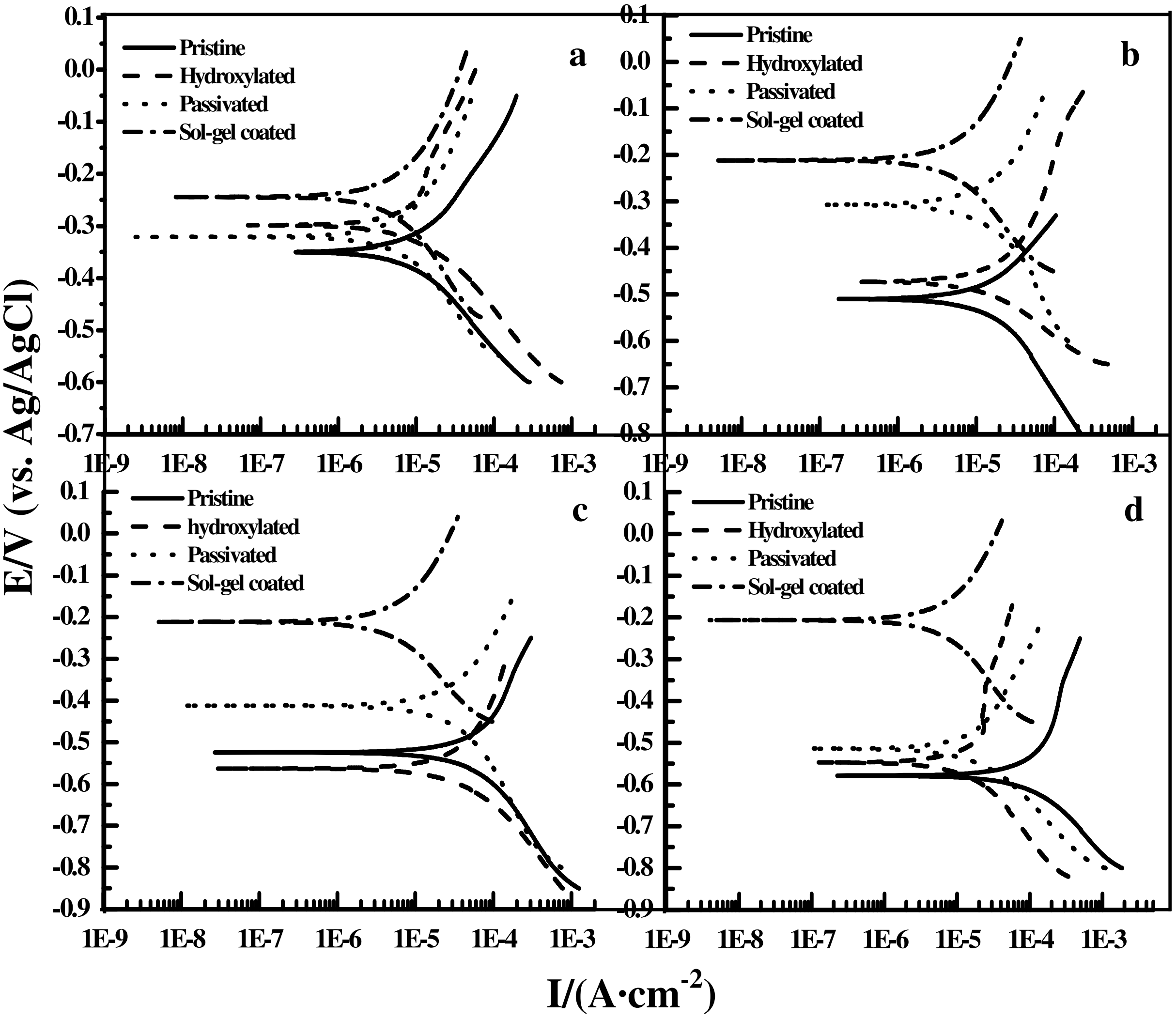

Figure 7.14 Tafel plots of the pristine, the hydroxylated, the passivated and the Ti oxide/butoxide-coated coupons after exposure to the SSMB medium inoculated with *D. desulfuricans* bacterium for (a) 3day, (b) 7 days, (c) 14 days, and (d) 21 days.

The corrosion behavior of the Ti oxide/butoxide-coated coupons is obviously different from those of the uncoated coupons. The corrosion potential, E_{corr}, of the Ti oxide/butoxide-coated coupons exhibits a slight noble shift from ~-0.25 to ~-0.20 V with exposure time, as apposed to the active shift in E_{corr} of the uncoated coupons, indicating that the multilayer Ti oxide coating probably has inhibited one of or both of electrode reactions in terms of the mixed potential theory. The cathodic Tafel slopes, β_c, of the Ti oxide/butoxide-coated coupons remain relatively constant, and are larger than those of the uncoated coupons, indicative of mass transport effect on the cathodic reaction. At the same time, the anodic Tafel slopes is also independent of exposure time, and fluctuates within a narrow range of 280 mV and 310 mV, indicative of the diffusion control at the anodic site due to high stability of the Ti oxide/butoxide coatings. Not only do the values of i_{corr} of the Ti oxide/butoxide-coated coupons always remain below 8 $\mu A \cdot cm^{-2}$ throughout the exposure period, but they also decrease with time during the initially 14 days. The phenomenon can probably be ascribed to the deposition of phosphate and calcium compounds. It can, therefore, be concluded that the well-defined Ti oxide/butoxide multilayer coatings can impart the desirable resistance to biocorrosion onto the coupon surface.

Table 7.4 Analysis of Tafel plots of different test coupons in the biotic SSMB medium containing *D. desulfuricans* for various exposure times

Time (days)	Samples	β_c (mV/dec)	β_a (mV/dec)	E_{corr} (V)	I_{corr} ($\mu A \cdot cm^{-2}$)	Corrosion rate ($mm \cdot y^{-1}$)
3	Pristine	-178	203	-0.350	11.35	0.118
	Hydroxylated	-164	315	-0.330	9.466	0.0980
	Passivated	-210	282	-0.322	8.567	0.0887
	Ti oxide/butoxide-coated	-226	314	-0.255	7.386	0.0765
7	Pristine	-183	247	-0.521	25.14	0.260
	Hydroxylated	-122	432	-0.504	25.81	0.267
	Passivated	-192	349	-0.314	19.32	0.199
	Ti oxide/butoxide-coated	-201	290	-0.223	6.317	0.0654
14	Pristine	-205	401	-0.526	77.32	0.800
	Hydroxylated	-215	373	-0.528	46.06	0.477
	Passivated	-224	304	-0.399	38.21	0.396
	Ti oxide/butoxide-coated	-200	310	-0.226	6.753	0.0699
21	Pristine	-181	488	-0.536	129.10	1.336
	Hydroxylated	-218	692	-0.578	73.28	0.759
	Passivated	-176	321	-0.511	59.69	0.618
	Ti oxide/butoxide-coated	-218	280	-0.210	7.762	0.0803

7.2.3.3 EIS measurement

EIS measurement of the pristine, the hydroxylated, the passivated and the Ti oxide/butoxide-coated coupons were performed to determine the evolution of the Ti oxide/butoxide multilayer coatings on the coated coupons and the passive film on the uncoated coupons, as well as to distinguish each sub-process occurring at the metal/biofilm interface.

Figure 7.15 shows the EIS data of the Ti oxide/butoxide-coated and uncoated coupons after various duration of exposure in the *D. desulfuricans* inoculated SSMB medium. These results are further analyzed by fitting the EIS data with a proper equivalent circuit. The fitting process and the circuit parameters are similar to those described in Section 3.3.1.2. Figure 7.16 illustrates the physical structures of different coupon surfaces and their corresponding equivalent circuits. Equivalent circuit (a) models two relaxation time constants, and is usually used to represent a porous and non-protective passive film on the coupon surface. Equivalent circuits (b) and (c) both include three time constants, and are used to model, respectively, the impedance spectra of the hydroxylated, the passivated and the Ti oxide/butoxide-coated coupons. The values of Chi-square (χ^2) are all in the order of 10^{-3} (Table 7.5), indicative of the satisfactory fitting with the proposed equivalent circuit.

For the pristine coupons with 3, 7, 14 and 21 days of exposure to the *D. desulfuricans* inoculated SSMB medium, the diameters of Nyquist semicircles decrease with exposure time, indicative of increase in the corrosion rates of SS coupons (Fig. 7.15a). The associated Bode phase angle plots show the peak maximum of the electric double layer being displaced towards the lower frequencies, which might be related to the high capacitance of the porous iron sulfide product (Fig. 15b). The respective Bode phase angle plots indicate the existence of two relaxation time constants: the one appearing at high frequencies is related to the response of the porous corrosion product layers (consisting mainly of the bacterial cells and ferrous sulfide), and the other one at low frequencies can be attributed to EDL. The fitted parameters of the EIS data for the pristine coupons are shown in Table 7.5. It can be seen that the value of charge transfer resistance, R_{ct}, decreases gradually with exposure time, indicative of the acceleration of corrosion of the pristine coupons under the influence of *D. desulfuricans*. The resistance of the passive film, R_f, appears to increase with time in the initial exposure periods (3 and 7 days) due to the formation of a thin iron sulfide layers, and then decrease with time owing to the initiation of pitting corrosion under the SRB biofilms and the iron sulfide layer on the coupon surface. The increase in thickness of the corrosion product layers results in the elevation of capacitive behavior of EDL. As shown in Table 7.5, the capacitance of EDL, C_{dl}, increases rapidly with exposure time from about 0.48 to about 39.6 mF. It has been reported that the porous iron sulfide corrosion products possess the extraordinarily high capacitance (Newman et al., 1991). The corrosion behavior of the pristine stainless steel is in good agreement with those of the earlier studies (Newman et al., 1991, Miranda et al., 2006).

In the case of the hydroxylated and passivated coupons, two depressed semicircles are observed in their Nyquist plots (Figs. 7.15c and 7.15e). The appearance of the semicircles at high frequencies is ascribed to the oxide/hydroxide layers formed on the coupon surface by acid pretreatment. The inset figures in Figure 7.15c and 7.15e shows the existence of the two semicircles in the Nyquist plots of the hydroxylated and passivated coupons. Under the synergistic attack of *D. desulfuricans* and the biogenic

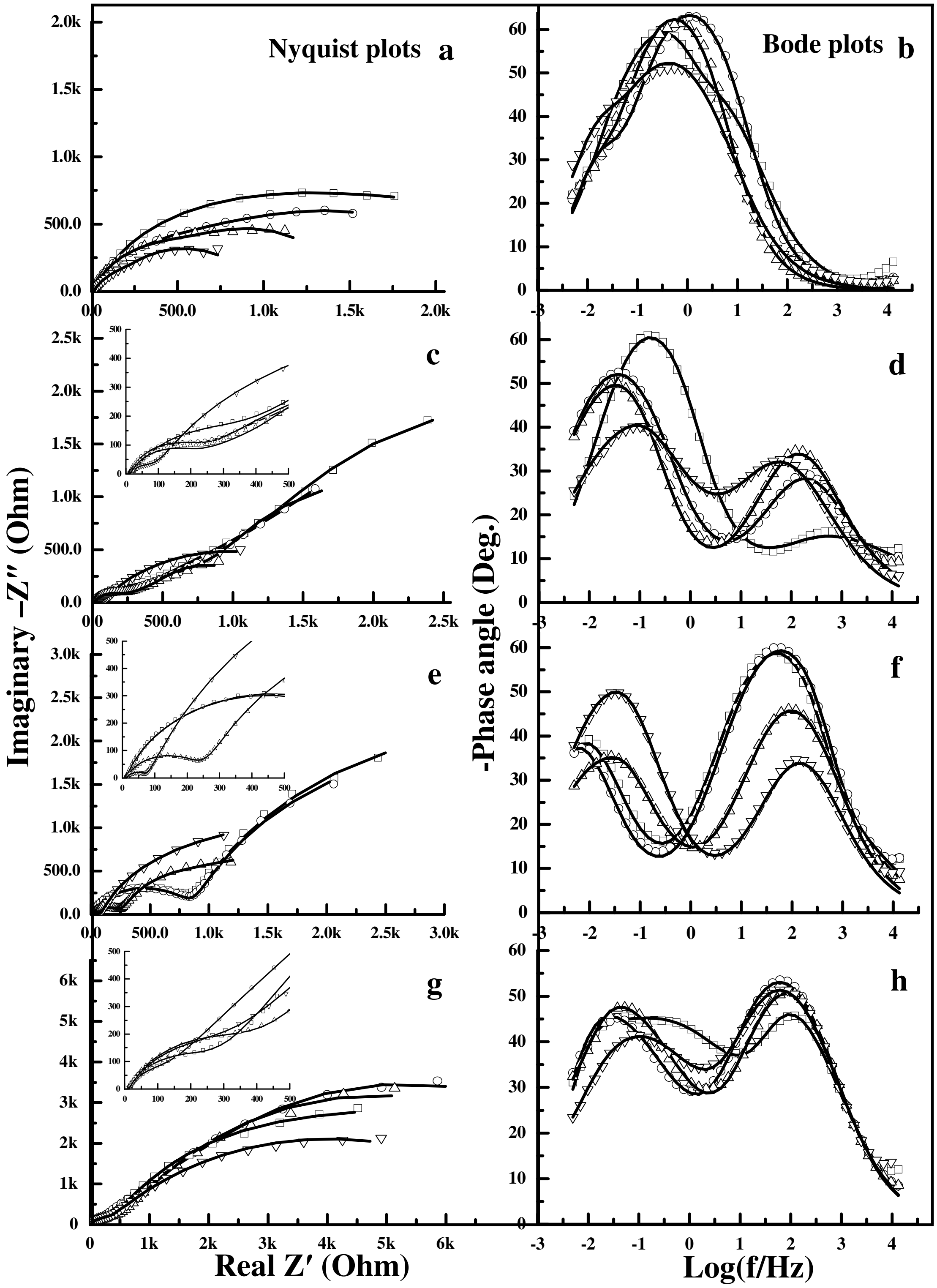

Figure 7.15 EIS spectra of (a, b) the pristine coupons, (c, d) the hydroxylated coupons, (e, f) the passivated coupons, and (g, h) the Ti oxide/butoxide-coated coupons after 3 days (open squares), 7 days (open circles), 14 days (open upper triangles), and 21 days (open lower triangles) of exposure in the biotic SSMB medium containing *D. desulfuricans* bacteria. Solid lines represent the fitted results based on the equivalent circuits.

sulfide ions, the diameters of the two semicircles of the hydroxylated and the passivated coupons both undergo an apparent decrease with exposure time, indicative of the enhancement of corrosion of coupons. It is noted that the diameters of semicircles at high frequencies for the passivated coupons are much larger than those of the hydroxylated coupons during the initial exposure periods (3 and 7 days), indicating that the passivated coupons are more resistant to biocorrosion. The difference in the impedance spectra between the hydroxylated and the passivated coupons can be easily distinguished from the corresponding Bode phase angle plots (Figs. 7.15d and 7.15f). The peak maximum in high frequency ranges of the passivated coupons remains as high as about 60^{o} during the initial exposure periods, and is much higher than that of the hydroxylated coupons. This result further confirms the better stability of the passive film formed on the passivated coupons in comparison with the hydroxylated coupons. Furthermore, the slight shift in the peak maxima towards the lower frequency range also occurs in the Bode phase angle plot of the hydroxylated and the passivated coupons, indicative of the deposition of the iron sulfide product on the coupon surface. The respective Bode phase angle plots of the hydroxylated and the passivated coupons indicate the existence of three relaxation time constants, attributable to the oxide/hydroxide layers, the porous surface layers of the bacterial cells and iron sulfide products, and EDL.

Table 7.5 shows the quantitatively analyzed results of the EIS data for the acid-pretreated coupons. Indeed, the magnitudes of resistance of the oxide/hydroxide layers, R_o, of the passivated coupons are much larger than those of the hydroxylated coupons throughout the exposure periods. This result further confirms the higher passivity of the oxide/hydroxide layers on the passivated coupons owing to the relatively high content of chromium (Cr) in the passive film. The relatively larger value of CPE power n_1 of the passivated coupons indicates that the oxide/hydroxide layers produced on the stainless steel surface by the nitric acid treatment are more homogenous and compact than those

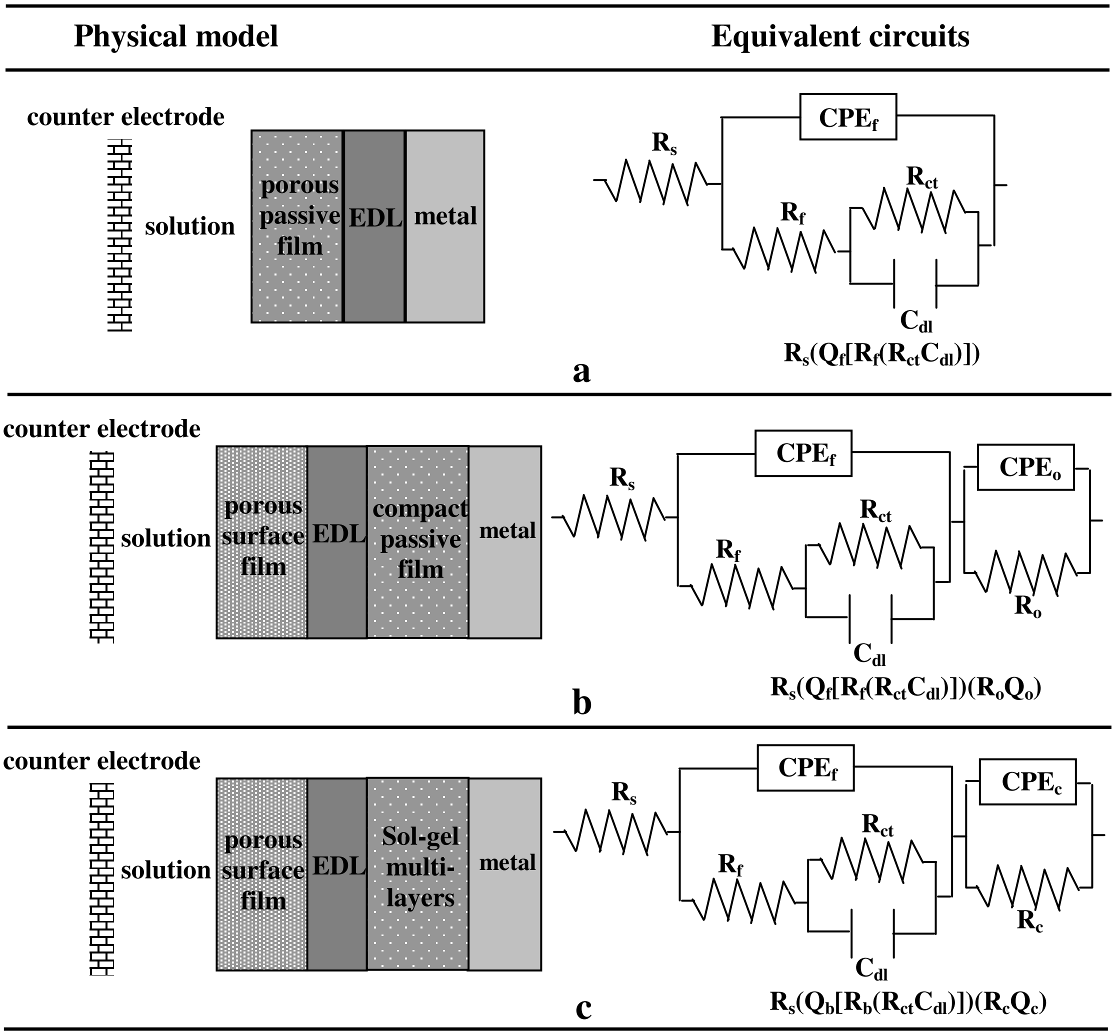

R_s, resistance of the electrolyte solution, C_{dl}, capacitance of the electrical double layer (EDL), R_{ct}, charge transfer resistance of EDL, Q_f, constant phase element (CPE) of the porous surface film, R_f, resistance of the porous surface film, Q_o, CPE of the oxide/hydroxide layers formed by acid pretreatment, R_o, resistance of the oxide/hydroxide layers formed by acid pretreatment, Q_c, CPE of the sol-gel multilayer coatings, R_c, resistance of the sol-gel multilayer coatings,

Figure 7.16 Three physical models and the corresponding equivalent circuits used for fitting the EIS spectra of different test coupons. Equivalent circuit a used for the pristine coupons, equivalent circuit b for the hydroxylated, the passivated, equivalent circuit c the Ti oxide/butoxide-coated coupons.

on the hydroxylated coupon surface (Wallinder et al., 1999). On the other hand, R_o values of both the passivated and the hydroxylated coupons decrease with exposure time, indicating that the passivating oxide/hydroxide layers are easily damaged by the synergistic effect of *D. desulfuricans* and the biogenic sulfide anions. The values of R_{ct} of the hydroxylated and the passivated coupons both undergo an apparent decrease with the increase in exposure time, and are close to those of the pristine coupons after 21 days of exposure, indicative of the initiation of pitting corrosion on the hydroxylated and the passivated coupons. Another important parameter is the resistance of the porous surface film, R_f, which originates from the deposition of the bacterial cells and iron sulfide products on the coupon surface. The values of R_f of the hydroxylated and the passivated coupons are independent of exposure time, and fluctuate with exposure time. This observation is consistent with the fact that the biofilm development is a dynamic process and the porous iron sulfide products are heterogeneously distributed on the coupon surface.

The EIS data of the Ti oxide/butoxide-coated coupons in the *D. desulfuricans* inoculated SSMB medium after various exposure times are shown in Figure 7.15g and 7.15h. The Ti oxide/butoxide-coated coupons undergo different corrosion processes in relative to the uncoated coupons due to the presence of well-defined multilayer Ti oxide/butoxide coatings on the coupon surface. In Nyquist plots (Fig. 7.15g), the diameters of depressed semicircles increase with time during the initial exposure periods, and reach the maximum value after 14 days of exposure. Thereafter, they show a slight decrease with time, but still remain at large values. These results suggest that the Ti oxide/butoxide coatings impart the desirable protective properties on the coupon surface. The stability of the coatings is further confirmed by the Bode phase angle plots of similar shape obtained throughout the exposure periods. The characteristic features of the respective Bode phase angle plot also reveal the existence of three relaxation time constants, attributable to the multilayer Ti oxide/butoxide coating (in the higher frequency region), the porous surface film (in the mid- to high frequency region) and EDL (in the lower frequency range). As the quantitative analysis results shown in Table 7.5, the values of the resistance of multilayer sol-gel coatings, R_c, are virtually more than 5.0 kΩ throughout the exposure periods, and appear to increase with time at certain period of exposure time, which is probably caused by the deposition of phosphate and calcium compounds on the surface (Ichinose et al., 1996, Li et al., 1994). Simultaneously, the charge transfer resistances, R_{ct}, of the Ti oxide/butoxide-coated coupons are also found to retain at large values throughout the exposure periods, indicating that localized corrosion does not occur on the Ti oxide/butoxide-coated coupons. In comparison with the oxide/hydroxide layers formed on the hydroxylated and the passivated coupons, it can be concluded that the well-defined multilayer Ti oxide/butoxide coatings are more stable and resistant to the synergistic effect of *D. desulfuricans* and the biogenic sulfide ions. These results further confirm that titanium alloys show remarkable resistance to biocorrosion by virtue of their tenacious oxide film (Schutz, 1991). The titanium oxide layers are reported to be attacked only by few substances, such as hot concentrated hydrofluoric acid and bromide (Schutz, 1992).

7.2.3.4 Cyclic polarization curves

Figure 7.17 shows the cyclic polarization curves of the Ti oxide/butoxide-coated and uncoated coupons after 21 days of exposure in the *D. desulfurican*s inoculated SSMB medium. For the pristine coupons, the onset of anodic current occurs at a potential of about -0.53 V (Fig. 7.17a). A narrow passivity zone appears in the potential range of ~-0.23 to ~0.25 V, where current increases slowly as potential increases. The onset of anodic current occurs at about -0.54 V (Fig. 7.17b) for the hydroxylated coupon, which is

Table 7.5 Fitting parameters of EIS spectra of different coupons after different exposure times in the SSMB medium inoculated with *D. desulfuricans* bacterium

Time (days)	Parameters / Samples	R_s (Ω)	R_f (kΩ)	Q_f		R_{ct} (kΩ)	C_{dl} (mF)	R_o (KΩ)	Q_o		R_c (kΩ)	Q_c		$\sum\chi^2*10^{-3}$
				Y_f*10^{-4} (Ω^{-1} s^n)	n_0				Y_o*10^{-3} (Ω^{-1} s^n)	n_1		Y_c*10^{-3} (Ω^{-1} s^n)	n_2	
3	Pristine[a]	13.22	0.246	20.98	0.724	2.011	0.479	–	–	–	–	–		0.486
	Hydroxylated[b]	14.91	0.314	2.339	0.708	1.477	15.04	3.39	1.525	0.597	–	–		1.175
	Passivated[b]	11.45	0.022	1.254	0.734	1.824	7.73	4.92	5.054	0.800	–	–		1.974
	Ti oxide/butoxide-coated[c]	11.94	0.071	1.311	0.883	3.08	5.38	–	–	–	5.50	0.847	0.571	1.720
7	Pristine	11.76	1.001	1.836	0.832	0.838	15.65	–	–	–	–	–		2.176
	Hydroxylated	11.74	0.199	0.895	0.837	0.980	24.57	2.083	1.630	0.579	–	–		1.154
	Passivated	11.02	0.167	1.503	0.728	1.385	7.58	4.30	7.116	0.809	–	–		1.707
	Ti oxide/butoxide-coated	12.28	0.340	1.363	0.801	3.116	8.31	–	–	–	6.62	1.419	0.593	1.206
14	Pristine	14.59	0.929	3.04	0.841	0.501	29.91	–	–	–	–	–		3.271
	Hydroxylated	12.16	0.275	6.859	0.666	0.633	74.3	1.011	5.088	0.652	–	–		0.809
	Passivated	13.43	0.261	2.788	0.692	0.703	23.96	2.604	7.631	0.720	–	–		1.895
	Ti oxide/butoxide-coated	11.82	0.224	1.362	0.800	3.292	7.34	–	–	–	5.72	1.507	0.604	1.246
21	Pristine	12.27	0.55	4.803	0.733	0.406	39.64	–	–	–	–	–		3.308
	Hydroxylated	12.08	0.166	3.551	0.795	0.541	53.03	0.518	4.037	0.507	–	–		4.937
	Passivated	12.81	0.227	1.701	0.737	0.586	26.93	2.092	7.433	0.632	–	–		0.632
	Ti oxide/butoxide-coated	12.27	0.247	1.690	0.792	2.356	14.30	–	–	–	5.46	1.592	0.613	0.944

a) The EIS spectra of the pristine coupons were fitted with equivalent circuit (a) in Figure 7.16,

b) The EIS spectra of the hydroxylated and the passivated coupons were fitted with equivalent circuits (b) in Figure 7.16,

c) The EIS spectra of the Ti oxide/butoxide-coated coupons were fitted with equivalent circuits (c) in Figure 7.16.

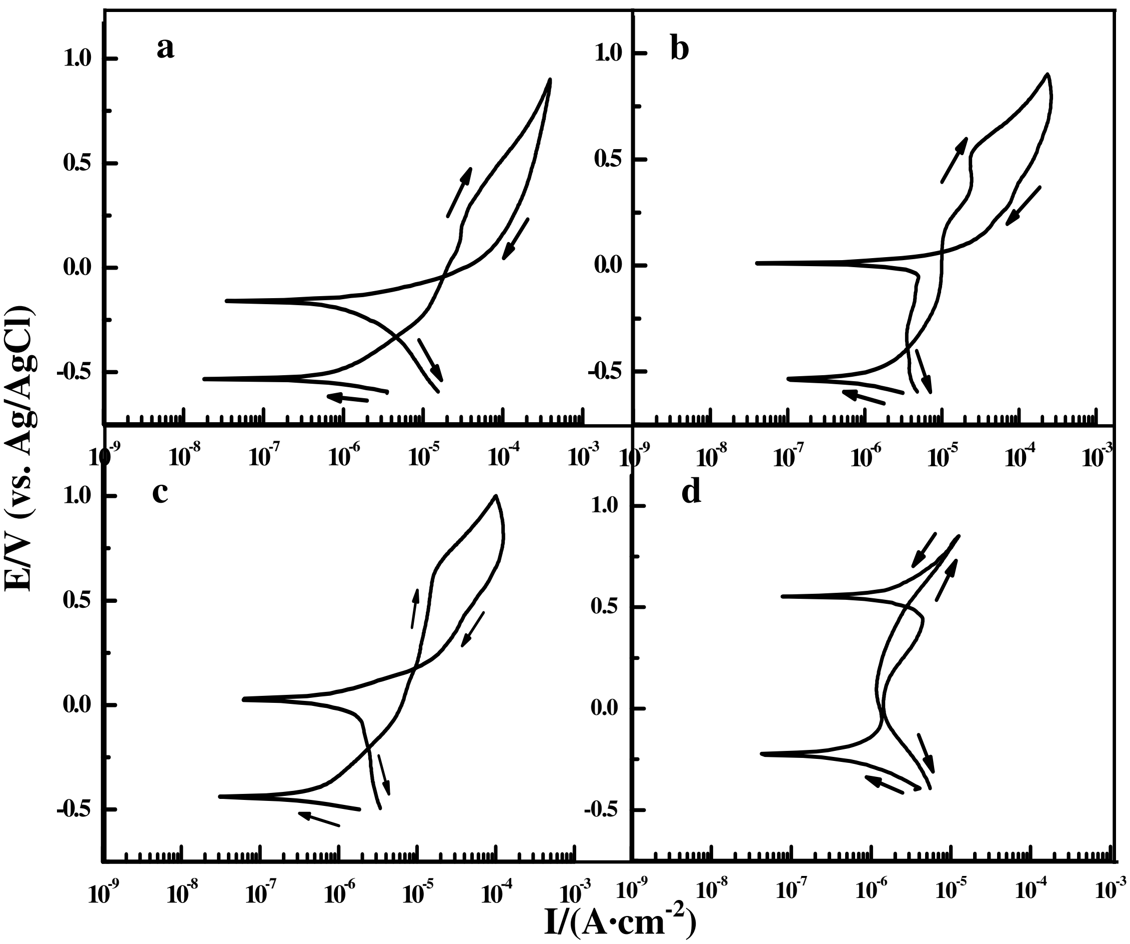

Figure 7.17 Cyclic polarization curves of (a) the pristine, (b) the hydroxylated, (c) the passivated, and (d) the Ti oxide/butoxide-coated coupons after 21 days of exposure in the SSMB medium inoculated with *D. desulfuricans* bacterium.

close to that of the pristine coupons, and a wide passivity region in the range of ~-0.21 to ~0.55 V appears owing to the presence of oxide/hydroxide layers by acid pretreatment. A slightly positive onset of anodic current (~-0.44 V) and a wider passivity region in range of ~ -0.18 to ~0.66 V indicates the oxide/hydroxide layers on the passivated coupons are relatively more resistant to biocorrosion. The positive hysteresis in cyclic polarization curves of the uncoated coupons indicates the detrimental effect of *D. desulfuricans* and biogenic sulfide ions on the passivity of the passive film on the coupon surface. However, a more positive voltage onset of anodic current (~-0.21 V) and a wider passive region (~-

0.18 to ~0.85 V) can be observed in the cyclic polarization curves of the Ti oxide/butoxide-coated coupons (Fig. 7.17d), indicative of the inert properties of the Ti oxide/butoxide multilayer coatings. The negative hysteresis also suggests the absence of pitting corrosion on the Ti oxide/butoxide-coated coupons. All these results confirm that the well-defined Ti oxide/butoxide coatings are more resistant, stable and tenacious to the synergistic effect of the bacterial cells and biogenic sulfide ions than the oxide/hydroxide layers formed on the coupon surface by acid pretreatment.

7.2.3.5 SEM observations and EDX analysis

SEM images were captured on all test coupon surfaces to validate of the adhesion of microorganisms and to reveal surface morphology after bacterial colonization and deposition of sulfide compound. EDX spectra of all test coupons were recorded to verify the mechanisms of film formation and to determine the elemental composition of corrosion deposits. Figure 7.18 shows the representative SEM images of all test coupons after 3 and 21 days of exposure to the biotic SSMB medium containing *D. desulfuricans*, as well as the representative EDX spectra recorded for the 21-day-exposed test coupons.

As shown in Figure 7.18a, high density of curved-rod shape *D. desulfuricans* cells, either individually or in small-size bacterial clusters, is unevenly distributed on the pristine coupon surface after 3 days of exposure. Black corrosion products and minor micropits are also spotted on the coupon surface. On increasing the exposure time to 21 days, the pristine coupon surface is covered with dense, brittle and lumpy deposits of corrosion products. Bacterial cells associated with amorphous exopolymeric materials can be clearly seen among the corrosion products. At the same time, cracks are also observed on the coupon surface due to the discontinuities of the biofilm/corrosion product layers. It has been reported that the discontinuities in the surface film favor localized attack of aggressive ions, such as Cl^- and S^{2-}, leading to the initiation of pitting or crevice corrosion (Moreno et al., 1991). EDX spectrum was recorded at the tubercles on the pristine coupons (Fig. 7.18b). In addition to the main elements of C, O, Fe, S, Cl, and Cr, other elements of Si, P, Mn, Ni, Na and Mg are also detected. The prominent S and Fe peaks in the EDX spectra indicate that the black corrosion products are iron sulfide, which commonly exists in the form of mackinawite (FeS_{1-x}). It is noteworthy that in light of the pH of medium (about 7.0) used, the iron sulfide could be Kansite (Fe_9S_8), which has very poor protective properties (Scott and Davies, 1992, De Cristofaro et al., 1986). The large amounts of C (63.74%) and O (14.40%) are associated with the organic materials of the cell bodies (bacteria and EPS). A phosphorus (P) peak in the EDX spectrum can also be related to the bacterial cells, as all living organisms contain ATP (Little et al., 2006). The appearance of Cl peak in the EDX spectrum reveals the ingress of aggressive Cl^- ions at the tubercle sites. Likewise, numerous and distinguishable bacterial cells are also found to colonize on the surface of the hydroxylated and passivated coupons after 3 days of exposure (Figs. 7.18c and 7.18e), whereas the occurrence of micro-pitting corrosion is indiscernible on the acid-pretreated coupon surface due to the presence of oxide/hydroxide layers. Upon prolonging the exposure time to 21 days, the heterogeneous surface films of black corrosion products and bacterial cells are observed on the hydroxylated and the passivated coupons. EDX spectrum was recorded at the crack sites on the hydroxylated coupons (Fig. 7.18d). The characteristics of EDX spectrum of the hydroxylated coupons are similar to that of the high content of Cl element indicates that aggressive Cl^- ions attack the coupon surface

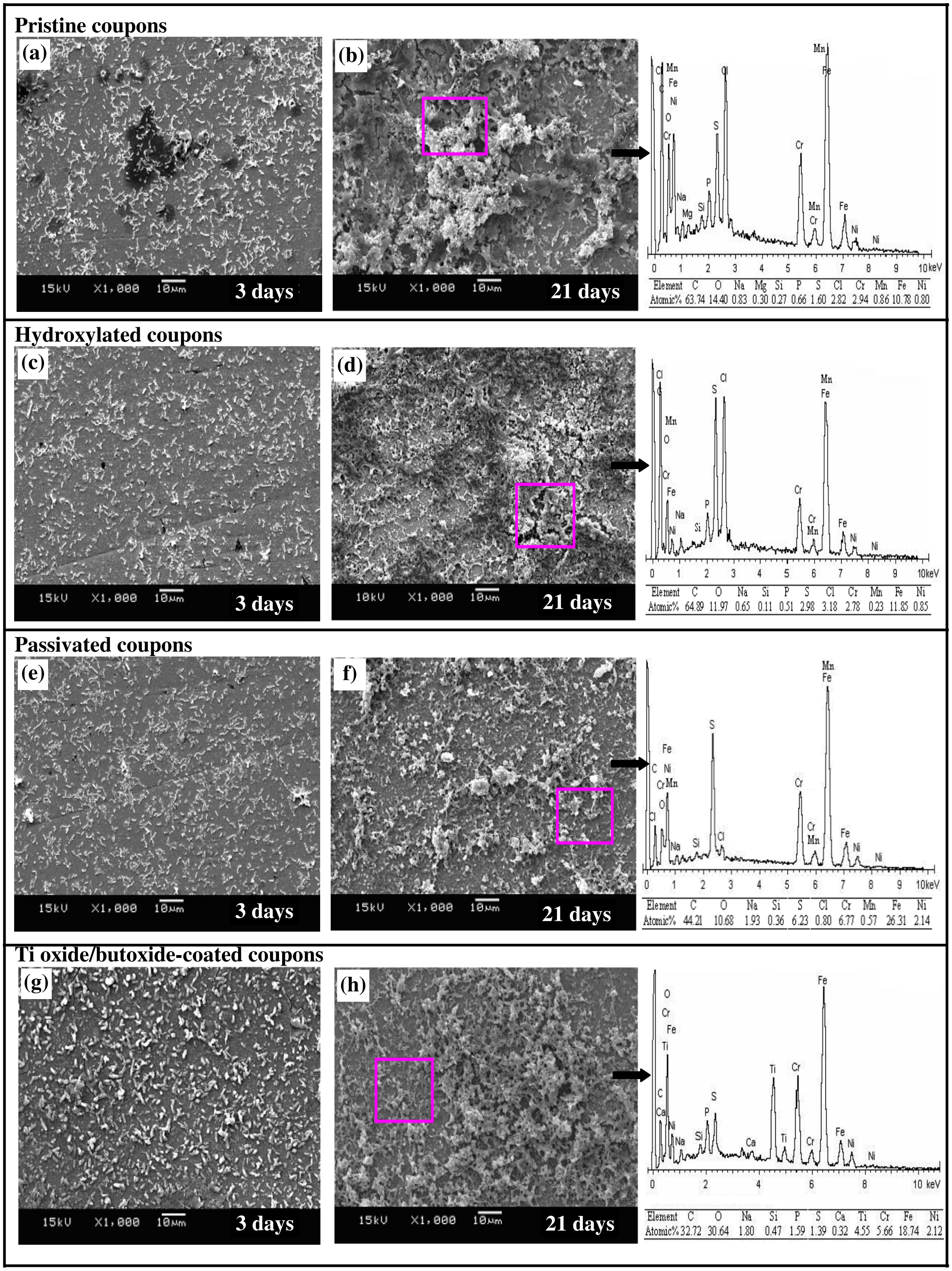

Element	C	O	Na	Mg	Si	P	S	Cl	Cr	Mn	Fe	Ni
Atomic%	63.74	14.40	0.83	0.30	0.27	0.66	1.60	2.82	2.94	0.86	10.78	0.80

Element	C	O	Na	Si	P	S	Cl	Cr	Mn	Fe	Ni
Atomic%	64.89	11.97	0.65	0.11	0.51	2.98	3.18	2.78	0.23	11.85	0.85

Element	C	O	Na	Si	S	Cl	Cr	Mn	Fe	Ni
Atomic%	44.21	10.68	1.93	0.36	6.23	0.80	6.77	0.57	26.31	2.14

Element	C	O	Na	Si	P	S	Ca	Ti	Cr	Fe	Ni
Atomic%	32.72	30.64	1.80	0.47	1.59	1.39	0.32	4.55	5.66	18.74	2.12

Figure 7.18 Representative SEM images of (a, b) the pristine coupons, (c, d) the hydroxylated coupons, (e, f) the passivated coupons, and (g, h) the Ti oxide/butoxide-coated coupons after 3 and 21 days exposure in the biotic SSMB medium EDX spectra correspond to the labeled area on the 21-day-exposed coupons.

pristine coupons, except for a slight change in elemental compositions. It has been reported that the simultaneous actions of bacterial cells, bacterial metabolites (such as S^{2-}) and chlorides (Cl^{-}) enhance localized attack (Lee et al., 1995, Little et al., 2006). EDX spectrum of the passivated coupons reveals the deposition of dense iron sulfide layer on the coupon surface (Fig. 7.18f). Comparison of the SEM images of the three uncoated coupons, no apparent difference is discernible on the bacterial attachment and colonization on the coupon surface. Although microbial colonization of metal surfaces is considered to be a crucial step in initiating biocorrosion, the factors determining cell adhesion are still obscure.

In the case of Ti oxide/butoxide-coated coupons, the bacterial colonization occurs much faster than that of the uncoated coupons. Hence, a thin and patchy biofilm forms on the coupon surface after 3 days of exposure in the *D. desulfuricans* inoculated SSMB medium (Fig. 7.18g). This is in good agreement with the previous conclusion that bacterial adhesion occurs rapidly on titanium surfaces, since titanium does not display any toxicity towards the organisms (Videla et al.,, 1992). After 21 days of exposure, the coupon surface is covered with a heterogeneous and thick biofilm (Fig. 17.18h). EDX spectrum of the Ti oxide/butoxide-coated coupons reveals the difference in elemental compositions as compared to the uncoated coupons. The appearance of Ti peak and the increase in the relative amount of O in the EDX spectrum are obvious due to the presence of multilayer Ti oxide/butoxide coatings (Fig. 7.18h). The appearance of Ca peak and the increase in the relative amount of P are probably associated with the deposition of apatite (Advincula et al., 2007, Li et al., 1993, 1994).

To assess the corrosion damage beneath the deposits on all test coupons and to validate the bioactive properties of the sol-gel coatings, SEM, coupled with EDX, was used to measure the test coupons after removal of bacterial cells and corrosion products. As shown in Figure 7.19a, some micropits can be clearly seen on the pristine coupon surface after 3 days of exposure, indicative of the initiation of pitting corrosion. Extensive micro-pits and crevice are visible on the coupon surface after 21 days of exposure (Fig. 7.19b). Similar results are obtained on the hydroxylated and the passivated coupons (not shown). EDX spectra further confirm the implication of aggressive Cl^- and S^{2-}anions in triggering the localized deterioration of stainless steel. For the Ti oxide/butoxide-coated coupons, despite of the accumulation of the heterogeneous biofilms and inorganic deposits, no pitting or crevice corrosion can be observed on the coupon surface (Figs. 7.19c and 7.19d), indicative of the high stability of Ti oxide/butoxide coatings. This result is consistent with the aforementioned electrochemical studies. On the other hand, the Ti oxide/butoxide-coated surface seems to become rougher with exposure time, associated with the deposition of apatite. The appearance of phosphorous (P) and calcium (Ca) in the EDX spectra confirm the existence of apatite nucleation. Because of the nature of the hydrated Ti-OH network in the Ti oxide/butoxide derived film, the electrostatic attraction of Ca and hydrogen bonding, or chelating of phosphate group, results in the accumulation of Ca and P ions within the hydrated titania (Li and Groot, 1993). Hence, it has been widely recognized that the precipitation and dissolution of Ca and P ions on the Ti oxide/butoxide-coated coupon surface is a dynamic process (Peltola et al., 1998). It has also been reported that titanium oxide layer acts as an excellent gettering surface for phosphorous adsorption (Hwang et al., 2002). Thereby, the deposition of Ca and P on the titanium oxide could be due to the high reactivity of O with Ti, as well as the electrostatic attraction for Ca. These results further demonstrate the bioactive properties of the sol-gel coatings. The deposition of apatite on the Ti oxide/butoxide coatings can help in explaining the increase in the R_c value with exposure time in the EIS study.

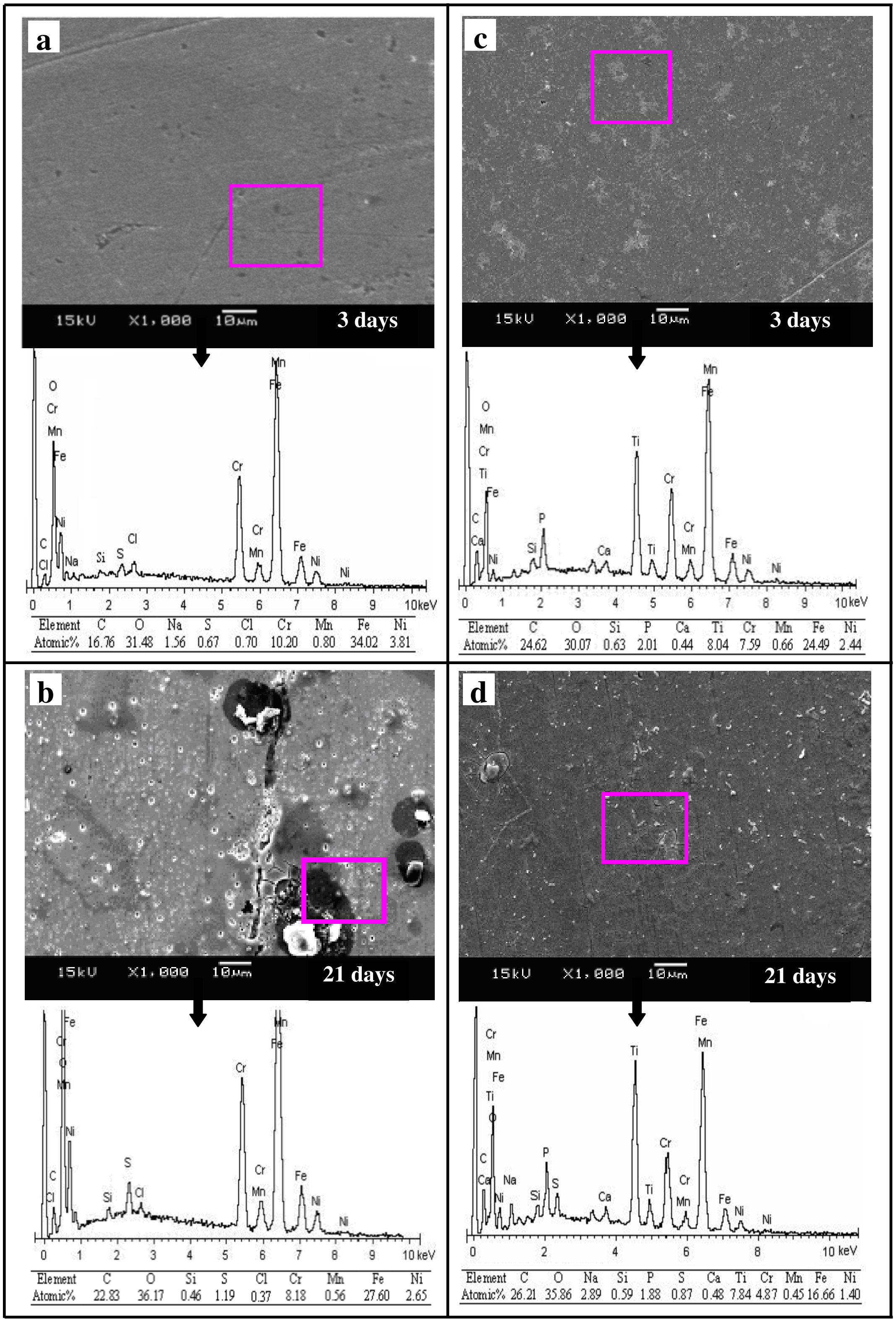

Element	C	O	Na	S	Cl	Cr	Mn	Fe	Ni
Atomic%	16.76	31.48	1.56	0.67	0.70	10.20	0.80	34.02	3.81

Element	C	O	Si	P	Ca	Ti	Cr	Mn	Fe	Ni
Atomic%	24.62	30.07	0.63	2.01	0.44	8.04	7.59	0.66	24.49	2.44

Element	C	O	Si	S	Cl	Cr	Mn	Fe	Ni
Atomic%	22.83	36.17	0.46	1.19	0.37	8.18	0.56	27.60	2.65

Element	C	O	Na	Si	P	S	Ca	Ti	Cr	Mn	Fe	Ni
Atomic%	26.21	35.86	2.89	0.59	1.88	0.87	0.48	7.84	4.87	0.45	16.66	1.40

Figure 7.19 Representative SEM images of the (a, b) the pristine, and (c, d) the Ti oxide/butoxide-coated coupons with the biofilm removal after 3 and 21 days of exposure The EDX spectra correspond to the labeled area on the 21-day-exposed coupons.

7.3 Summary

Anaerobic corrosion of 304 SS was found to be significantly accelerated by *D. desulfuricans* in the biotic SSMB medium due to the occurrence of extensive localized corrosion underneath the deposits of bacterial cells and sulfide films. The concentration of biogenic sulfide ions was determined with a novel polarogramic method. XPS studies revealed that sulfide films were mainly composed of mackinawite and pyrite, and mackinawite gradually converted to pyrite with exposure time in the biotic medium. To minimize localized corrosion of 304 SS coupons, LBL surface sol-gel processing was adopted to build up the well-defined multilayer Ti oxide/butoxide coatings on the coupon surface. Comparative studies of the corrosion behavior between the Ti oxide/butoxide-coated and the uncoated coupons were performed in the *D. desulfuicans* inoculated SSMB medium. Electrochemical studies indicated that although the passivated coupons exhibit relatively high corrosion resistance during the initial exposure periods, the corrosion of the uncoated coupons became accelerated under the synergistic attack of the bacterial cells and biogenic sulfide ions upon prolonging the exposure. Not only did the passivity of the multilayer Ti oxide/butoixde coatings on the coupon surface remain stable under the same harsh environments, the passivity was also enhanced with exposure time due to the deposition of calcium and phosphorous compounds. Furthermore, SEM observation coupled with cyclic polarization curves revealed that no pitting corrosion occurred on the Ti oxide/butoxide-coated coupons, in comparison to the presence of extensive micropitting corrosion and crevice corrosion on the uncoated coupons. The bioactive properties of sol-gel coatings were further verified by the accumulation of apatite with EDX spectra.

CHAPTER 8

CONCLUSIONS AND FURTHER STUDIES

8.1 Conclusions

Microbiologically influenced corrosion of metallic materials and its inhibition are important issues in corrosion science and engineering. The focus of this study is on the investigation of the influence of marine aerobic (*Pseudomonas* NCIMB 2021) and anaerobic (*Desulfovibrio desulfuricans* ATCC 27774) bacteria on the corrosion of 304 stainless steel and 70/30 Cu-Ni alloy by surface analytical and electrochemical methodologies. The project also attempts to develop alternative methods to protect the steel and copper alloys from the attack of microorganisms by novel surface modification techniques. The following conclusion could be obtained:

In the presence of aerobic *Pseudomonas* NCIMB 2021 bacterium, the corrosion of 304 SS was intensified and accelerated in nutrient-rich simulated seawater. Pitting corrosion was found to occur underneath the heterogeneous biofilms due to the synergistic effect of aggressive chloride ions and the colonization of bacterial cells and their EPS. The pits on the coupon surface could be quantified through AFM sectional analyses, and the depth of pits increased linearly with exposure time. The XPS results revealed that the elemental composition in the outermost layer of the surface films underwent a substantial change induced by the bacterial colonization with an enrichment of Cr and a depletion of Fe, which was probably correlated with the pitting corrosion under the biofilms. In comparison, 304 SS was found to remain stable in the nutrient-rich medium with a thin passive film of oxides/hydroxides.

The involvement of aerobic *Pseudomonas* NCIMB 2021 bacterium in the corrosion process of 70/30 Cu-Ni alloys was characterized. The corrosion rate of the alloy coupons was found to undergo a notable increase with exposure time due to micro-pitting corrosion underneath the bacterial clusters or the discrete biofilms, and reached higher by as much as 14 folds than that of the sterile control coupons after 42 days of exposure. XPS results revealed the correlation of the corrosion behavior of the alloy coupons with the oxide film formation on the alloy surface. The structure of the surface film was altered by the implication of the bacterial cells and the EPS in the formation process of the oxide films. The deterioration of the existent passive film or the inhibition of the passive film formation by the *Pseudomonas* bacteria was also manifested. In comparison, the corrosion rate of the alloy coupons gradually decreased with exposure time in the sterile medium due to the formation of a protective duplex oxide layers.

A novel surface modification technique was developed to impart antibacterial and anticorrosive properties onto the surface-oxidized Cu-Ni alloy to inhibit MIC, which was achieved in three steps: (i) silanization of the substrate surface by a self-assembled silane coupling agent (CTS) to act as initiators, (ii) immobilization of pyridine groups by chemical reactions between methyl-chloride groups and 4,4'-bipyridine, (iii) the quaternization of the terminal pyridine groups into pyridinium groups by coupling with benzyl chloride. The functionalized substrate exhibited high efficiency in prevent the bacterial attachment as well as a desirable good resistance to MIC by the coupled organic layers during the initial exposure periods. However, both the bactericidal activity and the corrosion-inhibition ability were reduced due to the occurrence of partial spalling of the coupled organic layer on the functionalized coupons after a long-term exposure. In addition, the oxide layers of Cu-Ni alloys were verified to be vulnerable to MIC, although it could decrease corrosion rate of the Cu-Ni alloy in the sterile medium.

Anaerobic corrosion of 304 SS was found to be significantly accelerated by *D. desulfuricans* in the biotic SSMB medium due to the occurrence of localized corrosion underneath the deposits of bacterial cells and sulfide films. The concentration of biogenetic sulfide ions was determined by a novel polarogramic method to be in a range of ~0.3 to ~45 ppm. XPS results revealed that sulfide films were mainly composed of mackinawite (FeS) and pyrite (FeS_2), and mackinawite gradually converted to pyrite with exposure time in the biotic medium. Thus, well-defined multilayers of Ti oxide/butoxide coatings were built up on the steel coupon surface with layer-by-layer sol-gel processing to minimize MIC. Electrochemical and SEM results demonstrated that not only was the passivity of the multilayer Ti oxide/butoixde coatings on the coupon surface remained stable under the harsh environments, the passivity was also enhanced with exposure time due to the deposition of calcium and phosphorous compounds. The thin and compact film Ti oxide/butoxide coatings were also verified to prevent the substrate surface from the localized corrosion under the conditions tested. The bioactive properties of the Ti oxide/butoxide coatings could be further optimized with other compositions or thickness to improve their performance in combating MIC. In addition, the passivity of the uncoated coupons were found to be compromised under the synergistic interactions of the bacterial cells and biogenetic sulfide ions, due to the increase in the corrosion rate and the presence of localized corrosion on the coupon surface.

8.2 Further studies

Three aspects are recommended for further studies. The first is to measure the bacterial adhesion force of the aerobic *Pseudomonas* and anaerobic *D. desulfuricans* bacteria on the surface of 304 SS and 70/30 Cu-Ni alloys by AFM. The AFM tip-cell interaction of forces over the bacteria and biofilm can be in terms of a force-distance curve between the AFM tip and bacterium surface. Another measurement is the bacterial adhesion force between the cell and substratum in order to better understand the biofilm formation process. Through immobilizing the bacterial cells on the AFM tip, the interaction forces between cells and substrate might be obtained. The measurement of adhesion force with AFM has been widely carried out to find out the mechanisms of the biofilm formation (Camesano and Logan, 2000; Dupres et al., 2005).

The second aspect is to analyze the Extracellular polymeric substance (i.e. EPS) of aerobic *Pseudomonas* and anaerobic *D. desulfuricans* bacteria used in this study. EPS secreted by bacteria is the matrix for bacteria embedding to form a biofilm on the metal surface, and has been reported to play a significant role in MIC. Binding of metal ions by EPS has been proposed as the main mechanism for MIC in recent years. To realize this, the 'free' EPS in the bulk solution and the 'biofilm' EPS are extracted and purified by the methods reported in previous studies (Zhang et al., 1999; Froslashlund et al., 1996). The extracted EPS was characterized with FTIR, XPS or gel electrophoresis etc. The detailed information on EPS could reveal the contributions of each component of EPS in the process of corrosion and biofilm formation, especially on the electrochemical reduction nature of EPS.

The final aspect for further studies is to develop antibacterial materials to inhibit the MIC of the metallic coupons. Antibacterial property of silver has been known for centuries. As silver is non-toxic to human beings, it has been used for healing wounds as well as water purification in swimming pools. This makes silver an ideal antibacterial element. Hence, an Ag-coated stainless steel can be developed using electroless-deposition methods on the polymeric layers, which will be firstly immobilized onto stainless steel as polymeric precursors as those described in chapter 6 and 8. The Ag-coated stainless steel is expected to exhibit significant antibacterial property, and the corrosion resistance is expected to be improved by the polymeric layers.

REFERENCE

1. Abreu C.M., Cristóbal M.J., Losada R., Nóvoa X.R., Pena G., Pérez M.C., 2006. *Electrochim. Acta*, 51, 1881-1890.
2. Advincula M.C., Petersen D., Rahemtulla F., Advincula R., Lemons J.E., 2007. *J. Biomed. Mater. Res. B Appl. Biomater.*, 80B, 107-120.
3. Alamr A., Bahr D.F., Jacroux M., 2006. *Corros. Sci.*, 48, 925-936.
4. Al-Darbi M. M., Muntasser Z.M., Islam M.R., 2002. *Energ. Source*, 24, 1009-1018.
5. Al-Hajji J.N., Reda M.R. 1994 *J. Electrochem. Soc.* 141, 1432-1439.
6. Al-Hajji J.N., Reda M.R., 1995. *J. Electrochem. Soc.,* 142, 2944-2953.
7. American Public Health Association (APHA), 1992. *Standard methods for the examination of water and wastewater,* 19th ed. Washington. DC, USA.
8. Angell P., Luo J.S., White D.C., 1995. *Corros. Sci.*, 37, 1085-1096.
9. ASTM G61, Test method for conducting cyclic potentiodynamic polarization measurements for localized corrosion susceptibility of iron-, nickel-, or cobalt-based alloys, 2003.
10. Atrens A., Jin S., 1987. *Appl. Phys. A – Mater.,* 42, 149-165.
11. Atrens A., Lim A.S., 1990. *Appl. Phys. A – Mater.,* 51, 411-418.
12. Baker M.A., Castle J.E., 1993. *Corros. Sci., 35*, 667-682.
13. Baker P.W., Ito K, Watanabe K., 2003. *Environ microbial.*, 5, 925-932.
14. Barnes L.M., M.F. Lo., Adams M.R., Chamberlain A.H., 1999. *Appl. Environ. Microbio.,* 65, 4543-4548.
15. Barton L.L., 1997. *Sulfate-reducing Bacteria.* International workshop on industrial biofouling and biocorrosion. Mulheim, Germany.
16. Barton L.L., Tomei F.A., In: Baton L.L. (ed.) *Sulfate-reducing Bacteria.* Plenum Press, New York, pg. 1-32.
17. Beccaria A.M., Castello G., Poggi G., 1995. *Brit. Corros. J.*, 30, 283-287.
18. Beech I. B., Gaylarde C. C., 1999. *Revista de Microbiologia,* 30, 177-190.
19. Beech I.B., 2003. *Microbiol. Today,* 30, 115-117.
20. Beech I.B., Cheung C.W.S., 1995. *Intl. Biodeter. Biodegrad.,* 35, 59-72.
21. Beech I.B., Cheung C.W.S., Johnson D.B., Smith J.R., 1996. *Biofouling,* 10, 65-77.
22. Beech I.B., Gaylarde C.C., 1991. *Intl. Biodeter.*, 27, 95-107.
23. Beech I.B., Gubner R., Zinkevich V., Hanjangsit L., 2000. *Biofouling,* 16, 93-104.
24. Beech I.B., Hanjagsit L., Kalaji M., Neal A.L., Zinkevich V., 1999. *Microbiol.,* 145, 1491-1497.

25. Beech I.B., Sunner J., 2004. *Curr. Opin. Biotechnol.,* 15, 181-186.
26. Beech I.B., Smith J.R., Steele A.A., Penegar I., Campbell S.A., 2002. *Colloid Surface B: Biointerfaces,* 23, 231-247.
27. Beech I.B., Zinkevich V., Hanjangsit L., Gubner R., Avci R., 2000. *Biofouling,* 15, 3-12.
28. Beech I.B., Zinkevich V., Tapper R.C., Gubner R., 1998. *Geomicrobiol. J.*, 15, 119-132.
29. Been J., Grauman J.S., 2000. Titanium and titanium alloy. In: *Uhlig's Corrosion Handbook,* 2nd ed., Revie R.W. Ed., John Wiley & Sons, Inc.
30. Benedetti A.V., Sumodjo P.T.A., Nobe K., Cabot P.L., Proud W.G., 1995. *Electochimi. Acta*, 40, 2657-2668.
31. Bidwell J.P., Spotte S., 1985. In: *Simulated Seawaters: Formulas and Methods*, Jones and Bartlett Publishers, Boston, USA, pg. 14.
32. Bird C.I., Kuhn A.T., 1981. *Chem. Soc. Rev.,* 10, 49-82.
33. Blunn G., 1986. In: Barry S., Houghton D.R., Llewellyn G.C., O'Rear C.E., (eds.) *Biological Fouling of Copper and Copper Alloys.* CAB international, Slough, pg. 567-575.
34. Bockris J.O.M, Pentland N. 1952. *Trans. Faraday Soc.,* 48, 833-839.
35. Boivin J, and Costerton J.W., 1991. In: Rossmore H.W. (ed.) *Biodeterioration and Biodegradation.* Elsevier Applied Science, London, England, pg. 53-62.
36. Boopathy R., Daniels L., 1991. *Appl. Environ. Microbiol.,* 57, 2104–2108.
37. Booth G.H., Tiller A.K., 1960. *Trans Faraday Soc.,* 56, 1689-1696.
38. Booth G.H., Tiller A.K., 1962. *Trans. Faraday Soc.,* 58, 110-115.
39. Booth G.H., Tiller A.K., 1968. *Corros. Sci.,* 8, 583-600.
40. Borenstein S., 1994. In: *Microbiologically Influenced Corrosion Handbook,* Woodhead Publishing Ltd, Cambridge, UK, pg. 23-24, 113-160.
41. Boukamp B.A., 1986. *Solid state Ionics,* 20, 31-44.
42. Boukamp B.A., 1993. In: *Equivalent Circuit Users Manual,* 2nd ed., University of Twente, Netherlands.
43. Brandon D.M., Fillo J.P., Morris A.E., Evans J.M., 1995. In: *Biocide and Corrosion Inhibition Use in the Oil and Gas Industry: Effectiveness and Potential Environmental Impacts*. SPE 29735, Society of Petroleum Engineers.
44. Bremer P.J., Geesey G.G., 1991a. *Appl. Environ. Microbiol.*, 57, 1956-1962.
45. Bremer P.J., Geesey G.G., 1991b. *Biofouling*, 3, 89-100.
46. Bremer P.J., Geesey G.G., Drake B., 1992. *Curr. Microbiol.,* 24, 223–230.
47. Breur H.J.A., de Wit J.H.W., van Tumhout J., Ferrari G.M., 2002. *Electrochim. Acta,* 47, 2289-2295.
48. Briggs D., Seah M.P., 1990. In: *Practical Surface Analysis,* John Wiley & Sons Ltd.: London.

49. Brözel V.S., Cloete, T.E., 1989. *The Role of Sulphate-reducing Bacteria in Microbial Induced Corrosion.* Paper SA.11/12/89, 30–36.

50. Bryant R.D., Jansen W., Bovin J., Laishley E.J., Costerton J.W., 1991. *Appl. Environ. Microbiol.*, 57, 2804-2809.

51. Bryant, R.D., and Laishley, E.J. 1989. *Can. J. Microbiol.* 36, 259–264.

52. Busalmen J.P., Frontini M.A., de Sánchez S.R., 1998. In: Campbell S.A., Campbell N., Walsh F.C. (Eds) D*evelopments in Marine Corrosion*. Cambridge: Royal Society of Chemistry, pg.119-131.

53. Busalmen J.P., Vázquez M., de Sánchez S.R., 2002. *Electrochim. Acta,* 47, 1857-1865.

54. Camesano T.A., Logan B.E. 2000, *Environ. Sci. Technol.* 34, 3354-3362.

55. Caldwell D.E., Korber D.R., Lawrence J.R., 1992. *J. Microbiol. Methods*, 15, 249-261.

56. Campbell S., Geesey G., Lewandowski Z. et al., 2004. *Corrosion,* NACE, 60, 670-680.

57. Cen L., Neoh K.G., Kang E.T., 2003. *Langmuir,* 19,10295-10303.

58. Chamberlain A.H.L., Garner B.J., 1988. *Biofouling,* 1, 79-96.

59. Chan C.S., de Stasio G., Welch S.A., Girasole M., Frazer B.H., Nesterova M.V., Fakra S., Banfield J.F., 2003. *Science,* 303, 1656-1658.

60. Chan K.Y., Xu L.C., Fang H.H.P., 2002. *Environ Sci Technol.*, 36, 1720-1727.

61. Chen G., Clayton C.R., 1997. *J. Electrochem. Soc.*, 144, 3140-3146.

62. Chen G., Clayton C.R., 1998. *J. Electrochem. Soc.*, 145, 1914-1922.

63. Chen G., Palmer R.J., White D.C., 1997. *Biodegradation,* 8, 189-200.

64. Chiorse W.C., 1988. In: A.J.B. Zehnder (ed.) B*iology of Anaerobic Microorganisms*, John Wiley, New York, pg. 305-331.

65. Chongdar S., Gunasekaran G., Kumar P., 2005. *Electrochimica Acta,* 50, 4655-4665.

66. Choudhary S.G., 1998. *Hydrocarb Process*, pg. 91-102.

67. Christense B.E., Characklis W.G., 1990. In: Characklis W.G. and Marshall K.C. (eds.) *Biofilms*. Wiley, New York, pg. 93-130.

68. Coetser S. E., Cloete T. E., 2005. *Crit. Rev. Microbiol.*, 31, 213–232.

69. Compère C., Bellon-Fontaine M.N., Bertrand P., Costa D., Marcus P., Poleunis C., Pradier C.M., Rondot B., Walls M.G., 2001. *Biofouling,* 17, 129-145.

70. Copello G.J., Teves S., Degrossi J., D'Aquino M., Desimone M.F., Diaz L.E., 2006. J. *Ind. Microbiol. Biotechnol.*, 33, 343-348.

71. Cord-Ruwisch R., Widdel F., 1986. *Appl. Microbiol. Biotechnol.,* 25, 169-174.

72. Costello J.A., 1974. *South Af. J. Sci.,* 70, 202-204.

73. Costerton J.W., 1994. In: H.C. Fleming, G.G. Geesey (eds.) *Biofouling and Biocorrosion in Industrial Water Systems* , Springer-Verlag, New York, , pg. 1-14.

74. Costerton J. W., Irvin R. T., Cheng K. J.; 1981. *Ann. Rev. Microbiology.* 35: 399-424.

75. Costerton J.W., Lewandowski Z., Caldwell D.E., Korber D.R., Lappin-Scott H.M., 1995. *Ann. Rev. Microbiol.,* 49, 711-745.

76. Costerton J.W., Stewart P.S., Greenberg E.P., 1999. *Science,* 284, 1318-1322.

77. Coutinho C.M.L.M., Magalhaes F.C.M., Jorge T.C.A., 1993. *Biofouling*, 7, 19-27.

78. Cragnolino G., Tuovinen O.H., 1984. *Intl. biodeterio.,* 20, 9-18.

79. Critchley M.M., Cromar N.J., McClure N.C., Fallowfield H.J., 2003. *J. Appl. Microbiol*., 94, 501-507.

80. Crolet, J.L., 1992. *Oceanol. Acta,* 15, 87-94.

81. Daumas S., Massiani Y., Crousier J., 1988. *Corr. Sci.*, 28, 1041-1050.

82. De Becdelievre A.M., Duret-Thual C., Vouagner D., Devaux R., 1994. *Corros. Sci.,* 36, 171-186.

83. De Beer D, Stoodley P., Roe F., Lewandowski Z., 1994. *Biotech Bioeng.,* 43, 1131-1138.

84. De Cristofaro N.B., Acosta C.A., Salvarezza R.C., Videla H.A., 1986. *Corrosion*, 42, 240-242.

85. De Mele M.F.L., de Saravia S.G.G., Videla H.A., 1995. In: Angell P, Boronstein S.W. et al. (eds.) *Proc. 1995 int. conf. on Microbially Influenced Corrosion*, NACE, Now Orleans, pg, 501-508.

86. Dexter, S. C. 1987. In: Metals Handbook, 9th Ed., Vol.13 – *Corrosion: Localized Biological Corrosion*, pg. 114-123.

87. Dexter S.C., 1995. In: Graylarde C.C., Videla H.A. (eds.) *Bioextraction and Biodeterioration of Metals.* Cambridge University Press, Cambridge, UK, pg. 129-140.

88. Dexter S.C., Chandrasekaran P. 2000. *Biofouling*, 15(4), 313-325.

89. Dexter S.C., Xu K., Luther G.W. 2003. *Biofouling*, 19(Suppl.), 139-149.

90. Dexter S.C., Duquette D.J., Siebert O.W., Videla H.A., 1991.*Corrosion*, 47, 308-318.

91. Dexter S.C., LaFontaine J.P. Corrosion, 54,851-861.

92. Dickinson W., Lewandowski Z., 1996. In: *Corrosion'96*. NACE, Houston, TX, paper No. 291.

93. Dong B.Y., Manolache S., E.B. Somers, Lee W.A.C., Denes F.S., 2005. *J. Appl. Polym. Sci.*, 97, 485-497.

94. Dowling N.J., Mittleman M.W., Danko J.C., 1990. In Proceedings of the International Congress, MIC Consortium, University of Tennessee, Knoxville, TN.

95. Dowling N.J., Guezennec J., 1997. In: Hurst C.J., Knudsen G.R., Stetzenbach L.D., Walter M.V. (eds.) M*anual of Environmental Microscopy,* ASM Press, Washington D.C., pg. 842-855.

96. Dowling N.J., Guezennec J., Lemoine M.L., Tunlid A., White D.C.,1988. *Corrosion,* 44, 869–874.

97. Drews M.J., Williams M., Barr M, 2000. *Ind. Eng. Chem. Res.,* 39, 4772-4783.

98. Druska P., Strehblow H.H., Golledge S., 1996. *Corros. Sci.*, 38, 835-851.

99. Duan J.Z., Hou B.R., Yu Z.G., 2006. *Mat. Sci. Eng. C,* 26, 624-629.

100.Dufrene Y.F., 2004. *Nat. Rev. Microbiol.*, 2, 451-460.

101. Dupres V., Menozzi F.D., Locht C. Clare B.H., Abbott N.L., Cuenot S., Bompard C., Raze D., Dufrene Y.F. 2005, *Nature Methods*, 2, 515-520.

102.El Dahan H.A., Mohamed T.Y.S., Abo El-Enin S.A., 1999. *Anti-Corros. Method*, 46, 358-363.

103.Edyvean R.G.J., Benson J., Thomas C.J., Beech I.B., Videla H.A., 1998. *Mat. Performance*, 37, 40-44.

104.Elachouri M., Hajji M.S., Kertit S., Essassi E.M., 1995. *Corros. Sci.*, 37, 381-389.

105.Enzien M.V., Pope D.H., Wu M.M., Frank J.F., 1996. *Corrosion/96,* NACE international, Houston, TX, paper No. 401.

106.Esterso M.A., Estrella C.N., Dolores de la Rosa M., Martinez-Trujillo R., Rosales M., Podesta J.J., 1992. *Mat. Sci. Forum*, 111-112, 85-90.

107. Fang H.H.P., Chan K.Y., Xu L.C., 2000. *J. Microbiol. Meth.,* 40, 89-97.

108. Fang H.H.P., Xu L.C., Chan K.Y., 2002. *Water Res.*, 36, 4709-4716.

109. Fang M., Kim C.H., Martin B.R., Mallouk T.E., 1999. *J. Nanoparticle Res.,* 1, 43-49.

110. Fauque G.D., Peck Jr. H.D., Murora J.J.G. et al., 1988. *FEMS microbial. Rev.,* 54, 299-344.

111. Fauque G.D., 1995. In: Barton L.L. (ed.) *Sulfate-reducing Bacteria.* Plenum Press, New York, pg. 217-241.

112. Féron D., Dupont I., 1998. In: Campbell S.A., Campbell N., Walsh F.C. (eds.), *Developments in Marine Corrosion*, Cambridge, Royal Society of Chemistry, pg. 89.

113. Feng Y., Teo W.K., Siow K.S., Hsieh A.K., 1996. *Corros. Sci.*, 38, 387-395.

114. Fleming H.C., 1996. In: *Microbially Influenced Corrosion of Materials,* Heitz E., Fleming H.C., Sand K.(eds.), Spring-Verlag, New York., pg. 5, 6-14.

115. Fonseca I.T.E., José Feio M., Lino A.R., Reis M.A., Rainha V.L., 1998. *Electrochem. Acta,* 43, 213-222.

116. Ford T.E., Mitchell, 1990. In: Marshall K.C. (ed.) *Advance in Microbial Ecology.* Plenum Press, New York, pg. 231-262.

117. Franklin M.J., Nivens D.E., Vass A.A., Mittelman M.W., Jack R.F., Dowling N.J.E., White D.C., 1991. *Corrosion,* 47, 128-135.

118. Franklin M.J., White D.C., Isaacs H.S., 1991. *Corros. Sci.,* 32, 945-952.

119. Franklin M.J., White D.C., Isaacs H.S., 1992. *Corros. Sci.*, 33, 251-260.

120. Franklin T.J., Snow G.A. (eds.), 1981. *Biochemisty of Antibacterial Action,* Chapman and Hall, London, pg. 58.

121. Froslashlund B., Palmgren R. Keiding K., Nielsen P.H., 1996. *Wat. Res.*, 30, 1749-1758.

122. Fu G.D., Shang Z.H., Hong L., Kang E.T., Neoh K.G., 2005. *Macromolecules*, 38, 7867-7871.

123. Gaines R.H., 1910. *J. Engineer Ind. Chem.*, 2, 128-130.

124. Gallardo J., Durán A., de Damborenea J.J., 2004. *Corros. Sci.,* 46, 795-806.

125. Gaylarde C.C., Videla H.A., 1992. In: *1st Pan-American Congress on Corrosion and Protection (AAC-NACE)*, Mar del Plata, Argentina, pg. 371-378.

126. Geesey G.G., Bremer P.J., 1990. *Mar. Technol. Soc. J.,* 24, 36-43.

127. Geesey G.G., Jiang L., 1985. In: Ehrlich H. L., Brierley C. L. (eds.) *Microbial Mineral Recovery,* McGraw-Hill, New York, pg. 223-247.

128. Geesey G.G., Mittleman M.W., Iwaoka T., Griffiths P.R., 1986. *Mater. Perf.*, 25, 37-40.

129.Geesey G.G., Gillis R.J., Avci R., Daly D., Hamilton M., Shope P., Harkin G., 1996. *Corros. Sci.*, 38, 73-95.

130. Geiser, M.; Avci, R.; Lewandowski, Z. 2002. *Int. Biodeter. Biodegr.* 49, 235-243.

131. George R.P., Muraleedharan P., Sreekumari K.R., 2003. *Biofouling*, 19, 1-8.

132. George R.P., Muraleedharan P., Parvathavarthini N., Khatak H.S., Rao T.S., 2000. *Mater. Corros.*, 51, 213-218.

133. Gerchakov S. M., Little B., Wagner P., 1986. *Corrosion,* 42, 689-692.

134. Gibson G.R., 1990. *J. Appl. Bacteriol.*, 69, 769-797.

135. Glick B.R., Martin W.G., Martin S.M., 1980. *Can. J. Microbiol.,* 26, 1214-1223.

136. González J.E.G., Santana F.J.H., Mirza-Rosca J.C., 1998. *Corros. Sci.,* 40, 2141-2154.

137. Gristina A.G., Hobgood C., Webb L., Myrvik Q., 1987. *Biomaterials,* 46, 423-426.

138. Gubner R., Beech I.B., 2000. *Biofouling*, 15, 25-26.

139. Guiamet P.S., Gómez de Saravia S.G., 2005. *Lat. Am. Appl. Res.*, 35, 295-300.

140. Guiamet P.S., Gómez de Saravia S.G., Videla H.A., 1999. *Intl. Biodeter. Biodegr.,* 43, 31-35.

141. Hadley R.F., 1948. In: Uhlig H.H. (ed.) *Corrosion Handbook.* John wiley, New York, pg. 466-481.

142. Hakkarainen T. J., 2003. *Materials Corros.,* 54, 503-509.

143. Hamilton W.A., 1985. *Annu. Rev. Microbiol.*, 39, 195-217.

144. Hamilton W.A., 1990. In: Dowling N., Mittleman M.W., Danko J. (eds.) *Microbially Iinfluenced Corrosion and Biodeterioration.* The University of Tennessee, Knoxville, pg. 1-4.

145. Hamilton W.A., 2003.*Biofouling*, 19, 65-76.

146. Hamilton W.A., 1994. In: Geesey G.G., Lewandowski Z., Flemming H.C. (Eds.), *Biofouling and Biocorrosion in Industrial Water Systems*. Lewis Publishers, Boca Raton, Florida, pg. 27-36.

147. Hansen T.A., 1993. In: Odom J.M., Singleton R.J. (eds.) *The Sulfate-reducing Bacteria: Contemporary Perspective*. Springer-Verlag, New York, pg. 21-40.

148. Hemandez G., Kucera V., Thierry D., Pedersen A, Hermansson M., 1994. *Corrosion*, 50, 603-608.

149. Hermansson M., 1999. *Colloids Surf. B*, 14, 105-119.

150. Hermas A.A., Nakayama M., Ogura K., 2005. *Electrochim. Acta,* 50, 2001-2007.

151. Hilberta L.R., Bagge-Ravnb D., Koldc J., Gramb L., 2003. *Int. Biodeter. Biodegrad,* 52, 175-185.

152. Hoar T.P., 1947. *Disc. Faraday Sot.* 1, 299-306.

153. Hogt A.H., Dankert J., Feijen J., 1986. *J. Biomed. Mater. Res.,* 20, 533-545.

154. Hu F.X., Keoh K.G., Cen L., Kang E.T., 2006. *Biomacromolecules,* 7, 809-816.

155. Huang G.T., Chan K.Y., Fang H.H.P, 2004. *J. Electrochem. Soc.,* 151, B434-B439.

156. Hwang K.E., Choi S.P., Shin K., Kim C.S., 2002. In European MRS Meeting, *Micro-structured Biomaterial Surfaces*, France, R/P No. 5.

157. Ichinose I., Senzu H., Kunitake T., 1996. *Chem. Lett.,* 37, 831-832.

158. Iverson W.P., 1966. *Science,* 151, 986-988.

159. Iverson W.P., 1968. *Adv. Appl. Microbiol.*, 32, 1-36.

160. Iverson W.P., 1968. *Nature*, 217, 1265-1267.

161. Iverson I.P., Olson G.J., 1983. In: *Microbial Corrosion*, Metals Society, London, pg. 46-53.

162. Iverson I.P., Olson G.J., Heverly L.F., 1986. In: *Proceedings of the International Conference on Biologically Induced Corrosion*. NACE, Houston, Texas, pg. 154-161.

163. Iverson W.P., 1987. *Adv. Appl. Microbio.*, 32, 1-36.

164. Iverson W.P., 2001. *Intl. Biodeter. Biodegrad.,* 47, 63-70.

165. Jack R.F., Ringelberg D.B., White D.C., 1992. *Corros. Sci.,* 33, 1843-1853.

166. Jack T.R., Rogoz E., Bramhill B.J., Roberge P.R., 1994. In: Kearns J.R., Little B.J. (ed.) *Microbially Influenced Corrosion Testing,* American society for testing of materials, pg. 108-117.

167. Jack T.R., Van Boven G., Wilmott M., 1996. *Mater. Performance,* 35, 39–45.

168. Jack T.R., Westlake D.W.S., 1995. In: Barton L.L. (ed.) *Biotechnology Handbooks,* Plenum Press, London, Vol. 8, pg. 264-292.

169. Jayaraman A. Cheng E.T., Earthman J.C., Wood T.K., 1997a. *Appl. Microbiol. Biotechnol.,* 48, 11-17.

170. Jayaraman A. Earthman J.C., Wood T.K., 1997b. *Appl. Microbiol. Biotechnol.,* 47, 62-68.

171. Jayaraman A., Cheng E.T., Earthman J.C., Wood T.K., 1997c. J. *Ind. Microbiol.,* 18, 396-401.

172. Jayaraman A., Hallok P.J., Carson R.M., Lee C.C., Mansfeld F.B., Wood T.K., 1999. *Appl. Microbiol. Biotechnol,* 52, 267-275.

173. Johansson L. S., Saastamoinen T., 1999. *Appl. Surf. Sci.,* 145, 244-248.

174. Jolley J.G., Geesey G.G., Hankins M.R., Wright R.B., Wichlacz P.L., 1989. *Appl. Spectrosc.*, 43, 1062-1067.

175. Jones D.A., 1996. In: *Principles and Prevention of Corrosion,* Upper Saddle River, NJ, Prentice Hall, pp 209-220.

176. Jones D.A.; Amy P.S., 2002. *Corrosion,* 58, 638-645.

177. Jones-Meehan J., Cofield J.W., Little B.J., Ray R.I., Wagner P.A., McNeil M., Mckay J., 1995. In: Angell P., Borenstein S.W., Buchanan R.A., Dexter S.C. (eds.) *International Conference on Microbially Influenced Corrosion*. NACE International, Houston, pg.1-12.

178. Kato C., Ateya B.G., Castle J.E., Pickering H.W., 1980. *J. Electrochem. Soc.,* 127, 1897-1903.

179. Kawabata N., 1992. *Prog. Polym. Sci.*, 17, 1-34.

180. Kear G., Barker B. D., Walsh F. C., 2004. *Corros. Sci.,* 46, 109-135.

181. Keresztes Z., Telegdi J., Beczner J., Kalman E., 1998. *Electrochim. Acta*, 43, 77-85.

182. King R.A., Miller J.D.A., 1971. *Nature,* 233, 491-492.

183. King R.A., Miller J.D.A., Smith J.S., 1973. *Brit. Corros. J.,* 8, 137-141.

184. King R.A., Wakerley D.S., 1973. *Br. Corros. J.*, 8, 41-45.

185. Kinzler K., Cehrke T., Telegdi J., Sand W., 2003. *Hydrometallurgy*, 71, 83-88.

186. Kjellerup B.V., Olesen B.H., Nielsen J.L., Frolund B., Odum S., Nielsen P.H., 2003. *Wat. Sci Technol*, 47, 117-122.

187. Koch, G.H., Brongers M.P.H., Thomson N.G., Virmani Y.P., Payer J.H., 2002. *Mater. Performance* (supp.), pg. 1-12.

188. Kwok D.Y., Gietzelt T., Grundke K., Jacobasch H.J., Neumann A.W., 1997. *Langmuir*, 13, 2880-2894.

189. Lawrence J.R., Wolfaardt G.M., Korber D.R., 1994. *Appl. Environ. Microbiol.* 60, 1166–1173.

190. Lee W., Charaklis W.G., 1992. *Corrosion*, 49, 186–199.

191. Lee W., De Beer D., 1995. *Biofouling*, 8, 273-280.

192. Lee W., Lewandowski Z., Nielsen P.H., Hamilton W.A., 1995. *Biofouling*, 8, 165-194.

193. Lewandowski Z., 1994. In: Geesey G.G., Lewandowski Z., Flemming H.C. (Eds.), *Biofouling and Biocorrosion in Industrial Water Systems.* Lewis Publishers, Boca Raton, Florida, pg. 175-188.

194. Lewandowski Z., Dickinson W., Lee W., 1997. *Wat. Sci, Technol.* 36, 295-302.

195. Lewandowski Z., Funk T., Roe F., Little B.J., 1994. In: Kearns J. R., Little B. J. (eds.). *Microbiologically Influenced Corrosion Testing, ASTM*, STP 1232, Philadelphia, PA, pg. 61-69.

196. Lewandowski Z., Lee W.C., Characklis W.G., Little B.J., 1988. Paper No.93, *Corrosion 88*, NACE international. Houston, TX.

197. Lewandowski Z., Lee W.C., Characklis W.G., Little B.J., 1989. *Corrosion*, 45, 92-98.

198. Li F., Harris B., Urrutia M.M., Beveridge T.J., 1994. *Appl. Environ. Microbiol.*, 60, 1525-1531.

199. Li P, Ohtsuki C., Kokubo T., Kazuki N., Naohiro S., de Grook K., 1994. *J. Biomed. Mater. Res.,* 28, 227-236.

200. Li P., Groot K., 1993. *J. Biomed. Mater. Res.,* 27, 1495-1500.

201. Li Y., Baba Y., Sekiguchi T., 2001. *Corros. Sci.,* 43, 903-917.

202. Lin J., Qiu S.Y., Lewis K., Klibanov A.M., 2002. *Biotechnol. Prog.,* 18,1082-1086.

203. Lin J., Tiller J.C., Lee S.B., Lewis K., Klibanov A.M., 2002. *Biotechnol. Lett.,* 24, 801-805.

204. Linhardt P., 1997. *Biodegradation*, 8, 201-210.

205. Little B.J., Ray R.I., Pope R.K., 2000. *Corrosion*, 56, 433-443.

206. Little B.J., Staehle R., Davis R., 2001. *Int. Biodeter. Biodegrad.*, 47, 71-77.

207. Little B.J., Wagner P.A., 1997. *Mater. Performance*, 36, 40-44.

208. Little B.J., Wagner P.A., 1995. *Mater. Sci. Forum*, 192, 433-446.

209. Little B.J., Wagner P.A., Mansfeld F., 1991. *Intl. Mater. Rev.*, 36, 253-271.

210. Little B.J., Wagner P.A., Mansfeld F., 1992. *Electrochim. Acta*, 37, 2185-2194.

211. Little B.J., Lee J.S., Ray R.I., 2006. *Corrosion*, 62, 1006-1017.

212. Little B.J., Mansfeld F., 1991. *Mater. Corrosion*, 42, 331–340.

213. Little B.J., Ray R., Wagner P., Jones-Mehan J., Lee C.C., Mansfeld F., 1999. *Biofouling*, 13, 253-272.

214. Little B.J., Ray R., 2002. *Corrosion*, 58, 424-428.

215. Little B.J., Wagner P.A., Lewandowski Z., 1998. In: Gaylarde C.C., Barbosa T.C.P., Gabilan N.H. (eds.), *LABS 3*,The British Phycological Society, UK, Paper No. 50.

216. Little B.J., Wagner P.A., Characklis W.G., Lee W., 1990. In: Characklis W. G., Marshall K. C. (Eds.), *Biofilms*. Wiley, New York, pp. 635-670.

217. Little B.J., Wagner P.A., Mansfeld F., 1997. In: *Microbiologically Influenced Corrosion, Corrosion Testing Made Easy*, Vol. 5. NACE, Houston. pg. 1-4, 29-52.

218. Little, B.; Ray, R.; Wagner, P.; Jones-Meehan, J.; Lee, C. Mansfeld, F., 1999. *Biofouling*, 13, 301-321.

219. Liu J.X., Yang D.Z., Shi F., Cai Y.J., 2003. *Thin Solid Films*, 429,225-230.

220. Liu X., Neoh K.G., Zhao L.P., Kang E.T., 2002. *Langmuir*, 18, 2914-2921.

221. Ma H.Y., Chen S.H., Zhao S.Y., Liu X.Q., Li D.G., 2001. *J. Electrochem. Soc.*, 148, B482-B488.

222. Macdonald J.R., 1987. In: *Impedance Spectroscopy – Emphasizing Solid Materials and Systems*, Wiley, New York, chapter 1-4.

223. Manian L., Hutt J.W., 2001. *Mater. Performance*, 40, 26-29.

224. Mansfeld. 1981. *Corrosion*, 37, 301-307.

225. Mansfeld F., Little B., 1991. *Corros. Sci.*, 32, 247-272.

226. Mansfeld F., Wang Y., Lin S.H., Xiao H., Shi H., 1993. In: Scully J. R., Silverman D. C., Kendig M. W. (eds.) *Electrochemical Impedance: Analysis and Interpretation*, ASTM, STP 1188, Philadelphia, PA, pg. 297-312.

227. Mansfeld F., Liu G., Xiao H., Tsai C.H., Little B.J., 1994. *Corros. Sci.*, 36, 2063-2095.

228. Mansfeld F., Little B., 1999. *Electrochim. Acta,* 37, 2291-2297.

229. Mansfeld F., Xiao H., 1994a. In: Kearns J.R., Little B. (eds.) *Microbiologically influenced corrosion testing*, *ASTM, STP 1232*. ASTM, Philadelphia, pg. 265-287.

230. Mansfeld F., Xiao H., 1994b. In: Kearns J.R., Little B. (eds.) *Microbiologically influenced corrosion testing*, *ASTM, STP 1232*. ASTM, Philadelphia, pg. 42-60.

231. Mara D.D., Williams D.J.A., 1972. *Biodeterior. Mater.*, 2, 103-113.

232. Marshall K.C., 1994. In: Geesey G.G., Lewandowski Z., Flemming H.C. (Eds.), *Biofouling and Biocorrosion in Industrial Water Systems.* Lewis Publishers, Boca Raton, Florida, pg. 15-26.

233. McCafferty E. 1997. *Corros. Sci.* 39, 243-254.

234. Mcdonnell G., Russell A.D., 1999. *Clin. Microbiol. Rev.*, 12, 147-179.

235. McNeil N.B. Little B.J., 1990. *Corrosion*, 46, 599-600.

236. Metosh-dickey C.A., Portier R.J., Xie X.G., 2004. *Mater. Performance*, 43, 30-34.

237. Miller. J.D.A., Metals, 1981. In: Rose A.H. (ed.) *Microbial Biodeterioration*, Academic Press, London, chapter 6, pg. 87.

238. Miranda E., Bethencourt M., Botana F.J., Cano M.J., Sánchez-Amaya J.M., Corzo J., 2006. *Corros. Sci.*, 48, 2417-2431.

239. Monk P.M.S., 1998. *The Viologens: Physicochemical Properties and Synthesis and Applications of the Salts of 4,4'-Bipyridine*. John Wiley & Sons Ltd: Chichester.

240. Morales, J.; Esparza, P.; González, S.; Salvarezza, R.; Arévalo, M. P., 1993. *Corros. Sci.,* 34, 1531-1540.

241. Moreno D.A., de Mele M.F.L., Ibars J.R., Videla H.A., 1991. *Corrosion*, 47, 2-9.

242. Moreno D.A., Ibars J.R., Beech I.B., Gaylarde C.C., 1993. *Bioufouling*, 7, 129-139.

243. Mueller R.F., Characklis W.G., Jones W.L., Sears J.T., 1992. *Biotechnol. Bioeng.*, 39, 1161-1170.

244. Mullet M., Boursiquot S., Abdelmoula M., Genin J.M., Ehrhardt J.J., 2002. *Geochem. Cosmochim. Acta,* 66, 829-836.

245. Mustin C., de Donato P.H., Benott R., Erre R., 1993. *Appl. Surf. Sci.,* 68, 147-158.

246. Nagiub A., Mansfeld F., 2002. *Electrochem. Acta.*, 47, 2319-2333.

247. Nakagawa T., Ogawa K., 1994. *Langmuir,* 10, 525-529.

248. Nakagawa Y., Hayashi H., Tawaratani T., Kourai H., Horie T., Shibasaki I., 1984. *Appl. Environ. Microb.,* 47, 513-518.

249. Nakagawa Y., Yamano Y., Tawaratani T., Kourai H., Horie T., Shibasaki I., 1982. *Appl. Environ. Microbiol.*, 43, 1041-1050.

250. Nanci A., Wuest J.D., Peru J., Brunet P., Sharma V., Zalzal S., Mckee M.D., 1998. *J. Biomed. Mater. Res.*, 40, 324-335.

251. Natishan P.M., Jones-Meehan J., Loab G.I., Little B.J., Beard M., 1999. *Corrosion*, 55, 1062-1068.

252. Neu T.R., Lawrence J.R., 1999. In: Wingender J., Neu T.R., Flemming H.C. (eds.) *Microbial Extracellular Polymeric Substances: Characterization, Structure and Function*. Springer, Berlin, pg. 21-42.

253. Newman R.C., Webster B.J., Kelly R.G., 1991. *ISIJ Int.*, 31, 201-209.

254. Ng S.W., Neoh K.G., Wong Y.T., Sampanthar J.T., Kang E.T., 2001. *Langmuir,* 17, 1766-1772.

255. Nielsen P.H., Jahn A., Palmgren R., 1997. *Wat. Sci. Technol.,* 36, 11-19.

256. Nivens, D.E., Anderson T.R., Chambers J.Q., and White D.C., 1991. *Microcontamination/91.* San Jose, pg.14-17.

257. O'Laire C., Timmins B., Kremer L., Holmes J.D., Morris M.A., 2006. *Anal. Lett.,* 39, 2255-2271.

258. Oblinger J.L., Koburger J.A., 1975. *J. Milk Food Technol.*, 38, 540-545.

259. Odom J.M., Peck Jr. H.D., 1981. *FEMS Microbiol. Lett.,* 12, 47-50.

260. Odom J.M., Peck Jr. H.D., 1984. *Annu. Rev. Microbiol.*, 38, 551-592.

261. Olefjord I., Wegrelius L., 1990. *Corros. Sci.*, 31, 89-98.

262. Olsson C.O.A., Hürnström S.E., 1994. *Corros. Sci.,* 36, 141-151.

263. Örnek D., Jayaraman A., Wood T.K., Sun Z., Hsu C.H., Mansfeld F., 2001. *Corros. Sci.,* 43, 2121-2133.

264. Örnek D., Wood T.K., Hsu C.H., Mansfeld F., 2002a. *Corros Sci,* 44, 2291-2302.

265. Örnek D., Wood T.K., Hsu C.H., Sun Z., Mansfeld F., 2002b. *Corrosion,* 58, 761-767.

266. Pak P.R., Lee H.J., Kim Y.K., Oh Y.S., Choi S.C., 2003. *J. Microbiol. Biotechnol*, 13, 937-941

267. Palit A., Pehkonen S.O., 2000. *Corros. Sci.,* 42, 1801-1822.

268. Pankhania I.P., 1988. *Biofouling,* 1, 27-47.

269. Pedersen A, Hermansson M., 1989. *Biofouling,* 1, 313–322.

270. Pedersen A, Hermansson M., 1991. *Biofouling,* 3, 1-11.

271. Pedersen A., Kjelleberg S., Hermansson M., 1988. *J. Microbiol. Methods*, 8, 191-198.

272. Peltola T., Rahiala P., Kangasniemi I., Yli-Urpo A., 1998. *J. Biomed. Mater. Res.,* 41, 504-510.

273. Pendyala J., Avci R., Geesey G.G., Stoodley P., Hamilton M., Harkin G., 1996. *J. Vac. Sci. Technol A,* 14, 1755-1760.

274. Peng C.G., Park J.K, 1994. *Wat. Res.,* 28, 1681-1692.

275. Pope D.H., Duquette D.J., Johannes A.H., Wagner P.C., 1984. *Mater. Performance*, 23, 14-18.

276. Pope D.H., 1986. In: *A Study of MIC in Nuclear Power Plants and a Practical Guide for Countermeasure*', Final Rep. NP-4582, Electric Power Research Institute, Palo Alto, CA.

277. Pope D.H., Zintel T.P., Aldrich H., Duquette D., 1990. *Mater. Performance,* 29, 49-55.

278. Postgate J.R., 1984. *The Sulfate-reducing Bacteria*, 2nd ed., Cambridge University Press, Cambridge, London, UK.

279. Pradier C.M., Bertrand P., Bellon-Fontaine M.N., Compère C., Costa D., Marcus P., Poleunis C., Rondot B., Walls M.G., 2000. *Surf. Interface Anal.*, 30, 45–49.

280. Prasad R., 1998. *Cororsion/98,* NACE international, Houston, TX, paper No. 276.

281. Pratt A.R., Nesbitt H.W., Mycroft J.R., 1996. *J. Geochem. Explor.,* 56, 1-11.

282. Rabus R., Hansen T., Widdel F., 2000. In: Dworkin M., Falkow S., Rosenberg E., Schleifer K.H., Stackebrandt E. (eds.) *The Prokaryotes: an Evolving Electronic Resource for the Microbiological Community.* Springer-Verlag, New York.

283.Rao T.S., Nair K.V.K., 1998, *Corros. Sci.* 40, 1821-1836.

284. Rao T.S., Kora R.J., Anupkumar B., Narasimhan S.V., Feser R., 2005. *Corros. Sci.,* 47, 1071-1084.

285. Revie R.W., 2000. In: Uhlig's corrosion hankdbook. 2nd Ed., John Wiley & Sons, Inc.

286. Rohwerder T., Gehrke T., Kinzler K., Sand W., 2003. *Appl. Microbiol. Biotechnol.,* 63, 239-248.

287. Rouxhet P.G., Genet M.J., 1991. In: Mozes N., Handley P.S., Busscher H.J., Rouxhet P.G. (eds.) *Microbial Cell Surface Analysis: Structural and Physico-chemical Methods,* VCH, New York, pg. 173-220.

288. Rouxhet P.G., Mozes N., Dengis P.B., Dufrêne Y.F., Gerin P.A., Genet M.J., 1994. *Colloids Surf. B: Biointerface,* 2, 347-369.

289. Ruppel D.T., Dexter S.C., Luther G.W., 2001. Corrosion, 57, 863-873.

290. Salvarezza R.C., de Male M.F.L., Videla H.A., 1983. *Corrosion*, 39, 27-32.

291. Sanders P.F., Hamilton W.A., 1986. In: *Biologically Induced Corrosion,* National Association of Corrosion Engineers, Houston, TX, pg 47.

292. Santana Rodríguez J.J., Santana F.J.H., González J.E.G., 2006. *Corros. Sci.,* 48, 1265-1278.

293. Santegodeds C.M., Schramm A., de Beer D., 1999. *Biodegradation,* 9, 159-167.

294. Sato N., 1990. *Corros. Sci.,* 31, 1-19.

295. Schiller C.A., Strunz W., 2001. *Electrochim. Acta,* 46, 3619-3625.

296. Schmitt G., 1991. *Corrosion,* 47, 285-308.

297. Schmitt J., Flemming H.C., 1996. In: Flemming H.C., Sand W. (eds.) *Microbially Influenced Corrosion of Materials.* Springer-Verlag, Berlin, pg. 143-157.

298. Schreiber D.R., Miller F.J., Gorden A.S., 1990. *Mar. Chem.,* 28, 275-281.

299. Schutz R.W., 1991. *Mater. Performance,* 30, 58-61.

300. Schutz R.W., 1992. *Mater. Performance,* 31, 57-62.

301. Schweinsberg D.P., Ashworth V., 1988. *Corros. Sci.,* 28, 539-545.

302. Scott J.F.D., 1993. *Corros. Sci.,* 35, 667-673.

303. Scott P.J.B., Davies M., 1992. *Mater. Performance,* 31, 64-68.

304. Scotto V., Lai M.E., 1998. *Corros. Sci.,* 40, 1007-1018.

305. Seed L.J., 1990. *Corros. Rev.,* 9, 3-101.

306. Shalaby H. M., Hasan A.A., Al-Sabti F., 1999. *Br. Corros. J.,* 34, 292-298.

307. Shi X., Avci R., Geiser M., Lewandowski Z., 2003. *Corros. Sci.,* 45, 2577-2595.

308. Shi Z.L., Neoh K.G., Kang E.T., 2005. *Biomaterials,* 26, 501-508.

309. Shoesmith D.W., Taylor P., Bailey M.G., Owen D.G., 1980. *J. Electrochem. Soc.,* 127, 1007-1015.

310.Smillie R.H., Hunter K., Loutit M. 1981. *Water Res.*, 5, 1351-1354.

311. Siedlarek H., Wagner D., Fischer W.R., Paradies H.H., 1994. *Corros. Sci.,* 36, 1751-1763.

312. Sreekumari K.R., Sato Y., Kikuchi Y., 2005. *Mater. T. JIM.,* 46, 1636-1645.

313. Starkey, R.L., Wright K.M., 1945. In: *Anaerobic Corrosion of Iron in Soil,* American Gas Association, New York.

314. Steele A., Goddard D.T., Beech I.B., 1994. *Int. Biodeter. Biodegrad.,* 33, 35-46.

315. Sukamto J.P.H, Smyrl W.H., Casillas N., Odan M.A.L., James P., Jin W., Douglas L., 1995. *Mater. Sci. Eng. A,* 198, 177-196.

316. Sung M.M., Sung K., Kim C.G., Lee S.S., Kim Y.S., 2000. *J. Phys. Chem. B,* 104, 2273-2277.

317. Syrett B. C., 1981. *Corros. Sci.* 21, 187-209.

318. Tait W.S., 1978. *Corrosion,* 34, 214-217.

319. Tait W.S., 1979. *Corrosion,* 35, 296-300.

320. Tait W.S., 1994. In: *An Introduction to Electrochemical Corrosion Testing for Practicing Engineers and Scientists,* Ph.D thesis, University of Wisconsin-Madison, Racine, USA, pg. 79-115.

321. Tan Y.S., Srinivasan M.P., Pehkonen S.O., Chooi S.Y.M., 2006. *Corros. Sci.,* 48, 840-862.

322. Tebbji K., Oudda H., Hammouti B., Benkaddour M., El Kodadi M., Ramdani A., 2005. *Colloid Surface A,* 259, 143-149.

323. Thompson I., Campbell D., 1994. *Corros. Sci.,* 36, 187-198.

324. Tide C., Harkin S.R., Geesey G.G., Bremer P.J., Scholz W., 1999. *J. Food Eng.,* 42, 85-96.

325. Tiller A.K., 1988. In: Sequeira C.A.C., Tiller A.K. (ed.) *Microbial Corrosion,* Elsevier Applied Science, London and New York, pg. 3-9.

326. Tiller J.C., Lee S.B., Lewis K., Klibanov A.M., 2002. *Biotechnol. Bioeng.,* 79, 465-471.

327. Tobin J.P., Hirshwald W., Cunningham J., 1983. *Appl. Surf. Sci.*, 16, 441-452.

328. Trzaskoma-Paulette P.P., Nazeri A., 1997. *J. Electrochem. Soc.*, 144, 1307-1310.

329. Tuovinen O.H., Kelly D.P., 1974. *Arch. Microbiol.*, 98, 351-358.

330. Uhlig, H.H, 1995. *Corrosion and Corrosion Control*, 3rd ed. Wiley, New York, pg. 2.

331. Vaidya R.U., Brozik S.M., Deshpande A., Hersman L., Butt D.P., 1999. *Metall. Mater. Trans. A,* 30, 2129-2134.

332. Vaidya R.U., Butt D.P., Hersman L.E., Zurek A.K., 1997. *Corrosion,* 53, 136-141.

333. Valcarce M.B., de Sánchez S.R., Vázquez M., 2005. *Corros. Sci.,* 47, 795-809.

334. Valcarce M.B., de Sanchez S.R., Vazquez M., 2006. *Electrochim. Acta,* 51 (18), 3736-3742.

335. Vallet-Regi M., Izquierdo-Barba I., Gil F.J., 2003. *J. Biomed. Mater. Res. A,* 67A, 674-678.

336. Van der Aa B.C., Dufrêne Y.F., 2002. *Colloids Surf. B: Biointerface,* 23, 173-182.

337. Varga K., Baradlai P., Barnard W.O., Myburg G., Halmos P., Potgieter J.H., 1997. *Corros. Sci.*, 42, 25-35.

338. Vasudevan T., Muralidharan S., Alwarappan S., Iyer S.V.K., 1995. *Corros. Sci,* 37, 1235-1244.

339. Verran J., Boyd R.D., 2001. *Biofouling*, 17, 59-71.

340. Videla H.A., 1995. In: Gaylarde C.C., Videla H.A. (eds.) *Bioextraction and Biodeterioration of Metals.* Cambridge University Press, Cambridge, UK, pg. 85-127.

341. Videla H.A., 1996. In: *Manual of Biocorrosion,* Lewis Publishers, CRC Press Incorporated, Boca Raton, FL, pg.129-132.

342. Videla H.A., 2000. *Biofouling,* 15, 37-47.

343. Videla H.A., 2001. *Intl. Biodeter. Biodegrad.,* 48, 176-201.

344. Videla H.A., 2002. *Int. Biodeter. Biodegrad.,* 49, 259-270.

345. Videla H.A., Characklis W.C., 1992. *Int Biodeter Biodegrad.,* 29, 195-212.

346. Videla H.A., Gómez de Saravia G.G., de Mele M.F.L., 1992. In: *Corrosion/92,* paper No. 189, NACE International, Houston, TX.

347. Videla H.A., Herrera L.K., 2005. *Int. Microbiol.,* 8, 169-180.

348. Volk C., Dundore E., Schiermann J., Lechevallier M., 2000. *Wat. Res.,* 34, 1967-1974.

349. Von Wolzogen Kuehr C.A.H., Van der Vlugt I.S., 1934. *Water,* 18, 147-165.

350. Wagner C.D., Moulder J.F., Davis L.E., Riggs W.M., 1992. In: *Handbook of X-ray Photoelectron Spectroscopy,* Perking-Elmer Corp., Physical Electronics Division; Minnesota.

351. Wagner C.D., Chamberlain A.H.L., Fisher W.R., Wardell J.N., Sequeria C.A.C., 1997. *Mater. Corros.*, 48, 311-321.

352. Wagner P., Little B., 1993. *Mater. Performance,* 32, 65-68.

353. Walker J.T., Keevil C.W., 1994. *Int. Biodeter. Biodegrad.,* 33, 223-236.

354. Wallinder D., Pan J., Leygraf C., Delblanc-bauer A., 1999. *Corros. Sci.,* 41, 275-289.

355. Walsh D., Pope D., Danford M., Huff T., 1993. *JOM,* 45, 22-30.

356. Wang J.H., Wei F.I., Shih H.C., 1996. *Corrosion,* 52, 900-909.

357. Wang Y.Z., Beccaria A.M., Poggi G., 1994. *Corros. Sci.*, 36, 1277-1288.

358. Webster B.J., Werner S.E., Wells D.B., Bremer P.J., 2000. *Corrosion,* 56, 942-950.

359. Whelan C.M., Kinsella M., Ho H.M., Maex K., 2004. *J. Electrochem. Soc.*, 151, B33-B38.

360. Widdel F., In: Zehnder A.J.B. (ed.) *Biology of Anaerobic Microorganisms*. John Wiley, New York, pg. 469-585.

361. Widdle F., Bak F., 1992. In: Balows A., Trüper H.G., Dworkin M., Harder W., Schleifer K.H. (eds.) *The Prokaryotes*, 2nd ed. Vol. 1, Springer-Verlag, New York, pg. 2252-3378.

362. Wikjord A.G., Rummery T.E., Doern F.E., Owen D.G., 1980. *Corros. Sci.,* 20, 651-671.

363. Wingender J., Neu T.R., Flemming H.C., 1999. In: Wingender J., Neu T.R., Flemming H.C. (eds.) *Microbial Extracellular Polymeric Substances: Characterization, Structure and Function.* Spinger, Berlin, pg.1-19.

364. Xu C.M., Zhang Y.H., Cheng G.X., Zhu W.S., 2007. *Mat. Sci. Eng. B,* 443, 235-241.

365. Xu K., Dexter S.C., Luther G.W. 1998. *Corrosion*, 54, 814-823.

366. Xu L.C., 2001. In: *Anaerobic Corrosion of Mild Steel in Seawater Induced by Sulfate-reducing Bacteria (SRB)*, University of Hong Kong, PhD thesis, Hong Kong, China.

367. Xu L.C., Chan K.Y., Fang H.H.P., 2002. *Mater. Charact.,* 48, 195-203.

368. Xu L.C., Fang H.H.P., Chan K.Y., 1999. *J. Electrochem. Soc.,* 146, 4455-4460.

369. Xu X.J., Ma H.Y., Chen S.H., Xu Z.Y., Su A.F., 1999. *J. Electrochem. Soc.,* 146, 1847-1853.

370. Yu Z., Pehkonen S.O., 2004. *Water Sci. Technol.,* 49, 73-81.

371. Zhang T., Fang H.H.P., Ko B.C.B., 2003. *Appl. Microbiol. Biotechnol.,* 63, 101-106.

372. Zhang X., Bishop P.L., Kinkle B.K., 1999. *Wat. Sci. Technol.,* 39, 211-218.

373. Zhang X.H., Pehkonen S.O., Kocherginsky N., Ellis G.A., 2002. *Corros. Sci.,* 44, 2507-2528.

374. Zhang H.J., Dexter S.C. 1995. *Corrosion*, 51, 56-66.

LIST OF PUBLICATIONS

1. **S.J. Yuan,** S.O. Pehkonen, Y.P. Ting, E.T. Kang, K.G. Neoh, Corrosion behavior of type 304 stainless steel in a simulated seawater-based medium in the presence and absence of aerobic *Pseudomonas* NCIMB 2021 bacteria, ***Industry & Engineering Chemistry Research***, DOI: 10.1021/ie071536x**..**

2. **S.J. Yuan**, F.J. Xu, S.O. Pehkonen, Y.P. Ting, E.T. Kang, K.G. Neoh, Biocorrosion behavior of titanium oxide/butoxide-coated stainless steel, ***Journal of the Electrochemical Society*** **2008**, **155 (5): C196-C210.**

3. F.J. Xu, J. Li, **S.J. Yuan**, Z.X. Zhang, E.T. Kang, K.G. Neoh, Thermo-responsive porous membranes of controllable porous morphology from triblock copolymers of polycaprolactone and poly(*N*-isopropylacrylamide) prepared by atom transfer Radical polymerization, ***Biomacromolecules*****, 9 (1), 331 – 339, 2008.**

4. **S.J. Yuan**, A.M.F. Choong, S.O. Pehkonen, The influence of the marine aerobic *Pseudomonas* strain on the corrosion of 70/30 Cu-Ni alloy, ***Corrosion Science***, **49 (12), 4352-4385, 2007.**

5. **S.J. Yuan**, F.J. Xu, E.T. Kang, S.O. Pehkonen, Modification of surface-oxidized copper alloy by coupling of viologens for inhibiting microbiologically influenced corrosion, ***Journal of the Electrochemical Society***, **154 (11), C645-C657, 2007**.

6. **S.J. Yuan**, S.O. Pehkonen, Microbiologically influenced corrosion of 304 stainless steel by aerobic Pseudomonas NCIMB 2021 bacteria: AFM and XPS study, ***Colloids and Surfaces B-Biointerfaces***, **59 (1), 87-99, 2007**.

7. **S.J. Yuan**, S.O. Pehkonen, Surface characterization and corrosion behavior of 70/30 Cu-Ni alloy in pristine and sulfide-containing simulated seawater, ***Corrosion Science*****, 49 (3), 1276-1304, 2007.**

8. F.J. Xu, **S.J. Yuan,** S.O. Pehkonen, E.T. Kang, Antimicrobial surfaces of viologen-quaternized poly((2-dimethyl amino)ethyl methacrylate)-Si(100) hybrids from surface-initiated atom transfer radical polymerization, ***NanoBiotechnology***, 2 (3-4), 123-134 (2006).